

An Integrated Physics-based Approach to Demonstrate the
Potential of the Landsat Data Continuity Mission (LDCM)
for Monitoring Coastal/Inland Waters

by

Nima Pahlevan

B.S. K.N.Toosi University of Technology, 2003

M.S. K.N.Toosi University of Technology, 2006

A dissertation submitted in partial fulfillment of the
requirements for the degree of Doctor of Philosophy
in the Chester F. Carlson Center for Imaging Science

Rochester Institute of Technology

16 February 2012

Signature of the Author _____

Accepted by _____

Coordinator, Ph.D. Degree Program

DISSERTATION RELEASE PERMISSION
ROCHESTER INSTITUTE OF TECHNOLOGY
CHESTER F. CARLSON CENTER FOR IMAGING SCIENCE

Title of Dissertation:

**An Integrated Physics-based Approach to Demonstrate the Potential of the Landsat
Data Continuity Mission (LDCM) for Monitoring Coastal/Inland Waters**

I, Nima Pahlevan, hereby grant permission to Wallace Memorial Library of R.I.T. to reproduce my thesis in whole or in part. Any reproduction will not be for commercial use or profit.

Signature _____ Date _____

Abstract

Monitoring coastal or inland waters, recognized as case II waters, using the existing Landsat technology is somewhat restricted because of its low Signal-to-Noise ratio (SNR) as well as its relatively poor radiometric resolution. The new generation of Landsat, Landsat Data Continuity Mission (LDCM) carrying the Operational Land Imager (OLI) and the Thermal InfraRed Scanner (TIRS), has enhanced features allowing for a more lucid characterization of water constituents with respect to Landsat-7 in case II waters. Motivated by the LDCM, this research effort is comprised of three tasks.

As a primary task, we introduce a novel technique, which integrates the Landsat-7 data with a 3D hydrodynamic model to monitor the dynamics of coastal waters near river discharges as well as in a small lake environment. The proposed approach leverages both the thermal and the reflective Landsat-7 imagery to calibrate the model and to retrieve the concentrations of optically active components of the water. To do so, the model is first calibrated by optimizing its thermal outputs with the surface temperature maps derived from the Landsat-7 data. The constituent retrieval is conducted in the second phase where multiple simulated concentration maps are provided to an in-water radiative transfer code (Hydrolight) to generate modeled surface reflectance maps. The model-derived surface reflectances are optimized against that obtained from the Landsat-7 imagery to find the optimal solution, which minimizes the disparity between the model outputs and the Landsat-7 imagery. The calibrated model can be further used to capture the dynamics of coastal waters at instances at which no remote sensing imagery is available.

Prior to any remote sensing task, one has to ensure that a dataset comes from a well-calibrated imaging system. Although the calibration status of Landsat-7 has been regularly monitored over multiple desert sites, it was desired to evaluate its performance over dark waters relative to a well-calibrated instrument designed specifically for water studies. In the light of this, several Landsat-7 images were cross-calibrated against Terra-MODIS data over deep, dark waters whose optical properties remain relatively stable.

In an independent case study, the potential of the OLI sensor was examined using an EO-1 dataset to simulate the OLI data. This is accomplished via applying a spectral optimization approach over case II waters. The water constituent maps generated from the EO-1 imagery were compared against those derived from Landsat-7 to fully analyze the improvement levels pertaining to the OLI's enhanced features in a water constituent retrieval framework.

Acknowledgements

This work would not be feasible without the help from several individuals. I would like to thank my advisor, Dr. John Schott, for his insights and constructive comments regarding this project. His many years of experience in conducting novel research helped me to efficiently implement different tasks associated with this research topic.

I appreciate Dr. Anthony Vodacek's help with the laboratory measurements. I should acknowledge his support in the admission process in 2007, which eventually led to my dream come true. I would like to thank Dr. Carl Salvaggio for allowing me to be a part of his research team, who uses the research computing resource. Additionally, he was a great help in all aspects of my research and course works during the past years at RIT. I should also appreciate Dr. Frank Sciremammano for reviewing my dissertation.

I sincerely appreciate Dr. Alfred Garrett because of his tremendous help in developing the ALGE model, which resulted in significant improvements in the quality of the present document. I should also thank my fellow, Dr. Aaron Gerace, who initiated this project and assisted me in the early stages of this project. His thoughtful comments during the course of this research were always helpful. I am grateful to Mrs. Nina G. Raqueno for her technical support during the field measurements. I must also thank Dr. Rolando Raqueno for his everlasting encouragement and support in this research. I also acknowledge the help from the RIT's research computing center for maintaining the parallel computing system, which significantly facilitated my research progress.

I should appreciate my fellow officemates, Kelly Canham and James Albano, for their friendship and help with different aspects of my graduate work. I also thank Dr. Emmet Ientilucci and Dr. Mike Gartley for their assistance in understanding the concept behind the MODTRAN simulations. I appreciate Dr. Dave Messinger's support and encouragements of my work with the Digital Imaging and Remote Sensing Laboratory (DIRS). I should also thank Cindy Schultz for her smiley face during the past years and all of the help with travel arrangements. I also appreciate Amanda, Sharon, and Deb for all the administrative work they did for me. I also thank Dr. Christy Tyler in the Department of Biology at RIT, who

facilitated my laboratory measurements by giving me access to her laboratory. I am grateful to Upstate Freshwater Institute (UFI), in particular Ms. MarryGail Perkins and Mr. Christopher Strait, for the provision of data and help in the field campaign at Onondaga Lake in June 2011. I am also grateful to Mr. Stuart Frye at NASA GSFC for his efforts in getting me an EO-1 dataset to be able to perform the Task III of this project. I would like to tank Mr. Paul Yu at US Army Corps, Buffalo, and Fred Pierce at NOAA, Buffalo, for providing me with the data crucial in this study.

I am delighted to have friends, such as Pejman Farrokh and Farhad Moghare Abed, for their friendship and support during the fieldwork. I am also grateful to my girlfriend Mahsa for her support and love during the progress of my research.

Last but not least, I am lucky to have a great family. The love and the support from my parents, Ziba and Mozaffar, always made me strong to overcome the hurdles in my life. My sweet-hearted sister, Ronak, her husband, Shahab, and the little Shahrad always supported me in different ways over the past four years.

Nima Pahlevan

Dedicated to

My parents, Ziba and Mozaffar

Table of Contents

1.	Introduction.....	1
1.1.	Remote Sensing of Coastal Environments.....	1
1.2.	Remote sensing Integrated with Numerical Modeling	3
1.3.	Landsat Data Continuity Mission	5
2.	Objectives	7
2.1.	Work Statement	8
2.2.	Description of Tasks	8
2.2.1	Task I	8
2.2.2	Task II.....	9
2.2.3	Task III.....	9
2.3.	Contribution to the Field.....	10
3.	Background and Theory.....	12
3.1.	Driving forces for Monitoring Coastal and Inland Waters	12
3.2.	Great Lakes Hydrodynamics.....	13
3.2.1	Wind-Driven Processes.....	15
3.2.2	Coastal Boundary Layer (CBL).....	15
3.2.3	Thermal Bar	16
3.2.4	River Plume	16
3.3.	Numerical Modeling Coupled with Remote Sensing	18
3.4.	ALGE Model	20
3.4.1	Governing Equations	20
3.4.2	Mixing equations	21
3.4.2.1	Horizontal Eddy viscosity.....	21
3.4.2.2	Vertical Eddy Viscosity	23
3.4.3	Material Transport	23
3.4.4	Energy Transfer	24
3.4.4.1	Sensible and Latent Heat Transfer.....	24
3.4.4.2	Solar Radiation.....	24

3.4.4.3	Long-wave Radiation.....	25
3.4.5	Mass and Energy sources and sinks.....	26
3.4.6	Boundary conditions.....	26
3.4.7	Nudging.....	27
3.4.8	ALGE Input Data.....	28
3.4.9	New Capabilities in the ALGE Model (2011).....	30
3.5.	Remote Sensing of Water.....	30
3.5.1	Sensor-reaching Radiance.....	33
3.5.1.1	Reflective Paths.....	33
3.5.1.2	Thermal Paths.....	34
3.5.1.3	Governing Equation.....	35
3.5.2	Sensor.....	37
3.5.2.1	Signal-to-Noise Ratio (SNR).....	38
3.5.2.2	Quantization Rate.....	39
3.5.2.3	Spectral Response.....	39
3.5.2.4	Post-launch Calibration.....	40
3.5.3	Signal Components.....	41
3.5.3.1	Bottom.....	42
3.5.3.2	Water Constituents.....	43
3.5.3.3	Atmosphere.....	44
(a)	Atmospheric Absorption.....	44
(b)	Atmospheric Scattering.....	44
(c)	Atmospheric Effect Removal.....	46
3.5.3.4	Glint Effects.....	48
(a)	Sun glint.....	48
(b)	Sky Glint.....	49
3.5.4	Water Constituent Retrieval.....	51
3.5.4.1	Bio-optical Models.....	51
3.5.4.2	In-water Radiative Transfer Models.....	52
(a)	Inputs.....	54
(b)	Mathematical Model.....	54
3.6.	Concluding Remarks.....	55
4.	Methodology.....	57
4.1.	Overview.....	57
4.1.1	Cross-calibration.....	58
4.1.2	L7-Model Integration.....	59
4.1.3	OLI's Potential over Case II Waters.....	61
4.2.	L7-MODIS Cross-calibration.....	61
4.2.1	Calibration Sites.....	61
4.2.2	The Criteria for Image Pair Selection.....	63
4.2.3	Conversion to the TOA Reflectance.....	65

4.2.4	Adjustments for the RSR Functions	66
4.2.4.1	Modeling the Site-specific Diffuse Surface Reflectance (r_d)	67
4.2.4.2	Estimating the Atmospheric Condition.....	67
4.2.4.3	Applying the RSR Adjustment Factor	68
4.3.	L7-Model Integration.....	70
4.3.1	Study Areas.....	70
4.3.1.1	Genesee River	70
4.3.1.2	Niagara River	72
4.3.1.3	Onondaga Lake	73
4.3.2	Datasets	74
4.3.2.1	Bathymetry Maps.....	75
4.3.2.2	L7 Imagery.....	75
	(a) Identifying Sun Glint/ Atmospheric Effects Masking.....	76
4.3.3	Field Observations	79
4.3.3.1	Field/Laboratory Procedure	80
	(a) Concentration Measurements	81
	(b) Absorption Measurements.....	82
	(c) Estimating the Scattering Coefficients	89
4.4.	Retrieval of Surface Physical Properties from L7 Data.....	91
4.4.1	Temperature Retrieval	91
4.4.2	Surface Reflectance Retrieval.....	94
4.4.2.1	Empirical Line Method (ELM).....	94
4.5.	ALGE Simulations.....	96
4.5.1	River Plumes.....	97
4.5.1.1	Lake-wide Simulations	97
4.5.2	Model Stabilization (Long-term Simulations).....	103
4.5.3	Model Calibration	105
4.5.3.1	Cost Functions and Optimization.....	107
4.5.3.2	Sampling Scheme.....	109
4.5.3.3	Optimization	109
4.5.4	Constituent Retrieval	112
4.5.4.1	Sensitivity Analysis	113
4.5.4.2	Procedure	115
	(a) Estimating Background Concentrations	117
	(b) ALGE-derived 2D LUTs.....	117
	(c) Hydrolight Simulations	118
	(d) Error Calculation and Optimization	119
4.6.	OLI's Potential for Coastal Water Studies.....	120
4.6.1	Datasets and Study Area	121
4.6.2	Data Preparation.....	123
4.6.3	Atmospheric Compensation.....	126
4.6.4	Constituent Retrieval	127

4.6.4.1	Hydrolight Initialization.....	127
4.6.4.2	LUT Generation.....	127
4.6.4.3	Optimization.....	129
4.7.	Concluding Remarks.....	130
5.	Results.....	131
5.1.	L7-MODIS Cross-calibration.....	131
5.1.1	Over-water Cross-calibration.....	132
5.1.2	Over-land Cross-calibration.....	136
5.1.3	Impact of Calibration Errors on Surface Reflectance Retrieval.....	137
5.1.4	Impact of Calibration Errors on Concentration Retrieval.....	143
5.1.5	Summary.....	145
5.2.	L7-Model Integration.....	147
5.2.1	Long-term Simulations (Model Stabilization).....	147
5.2.1.1	Genesee River Plume.....	147
5.2.1.2	Niagara River Plume.....	152
5.2.1.3	Onondaga Lake.....	157
5.2.2	Model Calibration.....	162
5.2.2.1	River Plumes.....	162
5.2.2.2	Onondaga Lake.....	166
5.2.3	Constituent Retrieval.....	166
5.2.3.1	River plumes.....	166
5.2.3.2	Onondaga Lake.....	170
5.2.4	Summary.....	172
5.3.	OLI's Potential for the Retrieval of Water Constituents.....	173
5.3.1	Qualitative Comparison.....	174
5.3.2	Quantitative Comparison.....	180
5.3.3	Summary.....	186
6.	Conclusions and Recommendations.....	187
6.1.	Cross-calibration.....	188
6.2.	L7-Model Integration.....	189
6.3.	OLI's potential for Water Studies.....	191
6.4.	Recommendations.....	192
7.	Bibliography.....	i

List of Figures

Figure 3.1. Schematic diagram of coastal zone regions.....	14
Figure 3.2. L7 thermal image (April 2005). The thermal bar prevents exchange of material between the nearshore and offshore zones. (Courtesy of NASA)	17
Figure 3.3. The <i>igird.dat</i> file with 1's and 0's as water.....	27
Figure 3.4. Major photon paths contributing to the sensor-reaching radiance in the reflective portion of the spectrum [Gerace, 2010].	34
Figure 3.5. The major self-emission components forming total photons reaching the sensor [Gerace, 2010].....	35
Figure 3.6. The signal components reaching the sensor. Path III carries information of interest.....	41
Figure 3.7. The schematic illustration of sun and sky glint. Solid lines represent rays due to sun glint and dashed lines indicate rays reflected off the water surface due to the sky light.	50
Figure 3.8. The scattering and absorption coefficients for different types of particles observed in various types of waters. In general, the shapes of the absorption/scattering spectra show the same trends while the magnitudes vary as high as 50% and 400% for the scattering and absorption coefficients.....	55
Figure 4.1. The flowchart illustrating the model calibration process in the thermal domain.	60
Figure 4.2. The flowchart illustrating the process conducted in two steps, namely thermal and reflective modes.	60
Figure 4.3. Lake Tahoe is located in the high mountains of the western US on the Nevada-California border.....	61
Figure 4.4. The relative spectral response functions of L7 (solid lines).....	66
Figure 4.5. The study sites located in upstate New York, USA, shown in the red boxes. The river plumes enter southern shores of Lake Ontario.	71
Figure 4.6. The Genesee River watershed	71
Figure 4.7. The average CHL/TSS concentrations collected during the past six years for the Genesee River site (black bars represent concentrations at the Lakeside) [Makarewicz, 2010].	72
Figure 4.8. The Average CHL/TSS concentration collected during the past 6 years (dark bar represent concentrations at Lakeside) [Makarewicz, 2010].	73
Figure 4.9. The hydrological and morphological structure of Onondaga Lake.....	74

Figure 4.10. River plumes in the L7 imagery. The Genesee plume on Oct. 18 th (left) versus the Niagara plume on May 18 th (right).....	76
Figure 4.11. The SWIR band-ratio method for identifying glint or atmospherically contaminated areas. The lower values denote contaminated pixels. The images were locally averaged to obtain smoother transitions between different areas. The effected areas are specified with the arrows. The zoomed areas indicate the Rochester Embayment area where the Genesee River flows into the lake (black boxes).	78
Figure 4.12. Field stations visited on May 2010.....	81
Figure 4.13. The reflectance spectra (a) together with the absorption measurements of CHL (b), TSS (c), and CDOM (d) associated with the field campaigns at the Genesee site ..	84
Figure 4.14. The spectral absorption measurements (a) as well as the radiometric measurements of the surface-leaving reflectance (b) made at the Niagara River mouth in Oct. 2010.....	86
Figure 4.15. Field measurements conducted in June 2011 at the Onondaga Lake site. The CHL specific absorption spectra measured at the surface for seven different stations shown in (b). The surface reflectance (%) measured <i>in situ</i> for two station (SD and NE). The concentrations of profiles measured at SD are illustrated in (d).....	87
Figure 4.16. The best curves matching the measured spectra at the a) Genesee, b) Niagara, and c) Onondaga Lake sites.	89
Figure 4.17. The spectral transmission and the up-welled radiance for a single MODTRAN run	93
Figure 4.18. The Planck curve for a 15-degrees-Celsius pixel (a) propagated through the atmosphere (b).	93
Figure 4.19. The measured sand reflectance spectra (solid line) compared with the retrospective measurements (dotted-line) along with the simulated deep water reflectance from Hydrolight.....	95
Figure 4.20. ELM equations of four different bands. S indicates reflectance values and R corresponds to at-sensor radiance.....	96
Figure 4.21. The locations of the stations where the wind data are used to produce the 2D wind field	98
Figure 4.22. Model-derived, lake-wide simulation results (temperature) against the corresponding surface temperature obtained from the satellite observations. The model reasonably predicts the thermal structure of the lake. However, the model performance diminishes when the surface data are spatially heterogeneous. The units are in degrees-Celsius.....	99
Figure 4.23. A temperature map [° C] derived from a lake-wide simulation overlaid with the surface current velocity vectors. The filled circles show the nodes from which the nudging vectors are extracted for each river plume simulation.....	101
Figure 4.24. The surface current velocity magnitude and directions for the Aug 11 simulation. The upper frames correspond to the simulation with the originally observed	

wind data while the lower plots show the values resulting from the nudging oscillations in magnitude and direction after wind adjustments of the lake-wide simulation.	102
Figure 4.25. The wind data (a), the river discharge (b), and the air/dew point temperature (c and d) shown for July 2009 and Oct. 2010 simulations at the GN and NI sites. The GN simulation-time is 260 hours whereas that of NI is 240 hours.....	103
Figure 4.26. Onondaga creek's temperature and discharge (a) shown along with the air/dew point temperature (b) for the spring of 2010.....	105
Figure 4.27. Three sample instances of ALGE-generated thermal plumes by varying input environmental variables. Variable ranges are arbitrary and for illustration purposes.	107
Figure 4.28. The sampling areas drawn for the case studies in July 2009 (Genesee) and Oct. 2010 (Niagara) to evaluate the model performance in the thermal domain. Depending on the shape of the plume the sampling area can differ.....	109
Figure 4.29. The schematic LUT formed of three dimensions. The sparse sampling of the three axes demands further optimization to search for the optimal solution. The best output is modeled by re-running the model using the inputs found in the optimization process.....	110
Figure 4.30. The Nelder-Mead simplex search method showing the reflection (a), the expansion (b), outside (c)/inside (d) contraction, and shrinking (e) [Lagarias <i>et. al.</i> , 1998].	112
Figure 4.31. The variability of sediment concentration (log-transformed) with respect to particle size. Other inputs such as particle density ($PD= 2.5 \text{ gcm}^{-3}$) were constant. Particle sizes are (clockwise from upper left) 2, 4, 6 and 8 μm . The plots are log-transformed.	114
Figure 4.32. The sediment distribution maps (log-transform) with varying particle density. On the left, particle density is equal to 2.5 gcm^{-3} while it is 1.5 gcm^{-3} on the right map. Particle size in both cases was fixed to 4 μm	115
Figure 4.33. The study area covering the Niagara River plume (Section 4.3.1.2) discharging into the western basin of Lake Ontario. The red box ($\sim 100 \text{ km}^2$) indicates the study area.	121
Figure 4.34. The band-specific, normalized RSRs of L7, OLI, and ALI shown for different portions of the spectrum [nm]. The differences are discernable in all of the bands, in particular in the NIR band.....	123
Figure 4.35. The spectral scene-derived SNR shown for different instruments.....	124
Figure 4.36. The schematic diagram of the LUT generation.....	129
Figure 5.1. The historical cross-calibration trends of the relative differences between L7 and Terra-MODIS computed for Lake Tahoe and the tropical-arid (Tr-Ar) sites. The calibration differences in the blue and the green bands have increased in the recent years. The percent differences are expressed in units of TOA reflectance.....	132
Figure 5.2. The site-independent annually averaged historical cross-calibration trends of the relative differences between L7 and Terra-MODIS. The data points from both sites were	

averaged for each year. The error bars indicate the standard deviation associated with each year.	134
Figure 5.3. The band-specific scatterplots of the averaged ROIs derived from the corresponding L7-MODIS imagery in units of apparent reflectance (%). The 2000-2008 image-pairs are only incorporated. The red line represents the one-to-one slope.	135
Figure 5.4. The percent differences for the L7-MODIS ROIs.....	136
Figure 5.5. The modeled surface reflectance (R_s) for different water types.	138
Figure 5.6. The band-specific retrieval errors derived for different aerosol types and visibility over Lake Tahoe waters.	139
Figure 5.7. The simulation results for Lake Tahoe's clear waters. The percent errors shown for the red channel at different times of the year when various aerosol visibility are present (a). The right panel (b) illustrates the reference and retrieved reflectance curves for DOY=210 and a typical aerosol visibility ($VIZ= 25 km$).....	140
Figure 5.8. The band-specific retrieval errors derived for different aerosol types and visibility over Lake Ontario waters.....	141
Figure 5.9. The simulation results for Lake Ontario's turbid waters. The percent errors shown for the red channel at different times of the year when various aerosol visibilities are present (left). The right panel illustrates the reference and the retrieved reflectance curves for DOY=210 and a typical aerosol visibility.	141
Figure 5.10. The CHL and TSS concentration maps derived from the originally observed L7 data (O) and the simulated un-calibrated imagery (U). The bottom frames show the <i>EMAPs</i> [%] calculated using Eq. 5-3. The calibration errors cause overestimation and underestimation of CHL and TSS concentrations, respectively.	144
Figure 5.11. The Genesee River plume simulation results for Oct. 2009 along with the L7-derived surface temperature map and the corresponding RGB image.....	148
Figure 5.12. The snapshots of the ALGE thermal simulations with various input parameters. Temperature values are in Celsius and WS, WD and RD denote wind speed, wind direction and river discharge, respectively.	149
Figure 5.13. The snapshots of ALGE particle simulations with various input parameters. The concentrations are log-transformed in units of g/m^3 . The WS, WD and RD denote wind speed, wind direction and river discharge respectively.	150
Figure 5.14. The Genesee plume simulation in July 2009 after the long-term simulation (263 hours)	151
Figure 5.15. The Niagara simulation results for the Aug. 2008. Frame (a) represents the image-derived "skin" temperature [$^{\circ}C$]. Plots (b) and (c) illustrates modeled surface temperature and normalized particle distribution maps, respectively.....	152
Figure 5.16. The Niagara simulation results for May 2009. Frame (a) represents the image-derived "skin" temperature [$^{\circ}C$]. The lower plots illustrate modeled surface temperature maps without (b) and with (c) applying the nudging vectors.	153

Figure 5.17. The Niagara simulation results for the Oct. 2010 period. The top frames show the modeled surface temperature (a) and L7-derived skin temperature (b). The lower plot (c) illustrates the normalized particle distribution map.	155
Figure 5.18. The Niagara simulation results for Aug. 2011 timeframe. The simulations were performed for two different sizes, i.e., the adopted size (b) and (c), and a larger domain (d) and (e).	156
Figure 5.19. The simulation results at Onondaga Lake along with the vertical profile shown for the south deep station (c). Frames (a) and (b) show the L7- (a) and model-derived (b) surface temperature maps, respectively. The plots (d) and (e) correspond to the modeled particle distribution map and the L7-derived normalized radiance field for the red channel, respectively.	158
Figure 5.20. The simulation results obtained from the originally observed wind data (a) and (b), and the smoothed wind data (c) and (d).	160
Figure 5.21. Model calibration results at the Genesee River site (a, b) shown with the L7-derived surface temperature map (c). The long-term simulation result (a) has improved after iterations and optimization (b). The histogram of the surface temperatures extracted over the plume area for the model output and the L7-derived map is shown in (d).	162
Figure 5.22. Model calibration results at the Niagara River site shown with the L7-derived surface temperature map. The long-term simulation result (a) has improved after iterations and optimization (b).	164
Figure 5.23. The calibrated model output (a) shown for Onondaga Lake along with the L7-derived surface temperature map. The temperature profiles measured/modeled at the south deep station.	165
Figure 5.24. The TSS and CHL derived from the L7 data (top row) and the best model output (second row) for the Genesee plume. The surface distribution obtained along the model and L7 products are shown in (e). The vertical profiles derived along the same transect are also plotted in (f).	167
Figure 5.25. The TSS and CHL derived from the L7 (a-b) data and the best model output (c-d) for the Niagara plume. The surface distribution obtained along the model and L7 products are shown in (e). The vertical profiles derived along the same transect are also plotted in (f).	169
Figure 5.26. The CHL and TSS maps derived from the ALGE model for Onondaga Lake. Frame (c) indicates the normalized radiance field associated with the red channel of L7.	171
Figure 5.27. The concentration maps derived from Hyperion, S-OLI, ALI, and S-ALI.	175
Figure 5.28. The histograms associated with the difference maps of CHL concentrations over the plume using the Hyperion-derived map as a reference.	178
Figure 5.29. The histograms associated with the difference maps of TSS concentrations over the plume using the Hyperion-derived map as a reference.	179

Figure 5.30. The histograms associated with the difference maps of CDOM index maps over the plume using the Hyperion-derived map as a reference.	179
Figure 5.31. The RMSE values obtained for each concentration map for different datasets over the plume area.	182
Figure 5.32. The RMSE values obtained for each concentration map for different datasets over the non-plume area.	182
Figure 5.33. The error maps [%] derived for each dataset.	184

List of Tables

Table 4.1. The specifications of the tropical-arid calibration sites	62
Table 4.2. The dataset applied in this study to calibrate the model	75
Table 4.3. The field campaign attempts.....	80
Table 4.4. The concentrations of CHL and TSS together.....	82
Table 4.5. Field stations for Onondaga Lake.....	87
Table 4.6. The coefficients used to re-start ALGE for the Genesee plume simulation	107
Table 4.7. The ranges of variables used in the sensitivity analysis	113
Table 4.8. The imaging geometry conditions	122
Table 4.9. The band specifications of the OLI sensor	123
Table 5.1. The variables applied for the MODTRAN simulation	137
Table 5.2. Band-specific percent errors (%) for different water types	142
Table 5.3. The area-specific basic statistics for the concentration maps	181

Chapter 1

1. Introduction

The overall objective of this research is to provide insight into the potential of a new generation of Landsat in a water constituent retrieval framework. In order to retrieve water constituents, a novel technique, which takes advantage of the thermal and reflective remotely sensed observations, is introduced. Such observations are used to calibrate a 3D hydrodynamic model and retrieve the surface and profiles of concentrations of water constituents. The proposed approach tested for the Landsat-7, hereafter L7, imagery is even more applicable to the next generation of Landsat. As a part of the remote sensing mission of studying water bodies, the calibration status of the L7 over water was also evaluated using a cross-calibration technique. Furthermore, an independent case study examining the potential of the new generation of Landsat over water was conducted.

1.1. Remote Sensing of Coastal Environments

Remote sensing has long been used to investigate the water quality conditions in near-shore zones [Jensen, 2006]. Based upon the extensive research carried out in such environments, two key findings are essential for grasping the complexity of water constituent retrieval through existing remote sensing data and algorithms. The first issue addresses the complex nature of coastal environments. The coastal areas are where land, water and atmosphere meet making them physically dynamic regions to study. To the extent that chemicals, nutrients, dissolved organic and inorganic materials are entering from rivers and streams, they add to the complexity of physical and biological processes occurring in such regions. The combined biological and physical processes contribute to the complexity of coastal waters and the need for optimal monitoring techniques of which remote sensing has been proven an effective option. The requirements for appropriate mapping and monitoring

of coastal waters through satellite-borne remote sensing raises the second issue, i.e., whether suitable remote sensing systems and methods are available to adequately address the dynamics of such environments. There are always trade-offs among the applications of different imaging systems regarding their capabilities for resolving spatial/spectral complexities in coastal waters. More importantly, in order to capture the temporal variability of coastal waters, we require high-frequency satellite systems acquiring imagery at least once/twice a day. The availability of the new generation of commercial satellites, including WorldView 2 and the earlier QuickBird, with flexible pointing technology, has made data acquisition with very high spatial/radiometric resolution possible. However, for long-term monitoring of coastal waters at regional/global scale, it may not be cost-effective to utilize such image products. Moderate Imaging Spectrometer (MODIS) and Sea-view Wide-Field of View (SeaWiFS) are the two imaging systems developed and designed for monitoring global/regional waters [Murtugudde *et. al.*, 1999; Franz *et. al.*, 2007]. Having appropriate spectral bands configured for water studies along with their high radiometric fidelity, i.e. 12-bit quantization rate, and high signal-to-noise ratio (SNR), MODIS and SeaWiFS, however, lack sufficient spatial resolution to reveal spatially heterogeneous waters in the near-shore regions. Although the Enhanced Thematic Mapper plus (ETM+) onboard L7 has been designed for monitoring land features, its 30 m pixel size and four broadband spectral channels in the Visible-Near-Infrared (VNIR) region have made it a suitable choice for some water quality studies in coastal/inland waters over the past decade. Nevertheless, with the advent of a new generation of Landsat, which carries two sensors, the Thermal InfraRed Scanner (TIRS) and the Operational Land Imager (OLI), higher signal-to-noise ratio (SNR) and quantization rates are achievable. Theoretically, any improvement in the SNR and radiometric resolution enhances the retrieval process in coastal areas [Gerace, 2010].

Using remote sensing, one can potentially retrieve optically active components (OAC) of water, including concentrations of total suspended solids (TSS) and chlorophyll-a (CHL), as well as colored dissolved organic matter (CDOM) absorption, which collectively determine the optical regime of coastal waters, also known as case II waters. Non-linear and complex interactions of these components together with optical properties of pure water contribute to the Apparent Optical Properties (AOPs) of water. The AOPs are commonly used in regression models or are supplied to bio-optical models for retrieval of water constituents. In

most case studies, the water constituents are retrieved solely at an instant in time for a scene. Under ideal atmospheric conditions (no cloud contaminations), when multiple scenes are available, the temporal variability of the water constituents can be monitored.

1.2. Remote sensing Integrated with Numerical Modeling

In order to monitor a highly variable environment, such as coastal/inland waters, using remotely sensed observations, high-frequency measurements are needed. Although providing adequate spatial details over coastal/inland waters, L7 has a 16-day revisit cycle, which may not be ideal for regular monitoring of such dynamic systems. This issue, however, can be compensated by leveraging numerical models allowing for simulating the state of the environment at any point-in-time.

In this research, we provide a link between a coupled-modeling system and remotely sensed data in an effort to quantitatively map water constituents in the receiving waters near river discharges as well as in a small lake environment. This task is achieved through utilization of thermal data in conjunction with reflective data to aid the retrieval process in a two-step scheme. In the first step, modeled surface temperatures are optimized against the thermal remote sensing data while the actual constituent retrieval process takes place in the second phase.

The bulk of this effort is aimed at modeling dissolved and particulate matter as well as making predictions on their vertical and horizontal distribution through a 3D hydrodynamic model, i.e. ALGE. The model is supplied with input variables representing the state of the environment on an hourly basis during the simulation period. Solving a set of differential equations, ALGE enables us to understand the physical process, such as thermal cycle and water circulation. ALGE, which is capable of simulating fine-scale features, can simulate the distribution of river plumes driven by lake hydrodynamics and appropriate environmental variables [Garrett, 1995]. However, there is no perfect numerical model for simulating physical phenomenology in the real world. In fact, any modeling procedure includes several assumptions or simplifications to estimate real world phenomena. Additionally, we do not have enough confidence in the input variables due to systematic errors associated with the observing instruments. This leads us to come up with techniques to account for inevitable uncertainties associated with the input parameters.

Hydrodynamics of lake waters induce movements of particles and dissolved matter which, in turn, influence the optical regime of lake waters. The optical complexity of the waters can be best modeled via in-water radiative transfer models, such as Hydrolight. This plane-parallel radiative transfer code should be supplied with profiles of water constituents, scattering and absorption coefficients of water and the in-water components, i.e., TSS, CHL, and CDOM. A combination of these variables along with the constituent concentrations determines the shape and the magnitude of the reflectance spectra at different depths. In other words, the outgoing light field is modeled according to interactions with the air-water surface, water constituents and substrates (in shallow waters). The primary obstacle in the retrieval process in coastal and inland waters is the proper quantification of the scattering and absorption properties of the water constituents.

The outcome of the simulations in the thermal and reflective domain is eventually compared and optimized relative to the L7 data as a surrogate for OLI. L7 has long been used as an effective tool in monitoring programs according to its cost-effectiveness, coverage and spatial resolution. Here, the procedure consists of two phases. In the first step, look-up-tables (LUTs) of various combinations of a subset of input variables are generated to predict various environmental conditions driving the thermal structure of the plume. Subsequently, the reference L7-derived thermal data is compared to the simulated temperature maps produced by multiple ALGE runs. Among different outputs, one represents the closest match determined through an optimization process. This allows us to lock down some of the input variables and move forward to conduct the constituent retrieval process in the next phase. In the second stage, another set of input variables are varied to generate several distribution maps of sediment and dissolved matter. Hydrolight is then used to convert a sub-sampled set of data from each concentration map to surface reflectance, which in turn is compared to atmospherically corrected L7 data (surface reflectance) within the visible bands. In order to find the best match providing minimum discrepancy with regard to the reference data, an optimization technique is implemented.

Through this process, one can relate each individual image pixel to its corresponding profile of sediment and CDOM concentrations. It should be noted that CHL is simply modeled in the same manner as CDOM, and the biological factors driving chlorophyll distribution (e.g. reproduction, grazing, etc.) are ignored for the purpose of this study. Due to

the application of an optimization technique, the predicted concentrations should translate to minimum errors.

1.3. Landsat Data Continuity Mission

Over the past four decades, Landsat has been providing the science community with an invaluable dataset for monitoring the Earth's resources. Landsat-1 was launched in 1972 with the Multi-Spectral Scanner (MSS), which was specifically designed for land remote sensing. This sensor appeared so valuable that it was used with four subsequent Landsat missions. In 1982, Landsat-4 was launched with two sensors, MSS and a new sensor, the Thematic Mapper (TM), which had significant improvements in spatial resolution, as well as additional bands. The same payload was launched on Landsat-5 in 1984. Landsat-6 was launched in 1993 but failed to reach orbit. L7 was launched in 1999 with an improved TM sensor called the Enhanced Thematic Mapper (ETM+). ETM+ had a similar design to that of the TM technology but provided finer spatial resolution for the thermal sensor, i.e., 60 *m* and a new panchromatic band at 15-*m* resolution. The Advanced Land Imager (ALI) was launched in 2000 on the Earth Observing 1 (EO-1) satellite to test new technology that could be used for sensors aboard the next Landsat platform, LDCM [Bryant *et. al.*, 2003].

As part of this research, we will examine the capability of the new Landsat for water studies. The enhanced features of the OLI sensor noted in Section 1.1 suggest a dramatic improvement in performance over targets of low-signal levels, such as water. Due to its global coverage and enhanced characteristics, LDCM imagery is anticipated to be widely utilized towards studying coastal/inland waters where ocean color systems fail to resolve spatial features critical in such environments. Therefore, over-water algorithms will be developed to produce surface-related physical products and, eventually, products associated with in-water components. In order to ensure the success of such algorithms, the imaging system has to be well calibrated for the specific needs defined for a certain study. Although Landsat satellites have been regularly monitored using calibration sites where medium- to high-reflective targets are investigated, its calibration status over dark targets have never been rigorously evaluated. This is perhaps due to the primary objective of the Landsat mission intended for monitoring land objects. However, the calibration issue is more crucial when LDCM, with its potential for water studies, is in orbit. In this research, we propose a

cost-effective calibration technique to monitor the stability of L7 over deep, dark waters, which will also be applicable for LDCM.

Chapter 2

2. Objectives

As stated, the ultimate goal of this research is to demonstrate a new technique in which the water constituents through the water column are found via a coupled modeling approach. We use the existing L7 imagery to examine the robustness of the method, which is applicable to the LDCM. This is achieved by generating LUTs through multiple runs of the ALGE model in the thermal and reflective domains, which lead to various spatial distributions and material loads of the plume. The major parameters assumed to control the physical shape of the plume are wind speed, wind direction, river discharge and its temperature whereas initial concentrations of sediment and dissolved tracer, particle size and particle density determine the concentration load and distribution at a targeted hour nearly coincident with the satellite overpass. The modeled surface reflectances produced from the Hydrolight simulations [Mobley, 1994] of the ALGE outputs are then compared to the Landsat imagery to find the optimum constituent concentrations. Through this process, we investigate the potential of LDCM, which represents enhanced features, i.e. improved SNR, 12-bit quantization rate, and a new spectral channel, with respect to L7. The method proposed for this research is applied to two river plumes and a small lake environment to fully realize the robustness of the technique. In any remote sensing task, however, one has to ensure that the remotely sensed imagery come from a well-calibrated instrument. Since the calibration status of L7 has rarely been investigated over dark targets, a cross-calibration method was applied to confirm the L7's calibration stability over the past decade. In an independent case study, the potential of the new Landsat (LDCM) is investigated in a physics-based constituent retrieval approach. In this study, the EO-1 imagery were used to demonstrate the new Landsat's potential for water studies, and the results were compared against those obtained from the L7 imagery.

In this chapter we begin with stating the tasks that are required to accomplish this research. The tasks are then described in details in the subsequent sections. We close this chapter by stating the work's original contribution to the field of remote sensing.

2.1. Work Statement

The tasks required for the successful completion of the research effort described in this manuscript are presented in the following order:

- I. Cross-calibrate the L7 instrument with the Terra-MODIS sensor over deep, dark waters.
- II. Develop a method for fusing the thermal and the reflective L7 imagery to map water constituents through a coupled modeling system implemented for two river plume systems as well as a small lake environment.
- III. Demonstrate the capability of the OLI sensor relative to the L7 using an EO-1 dataset in a water constituent retrieval framework.

2.2. Description of Tasks

2.2.1 Task I

This task builds upon the previous research efforts made for the over-water characterization of MODIS and land-based monitoring of L7 either vicariously or relatively [Thome *et. al.*, 2003; Chander *et. al.*, 2004; Kwiatkowska *et. al.*, 2008]. The historical trends of L7-MODIS relative calibration (2000-2011) obtained over a mid-latitude lake as well as over tropical and arid waters with relatively stable optical properties are presented. In order to ensure the robustness of our methodology, the procedure is also tested over a known calibration site for a limited number of scenes during 2008-2011. By treating the calibration differences derived from the trending study as bias-only errors, a series of simulations are conducted to evaluate the significance of such errors on the retrieved surface reflectance. To do so, a physics-based model is provided with different surface reflectance spectra as representations of different water types. Various atmospheric conditions are also simulated to fully understand the mis-calibration effects in this process. In order to quantify how such retrieval errors would influence the retrieved water constituent concentrations, i.e., CHL and TSS, a subset of an atmospherically compensated L7 scene was processed using a physics-based approach. The calibration-induced errors obtained in the retrieval of surface reflectance are applied to the originally derived surface reflectance map to mimic an un-calibrated

surface reflectance map. The retrieved concentration maps are then analyzed regarding the differences in the distributions of the concentrations.

2.2.2 Task II

Our main objective is to develop a method to retrieve water constituents on a pixel-by-pixel basis using a coupled modeling system. The integration of L7 and the coupled modeling system enables capturing the dynamics of coastal waters. With traditional methods of remote sensing, the water constituents are obtained solely for an instant of time. In the light of this, the ALGE model is run for a certain period through which the model is stabilized. From this point on, the procedure is followed separately in the thermal and reflective domains by re-starting ALGE for a short period. In the first step, the model is calibrated via a model-matching technique in which the modeled surface temperatures, which are generated through multiple simulations, are optimized with the L7-derived surface temperature maps. In the second step, ALGE is re-started again by varying a set of variables controlling the material distribution throughout the model domain. This is followed by the application of an in-water radiative transfer model to convert profiles of material concentrations to surface reflectance. The best match is then determined via optimization against L7 surface reflectance products. This two-step approach is tested for two different river plumes, namely the Genesee River and the Niagara River, as well as Onondaga Lake located in New York state, USA. The proposed approach is implemented in six different timeframes for the river plume simulations and two periods for the Onondaga Lake simulations. This helps understand how well this approach works in different environmental conditions at different sites.

2.2.3 Task III

The final task is comprised of demonstrating the potential of the OLI sensor for the retrieval of water constituents. This task aims at performing a cross-comparison between Hyperion, ALI, L7, and simulated OLI, in a water constituent retrieval framework over case II waters. A physics-based spectral optimization technique is employed to map surface water constituent concentrations using each of the above-noted sensors. To accomplish this approach, different model types are modeled through many Hydrolight simulations. The per-pixel water constituents, including TSS, CHL and the CDOM absorption, are determined

through minimizing the disparity between the modeled spectra and that derived from the imagery. The image-derived concentrations are then compared in terms of the system's specifications, i.e., differences in the spectral channels and quantization rate. The Hyperion-derived concentration maps together with the limited field samples taken coincident with the image acquisition are utilized as validation. It should be noted that the absorption and scattering properties of water constituents are also determined through a combination of *in situ* measurements and a curve-fitting approach.

2.3. Contribution to the Field

This research contributes to the field of remote sensing in several ways.

First, this research introduces a dark-target method for the cross-calibration of L7 imagery using the well-calibrated Terra-MODIS imagery. The Landsat systems designed primarily for land observations have to be monitored over dark targets to enable applying rigorous physics-based models for atmospheric correction, and, as a result, a reliable constituent retrieval. This is particularly crucial when the OLI sensor is in orbit, as slight calibration errors, which are minimal when sensing land targets, can adversely influence the whole image processing chain, i.e., atmospheric correction and water constituents.

Second, the coupled modeling system, applied in this effort, allows for quantitative mapping of water constituents through a LUT-based approach. The hydrodynamic model when calibrated is capable of monitoring the dynamics of coastal/inland waters near river discharges. When LDCM is in operation the revisit period of the Landsat systems is reduced to eight days, which can add to the potential of this approach when monitoring material transport.

Third, an approach is proposed that takes advantage of both thermal and reflective remotely sensed data within a water constituent retrieval framework. Due to very low penetration depth in the thermal region of the spectrum, thermal data carry no information

regarding constituent concentrations. Nevertheless, in this effort, thermal data are indirectly used in the retrieval process to calibrate the model.

Finally, the potential of the new Landsat system for water constituent retrieval is demonstrated using the EO-1 imagery. The concentration maps derived from the EO-1 datasets by applying a spectral optimization technique are compared with the maps produced from the existing 6. This multi-sensor comparison provides insight into how well the OLI sensor performs with respect to L7 over case II waters.

The following chapter gives an overview of the background materials that are necessary to achieve these goals.

Chapter 3

3. Background and Theory

3.1. Driving forces for Monitoring Coastal and Inland Waters

Coastal and inland regions are very special environments where land, sea and atmosphere meet. Each of these contributes to the dynamics of coastal waters, making these regions very interesting and challenging subject to study. Coastal areas are also the location of major human settlements, and human activities can have significant impacts on the operation of coasts in terms of environmental and socio-economic degradation [Dudgale, 2007]. The study of coasts, therefore, is highly interdisciplinary incorporating the fields of geology, physical geography, oceanography, engineering, and many others.

Coastal changes are highly induced by two primary factors, namely climate change and the human exploitation of coastal resources. The climate change, on one hand, gives rise to sea-level change leading to changes in sediment distribution and deposition patterns, or a decrease or increase in nutrient loads influencing biological processes [Wright, 1997]. On the other hand, coastal areas are some of the most populated regions in the world, and the interactions between human and the environment often throw the natural coastal system out of equilibrium. The cumulative impacts of these driving forces result in the loss of resources and degradation of coastal ecosystem, which, in turn, affect human life and productivity of the coasts. In order to minimize these impacts, coastal areas should be appropriately managed. The aims of the coastal management programs are to facilitate the use of the coastal zones while reducing the impacts of human use, and to protect human interests at the coasts from negative impacts from natural and human induced processes.

Inland waters may be even more susceptible to such driving factors as they are closed systems and have limited access to open waters. Among all of the lakes existing in the North American region, the Great Lakes form the largest bodies of inland waters. Consisting of Lakes Superior, Lake Michigan, Lake Huron, Lake Erie, and Lake Ontario, they form the largest group of freshwater lakes on Earth by both total surface areas and volume [Rao and

Schwab, 2007]. The following section gives an overview of the dynamics of inland waters with particular reference to Lake Ontario.

3.2. Great Lakes Hydrodynamics

Coastal zones of lakes are dynamic ecological systems because of the inputs from river runoff and human activities as well as from the dynamics of open lake waters induced by wind and waves. Several physical factors combine to make the coastal waters complex in terms of the hydrodynamics and the associated physical transport and dispersal processes. Physical transport processes are the dominant factors in forming geochemical and biological processes in the coastal waters [Rao and Schwab, 2007]. The transport of sediment and nutrients discharged through rivers and non-point sources into the near-shore zone are one example of the impact of coastal physics on the biological chain.

In the North American region, the Great Lakes are systems dominated by their coastal nature [Hayashida *et. al.*, 1999]. In other words, the lakes are not only affected by earth rotation but also they are closed basins, which magnify the influence of coastal processes over coastal marine systems. The fact that the Great Lakes are recognised for their complex coastal environments has drawn attention among scientists towards modeling their physical and biological process. In this light, there have been several numerical models developed to simulate physical and biological processes in Great Lakes [Rao and Schwab, 2007]. In line with this research, a brief overview of mechanisms that most contribute to understanding of physical processes driving material transport within coastal regions is desired. Among these mechanisms are wave-driven processes, the coastal boundary layer with upwelling and downwelling flows, the formation of the thermal bar and the river plumes [Rao and Schwab, 2007].

To begin, we need to define coastal zones. Coastal waters are typically characterized with their shallow depth, less than 20 *m*, when compared to depths of 100 *m* within open lake waters. For the Great Lakes, based upon the SOLEC (State of the Lake Ecosystem Conference) report in 1996, the coastal region is defined as a region from the shoreline to the deepest lakebed depth contour. This classification includes surf and swash zones (the upper part of the beach between backbeach and surf zone) in the littoral zones (Figure 3.1). The shoreline restricts water movements tending to divert currents in a way that they flow parallel

to shoreline. The density of the coastal waters is usually different than that of open waters because of the influx from fresh water runoff from the land. In general, for a similar heat flux through the sea surface, the shallower waters are attributed with larger temperature difference than in deeper waters. Due to these effects, the Great Lakes exhibit significant horizontal gradients of density. The thermal structure of the Great Lakes is largely dependent on seasonal effects due to the large annual variation of surface heat fluxes. During the unstratified seasons, storm events are the primary driving factor as higher wind speeds cause the wind forcing to penetrate deeper into the water. The flow regimes of coastal waters are not uniform from nearshore to offshore regions as water depths extensively vary. The scales of the motions in Great Lakes are reported to range from 10 *m* in nearshore areas for surface gravity waves to 100s of kilometres due to large scale wind driven flows or gravitational seiches [Rao and Schwab, 2007]. For convenience, the coastal zone is divided into three categories, namely the nearshore area, the coastal boundary layer (CBL), including the frictional and the inertial boundary layer (FBL and IBL), and the open lake (Fig. 3.1). In the open lakes, frictional forces are small while in FBL bottom friction and lateral friction control current movements. The inertial boundary layer is also developed to adjust the inertial oscillations to shore-parallel currents [Boyce, 1974]. With this introductory description, major physical processes in coastal zones are concisely described in the following sections [Rao and Schwab, 2007].

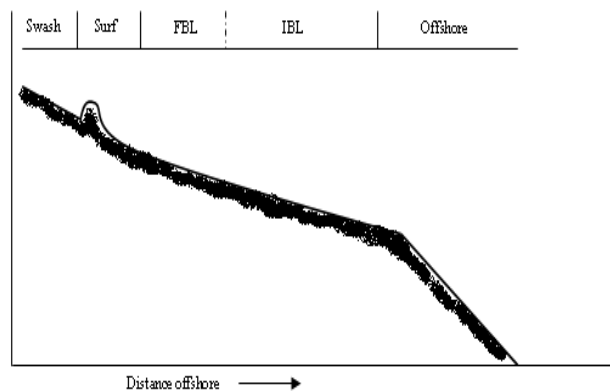


Figure 3.1. Schematic diagram of coastal zone regions.

3.2.1 Wind-Driven Processes

The most common wind direction blowing over Great Lakes originates in the south-west to west direction, however, due to the dynamic climatic condition, winds blow from other directions as well. There exist numerous papers that predict and model the waves generated by winds over Great Lakes [Scott, 2004]. As the wind-generated waves move toward the shoreline, the decreasing depths affect near-bottom orbital motions, altering the wave kinematics. Thus, wind stress influences the surf and the swash zones with the strongest resulting in coastal erosion. Inputs from runoff when combined with sewer overflows and streams make the flow regime quite unsteady. The surf zone, defined as the area of water between the swash zone and the seaward side of the breaking waves (Figure 3.1), has a narrow width compared to the total width of the coastal boundary. The transport process, however, is extremely complex as circulations are majorly derived from dissipation of breaking waves. The onshore transport of water induced by wave actions within the breaker zone, the lateral transport inside the breaker zone and the seaward return of the flow from the nearshore are the processes driving the circulation system. Wave-generated currents also carry particles along the bottom as bed load whereas other particles are carried away at some height above the bed as suspended load. Schwab (1984b) also showed that the dominant forces are not only the wind stress and alongshore currents, but also the bottom friction [Schwab, 1984b]. Moreover, wave orbital motions give rise to re-suspension from the bottom in shallow zones of the Great Lakes.

3.2.2 Coastal Boundary Layer (CBL)

The coastal boundary layer is the area between the wave-breaking region and the open lake where dominant forces include bottom friction and steering effects of the shoreline. As in the nearshore region, wind controls the circulation pattern within this region; however, stratification plays an important role during summer. When a steady wind pushes water downwind, the water level rises causing a pressure gradient to generate flow in the deeper parts of the lake forming two gyres. That being said, at mid-latitudes, winds rarely have a steady pattern and are significantly variable [Rao and Schwab, 2007]. During the stratified period, upwelling and downwelling of the thermocline may occur following significant wind events. If the coast is downwind, downwelling near the coast takes place. Surface transport

occurs towards shore while transport below the surface layer is away from shore. The opposite is the case when the coast is upwind. The changeover from downwelling to upwelling highly contributes to material transport, which also influences biological mechanisms particularly in the summer.

Hydrodynamic models of the coastal boundary layer provide comprehensive views of its characteristics and involve a broad range of forcing conditions. Hayashida *et.al.* (1999) developed a finite element hydrodynamic model to investigate nearshore flow at the mouth of the Niagara River [Hayashida *et. al.*, 1999] . They stated that the spatial resolution of less than 100 *m* is needed to capture hydrodynamic subtleties existing in the coastal boundary layer. In another study, it was demonstrated that nested-grid hydrodynamic models are suitable to simulate circulations and thermal structures in such regions [Sheng and Rao, 2006]. Based on these experiments, it appears that the numerical models operating under high spatial and vertical resolution should be able to reasonably model the hydrodynamics of the CBL providing the availability of high computing power.

3.2.3 Thermal Bar

The thermal bar is a hydrodynamic feature that forms in temperate lakes during spring time when nearshore waters begin to warm [Li, 2007]. During this event, the offshore zone stays cooler and un-stratified or reverse stratified as nearshore zone is stratified and separated with the temperature of maximum density occurring at the bar. The thermal bar acts as a “barrier” in material transport and inhibits exchange of water between nearshore and offshore regions. This effect is extremely important to understand the links between ecosystem and hydrodynamics, which results in determining the impact of nutrient loadings to the lake. Although there is enough evidence that the thermal bar suppresses horizontal transport within shallow areas, its impact in the offshore zone is not that significant [Rao and Schwab, 2007]. The vertical mixing is relatively high during the thermal bar in the offshore while the nearshore zone continues to stratify steadily. Figure 3.2 illustrates the formation of thermal bar at the Niagara River mouth as it appears in Landsat 7 thermal image.

3.2.4 River Plume

The discharge from rivers containing sediments and nutrient loads has a significant contribution to water quality near the river mouth. Modeling the dispersion and mixing of the

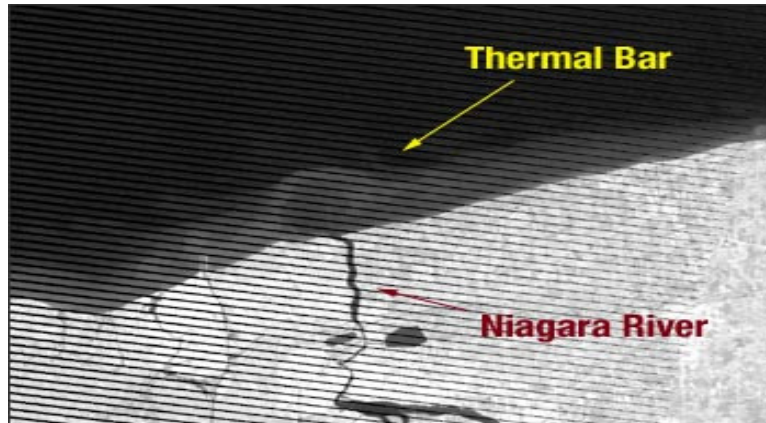


Figure 3.2. L7 thermal image (April 2005). The thermal bar prevents exchange of material between the nearshore and offshore zones. (Courtesy of NASA)

river plumes, which determine distribution and fate of the water-borne material, is a crucial task in coastal water management. Most of the simulations are suited for the discharge of fresh waters into the salty seawater. In open seaways, river plume distributions are controlled by baroclinic and tidal forces while lake circulations and wind stress are the driving factors within closed systems. Although there have been a few papers on modeling river plume dissipations in the Great Lakes, they often fail to properly account for actual material load in the offshore zone [Rao and Schwab, 2007]. The primary reason is failing to adequately characterize the boundary condition where the simulation domain is linked with open waters. In fact, reconstructing the open boundary condition for wind-generated flow is more difficult than for that for tide-induced currents. This is because wind driven currents are considerably more variable due to the nature of wind stress and meteorological condition. Rao and Schwab (2007) state that the dynamics and the characteristics of a river plume are significantly different based on its discharge rate and its extent. The Niagara River plume, for instance, is determined by prevailing wind conditions and lake circulation while flow patterns produced by small rivers, e.g. Grand River entering Lake Erie, are largely dominated by wind-induced circulation.

Because of this discussion, it is inferred that the wind, solar radiation (even though not discussed here), gravity and inputs from rivers are the most important factors driving coastal processes in the shores of the Great Lakes. These driving forces are to be taken into account

in any numerical model aiming at modeling hydrodynamics of water bodies [Li, 2008], [Kunte *et. al.*, 2005].

3.3. Numerical Modeling Coupled with Remote Sensing

Numerical modeling has long been used for simulation and prediction of the thermal structure and the material transport in coastal and inland waters. Determination of the in-water components provides insight into the coastal ecosystem condition as well as the ongoing physical processes at the vicinity of the land-water interface. There exist numerous hydrodynamic and transport models in which governing equations, which consist of the equations of conservation of momentum, energy, and mass, are solved with different levels of simplifications and numerical schemes. The ability of such models to accurately simulate coastal processes is improving as the complexity and sophistication of models increases. With the advancements in computer technology, implementing accurate numerical methods of extensive domains with small grid spacing are possible in a timely fashion. The efficacy of a model, however, depends considerably upon initial and boundary conditions.

Numerical models when coupled with remotely sensed data act as a great tool for monitoring purposes. Many researchers have combined remote sensing imagery with numerical modeling and in-situ measurements to find out the underlying processes throughout the area under investigation. Jensen *et. al.* (1989) used 2D shallow water equations to model salinity and suspended sediment [Jensen *et. al.*, 1989]. They found a good agreement between the transformed Landsat Thematic Mapper (TM) chromaticity channel and total suspended sediment concentration. Ouillon *et al.* (1998) combined remote sensing data with numerical modeling and stated that the inverted TSS concentration map can be used to test different assumptions in the sediment transport model, and to improve the simulation results. The MODIS red channel was also used by Miller *et. al.* (2005) to calibrate and validate a sediment transport model. In this way, the modeled sediment distribution map was compared against the sediment map derived from the MODIS data in Lake Pontchartrain, LA, USA. Miller and Cruise (1995) used a hydrologic model to simulate the runoff and sediment transport from a drainage basin in Puerto Rico entering the coastal waters that contain coral reefs. They calibrated their model with spatial maps of suspended sediment concentrations derived from Calibrated Airborne Multispectral Scanner (CAMS)

imagery. Kouts *et al.* (2007) also combined satellite remote sensing with numerical modeling, consisting of a hydrodynamic model, a particle transport model and a benthic macroalgae growth model, to calculate distributions of sediment. In most of the above studies, sediment-derived maps were solely compared against the spatial distribution of sediment and were not incorporated into the modeling effort. Chen *et al.* (2010) integrated the MERIS-derived sediment maps (as initial sediment distribution) with numerical modeling. They also used retrieved sediment maps to calibrate model input parameters on the premise that satellite-derived data are satisfied [Chen *et al.*, 2010].

In this effort, we intend to make use of a 3D hydrodynamic model (ALGE), which predicts temperature, material transport, and deposition of a stream plume. In addition to solving common hydrodynamic equations for simulating movement of fluids, ALGE accounts for energy transfer between the water surface and the surrounding atmosphere allowing for better calculation of heat loss or exchange. ALGE has proven a useful tool in several studies. Garrett *et al.* (2000) investigated the transport and dispersal of thermal and other effluent from Oak Ridge Reservation in the Clinch River using ALGE. They compared the simulated results with airborne thermal imagery, which demonstrated a reasonable prediction of surface temperature maps [Garrett *et al.*, 2000]. Garrett (2002) showed how thermal imagery could lead to better understanding of the behaviour of the transport of the waste heat in the environment. He concluded that wind speed and wind directions are the major contributors to the fidelity of the model results [Garrett, 2002]. Li *et al.* (2008) found that the ALGE-derived temperature map of Conesus Lake (New York, USA) matches well with the corresponding remotely sensed data. They also investigated lake circulation patterns as well as water circulation and sediment transport at stream mouths [Li *et al.*, 2008].

As stated, ALGE has been applied primarily to investigate the thermal structures of stream plumes entering open bodies of waters by comparison with remotely sensed thermal data. However, Li (2007) performed an integrated approach using a coupled modeling system to predict the sediment distribution at the Genesee River plume discharging into Lake Ontario. She incorporated the MODIS reflectance products into a feedback loop to update predictions of the ALGE model through an Ensemble Kalman Filtering approach [Li, 2007]. Here, ALGE is not only examined in terms of its thermal outputs but also it is used to model the material distribution maps supplied to an in-water radiative transfer code (Hydrolight).

The water-leaving reflectance simulated via Hydrolight is then compared against the L7-derived surface reflectance maps. In contrast to the previous studies where remotely sensed products, such as sediment maps, are applied as a basis for evaluating the modeling results, the comparison is made in the surface reflectance domain.

3.4. ALGE Model

ALGE is a three-dimensional, time-dependent, hydrodynamic model that provides realistic predictions of movement and dissipation of stream plumes as well as transport, diffusion, and deposition of materials. ALGE applies differential equations to model conservation of momentum, mass and thermal energy. It simulates wind-driven circulations, and can combine wind stress and buoyancy forces. Energy exchange is modeled through turbulent sensible and latent heat transfer as well as shortwave and long-wave radiation transfer, including cloud effects [Garrett, 1995]. The model has been used in several independent hydrodynamic studies as well as in conjunction with remotely sensed data used as a validation tool [Garrett, 1997]. In order to clarify how ALGE works, we begin with explaining the governing equations and numerical methods developed in the code structure.

3.4.1 Governing Equations

ALGE solves a set of hydrodynamic equations including conservation of momentum and mass as well as heat transfer in water bodies. The conservation of momentum (Eq. 3-1 to 3-5) is based on the Newton's second Law, which relates the change of momentum of a fluid mass to the applied forces that consists of four different components. In other words, this expression is a partial derivative of velocity with respect to a point in space. The pressure gradient term describes in which direction and at what rate the pressure changes the most rapidly around a particular location. The fourth term incorporates Coriolis effects whereas the rest of the terms are the contribution of the frictional forces driving the fluid mass. The set of governing equations include

$$\frac{\partial u}{\partial t} = -u \frac{\partial u}{\partial x} - v \frac{\partial u}{\partial y} - w \frac{\partial u}{\partial z} - \frac{1}{\rho} \frac{\partial p}{\partial x} + fv + \frac{\partial}{\partial x} \left[k_H \frac{\partial u}{\partial x} \right] + \frac{\partial}{\partial y} \left[k_H \frac{\partial u}{\partial y} \right] + \frac{\partial}{\partial z} \left[k_z \frac{\partial u}{\partial z} \right] \quad 3-1$$

$$\frac{\partial v}{\partial t} = -u \frac{\partial v}{\partial x} - v \frac{\partial v}{\partial y} - w \frac{\partial v}{\partial z} - \frac{1}{\rho} \frac{\partial p}{\partial y} + fu + \frac{\partial}{\partial x} \left[k_H \frac{\partial v}{\partial x} \right] + \frac{\partial}{\partial y} \left[k_H \frac{\partial v}{\partial y} \right] + \frac{\partial}{\partial z} \left[k_z \frac{\partial v}{\partial z} \right] \quad 3-2$$

$$\frac{\partial T}{\partial t} = -u \frac{\partial T}{\partial x} - v \frac{\partial T}{\partial y} - w \frac{\partial T}{\partial z} + \frac{\partial}{\partial x} \left[k_H \frac{\partial T}{\partial x} \right] + \frac{\partial}{\partial y} \left[k_H \frac{\partial T}{\partial y} \right] + \frac{\partial}{\partial z} \left[k_z \frac{\partial T}{\partial z} \right] \quad 3-3$$

$$\frac{\partial w}{\partial z} = -\frac{\partial u}{\partial x} - \frac{\partial v}{\partial y} \quad 3-4$$

$$\frac{\partial p}{\partial z} = -\rho g \quad 3-5$$

In the above equations u and v are the horizontal velocity components and w is the vertical velocity components, T is temperature, k_H and k_z are the horizontal and vertical diffusion coefficients, f is the Coriolis parameter, g is the gravitational acceleration, p is the hydrostatic pressure, and ρ stands for water density. Equation 3-4 is the mass conservation equation under the assumption of incompressibility of the fluid and the last Equation (3-5) accounts for the rate of the pressure change in the vertical direction. The vertically integrated versions of Eq. 3-1, Eq. 3-2, and Eq. 3-4 are then derived to allow for calculating time-varying free surface (surface that is subject to constant perpendicular normal stress and zero parallel shear stress) to estimate the pressure gradient in Eq. 3-1 and Eq. 3-2 as well as pressure in Eq. 3-5 in an iterative fashion [Garrett, 1995]. Other sets of parameters such as bottom drag coefficients at the bottom layers, air-water surface drag coefficients, azimuth angle, wind speed, and mass source are also added to the vertically integrated equations.

3.4.2 Mixing equations

Clearly mixing within a water body occurs in both horizontal and vertical directions. Therefore, expressions modeling material transport are comprised of different components.

3.4.2.1 Horizontal Eddy viscosity

The horizontal eddy viscosity and diffusivities (K_H) are represented by three terms:

$$K_H = K_f + K_s + K_b \quad 3-6$$

The three components refer to turbulent mixing induced by bottom roughness, horizontal velocity shear, and buoyancy forces, respectively. The bottom roughness term is formulated as [Garrett, 1995]

$$K_f = 0.6u_*h + K_o \quad 3-7$$

where u_* represents friction velocity, h is the depth and $K_o = 0.1m^2/s$. As expected, the bottom friction is considered important where current velocities are high and the horizontal mesh size, i.e., the spatial resolution, is small. Horizontal velocity shear is given as below [Garrett, 1995]

$$K_S = C_{sh}S\sqrt{\Delta_x\Delta_y} \quad 3-8$$

where C_{sh} is set to 0.02, Δ_x and Δ_y are grid spacing in x and y directions, and S , the strain rate tensor, is estimated as $S = [0.5(\partial u/\partial y + \partial v/\partial x)^2]^{0.5}$. The strain rate tensor is a measure of how fast the two velocity components change in each of the two directions. The third component takes the effect of the density gradient into account by using a velocity vector based on a balance between buoyancy and frictional drag:

$$K_b = V_b C_b \sqrt{\Delta_x \Delta_y} \quad 3-9$$

where $V_b = \sqrt{u_b^2 + v_b^2}$ is the horizontal velocity vector and $C_b = 0.03$. In this equation the velocity components are defined as

$$u_b = \sqrt{\frac{gh^2}{C_D \rho_0} \left| \frac{\partial \rho}{\partial x} \right|} \quad 3-10$$

$$v_b = \sqrt{\frac{gh^2}{C_D \rho_0} \left| \frac{\partial \rho}{\partial y} \right|} \quad 3-11$$

in which density gradients $(\partial \rho/\partial x, \partial \rho/\partial y)$ in horizontal directions are taken into account. In Eq. 3-10 and 3-11, g is the gravitational acceleration, h represents depth, ρ_0 is the reference density, and C_D is the bottom drag coefficient. The higher the density gradient the more buoyancy forces contribute to horizontal mixing. However, this component is insignificant when current velocities are high whereas it contributes the greatest once the velocities are low and buoyancy forces are responsible for water movements.

3.4.2.2 Vertical Eddy Viscosity

Since the movements of water are less affected by the vertical forces compared to horizontal components, ALGE computes vertical viscosity with a first-order scheme:

$$K_z = ku_*z(1-z/h)/(1+\alpha R_l)^2 \quad 3-12$$

where u_* is the maximum of bottom and surface friction, z is the depth, h is the total depth, $\alpha = 5$ and R_l stands for the layer Richardson number.

3.4.3 Material Transport

The transport equations are obtained in a similar fashion as in Eq. 3-1 with contribution from advection and diffusion and additional terms representing re-suspension flux, deposition flux and settling velocity.

- Dissolved tracer (C_d)

$$\begin{aligned} \frac{\partial C_d}{\partial t} = & -u \frac{\partial C_d}{\partial x} - v \frac{\partial C_d}{\partial y} - w \frac{\partial C_d}{\partial z} + \frac{\partial}{\partial x} \left[k_H \frac{\partial C_d}{\partial x} \right] + \frac{\partial}{\partial y} \left[k_H \frac{\partial C_d}{\partial y} \right] + \frac{\partial}{\partial z} \left[k_z \frac{\partial C_d}{\partial z} \right] \\ & - \alpha (CK_D C_d - C_p) + S_d \end{aligned} \quad 3-13$$

- Particulate tracer (C_p)

$$\begin{aligned} \frac{\partial C_p}{\partial t} = & -u \frac{\partial C_p}{\partial x} - v \frac{\partial C_p}{\partial y} - w(w - w_s) \frac{\partial C_p}{\partial z} + \frac{\partial}{\partial x} \left[k_H \frac{\partial C_p}{\partial x} \right] + \frac{\partial}{\partial y} \left[k_H \frac{\partial C_p}{\partial y} \right] \\ & + \frac{\partial}{\partial z} \left[k_z \frac{\partial C_p}{\partial z} \right] - \alpha (C_p - CK_D C_d) + S_p \end{aligned} \quad 3-14$$

- Sediment (C_s)

$$\begin{aligned} \frac{\partial C_s}{\partial t} = & -\frac{\partial u C_s}{\partial x} - \frac{\partial v C_s}{\partial y} - \frac{\partial w(w - w_s) C_s}{\partial z} + \frac{\partial}{\partial x} \left[k_H \frac{\partial C_s}{\partial x} \right] + \frac{\partial}{\partial y} \left[k_H \frac{\partial C_s}{\partial y} \right] \\ & + \frac{\partial}{\partial z} \left[k_z \frac{\partial C_s}{\partial z} \right] - \delta_k (E_s - D_s) / \Delta z_b \end{aligned} \quad 3-15$$

where E_s and D_s represent re-suspension and deposition flux, w_s denotes the settling velocity and Δz_b is the vertical spacing of the grid cells. All of the other variables have been

defined in Section 3.4.1. In the above equations, the last component controls the nature of transport of the associated variable.

3.4.4 Energy Transfer

ALGE handles energy transfer through maintaining the balance of the short wave (solar) radiation (S_w), the long-wave radiation (L_w), the Sensible heat transfer (H_s), and the Latent heat transfer (H_L) between air and water [Garrett, 1995]. In mathematical form, the energy exchange between water and the surrounding atmosphere can be expressed as:

$$\frac{dT}{dt} = (H_s + H_L + S_w + L_w) / (\Delta z \rho_w c_{pw}) \quad 3-16$$

Where Δz is the surface layer depth, ρ_w is the water density, and c_{pw} is the specific heat water. The above equation is described in more detail in the following sub-sections:

3.4.4.1 Sensible and Latent Heat Transfer

The Sensible heat is a function of temperature difference between air and adjacent water while Latent heat, which is defined as the temperature that arises from change in the state of a molecule, is driven by relative humidity. The Sensible and Latent heat fluxes are computed according to the following expressions

$$H_s = a^2 W \Delta \theta F \rho_a C_p \quad 3-17$$

$$H_L = a^2 W \Delta q F \rho_a L \quad 3-18$$

Where ρ_a is air density, W is wind speed, C_p represents specific heat of air, L is the Latent heat of evaporation, $\Delta \theta$ is temperature difference across surface layers, Δq is the specific humidity difference across surface layer, F is the profile parameterization, and $a^2 = k^2 / [\ln(z/z_0)]^2$ in which $k=0.4$ and $z_0 = 0.0002$.

3.4.4.2 Solar Radiation

ALGE treats incoming solar radiation such that all radiation is assumed to be absorbed in the uppermost layer of the simulated body of water [Garrett, 1995]. That being said, direct and diffuse solar light reaching the water surface is calculated as

$$F_s = S_o (\tau_d \tau_{ws}^w \tau_{wa}^w)^M \cos \zeta \quad 3-19$$

In the above equation, τ_d , τ_{ws}^w , τ_{wa}^w characterize the effects of dry air scattering, water vapor transmission and water vapor absorption, respectively. The exponent w is the total atmospheric water vapor content expressed as an equivalent water depth (cm) and M is the pressure-adjusted optical depth. S_o is the top-of-troposphere solar flux and ζ represent zenith angle. The transmission terms are simplified as below

$$\begin{aligned}\tau_d &= 0.9 + 0.01(-0.1m^2 + 1.3m - 0.6) \\ \tau_{ws} &= 0.975 \\ \tau_{wa} &= 1 - \frac{0.19685}{[1 + 1/(0.6992\sqrt{mw})]}\end{aligned}\tag{3-20}$$

In the presence of clouds, particularly Cumulus and Stratocumulus, which deplete solar radiation, transmission functions are modified to account for such clouds.

3.4.4.3 Long-wave Radiation

The total long-wave radiation is computed based on the simplified model, which treats clouds as black bodies and neglects emission and absorption above the troposphere. The expression is given as below:

$$\begin{aligned}L_{wj} &= \sigma(T_s^4 - T_1^4) + p_j \sum_{i=1}^{I_c} \frac{\phi}{k_j} (e^{-k_j w_{i+1}} - e^{-k_j w_i}) \\ &+ (1 - \sigma_c) \left[p_j \sum_{i=L_c+1}^{I_r} \phi_i (e^{-k_j w_{i+1}} - e^{-k_j w_i}) / k_j \right] + p_j e^{-k_j w_l} B(T_l)\end{aligned}\tag{3-21}$$

Where

$$\phi_i = \frac{B(w_{i+1}) - B(w_i)}{w_{i+1} - w_i} \text{ and } L_w = \sum_{j=1}^J L_{wj}$$

The other variables/indices are listed as following

σ : Stefan-Boltzmann constant

T_s : water surface temperature

T_1 : surface layer air temperature

p_j : weighting coefficient

k_j : absorption coefficient

w : atmospheric equivalent water depth

σ_c : cloud cover

B : computational level

I_c : cloud level (km)

I_T : tropopause level

3.4.5 Mass and Energy sources and sinks

Mass (water in units of m^3/s) can be added to any cell throughout the water areas. The mass can be either constant or hourly variable over the simulation time. It may be modeled by increasing the water surface elevation at a rate specified by the user. Mass sink, which is always assumed to be at the lowest level, and mass source can be defined manually by the user [Garrett, 1995]. Energy is fed into the model by specifying the mass source temperature (river temperature). If the mass source is subsurface, the temperature in the volume at that level is changed at a rate identical to mass supply rate.

3.4.6 Boundary conditions

One of the most challenging issues in any hydrodynamic modeling is how to define the boundary conditions so that the model obtains appropriate inputs from the surrounding environment. There are three alternatives in ALGE for defining the lateral boundary conditions:

- Zero-gradient boundary for temperature and velocity when normal velocity component of one cell from the boundary is directed in any directions other than inward direction. In order to set this condition, the user is required to put 8's on the boundary in the input grid file.
- Zero-gradient boundaries anywhere throughout the domain in which 9's are used in the grid input file.
- Fixed boundaries where the temperature and velocity remain constant at their initial values (1's).

The *igrd.dat* data file, one of the ALGE input files, specifies one of the above-mentioned conditions. This input file, generated using a bathymetry map, enables the ALGE model to distinguish land and water areas by allocating 1's to the body of water while assigning 0's to land regions. The boundary nodes where area under study meets open waters are assigned

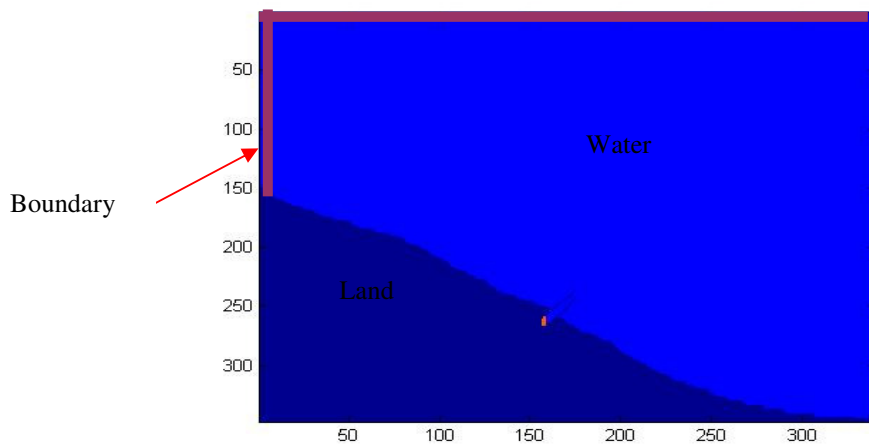


Figure 3.3. The *igird.dat* file with 1's and 0's as water and land pixels. The thick red lines indicate 9's at boundaries.

with one the above-noted values. Figure 3.3 illustrates an example of *igird.dat* input file. The lower boundary condition is defined by the bathymetry map, which is contained in the *depth.dat* input file. The values are fixed at initial values unless tidal simulation is incorporated. The upper boundary of the model is the free surface where wind stress, evaporation and radiative equations are involved to model momentum and energy transfer from and to the atmosphere.

3.4.7 Nudging

As stated in section 3.1, the success of hydrodynamic modeling of lake environments, to a great extent, depends on the domain's grid size. In the case of the Niagara River plume simulations, for example, the grid size is suggested to be on the order of 100 m [Hayashida *et. al.*, 1999]. However, performing a simulation at this resolution throughout an entire lake (Lake Ontario) or a bay is extremely computationally expensive. Therefore, a technique termed nudging is applied to drive a high resolution, limited area simulation of the river plumes via data provided by field observations or a large area, low resolution lake-wide simulation [Garrett, 1995]. In order to conduct this task, ALGE reads in two input files namely, *ndg.dat* and *wgtar.dat*. Surface velocity vectors at hourly rates are included in the former file whereas *wgtar.dat* is a grid, the same size as the domain size, which weighs the surface velocity of each cell based on the distance from the deepest cell within the domain.

As a result, the surface velocity vectors near land areas are assigned low values. This is done to avoid unrealistic forcing condition specific for open waters away from shore at areas near the shore. In order to perform the nudging, three surface velocity vectors from a lake-wide simulation are obtained and assigned to three boundary cells of the localized simulation, which is then interpolated for the remaining cells within the model domain. The vertical profile of the velocity vectors is calculated based on

$$U_N^i = \xi U_N \quad 3-22$$

where U_N^i is the nudging velocity at level i , U_N represent surface nudging velocity and

$$\xi = \frac{\ln[(h - z_i)/z_o]}{\ln[h/z_o]} \quad 3-23$$

where $z=0$ for surface and h is the total depth.

3.4.8 ALGE Input Data

The input to the ALGE model consists of the meteorological data, the upper-air atmospheric column, the land-water distribution, a bathymetry map, the river temperature, the river discharge, and tidal forcing if applicable. Moreover, other settings such as the mesh size, the start time, the hours of simulations, as well as other input data resides in a separate data file, i.e., *param.dat*.

- Surface Meteorological data

The hourly surface meteorological data read into ALGE contains wind direction (*deg*), wind speed *m/s*, air temperature *K*, dewpoint temperature *K*, cloud cover, cloud height [*km*] and pressure *mb*. In the absence of the observational stations at the desired locations (river mouth), data are to be used with caution as such environmental data are considerably spatially variable.

- Upper-air Meteorological Data

The radiosonde data are used to generate profiles of temperature and precipitable water at 11 levels starting from 100 *m* above the ground. Temperatures are in units of *K* and precipitable water is expressed in *cm*.

- Land-water Distribution

This is a data file with which ALGE distinguishes land pixels (1's) from water pixels (0's). Through this array, the ALGE code also identifies inflow/outflow boundaries (8/9's) and nodes correspond to mass source (7's) and mass sink (6's).

- Water depth

The bathymetry map is an essential part of the ALGE simulations. In this array, land pixels are identified by 0's. In the version of ALGE that is used in this research, explicit depth values in units of [m] are fed into the model.

- River Discharge

The volumetric flow rate is a critical variable, which contributes considerably to the fidelity of resultant plume distribution. The user can plug in either a constant value or hourly varying data as river discharge [m^3/s].

- Nudging Data

The surface velocity vectors associated with three nodes are extracted from a lake-wide simulation to link the localized simulation with open water currents. The corresponding data is on an hourly basis and may be obtained from in-situ measurements as well.

- Temperature profiles

The capability to incorporate time-series of temperature profiles prescribed at the boundaries of the localized simulations has been recently added to ALGE. This capability further adds to the importance of the lake-wide simulation, which has to be very consistent with the localized simulations. The temperature profiles are obtained from the lake-wide simulations after spatially upsampling them to the localized simulations' grid sizes. The profiles are stored in a file called *thadv.dat*.

- Other Input Parameters

Other input variables defined in the *param.dat* file include the horizontal and vertical grid spacing, the geographic location, the Julian day, the bottom roughness length, the initial concentrations, the angle of *x*-axis from north, the number of nodes in *x* and *y* direction and flags for the time interval between heat transfer updates, the use of nudging data and variable or constant discharge rate. Providing all of the input variables and experimental parameters, such as the bottom drag coefficients, friction velocity and others are estimated or measured,

ALGE can reasonably predict the water circulation, the transport of material and the thermal structure of water bodies. Of particular interest among the ALGE outputs are maps of temperature, sediment and dissolved matter, which can be linked to the surface reflectance through application of an in-water radiative transfer model. The following section describes the basic principles required to understand the underlying remote sensing approach through which the satellite-derived physical properties of bodies of water are produced.

3.4.9 New Capabilities in the ALGE Model (2011)

During the course of this study (2009-2011), the ALGE model has undergone several modifications, which enhanced the model performance when modeling both river plumes and lake simulations. The ALGE code has been enabled to receive

- A 2D wind field over the entire domain size

- Time-varying inflow temperature and dissolved matter concentration

- Time-varying temperature profiles to be prescribed at the domain boundaries

- Two variable inflow discharges (mass source and second source)

3.5. Remote Sensing of Water

Remote sensing has long been recognized as a powerful tool for studying the dynamics of water [Hakvoort *et. al.*, 2002; Jensen, 2006; Tzortziou *et. al.*, 2007]. The bulk of information extracted from remotely sensed data is always greater than the amount obtained from a field sampling effort where the investigator has to come in physical contacts with the water body for a single observation [Raqueno, 2003]. Remotely sensed data, instead, gives a synoptic overview of a water body in the form of digital counts as an indication of its physical quantities. Physical properties of oceans, such as their temperature, their wave heights, their circulation patterns, and their constituents, can be sensed from various platforms carrying either imaging or non-imaging systems. In environmental applications where the concentrations of water constituents are of major concern, the end goal of remote sensing is to provide a link between signal arising from the water and the water quality parameters whose optical properties affect sensor-reaching signals. When addressing water constituents, one should understand the components that have optical signatures determining the water color. As we know, water is a very complex and dynamic environment comprised of myriads

of constituents. In coastal and inland waters, recognised as case II waters, only three components of water dominate the color of the water body. These components include chlorophyll-a (CHL), total suspended solids (TSS), and colored dissolved organic matter (CDOM) recognized as Optically Active Components (OAC) of water. The chlorophyll-a is an absorptive component of the water column that provides cues on phytoplankton biomass and the trophic status of the waters under investigation. Due to their dissolved nature, dissolved organic matter (DOM) also induces light absorption, particularly in the UV-blue parts of the spectrum, i.e., 350-450 *nm*. Inflows from land-based waters introduce different organic/inorganic particles, known as Total Suspended Solids (TSS). Not only do particles alter the physical and biological processes in coastal waters, but also they contribute to increase the magnitude of water-leaving optical signatures because of their high-scattering nature [Mobley, 1994; Binding *et. al.*, 2005; Bowers *et. al.*, 2009]. In open oceanic waters, these components are reduced down to CHL and CDOM, which, clearly, simplifies the retrieval process. In other words, coastal and inland waters are considered optically complex environments due to the presence of particles driving higher levels of scattering and absorption within the water column.

Determining the signal arising from the water column is the key factor in quantifying concentrations of OACs. That being said, establishing such a link between water constituents of interest and the signal containing clues on the water constituents is not an easy task. In other words, this task requires the decomposition of the signal reaching the imaging system. The following points highlight the impediment factors, which increase uncertainty in the constituent retrieval process:

- Atmospheric interference
- Low signal level
- Determination of inherent optical properties (IOPs)

In passive remote sensing systems operating within the reflective spectrum, the total downwelling solar radiation interacting with targets of interest reflects towards the sensor where it is degraded due to the sensor characteristics. The strength of the signal emanating from the water body is an issue as the number of photons carrying the optical signatures of water constituents are reduced, i.e. within-water scattering and absorption phenomena

weaken the outgoing signal. The low signal is further contaminated by the atmospheric scattering, which boosts the signal level but adds no useful information to its content. Characterizing the atmospheric effects associated with the signal is crucial in such studies and requires thorough knowledge of the composition of atmospheric gaseous, water vapor, CO_2 , O_2 , etc., as well as the distribution and size of the suspended particles known as aerosol within the atmosphere. In addition to radiative transfer models commonly used for modeling the state of the atmosphere, empirical methods exist, i.e., image based methods, that help deduce the atmospheric effects.

The inherent optical properties (IOPs) of water are those properties that depend only upon the medium and are not a function of the ambient light field. The absorption and scattering coefficients of water and its constituents are the primary IOPs that contribute to the characterization of a water body. The overall effect of absorption and scattering phenomena results in the attenuation of light that gives water its dark-blue appearance. Another inherent optical property of water is the volumetric scattering phase function. Angular distribution of the outgoing light field due to the flux incident upon a small volume of water is described by the volumetric scattering phase function. In other words, the volumetric scattering phase function specifies the possibility of light scattered in different directions within an entire sphere. The absorptive components of the IOPs can be measured by either deploying appropriate instrumentation *in situ* or performing spectrometry measurements in the lab. On the other hand, scattering components and phase functions may be determined through *in situ* measurements or application of analytical solutions. Depending on the composition of water content, IOPs are very much spatially and temporally variable within coastal and inland waters [Binding *et. al.*, 2005]. Therefore, the proper characterization of IOPs is often cumbersome and time-consuming, and assumptions have to be made to generalize measured/estimated quantities, i.e., the measured IOPs at one location may not represent the IOPs in other locations.

The complexities associated with the signal reaching the sensor necessitates the application of high-fidelity imaging systems whose specifications allow for accurate retrieval of water constituents. In other words, the sensors' specifications largely determine the robustness of the retrieval process. Moreover, the "aging" of the instrument may introduce degradations in different components of the systems leading to delivering un-calibrated

datasets. Therefore, the calibration status of the system has to be monitored and well characterized. The following section addresses all of the factors that should be taken into account when investigating water quality using remote sensing.

3.5.1 Sensor-reaching Radiance

The sensor-reaching radiance is the total flux per unit area per solid angle hitting the sensor head, which contains some information about a target of interest. However, not all the photons found at the front of the sensor contain information regarding objects of interest. In other words, photons travel various paths and originate from different sources, including the atmosphere or background objects. Overall, in passive remote sensing, the primary source of photons is solar radiation interacting with the target, atmosphere or any other object from which photons are partially re-reflected to the sensor field-of-view. In this section, different photon paths, once they enter the Earth's atmosphere, are described. Since the components specifying the energy reaching the sensor are different within the reflective and thermal portion of the electromagnetic spectrum, it is more convenient to divide the corresponding discussion into two parts, namely reflective and thermal paths.

3.5.1.1 Reflective Paths

This section is concerned with solar energy being reflected or scattered by a target of interest, the atmosphere or any other objects, which direct photons toward the front of the sensor. However, of major interest in remote sensing is inspecting only the photons containing information about the targets. Therefore, a comprehensive knowledge of the possible paths is imperative. Figure 3.4 shows four major solar paths through which photons make their way to the imaging system. Path *A* contains photons from the sun that pass through the atmosphere, reflect off a target, and again pass through the atmosphere on their way to the sensor. This is actually the group of photons that we wish to isolate to retrieve information regarding a target. Path *B*, also referred to as skylight, is the sunlight scattered by atmospheric particles (or molecules) heading downward, reflecting off the target of interest and propagating upward through the atmosphere. Path *C*, also known as path radiance, shows

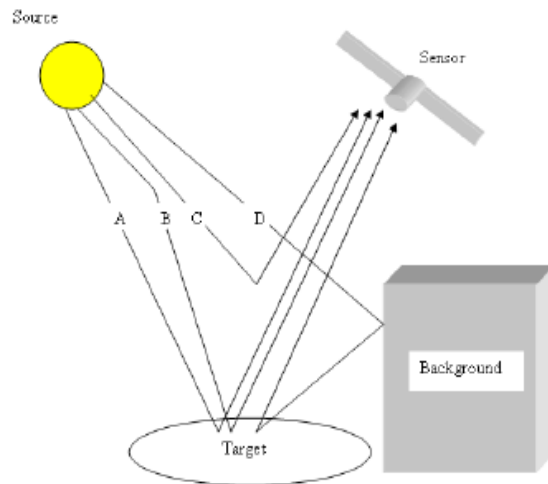


Figure 3.4. Major photon paths contributing to the sensor-reaching radiance in the reflective portion of the spectrum [Gerace, 2010].

photons that originate from the sun and get scattered in the direction of the sensor, which implies that these photons carry no information about the target. Lastly, photons from path *D* represent photons from the sun that travel through the atmosphere, interact with adjacent objects, reflect off the target of interest and make their way through the atmosphere to the front of the sensor. In water studies, we are commonly less concerned about path *D* unless image pixels adjacent to the shoreline are to be dealt with. By isolating photons carrying information about the target, we can study its reflective properties, which, to some extent, reveal the target's characteristics. Along with the reflective considerations, thermal properties of objects can aid us in more accurately quantifying a target.

3.5.1.2 Thermal Paths

Photons can also be emitted, in the form of thermal energy. This is also referred to as self-emission. When imaging within the thermal infrared region, the sensor-reaching radiance emanating from the target due to its temperature can be modeled via the Planck blackbody equation along with the wavelength-dependent emissivity. Figure 3.5 illustrates different thermal paths. Path *E* represents photons emitted from the atmosphere, reflected from the target and ending up within the field of view of the sensor. Self-emission due to the atmosphere itself makes up photons within path *F*. Path *G*, the desired signal, shows photons arising from the target reaching the front of the sensor.

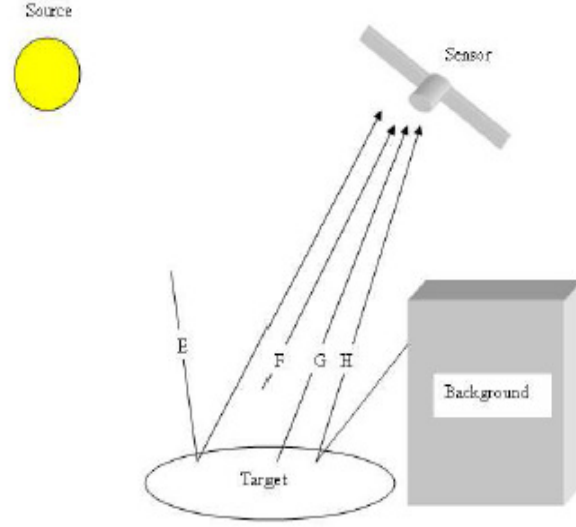


Figure 3.5. The major self-emission components forming total photons reaching the sensor [Gerace, 2010]

Finally, background targets self-emitted photons within path *H* which combine with the total signal recorded at the back of sensor. Since it is the intent of this project to make use of both the reflective and the thermal satellite-derived data to retrieve water constituents, all components (paths) of the sensor-reaching radiance need to be expressed in the governing equation detailed in the following section.

3.5.1.3 Governing Equation

Schott (2007) expresses the fundamental remote sensing equation that conceptually accounts for photon interactions and how they contribute to the signal reaching the imaging system. This equation incorporates both reflective and emissive photon paths:

$$L = L_A + L_D + L_B + L_E + L_G + L_H + L_C + L_F \quad 3-24$$

where *L* corresponds to the total radiance reaching the sensor's aperture and each component refers to radiance associated with each path described in the previous section. The radiance components can be decomposed as follows:

$$L = [E_{s\lambda} \cos(\sigma) \tau_1(\lambda) \frac{r_d(\lambda)}{\pi} + \varepsilon(\lambda) L_{T\lambda} + F(E_{ds\lambda} + E_{de\lambda}) \frac{r_d(\lambda)}{\pi} + (1-F)(L_{bs\lambda} + L_{be\lambda} r_d(\lambda)) \tau_2(\lambda) + L_{us\lambda} + L_{ue\lambda} \quad 3-25$$

Each term is defined below:

$E_{s\lambda}$: Exo-atmospheric solar irradiance [$W/m^2 \mu m$]

σ : Solar zenith angle [$degrees$]

$\tau_1(\lambda)$: Transmission loss along sun-target path [$unitless$]

$r_d(\lambda)$: Diffuse reflectivity of the target [$unitless$]

$\varepsilon(\lambda)$: Target emissivity [$unitless$]

$L_{T\lambda}$: Blackbody radiance at temperature T [$W/m^2 \mu m sr$]

F : Shape factor indicating fraction of sky over which target receives skylight [$unitless$]

$E_{ds\lambda}$: Downwelling skylight (reflective) [$W/m^2 \mu m$]

$E_{de\lambda}$: Downwelling skylight (thermal) [$W/m^2 \mu m$]

$L_{bs\lambda}$: Radiance due to background (reflective) [$W/m^2 \mu m sr$]

$L_{be\lambda}$: Radiance emitted from background [$W/m^2 \mu m sr$]

$\tau_2(\lambda)$: Target-sensor path transmission [$unitless$]

$L_{us\lambda}$: Path radiance (reflective) [$W/m^2 \mu m sr$]

$L_{ue\lambda}$: Path radiance (thermal) [$W/m^2 \mu m sr$]

In remote sensing of water bodies where there is no obscuration due to adjacent targets, one can neglect terms indicating photons along paths H and G , and set $F=1$ in Eq. 3-25. It should also be noted that the basic assumption made here is that the target exhibits Lambertian properties, i.e. its reflectance is not a function of viewing angle. We can also use the bidirectional reflectance factor measured for an object which is the ratio of the radiance reflected into one particular direction to the radiance that would be reflected in the same direction by a Lambertian target illuminated in the same manner [Schott, 2007]. In the case the target has non-Lambertian properties, the target-specific bi-directional reflectance distribution function (BRDF) has to be incorporated as a replacement for the diffuse reflectivity.

An overview of the characteristics of an imaging device crucial in water studies are given in the following section.

3.5.2 Sensor

Once radiance reaching the aperture enters the sensor, it undergoes degradations according to the imaging systems' specifications, such as their optical transmission, their filters, the detector's quantum efficiency (QE), and the analogue-to-digital (A-D) convertor's efficiency [Holst, 2008]. However, these specifications are different from one system to another, due to the requirements for the system design. Due to their relevance to this research, spectrometers, scanning systems, and pushbroom systems are overviewed followed by brief explanations of the signal-to-noise (SNR), the quantization, the spectral response functions, and the post-launch calibration methods.

Imaging spectrometers are systems that deliver imagery with contiguous spectral data allowing for recovery of a nearly continuous spectrum, ranging commonly from 350-2500 *nm*, for objects of interest. In addition to the systems' optical elements, the spectrometers include a diffraction grating/prism to disperse the incoming beam onto a focal plane array, which spectrally and spatially samples the light. An example of such systems is the Hyperion instrument onboard EO-1 mission that has two spectrometers covering the visible-near-infrared (VNIR) and the short-wave-infrared (SWIR) portions of the spectrum [Green *et. al.*, 2003].

The scanning sensors, on the other hand, apply a scanning mirror (prism/mirror) to project a portion of the ground onto the detector at a time. In this way, a line is scanned across track and a swath is imaged by along track progress of the satellite/aircraft. These systems are known for their simplicity in the optical design and in the band-to-band spectral registration [Schott, 2007]. The Landsat (TM) instrument and MODIS onboard Aqua/Terra are such systems.

The pushbroom systems use linear arrays of detectors each of which sample one spot in the across track direction allowing for longer integration time. Multiple arrays combined with filters are applied to cover the desired spectral bands. This requires post-processing efforts to spectrally register the resultant shifted images. The new generation of Landsat (LDCM) carries the OLI and the TIRS instruments that spectrally image within the VNIR and the thermal infrared regions, respectively. The OLI, built with a pushbroom design, has the same

spatial resolution as Landsat-5 and Landsat-7 while exhibiting enhanced radiometric and spectral resolution. Furthermore, the pushbroom design enables a longer integration time leading to a higher SNR [Gerace, 2010].

3.5.2.1 Signal-to-Noise Ratio (SNR)

The SNR calculation for any imaging system can be expressed as [Schott, 2007]

$$SNR = \frac{Signal}{Noise} \quad [dB] \quad 3-26$$

where the signal, in the reflective domain, is calculated as

$$Signal = \frac{L_{\lambda} A_d \Delta\lambda \lambda t_{int} \tau_s \tau_T \pi QE}{(1 + 4F\#^2) hc} \quad [electrons] \quad 3-27$$

$$Noise = \sqrt{N_{shot}^2 + N_e^2} \quad [electrons] \quad 3-28$$

The notations are listed as below

L_{λ} : Surface-leaving radiance [$W/m^2 \text{ um sr}$]

A_d : Area of the detector [m^2]

$\Delta\lambda$: Bandwidth [um]

t_{int} : Integration time [s]

QE : Quantum efficiency (photon-electron conversion) [*unitless*]

$F\#$: Ratio of the focal length to the aperture diameter [*unitless*]

h : Planck constant (6.626×10^{-34}) [$J.s$]

c : Speed of light propagation (3×10^8) [m/s]

τ_s : Spectrometer transmission [*unitless*]

τ_T : Telescope transmission [*unitless*]

N_{shot} : shot noise [*electrons*]

N_e : Noise due to electronics and quantization [*electrons*]

It is evident that increasing the bandwidth, the integration time, the detector's pitch, and the $QE(\lambda)$ increase signal level and, as a result, the SNR. It should also be noted that increasing the $F\#$ reduces the number of the electrons recorded at the back of the sensor. As stated, the primary restriction of the scanning systems when compared to pushbroom designs is the short integration time for each single ground sample. In addition to shot noise, which originates from the signal level, the noise due to the electronics has a major impact on retrieving the desired signal, i.e., water-leaving quantities. This source of noise comes mainly from the amplifiers, which are part of the read-out-circuits (ROC). Overall, designing an imaging system demands a thorough trade study in which all of the key components are optimized to meet the scientific specifications defined by a science community.

3.5.2.2 Quantization Rate

The quantization rate, also referred to as radiometric resolution, is the number of output (energy) levels generated by the A-D converter. The greater the numbers of energy levels, the more radiometric details of the targets of interests are revealed if not limited by the SNR. Quantization is commonly expressed in bit-depths, e.g. an 8-bit system exhibits 256 energy levels. The majority of the newly built satellite-borne imaging systems are equipped with 12-bit quantizers, which make them superior to the older designs. The quantization rate also contributes to the amount of system noise because a specific range of analog inputs are assigned with only one digital output. When imaging targets with low reflectivity (few photons reaching the sensor), the quantization noise can be significant [Holst, 2008]. In other words, the low signal levels require high radiometric fidelity to enable distinguishing subtle spatial variations between adjacent pixels in a scene, particularly when imaging water.

3.5.2.3 Spectral Response

The spectral response is a wavelength-dependent function and defined as the signal out S [V] per unit flux Φ [W] incident on the detector. The sensor response, expressed as a function of wavelength, $R(\lambda)$, can be thought of as the cascade of the $QE(\lambda)$, the optical transmission $\tau(\lambda)$, and the filter responses that, overall, amount to the signal loss through the

system within a band-pass. This indicates that the spectral response functions specify the bandwidth, i.e., spectral channel, through which the photons are collected. While multispectral sensors, such as OLI and L7 have a few broad spectral responses, hyperspectral systems, like Hyperion, enable obtaining a nearly continuous Top-of-atmosphere (TOA) spectral radiance via resampling the sensor-reaching radiance over many narrow spectral bands. The effective radiometric quantity is computed by cascading the response of the system with the spectral radiance obtained/modeled from Eq. 3-25. The corresponding expression can be formulated as

$$L_{eff}(\lambda) = \int_{bandpass} L(\lambda)R(\lambda)d\lambda \quad 3-29$$

where $L(\lambda)$ is the spectral radiance and $R(\lambda)$ is the band-specific spectral response. The effective spectral radiometric quantity may also be calculated using the relative spectral response ($RSR(\lambda)$) representing the normalized spectral response:

$$L_{eff}(\lambda) = \frac{\int_{bandpass} L(\lambda)R'(\lambda)d\lambda}{\int_{bandpass} R'(\lambda)d\lambda} \quad [W/m^2 \text{ um sr}] \quad 3-30$$

3.5.2.4 Post-launch Calibration

When imaging low reflective targets, such as water, the requirement of a well-calibrated sensor with low noise levels becomes more important. In the pre-flight calibration process, each detector's response with respect to a known source of flux is characterized. In this process, the average band-specific gain and offset for the entire array is determined and used to convert the digital numbers to radiance units $[W/m^2 \text{ um sr}]$. However, over years of operation, the calibration status of an imaging system has to be quantified frequently. This is usually conducted via imaging onboard calibrators on a regular basis. Although the onboard calibration process appears an ideal method for calibration, the calibration sources may degrade throughout the life cycle of the imaging sensor. Therefore, it is important to monitor the calibration status of the sensors using other calibration methods, such as vicarious and cross-calibration techniques. In the vicarious calibration, the imaging system's response is examined over radiometrically stable targets versus model-derived responses for the same targets. The desert sites in northern Africa and in the western USA are among the interesting

targets to enable the characterization of the calibration status of an imaging system. Despite its robustness, the vicarious calibration commonly demands simultaneous, *in situ* radiometric measurements. In addition, the vicarious calibration over bright targets, such as desert sands, may not provide an accurate estimation for dark, low reflective targets. For dark waters and in the absence of *in situ* measurements, the cross calibration provides a means to characterize the status of an imaging system. Under certain conditions, a well-calibrated sensor can be utilized to verify or determine the calibration status of another system [Teillet *et. al.*, 2001; Thome *et. al.*, 2003]. In other words, two sensors with similar acquisition geometry and atmospheric condition should observe the same physical quantity. Although L7 has been calibrated for medium- to high-reflective targets, its calibration status over dark waters have to be investigated prior to applying physics-based models to account for the atmospheric effects.

Following a brief introduction on the system components and the factors affecting the retrieval of the water-leaving optical properties, various components that form the over-water signals are described in the following section.

3.5.3 Signal Components

- As described in Section 3.5.1, the signal recorded at the back of the sensor arises from different sources out of which only a small portion is of interest for the constituent retrieval.

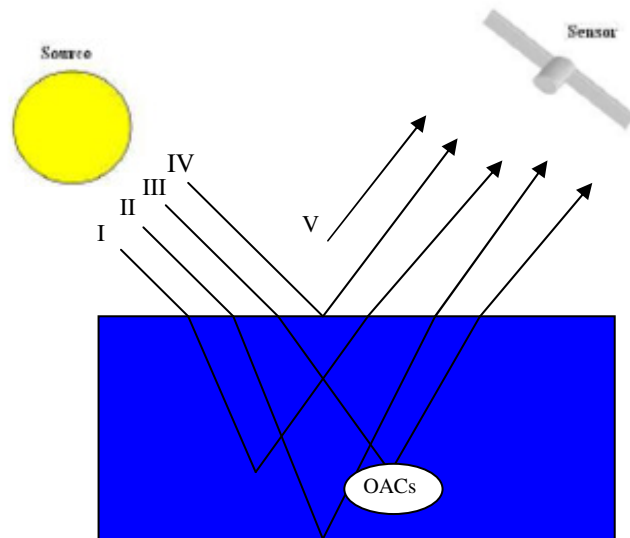


Figure 3.6. The signal components reaching the sensor. Path III carries information of interest

Figure 3.6 illustrates various contributions to the sensor-reaching signal. This signal originates from the following components:

- Pure water (I)
- Bottom (II)
- Optically active water constituents (III)
- Atmosphere (V)
- Glint Effects (IV)

Thus, pure water is a major absorber of incident signal within and beyond the NIR while it scatters light in the visible region according to the Rayleigh theory (described in Section 3.5.3.4). The fact that there is no penetration into water column within the thermal region can be also explained by this theory and the physical properties of water itself. In other words, the thermal signals carry no direct information regarding water constituents and only interact with the very top surface layer of the water body. Furthermore, when dealing with inland waters, one should notice that fresh water scattering and absorption coefficients represent different characteristics when compared to salty seawater.

3.5.3.1 Bottom

In shallow case II waters, i.e., $< 10-15\ m$, where there is not much suspended inorganic/organic matter within the water column, there is always some reflection from the bottom that increases the signal strength. When examining water quality, this signal is unwanted and should be isolated from the total signal. However, in bottom mapping studies, signal arising from benthic cover is considered as the desired signal. The majority of bottom mapping efforts have been concentrated on mapping coral reefs, algae, and algal turf in clear waters of tropical areas. In these studies, where impacts of water constituents are relatively minimal, the optical signatures of the benthic cover provide clues on their living condition. In the present study, it is assumed that due to the ubiquitous presence of suspended particles, i.e., $> 0.1\ g/m^3$, in the study areas the bottom has zero contribution to the water-leaving signal.

3.5.3.2 Water Constituents

As stated, optically active components (OACs) include CDOM, chlorophyll-a (CHL) and Total Suspended Solids (TSS). The Colored Dissolved Organic matters (CDOM), also known as yellow substance or Gelbstoff, is an important component in light attenuation in the Ultra-Violet (UV) and the blue regions of the spectrum. For coastal areas, freshwater inputs, which result from decaying material, are the principle source of CDOM. Although absorption within the blue region of the spectrum is largely dominated by CDOM, high concentrations of the other two components may reduce the role of CDOM in water-leaving signal and lead to confusion in the retrieval process [Del Castillo and Miller, 2008], [Kutser *et. al.*, 2005].

Another component of the water column is CHL resulting from photosynthetic activity of phytoplankton communities. CHL is a green pigment measurable through remote sensing, and is tied with phytoplankton, which is the source of the food chain in aquatic environments [Gitelson *et. al.*, 2007], [Raqueno, 2003]. Therefore, the state of the ecosystem can be inferred by determining chlorophyll concentration, i.e. high concentration (algal bloom) is due to high nutrient and chemical loads whereas low concentration is indicative of low productivity and/or high presence of zooplankton. Chlorophyll is the principle absorber of light within the blue and red portions of the spectrum. Based on its chemical composition, two types of chlorophyll are defined, chlorophyll-a and chlorophyll-b. While chlorophyll-a is the principle pigment found in plants, chlorophyll-b only alters (broadens) the shape of the absorption spectrum. The focus of oceanographers and scientists, hence, is to retrieve chlorophyll-a (CHL).

The Total Suspended Sediment (TSS) is loosely defined as all of the particles existing within coastal and inland waters and has a major contribution to the level of turbidity of waters. Particulate matter, in general, includes inorganic and organic particles whose concentrations can be determined via gravimetric lab measurements [Binding *et. al.*, 2008], [Bowers *et. al.*, 2007]. The scattering and absorption properties of particles are highly dependent on the composition of particles, i.e., their index of refraction, size and distribution [Bowers *et. al.*, 2009]. For example, the absorption and scattering coefficients associated with clay are different from those of silt. Therefore, in case of investigating extensive areas

of multiple input flows, averaged spectra should represent a reasonable estimate of the attenuation induced by the total suspended particles.

3.5.3.3 Atmosphere

As briefly described earlier, the atmosphere is a major impediment factor in remote sensing of water due to the low signal levels leaving the water body. The effect of the atmosphere on a beam of light can be described by the atmospheric absorption and scattering. While the former results in loss (removal) of energy, scattering induces photons to change direction and form a spectral distribution of the energy in the beam.

(a) Atmospheric Absorption

Absorptive characteristics of the atmosphere are determined by the absorption coefficient:

$$\beta = mC_{\alpha} \quad 3-31$$

Where m represents the number density of the molecules and C_{α} is the absorption cross-section. The transmission due to the absorption can be expressed in the following fashion

$$\tau_a = e^{-\beta z} = e^{-\delta} \quad 3-32$$

Where z is the path length over which we attempt to characterize absorption and δ is the unitless optical depth. The overall absorption due to the total atmospheric constituents is obtained by the product of transmissions associated with all of the constituent [Schott, 2007].

(b) Atmospheric Scattering

Scattering can be described by three different theoretical approximations, namely Rayleigh, Mie and non-selective scattering [Schott, 2007]. The Rayleigh scattering model is used when light interacts with particles or molecules whose sizes are significantly smaller than the wavelength of the incident flux. Based on this theorem, the scattering coefficient is proportional to the inverse of the fourth power of wavelength, i.e.

$$\beta \propto \frac{1}{\lambda^4} \quad 3-33$$

When the wavelength of the incident light is approximately equal to the particle size, the Mie scattering theory is applied. The Mie theory states that the scattering coefficient is approximately proportional to the inverse of the wavelength of the incident light. Such particles include aerosols, fossil fuel combustion products, and small dust particles. In general, the Mie scattering introduces higher complexity in lower atmosphere layers due to the presence of large particles (aerosols) whose composition is very variable spatially and temporally. In the non-selective region, scattering is independent of the wavelength and the size of the particles is much larger than the wavelength of the incident energy. Water droplets and large dust particles are among such particles. Compared to the absorption, the scattering coefficient is characterized in a different manner as the angular scattering coefficient, which describes the amount of energy scattered into a solid angle at an angle θ from the propagation direction. Depending on the atmospheric composition, different angular scattering coefficients can be introduced to determine the total scattering coefficient. One of the first angular scattering coefficients is the Rayleigh coefficient, written as

$$\beta_r(\theta) = \frac{2\pi^2}{m\lambda^4} (n(\lambda) - 1)^2 (1 + \cos^2 \theta) \quad [m^{-1}sr^{-1}] \quad 3-34$$

Where $n(\lambda)$ is the index of refraction of the molecules and m represents number density of molecules. By integrating 3.34 over all possible angles the total scattering coefficient [m^{-1}] is obtained. Describing the Mie scattering in the same fashion is not as straightforward as in the Rayleigh scattering. However, it is interesting to know that the Mie scattering is highly forward scattering while Rayleigh scattering is symmetric in forward and backward directions [Schott, 2007].

A combination of such events, termed atmospheric attenuation, contributes to reducing the signal originating from water body as propagating through the atmosphere. Overall, the effect of the atmosphere on the signal reaching the sensor may be expressed with three terms described in Eq. 3-25, i.e. the down-welled, the up-welled, and the sensor-target path transmission. Extensive research has been conducted to characterize the state of the atmosphere and to develop atmospheric compensation methods for remote sensing purposes; nevertheless, there is still ongoing work improving the existing algorithms. The following section gives an overview of the commonly used techniques for atmospheric removal over water bodies.

(c) Atmospheric Effect Removal

As described in Section 3.5, the atmospheric interference in the reflective and the thermal portions of the spectrum is treated separately. Hence, different atmospheric removal techniques have been devised for water bodies. As explained in the previous section, scattering phenomenon is wavelength-dependent, and, therefore, has minimal effects in the thermal infrared region. In other words, when sensing the water surface temperature, the absorption properties of the atmospheric composition, water vapor and other gases, should be modeled to solve for the unknowns in Eq. 3-25, i.e., the transmission, the downwelled and upwelled radiance.

The MODerate resolution atmospheric TRANsmission (MODTRAN) is a radiative transfer model that determines different components of the signal reaching the sensor based on the user-supplied inputs [Berk *et. al.*, 1999]. By defining the sun-target-sensor geometry and built-in atmospheric models, or alternatively user-supplied data, MODTRAN reasonably estimates the associated unknown components in Eq. 3-25. In addition to MODTRAN, there exist other numerical methods, which require some knowledge of the state of the atmosphere, to approximate the atmospheric contribution to the total signal.

In the thermal domain, in the absence of knowledge of water vapor column within atmospheric layers, one may wish to apply experimental methods to diminish atmosphere effects. Cross-calibration of thermal imagery is among the techniques that reasonably accounts for atmospheric effects. Thomas *et. al.*, 2001 used SST products of Advanced Very High Resolution Radiometer (AVHRR) to convert Landsat-derived TOA radiance to the corresponding SST. [Thomas *et. al.*, 2002]. When the thermal infrared imager is equipped with two spectral channels within the thermal window, it is possible to conduct a split-window technique to retrieve water vapor content within the atmospheric column [Kleespies and McMillin, 1990]. Estimating the atmospheric profiles of precipitable water enables the removal/reduction of atmospheric interference in the radiance measured by the satellite. This technique requires no knowledge of mean air temperature and is expressed as

$$\frac{\tau_a}{\tau_b} = \frac{T_a^1 - T_a^2}{T_b^1 - T_b^2} \quad 3-35$$

where τ_a and τ_b , respectively, denote transmissions in band centers a and b while $a > b$ and T represents the brightness temperature. The superscripts indicate two different

measurements that provide enough temperature contrast. Klepsie and MC Millin (1990) found that there is a linear correlation between the transmission ratio, Eq. 3-35, and water vapor content. The absolute transmissions in individual bands are then computed by estimating transmission in one band. Several authors developed modifications of this method, which are avoided for brevity.

The atmospheric effects in the reflective domain is of major concern in water studies primarily due to the molecular and particulate scattering of atmospheric molecules and particles in the lower atmosphere. Depending upon the remote sensing task and the availability of the *in situ* data to characterize the atmospheric condition, different correction techniques may be applied. The atmospheric compensation methods range from simple techniques, such as dark object subtraction and empirical line method (ELM), to more rigorous, complicated techniques, i.e., physics-based models. Most of the model-based methods rely upon the zero-reflectance assumption within the NIR bands over open waters. However, this assumption does not hold over coastal/inland waters where the concentrations of organic/inorganic particles increase water-leaving radiance in the NIR. Moreover, these techniques are subject to calibration issues associated with the imaging systems.

Most of the model-based approaches are based on some iterative processes via adjusting a set of unknown atmospheric parameters. Depending on the technique and the model-specific parameters (e.g. particle size-distribution of aerosols, aerosol models, aerosol scattering, etc.), the unknown parameters may vary. These commonly include parameters characterizing the aerosol in the NIR region. The image-derived components to be used in model-matching procedures has commonly been band ratios. For instance, Ruddick *et. al.* chose band 7 and 8 of the SeaWiFS to define the band-ratio metric (ε), i.e., $\varepsilon = \rho^7 / \rho^8$ [Ruddick *et. al.*, 2000]. The techniques are generally implemented on Rayleigh-corrected data obtained from a different set of simulations. Some of these methods couple bio-optical models with atmospheric models in an attempt to simultaneously solve for the water constituents (or their optical properties) and the atmospheric parameters [Gordon and Wang, 1994].

When dealing with a multi-spectral dataset, such as L7, which lacks two well-calibrated NIR bands, we are restricted to other empirical methods. Therefore, for this study, we make use of some empirical methods, which work well with a few spectral channels. It turns out

that ELM is a robust method for atmospheric compensation of multispectral datasets [Gerace, 2010]. This method simply provides a linear regression relating at-sensor radiance (dependent variable) to surface reflectance (independent variable) of at least two targets. Applying the resultant regression equations on the image converts the radiance images to surface reflectance products. The choice of the targets is important in that they have to, at least, include a dark (e.g. deep water) and a bright (e.g. beach sand) object. Besides, targets (also referred to as pseudo invariant features (PIFs)) should be characterized with two properties. Firstly, they should be radiometrically stable, invariable with respect to seasonal changes, and exhibit Lambertian properties. Secondly, PIFs should be sufficiently large to avoid adjacency effects. The large extent of the targets ensures the pixels' purity with low local standard deviations. Clearly, the greater the number of targets the more robust the regression; although they all should satisfy the above-mentioned conditions. Even though deep water appears to meet the second condition, the first condition may not be valid as concentrations of water constituents can be heavily temporally variable. It is, therefore, necessary to account for appropriate estimation of concentrations and associated IOPs if one is willing to simulate water surface reflectance through Hydrolight. It should be noted that when the PIFS or the calibration targets within areas of interests are unavailable, due to cloud cover, undesirable atmospheric condition, or mixed pixels, it is possible to use turbid waters as the bright target, over local areas to perform the regression. This is feasible providing that the concentrations and IOPs of the waters are well known for the time of image acquisition. The ideal ELM, however, is implemented when *in situ* reflectance of some calibration panels are measured coincident with the satellite overpass.

3.5.3.4 Glint Effects

(a) Sun glint

Water-leaving reflectance is sometimes contaminated with glint effects resulting from sun light reflected off the air-water surface. This surface reflection is caused by the differences in the indices of refraction of air and water, and can be described by Snell's Law. One may think of the water surface as formed of thousands of facets out of which only several facets redirect incident light towards the sensor. The average of all facets, within a patch of water, reflecting incident light into the line of sight of the sensor make up the sun

glint [Gerace, 2010]. The number of image pixels deteriorated by the sun glint is a function of sun-object-sensor geometry, wave condition and cloud coverage. This indicates that the likelihood of having glint-contaminated pixels is greater when high spatial details are captured with the imaging device, i.e., 30 *m* pixels of L7 versus MODIS 1 *km* pixels. In fact, at relatively high spatial resolutions, slight variations in the local incident angles due to different wave facets can lead to surface reflection towards the imaging system. One should note that the image-derived surface reflectance of the areas contaminated with the sun glint closely resembles the solar spectrum or “white light”; therefore, the NIR and SWIR responses of such pixels appear much brighter than those of common water pixels. There are different algorithms for sun glint removal most of which are base upon the concept that the water-leaving radiance is zero within the NIR band and longer wavelengths; thus, under clear sky conditions, any contribution to the signal is due to the sun glint [Kutser *et. al.*, 2009]. A simple band ratio between the SWIR bands also enables identifying sun-glint contaminated areas. Such a first order estimate would also reveal the presence of atmospheric fronts, cloud coverage, or low fog conditions.

(b) Sky Glint

In general, sky glint is the surface reflection off of the water surface, which is more crucial because it is less dependent on the viewing geometry, i.e. many incident angles may exist [Doxaran *et. al.*, 2004]. Needless to say that the effect of sky glint is much less than that of the sun glint, and is a function of the sky downwelled radiance (L_d), i.e., higher in the blue region and smaller in longer wavelengths. However, the percentage of the contribution of the sky glint to the total sensor reaching radiance is the most notable for the longer wavelengths owing to the lower signal levels in such bands. For accurate constituent retrieval, the sky glint impacts should be accounted for. It is assumed that the sky glint contribution to the sensor reaching radiance can be formulated via the following expression:

$$L_{sg} = \rho_F(\lambda)L_d(\lambda)\tau_2(\lambda) \quad [W/m^2 \text{ um sr}] \quad 3-36$$

where L_{sg} is the TOA radiance due to the sky glint, $\rho_F(\lambda)$ stands for the Fresnel reflection coefficient, $L_d(\lambda)$ is the downwelled sky radiance, and $\tau_2(\lambda)$ represent the sensor-target transmission. The Fresnel reflection coefficient for the nadir-viewing geometry in calm water

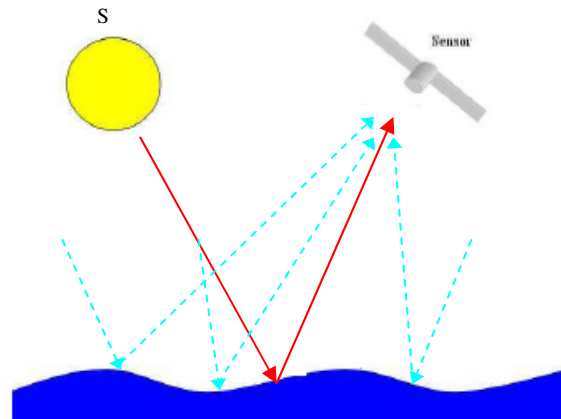


Figure 3.7. The schematic illustration of sun and sky glint. Solid lines represent rays due to sun glint and dashed lines indicate rays reflected off the water surface due to the sky light.

conditions may be approximated as a constant over the entire spectrum, i.e., $\rho_F = 0.02$. This parameter is very complex to quantify in real world conditions where wave-induced actions yield a non-uniform surface. In general, ρ_F is a function of imaging geometry, wavelength, and the concentrations of water constituents [Lee *et al.*, 2010]. Also, care must be taken when measuring the above-water, water-leaving radiance *in situ*, particularly when the measurements are desired to be linked to the in-water components. The other two parameters in Eq. 3-36 can be either measured or derived from simulations. Figure 3.7 illustrates the optical rays that reflect off the water surface and contribute to the formation of sun and sky glint. After describing the components forming the signal reaching the sensor we can turn our discussion to the methods which establish the link between water-leaving reflectance and water constituents. Since physics based models perform a better job in building up this link relative to empirical methods, we focus our attention upon physics based methods in which light-water interaction is rigorously taken into account. The in-water radiative transfer code used in this research is Hydrolight, which has been proven to properly simulate the angular distribution of light fields at different depths by taking in the IOPs and concentrations of water constituents such as TSS, CHL and CDOM [Raqueno, 2003]. The following section elaborates on this radiative transfer code [Mobley, 2008].

3.5.4 Water Constituent Retrieval

There are, in general, three approaches to retrieve water constituents. The earliest approach relies upon simple statistical regression between the *in situ* measured water constituents and image-derived products, such as TOA radiance or surface reflectance of individual, or a combination of, bands. After establishing a relationship between the remotely sensed quantities and the *in situ* measured concentrations for a sub-sample of the imagery, one could generalize the regression model to the entire image. This method, however, is very site-specific and not robust. Another approach applies semi-analytical models and relates measured remote sensing reflectances (R_{rs}) to bio-optical properties of the water body. In the third method, a physics-based model is used to model various water types, generate an LUT, and perform a spectral optimization to assign water constituents to each pixel. While each of these methods has its pros and cons, a reasonable knowledge of the IOPs of the areas under investigation is crucial when applying physics-based techniques. Since the focus of this research for the water constituent retrieval is on the use of physics-based (radiative transfer) models, a relatively thorough discussion of such models is presented. However, for completeness, a brief introduction of the bio-optical models is also given in the following section.

3.5.4.1 Bio-optical Models

The bio-optical models, in general, are simplifications of complex physics-based models. The water constituent retrieval using bio-optical models can be thought as an inverse model problem. The photons interacting with water constituents and leaving the water surface can be measured either *in situ* or remotely. Mobley (1994) states that the water-leaving reflectance in case II waters is proportional to the ratio of the total particle backscattering over the summation of total particle backscattering and absorption. This proportionality becomes an equality by applying a scaling factor (K):

$$\rho^{-0} = K \frac{b_b(\lambda)}{b_b(\lambda) + a(\lambda)} \quad 3-37$$

where ρ^{-0} is the water-leaving reflectance just below the water surface, b_b denotes the total backscattering coefficients and a represents the cumulative absorption, i.e., the summation of

all of the in-water components. The above equations can be expanded to include parameters of interest in the retrieval process [Lee *et. al.*, 1994]:

$$\rho^{-0} = K \left[\frac{b_b^W + b_b^{CHL} CHL + b_b^{TSS} TSS}{b_b^W + b_b^{CHL} CHL + b_b^{TSS} TSS} \right] + \left[\frac{a^W + a^{CHL} CHL + a^{TSS} TSS + a_{CDOM}}{a^W + a^{CHL} CHL + a^{TSS} TSS + a_{CDOM}} \right] \quad 3-38$$

where the subscripts indicate the specific absorption/scattering coefficients for each component, W stands for water, TSS and CHL denote the corresponding concentrations, and a_{CDOM} is the CDOM absorption. Given the specific absorption/scattering coefficients and the parameter K , one can solve for the water constituents. The most important factor that has to be determined to be able to perform the inverse modeling is the parameter K . This parameter is a function of imaging geometry and accounts for the signal loss due to the air-water interface and wave conditions. Several researchers have made attempts to quantify this empirical factor by fitting *in situ* measured surface reflectances with those derived from the model (Eq. 3-38) for different types of waters in different geographic locations [Yang and Gordon, 1997; Maritorena *et. al.*, 2002; Wang *et. al.*, 2005]. As seen in this equation, the impacts of different phase functions are not explicitly incorporated and are buried in b_b . Furthermore, the IOPs are commonly modeled using analytical/experimental methods, which are well known for case I waters but not for case II waters.

3.5.4.2 In-water Radiative Transfer Models

Since the water constituent retrieval in this research is conducted using the Hydrolight model, the major focus of this section is on describing this model and its component. A complete description of the model is given in [Mobley, 2008].

Hydrolight is a time-independent, plane-parallel radiative transfer model, which predicts the radiance distribution of a light field within and out of a water body. The considerations of time-independency and water layers formed of parallel layers appear to be valid assumptions for large stable water bodies. Regarding the latter assumption, one can claim that horizontal scales of significant optical variability of a water body are much greater than its vertical variability. In the light of this, one can think of water bodies as separate patches of water that can be modeled independently as horizontally homogenous layers of water whose optical properties vary only in vertical direction. It is then possible to run 1D radiative transfer

equations at the center of each patch to simulate radiance distribution within a water column. In order to obtain radiance distribution over an entire area of interest, a number of simulations have to be conducted. In the simulations associated with remote sensing studies, it is valid to think of each patch of water as one "ground sample distance" (GSD). The piecewise simulation holds true as long as the size of the patches of water is at least several photon mean free paths (the inverse of beam attenuation). In clear waters horizontal variability is on the order of kilometers, photon mean free path is never more than 50 *m*. In contrast, coastal waters exhibit high horizontal variability but the photon mean free path is on the scale of tens of meters [Mobley, 2008]. This is particularly of concern in cases where river runoff and particulate matter are introduced to coastal waters. In such examples, boundary conditions are on the order of tens of centimeters to a few meters. In either case, the use of one-dimensional equations can be justified by carefully estimating horizontal variability. The use of time-independent radiative transfer is also valid when the time scales for changes in environmental conditions (typically seconds to seasons) are much greater than the time required for the light field to propagate within the water body after a change in the optical properties or boundary conditions (milliseconds).

Aside from the above assumptions, there are also other physical considerations incorporated in the Hydrolight code which include

- Arbitrary depth-dependent IOPs
- wavelengths range: 300-1500 *nm*
- Cox-Munk capillary-gravity wave sea-surface slope statistics
- Finite or infinitely deep (non-Lambertian) water-column bottom
- Multiple scattering
- Option for Raman scattering by water
- Option for incorporating fluorescence by chlorophyll and CDOM

(a) Inputs

In order to run Hydrolight, the following sets of variables are to be provided to the model. It should be noted that, these input data files are either measured or analytically generated through experiments or computational methods.

- Wavelength-dependent IOPs: As stated earlier, absorption and scattering coefficients as well as scattering phase functions of water and its constituents are considered as IOPs. Two examples of IOP spectra are shown in Fig. 3.8.
- The state of the wind-blown sea surface. The sea surface is modeled using the Cox-Munk capillary-gravity wave-slope statistics, which adequately describe the optical reflection and transmission properties of the sea surface for moderate wind speeds and solar and viewing angles away from the horizon. Only the wind speed needs to be specified to enable predicting the wave statistics used in simulations.
- The sky spectral radiance distribution. This radiance distribution (including background sky, clouds, and the sun) can be obtained from semi-empirical models that are built into the model, from observations, or from a separate user-supplied atmospheric radiative transfer model, such as MODTRAN.
- The nature of the bottom boundary. The bottom boundary is described in terms of a BRDF. For finite-depth bottoms, the BRDF is computed from the given reflectance of the bottom type. For infinitely deep water, the inherent optical properties of water body below the region of interest are used to compute the (non-Lambertian) BRDF[Mobley, 2008].

(b) Mathematical Model

The fundamental quantity in the model calculations is the spectral radiance $L(z, \theta, \phi, \lambda)$ which defines the directional dependency of the light field at different depths and wavelengths. When looking through an imaging sensor, the system collects photons, which lie within its FOV. In order to characterize radiance heading toward the imaging system, spectral radiance is discretized within various angles (Quads) at which radiance is independently calculated. Based on the spectral radiance, other quantities of interest

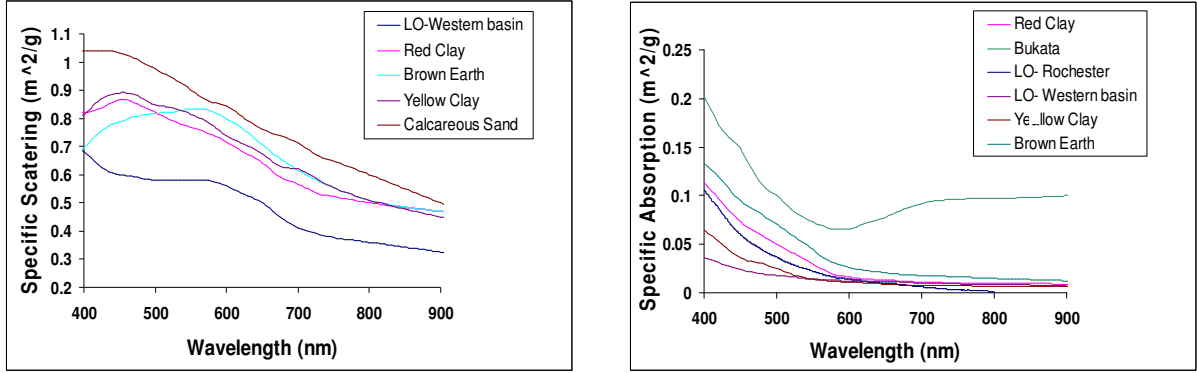


Figure 3.8. The scattering and absorption coefficients for different types of particles observed in various types of waters. In general, the shapes of the absorption/scattering spectra show the same trends while the magnitudes vary as high as 50% and 400% for the scattering and absorption coefficients

such as beam attenuation, sky radiance, and various irradiances can also be computed. Of our particular interest is water-leaving energy (just above the surface) heading towards the sensor, containing signals associated with water constituents. The way Hydrolight calculates this variable is equivalent to the definition of remote sensing reflectance which essentially specifies the BRDF:

$$R_{rs}(\theta_i, \phi_i, \lambda) = \frac{L(\theta_i, \phi_i, \lambda)}{E(\lambda)} \quad [sr^{-1}] \quad 3-39$$

where $L(\theta, \phi, \lambda)$ stands for the spectral radiance [$W/m^2 \mu m sr$] and $E(\lambda)$ is the total incident downwelling irradiance [$W/m^2 \mu m$]; However, characterizing the BRDF using available instrumentation is quite cumbersome [Schott, 2007]. Instead, directional-independent diffuse reflectance (unitless), the quantity typically expressed in the science community, is generally used. The simulated remote sensing reflectance leaving the water surface can also be converted to the unitless reflectance. This is accomplished by multiplying the remote sensing reflectance heading toward a sensor's field-of-view by π .

3.6. Concluding Remarks

In this chapter an overview of fundamental concepts crucial to this research was presented. We began by describing the motivations of this work in terms of its environmental

perspective followed by issues regarding the dynamics of coastal waters with particular reference to the Great Lakes. In the light of this, coastal zones were defined and the driving factors causing all variability within coastal waters were elaborated. A hydrodynamic model, ALGE, along with its corresponding governing equations was also treated. It is acknowledged that the primary impediment factor in simulating water hydrodynamics is how to define the boundary condition. This might describe some level of uncertainty in model results. The remote sensing of water and its components were also described. A brief overview of the remote sensing governing equation was given followed by the sensor considerations needed for such studies. The signals arising from a water body were decomposed in the following sections. Hydrolight and its input parameters were then thoroughly overviewed to give an insight into an in-water radiative transfer model and its components. It turns out that IOPs are an essential part of Hydrolight and care must be taken in their measurements or estimation. This section is an effort to establish the link between modeling result and remote sensing imagery.

Chapter 4

4. Methodology

4.1. Overview

The purpose of this chapter is to lay out the procedures for the three tasks that have been conducted as parts of this research effort.

In order to begin a remote sensing project, one has to first ensure that the desired remotely sensed data come from a well-characterized imaging system(s). Although L7 calibration status has been well monitored for bright targets, its performance over targets of low signal levels (water) has rarely been examined. Therefore, the first task of the present research, involves validating the calibration status of L7 relative to the Terra-MODIS instrument over clear, dark waters. The optically stable waters are selected as calibration sites to compare the nearly simultaneous L7 and Terra-MODIS responses. The Terra-MODIS designed for global monitoring of large-scale phenomena across the globe has been heavily used for studying oceanic waters. Its design, band configuration, and high SNR over dark targets have enabled reliable mapping of ocean color over more than a decade.

The second task that has been the main focus of this research effort is to integrate the hydrodynamic model (ALGE) with the L7 data to enable monitoring the dynamics of coastal waters when remotely sensed data is unavailable. In order to do so, the L7's thermal and reflective bands are applied to calibrate the meteorologically driven model. This is done in a two-step procedure. The ALGE model is first calibrated for its input meteorological data by optimizing with the L7-derived temperature maps. The profiles of constituent concentrations are then estimated through a model matching technique in the surface reflectance domain where the L7-derived surface reflectance maps is compared to those obtained from

Hydrolight modeling. This task is largely designed as a path finder to develop tools for the OLI mission.

The third task is to investigate the potential of the new generation of Landsat in a water constituent retrieval framework. The Operational Land Imager's (OLI) data is simulated by spectrally resampling a Hyperion dataset acquired nearly simultaneous with a L7 image. In addition to simulating the OLI sensor data using Hyperion, the ALI imagery was also incorporated in the retrieval process. The concentrations of water constituents retrieved from the simulated OLI imagery are then compared to those obtained from Hyperion, ALI, simulated L7, and the observed L7 data. This cross-comparison is conducted to fully consider the improvement levels of the OLI sensor in terms of its enhanced features for water studies.

4.1.1 Cross-calibration

Landsat has been recognized as a valuable means for monitoring earth resources over the past four decades. Landsat's continuing mission over the next decades enables a consistent, long-term monitoring of the earth by the science community. Although L7 has not been configured for water studies, if well-calibrated, it can be utilized in conjunction with LDCM, as a tandem mission, for future water studies. Furthermore, the availability of L7 imagery over the past decade may provide a valuable means for studying long-term trends in areas where other coarse (spatial) resolution remote sensing systems are unable to resolve the desired spatial details.

In this effort, the historical trends of L7-MODIS relative calibration obtained over a mid-latitude lake as well as over tropical/arid waters of relative optical stability are presented. In order to test the robustness of our methodology, the procedure is also applied over a well-known calibration site for a limited number of scenes during 2008-2011. By treating the calibration differences derived from the trending study as bias-only errors, a series of simulations are conducted to evaluate the impact of such errors on the retrieved diffuse surface reflectance (r_d). To do so, the MODTRAN code is provided with four surface reflectance spectra as representations of different water types. Various atmospheric conditions are also simulated to thoroughly understand the mis-calibration effects. In order to quantify how such retrieval errors would influence the retrieved water constituent concentrations, i.e., CHL and TSS, a subset of an atmospherically compensated L7 scene was

processed using a physics-based approach. The calibration-induced errors obtained in the retrieval of r_d were applied to the originally derived surface reflectance map to mimic an uncalibrated surface reflectance map.

4.1.2 L7-Model Integration

As described, in this study, the L7 imagery is utilized to calibrate the ALGE model for its thermal and material load predictions. Integrating Landsat, and the 3D hydrodynamic model enables a) the retrieval of profiles of water constituents and b) capturing the dynamics of coastal systems at instances and locations for which no imagery is available. The integrated, physics-based approach in which the simulations are conducted nearly at the L7's spatial scale ($\sim 100\text{ m}$) aid in a detailed quantitative mapping of coastal/inland waters where other coarse-resolution systems, such as MODIS, are unable to meet the science needs.

In order to begin with the simulations, the hydrodynamic model is allowed to stabilize by running for a sufficient period (model stabilization). However, the meteorological data supplied to the model are attributed with some uncertainties, which introduce errors in the model predictions. In order to compensate for such observational errors, the model is first calibrated using a model-matching technique based on its thermal outputs. In this procedure, many simulations are re-started for the last few hours of simulations by varying key input parameters controlling the thermal structure of the water body. The model-derived surface temperature maps are then optimized against L7 imagery to select the best match (Figure 4.1). When calibrated for its meteorological inputs, the ALGE model is used to retrieve the profiles of water constituents. To do so, the concentration of color agents, the particle size, and particle densities are adjusted to generate various concentration maps. The Hydrolight model is then applied to simulate the outgoing optical field towards the L7's FOV for each ALGE-derived output concentration map. The water-leaving optical field chosen for this model-matching technique is the diffuse surface reflectance, i.e., r_d . The coupled model outputs are then compared with the surface reflectance products created from the L7 reflective bands. The goodness of fit for each output is expressed in terms of RMSE in units of surface reflectance. Figure 4.2 illustrates the procedure pursued in the reflective domain. For a more detailed description of the approach see Section 4.5.

The primary assumption in this two-step procedure is that there is a high correlation between the spatial distribution of the water constituents and their thermal distribution. In other words, the input flows from rivers/streams should exhibit distinct thermal and physical structures when compared to those of the ambient lake waters. This assumption ensures the validity of this method and its implementation in two independent phases.

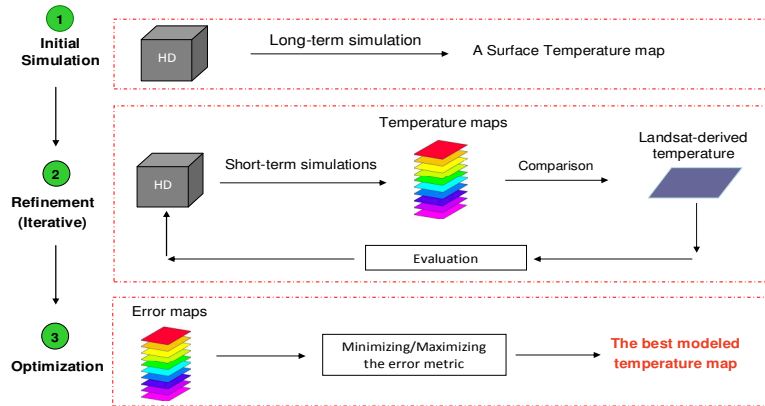


Figure 4.1. The flowchart illustrating the model calibration process in the thermal domain

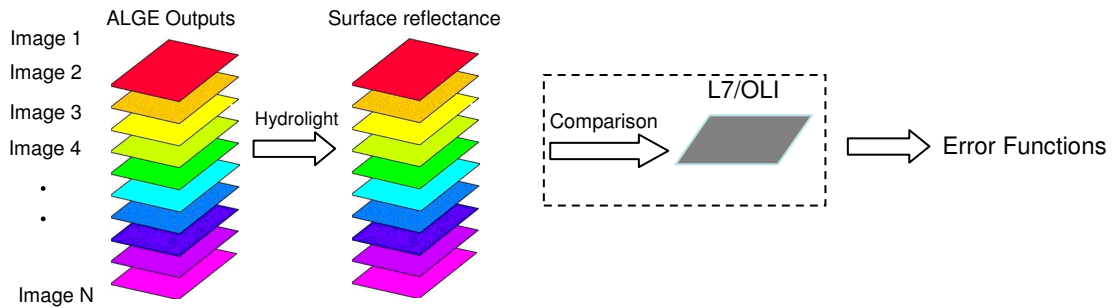


Figure 4.2. The flowchart illustrating the process conducted in two steps, namely thermal and reflective modes.

This technique leverages the remotely sensed thermal and reflective imagery to predict the horizontal and vertical structure of the water constituents in coastal/inland waters.

4.1.3 OLI's Potential over Case II Waters

In an independent study, the capability of the OLI sensor for constituent retrieval is investigated. The Hyperion imagery, acquired simultaneously with L7, is spectrally resampled to OLI's spectral response functions to simulate what OLI would “see” for the area under investigation. In order to thoroughly determine the enhancement levels of OLI relative to L7, the OLI-derived water constituent maps are compared with those obtained from the simulated L7, the observed L7, the simulated ALI, and the ALI data. The ELM approach was adopted to atmospherically correct the set of imagery. In order to retrieve water constituents, a LUT of various concentration levels is populated through many Hydrolight simulations. A spectral matching method was employed to search the LUT for the best fit to the surface reflectance derived for a single pixel. The measured water constituent concentrations, Hyperion-derived concentrations, and MODIS-derived CHL concentrations were utilized as reference data for validation. The uncertainty associated with the concentration maps is expressed in units of reflectance, which gives some insight into errors corresponding to concentrations. Section 4.6 elaborates on the procedure described here.

4.2. L7-MODIS Cross-calibration

4.2.1 Calibration Sites

For the purpose of this study, bodies of waters with relatively optically stable properties are utilized for evaluating L7's visible bands. To a first order approximation, under ideal environmental conditions and near-nadir viewing angles, we can assume that the water surface is nearly Lambertian.

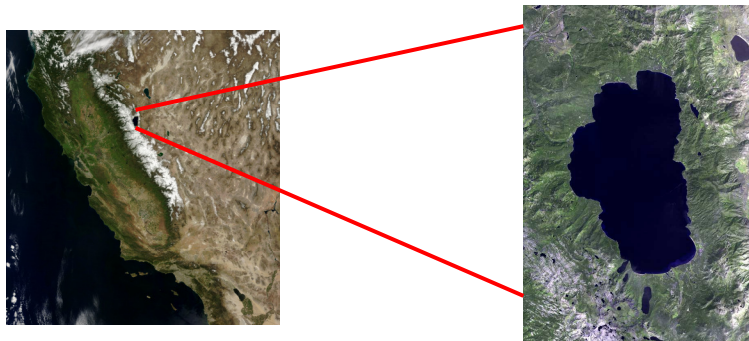


Figure 4.3. Lake Tahoe is located in the high mountains of the western US on the Nevada-California border

Table 4.1. The specifications of the tropical-arid calibration sites

Sites	WRS-2 path/row	UTM zone	Latitude, Longitude	Elevation (km)	Range of CHL-a ($\mu\text{g}/\text{l}$)	# of image pairs
Lake Tahoe	43/33	10	38.9 N, 120W	2.170	0.2-0.6	52
Lake Malawi	168/69	36	13S, 34.6E	0.777	0.4-0.8	6
Red Sea	174/41	36	27.4N, 34.3E	Sea level	0.1-0.3	25
Striat of Hormuz	159/42	40	26N, 57.1E	Sea level	0.2-0.6	11
RVPN	40/33	11	38.5N, 115.7W	1.350	NA	11

Moreover, it is desired that the corresponding site be situated in an area where the effects of atmospheric gases and aerosols are minimal. Lake Tahoe, a high-altitude, mid-latitude lake located on the border of California-Nevada, USA, was found to satisfy the aforementioned conditions (Figure 4.3). Due to its thermal stability and deep bathymetry, Lake Tahoe, ($39^{\circ}\text{N}, 120^{\circ}\text{W}$), has been used as a calibration/validation site for monitoring thermal channels of a variety of remote sensing systems [Hook *et. al.*, 2005]. This thermal stability also mitigates wind-induced surface waves, which in turn reduces the sun glint effects in L7 scenes. Having a watershed area of 800km^2 , Lake Tahoe receives inputs from more than 60 river/streams among which the Upper Truckee River provides the largest stream flow into the southern lake areas, i.e., annual average of $10\text{ m}^3/\text{s}$ [Schladow, 2011]. Therefore, the southern parts of the lake are avoided in this study. Over the past decade, the NASA's Jet Propulsion Laboratory together with Tahoe Environmental Research Center have established collection sites to monitor the lake's physical/biological process. Among their observations, the water clarity and chlorophyll-a concentration are of our primary interest.

The Secchi depth of over 20 m and average chlorophyll-a (CHL) concentrations of $< 0.6\text{ }\mu\text{g}/\text{l}$ over the past 10 years indicate the lake's optical stability [Steissberg *et. al.*, 2010]. Cloud-free image pairs spanning from end of spring to mid fall during the two missions'

lifetime are used. The main drawback of Lake Tahoe as a calibration site is its relatively limited spatial extent ($\sim 500 \text{ km}^2$) as opposed to the open waters that enable choosing regions of interest (ROIs) with consistent atmospheric condition despite partial cloud contaminations.

Since studying Lake Tahoe restricts our analysis to a limited range of signal levels, other sites situated in low-latitude, tropical-arid regions, hereafter Tr-Ar, are also investigated (Table 4.1). Incorporating higher sensor-reaching radiances aids in quantifying the possible changes in the relative gain and offset between the two sensors. These sites include Lake Malawi in tropical east Africa, the northern Red Sea, and the Strait of Hormuz in the Persian Gulf. Due to the climatic conditions, the suitable scenes were only available in the late fall and in the winter periods. Although recognized as mesotrophic waters during this timeframe, the above-noted waters exhibit less optical stability than Lake Tahoe and the concentrations of CHL have to be checked for anomalous scenes. Under ideal atmospheric conditions with low aerosol loading, the MODIS-derived CHL maps (available from NASA's Ocean Biology Group website) provide a reasonable estimate of their optical regime predominantly driven by the concentration of chlorophyll-a. Furthermore, the atmospheric composition over such regions is temporally and spatially variable and is less known than that over Lake Tahoe. The complex atmospheric condition reduces the number of successfully acquired scenes for this study. Table 4.1 indicates the path-row, the site locations/elevations, the range of possible CHL concentrations, and the total number of scenes used.

In order to validate our proposed approach for the cross-calibration over the dark, mesotrophic waters, the procedure is also implemented for the Railroad Valley Playa Nevada (RVPN) site for the past four years of L7 and Terra, i.e., 2008-2011. The RVPN is a desert calibration site with typically clear atmospheric conditions [Thome *et. al.*, 2003]. The site also has a reasonable, spatial uniformity making it a suitable bright target to examine whether our findings are in agreement with those from other studies. To do so, a handful of nearly coincident, cloud-free L7-MODIS image pairs collected in 2008-2011 timeframe are utilized.

4.2.2 The Criteria for Image Pair Selection

For the purpose of this study, the 500 m L1B calibrated Terra-MODIS products [$W/m^2 sr \mu m$] were projected onto the UTM projection with the WGS84 as the reference datum to maintain consistency with the L1T Landsat products with 30 m GSD. The ROIs

taken from the image pairs were situated in the near-nadir sensors' line of sight. It is highly desirable to choose a site imaged with a similar geometry by the two sensors. Both L7 and MODIS, for instance, observe Lake Tahoe at slight off-nadir scanning angles, i.e., $< 3^\circ$. This similarity in the acquisition geometry mitigates artifacts introduced by the wide scanning angles of MODIS, i.e., polarization sensitivities. Moreover, the large scanning angles of MODIS cause significant differences in the path-lengths, the atmospheric conditions, and the BRDF effects that may invalidate our Lambertian assumption for the bodies of waters if common line of sight were not used.

Although the ROIs were imaged from very similar viewing geometry, the relative sun-sensor azimuth angles are slightly different due to the approximately 25-minute time difference. Such disparities are inevitable and assumed negligible owing to the near Lambertian properties of the sites. The change in the solar elevation angles, however, is taken into consideration and is described in the next section. The ROIs are rectangular areas of 1 km^2 containing four MODIS pixels equivalent to approximately 900 L7 pixels. The area-averaged TOA radiance values calculated for L7 should account for its lower SNR and quantization rate, glint effects, differences in wave facets, and whitecaps. It should be noted that the ROIs were drawn over spatially uniform waters while nearshore areas in the vicinity of discharges were avoided. This also minimizes the adjacency effects and possible mis-registration errors.

The corresponding ROIs are also expected to retain minimum variability, i.e., low standard deviation. This condition minimizes the variability due to the inherent composition of the water bodies. To meet this condition, the coefficient of variation (CV), i.e., the ratio of standard deviation to mean value, was allowed to reach a maximum of 3%, 5%, 10%, and 17% for L7's VNIR bands respectively. The corresponding values adopted for MODIS-derived ROIs were 0.2%, 0.7%, 0.6%, and 2%. Note that the larger variations in the L7-derived values are mandated by its poorer SNR and coarser radiometric resolution.

Besides restricting the calibration sites according to the viewing geometry and the spatial uniformity, the atmospheric conditions between the two acquisitions were controlled via comparing the sensors' responses in the SWIR-bands. Following preliminary studies and simulations, it was decided to discard the image pairs showing more than 8% and 30% differences in the SWIR-I and SWIR-II bands, respectively. Such a criterion ensures the

consistency in the atmospheric conditions during the L7 and MODIS overpass. The approximately 20% difference for the two bands gives an estimate of the collective differences in the relative spectral response (RSR) functions, the relative calibration, the BRDFs, the solar zenith angles (SZA), and the environmental conditions. Note that due to its narrow spectral bands and the descending trend in the water-leaving radiance spectrum (SWIR), MODIS should always exhibit larger responses in these bands. With this strict requirement, out of approximately 150 image pairs over the sites, which were initially selected, nearly 40% were filtered out. It should also be noted that this criterion was restricted for the most recent MODIS scenes, i.e., 2010-2011, over Lake Tahoe as negative values were recorded for most pixels. In addition to the calibration issues associated with Terra-MODIS, the limited number of photons reaching the sensor from a mid-latitude lake characterized with clear atmospheric conditions can explain the incorrect observation of the surface properties at the top of the atmosphere.

For the cross-calibration study over the RVPN site, an average surface reflectance of the site [Czapla-Myers, 2011] was provided to the MODTRAN code. The ROIs consisting of four MODIS pixels were drawn to obtain the basic statistics. The CV for each individual image was controlled to ensure the relative spatial uniformity and avoid mis-registration errors. The conditions stated for the over-water calibration sites, such as optical stability and very similar viewing geometries, do not hold for the RVPN. However, only 11 cloud-free image pairs during 2008-2011 were found for this study (Table 4.1).

4.2.3 Conversion to the TOA Reflectance

As Terra-MODIS acquires imagery nearly 25 minutes after L7 overpass, the total solar radiation reaching the earth surface varies due to the change in the solar zenith angle (SZA). Moreover, the available solar radiation is different at different days (DOY) throughout the year. In order for a consistent analysis to occur across all of the image pairs, the above-noted factors were taken into account by applying the following equation, which transforms the observed TOA radiance quantity to the unitless TOA reflectance (ρ^{TOA}):

$$\rho_{\lambda_0}^{TOA} = \frac{\pi L_{\lambda_0}^{TOA} d^2}{E_{\lambda_0}^{exo} \cos(\theta_s)} \quad 4-1$$

where $\rho_{\lambda_0}^{TOA}$ stands for the unitless TOA reflectance (planetary/apparent reflectance) at λ_0 , $L_{\lambda_0}^{TOA}$ is the TOA radiance for the same wavelength, d is the astronomical earth-sun distance [AU], $E_{\lambda_0}^{exo}$ [$W/m^2\mu m$] is the band-specific exo-atmospheric solar irradiance, and θ_s is the solar zenith angle (SZA) in degrees. The SZA was computed for each individual image at the location where the ROI was drawn. This is, in particular, important when determining the SZA for the MODIS-derived ROI. For this work, the exo-atmospheric solar irradiance was derived from MODTRAN4 database (Thuillier) and was resampled to appropriate wavelength values for individual sensor response functions.

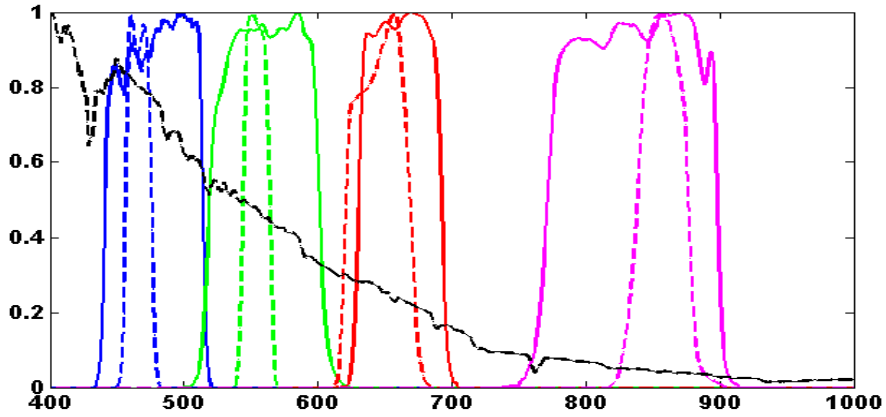


Figure 4.4. The relative spectral response functions of L7 (solid lines) and MODIS (dash lines) overlaid onto an average modeled TOA radiance normalized to its peak value.

4.2.4 Adjustments for the RSR Functions

As illustrated in Figure 4.4, L7's RSR functions cover broad spectral regions relative to those of MODIS. This difference introduces significant inconsistencies when imaging a reference TOA radiance curve representing a large, band-to-band gradient [Teillet *et al.*, 2007]. This is most noticeable over dark targets when the signal is primarily dominated by the atmospheric interference. In order to take into account the differences in the band-specific RSRs of the two sensors, a model-based approach similar to that of Teillet *et al.* (2007) was adopted for this study. This technique relies upon hyperspectral TOA radiance spectra generated through simulations. Chander *et al.* (2010) also proposed a similar method

applying Hyperion measurements to estimate the RSR adjustment factors when imaging desert sites [Chander *et. al.*, 2010(b)]. Depending on the shape and the magnitude of the ground target and the atmospheric conditions, the effects of the differences in the RSRs would differ. If a dark target, such as water or dense vegetation, is considered as the ground target then the atmospheric condition must be well estimated (Section 2.4.2).

4.2.4.1 Modeling the Site-specific Diffuse Surface Reflectance (r_d)

In this study, a radiative transfer code, i.e., MODTRAN [Berk *et. al.*, 1989], is employed to simulate the TOA radiance spectrum observed by the two sensors at a given time, which represents the mean overpass time of the two sensors. The diffuse surface reflectance spectrum (r_d) of Lake Tahoe and the Tr-Ar sites were simulated using the Hydrolight code. The average IOPs of the sites and a realistic range of the concentrations of CHL (Table 4.1) were provided to the Hydrolight code. For each site, three different waters representing different CHL concentrations (increments of 0.2 $\mu\text{g}/\text{l}$ in Table 4.1) were supplied to MODTRAN to simulate the TOA radiance over such Mesotrophic waters. The slight variations in the CHL concentrations account for the uncertainties in the estimated IOPs with which the reflectance properties are predicted for each site. The CHL concentrations for several image pairs, however, were validated using the MODIS-derived products. The variations of the CHL concentrations are carried out simultaneously by adjusting the aerosol properties described in the following section. Note that the absorption due to the colored dissolved organic matter (CDOM) component of the waters is neglected in this study as L7 lacks the necessary band configuration to distinguish slight signal variations below 450 nm .

4.2.4.2 Estimating the Atmospheric Condition

The modeled r_d of the calibration sites are propagated through the atmosphere to achieve the TOA radiance spectra. For the simulations over Lake Tahoe, the MODTRAN code is provided with the modeled atmospheric profiles derived from North American mesoscale Model (NAM) available from NOAA's National Center for Environmental Prediction (NCEP) office. An atmospheric profile, at 12pm local time, for each day of year (DOY) corresponding to a successful L7-MODIS collect was obtained from the NAM model. For the Tr-Ar, average upper-air atmospheric profiles typical of the sites were supplied to the code.

The MODTRAN-derived TOA radiance curves are spectrally resampled with the RSR functions to reconstruct the multi-spectral curves as seen by L7 and MODIS. To do so, Eq. 3-30 was applied. The aerosol type and visibility associated with each individual image pair was estimated via a spectral matching technique between the MODIS-derived TOA radiance curves and multiple MODTRAN simulations. While only rural aerosols are regarded as a representation of the dominant Lake Tahoe aerosol content, both maritime and rural aerosol types were adjusted for the Tr-Ar. The aerosol visibility was found by minimizing the root RMSE calculated between the model outcomes and the reference curve across all of the seven bands, corresponding to the L7's reflective spectral channels. The RMSE represents the similarity of each individual simulated TOA radiance and the one observed at the top of the atmosphere by the MODIS instrument. This process is repeated for each image pair for the image acquisition day (day of year).

It should be noted that ideally the exact shape/magnitude of the MODIS-derived curve is desired through simulations; however, the goal is to make an appropriate approximation of the ratio of the sensors' responses under an atmospheric condition that closely resembles the conditions at the time of imaging. In other words, we do not intend to quantify the aerosol condition through this method and a reasonable estimate will satisfy our objectives.

4.2.4.3 Applying the RSR Adjustment Factor

After approximating the aerosol contents for each L7-MODIS image pair, the TOA radiances are passed through the sensors' RSRs (Eq. 3-30) followed by conversion to the TOA reflectance for a mean SZA and d . In this way, the only contributor to the differences in the simulated band-specific TOA reflectance curves at each λ_0 is the differences in the RSRs. Therefore, the following expression yields the RSR adjustment factor

$$\alpha_{\lambda_0} = \frac{\rho_{TOA}^{MODIS}}{\rho_{TOA}^{L7}} \quad 4-2$$

where ρ_{TOA}^{MODIS} and ρ_{TOA}^{L7} correspond to the MODTRAN-derived TOA reflectances for MODIS and L7, respectively. The L7-derived TOA reflectance values can then be adjusted by applying the RSR adjustment factor (α_{λ_0}) as a multiplicative coefficient, i.e.,

$$\rho_{TOA}^{\prime L7} = \alpha_{\lambda_0} \rho_{TOA}^{L7}$$

4-3

The average RSR adjustment factors obtained for Lake Tahoe were found to be 1.1027 ± 0.0048 , 1.0327 ± 0.003 , 1.0757 ± 0.0045 , and 0.9055 ± 0.0059 for the blue, green, red, and NIR bands. The corresponding averaged coefficients for the Tr-Ar sites were 1.0949 ± 0.0119 , 1.0342 ± 0.0026 , 1.064 ± 0.0074 , and 0.918 ± 0.0185 . As it appears, the largest disparity is observed in the blue band while the sensors' responses in the green bands exhibit rather high degree of resemblance by approximately 3% adjustment factor. In general, for water targets, the greater the TOA radiances, the flatter the spectral shape and, therefore, the sensor-to-sensor disparity diminishes. The coefficients primarily vary with the change in the magnitude of the TOA radiance mainly driven by the atmospheric conditions. Nonetheless, depending on the atmospheric conditions, the CHL concentrations can also slightly influence the coefficient associated with the blue band. As expected, the α_{λ_0} over the RVPN site are close to unity, i.e., 0.9935, 1.003, 0.9865, and 1.023, because of the relatively flat shape of the site's spectrum [Teillet *et. al.*, 2007]. These coefficients are applied to normalize the L7-derived radiance values with respect to those of MODIS.

The difference between the corresponding imagery expressed in percentage, i.e., $\left(\left(\rho_{TOA}^{\prime L7} - \rho_{TOA}^{MODIS} \right) / \rho_{TOA}^{MODIS} \right) \times 100$, is then calculated as the criterion to measure the disparity in the calibration of the two sensors.

To summarize, the following steps are to be followed to perform a cross-calibration task for an image pair over the water sites:

1. Geo-registration of the image pairs
2. Select the ROIs from the images based on the criteria described in Section 2.2
3. Calculate the mean values
4. Convert the image-derived TOA radiances to the TOA reflectances
5. Compute the RSR adjustment factor (α_{λ_0}) through predicting the TOA reflectances by going through the following steps
 - a. Provide the radiative transfer code with three different water types
 - b. Configure the code for the mean time of the two acquisitions

- c. Find the best estimate for the MODIS-derived curve by simultaneously adjusting water types, aerosol types, and aerosol visibility
 - d. Resample the matched TOA radiance curve to the L7 and MODIS RSRs
 - e. Convert to the TOA reflectance (Eq. 1)
6. Apply the RSR adjustment factor (Eq. 4)

The adjustments for the differences in the RSRs, which normalize the responses of the two sensors in the TOA reflectance domain, is a vital part of the cross-calibration over the dark waters. The uncertainties associated with this process, including the sites' optical properties and the ambient atmospheric conditions, were mitigated via multiple physics-based simulations to model various environmental conditions at the mean overpass time of the two platforms.

4.3. L7-Model Integration

4.3.1 Study Areas

For the purpose of this part of the research, two river plumes and a small lake are studied to verify the robustness of our method. The two river plumes, namely the Genesee River and the Niagara River, discharging into Lake Ontario, represent different characteristics making them suitable plumes to test the model for the prediction of the thermal structure and material transport near the discharges. In addition, Onondaga Lake, a small, eutrophic lake, is the other site, which enables us to examine the model's performance in a different environment. Figure 4.5 shows the geographic location of the three sites situated in upstate New York, USA. The following subsections briefly explain the physical and environmental properties of the three sites.

4.3.1.1 Genesee River

The Genesee River is a relatively small river originating from the mountains of Pennsylvania. However, the long travelling distance causes the river to be the key contributor to the water quality of the lake within the Rochester embayment. It originates from the Allegheny Plateau of Northern Pennsylvania and travels 240 *km* northwards before emptying into Lake Ontario at the Rochester embayment. The Genesee watershed covers seven

counties in western New York state, totalling 26000 km^2 , based on Department of Environmental Conservation reports. Figure 4.6 illustrates the watershed map [Makarewicz, 2010]. The water quality in the Genesee River watershed generally complies with the Environment Protection Agency standards; however much of the concern is attributed to the northern industrial and urban runoff and agricultural pollutants.

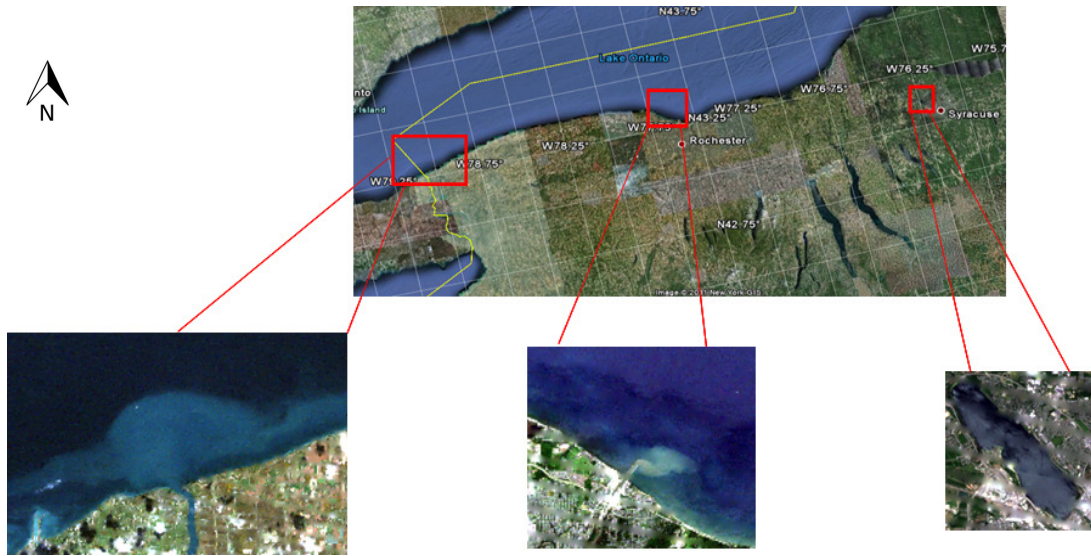


Figure 4.5. The study sites located in upstate New York, USA, shown in the red boxes. The river plumes enter southern shores of Lake Ontario.

Among the other anthropogenic activities degrading water quality in the City of Rochester, several wastewater plants including Eastman Kodak and Honeoye sewage plants discharge into the river. Such degradations periodically result in beach closure due to nuisance algae and excessive algal growth along the lake shoreline.

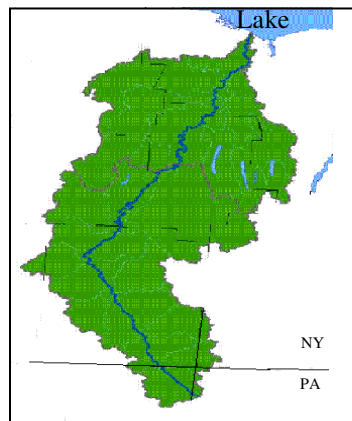


Figure 4.6. The Genesee River watershed

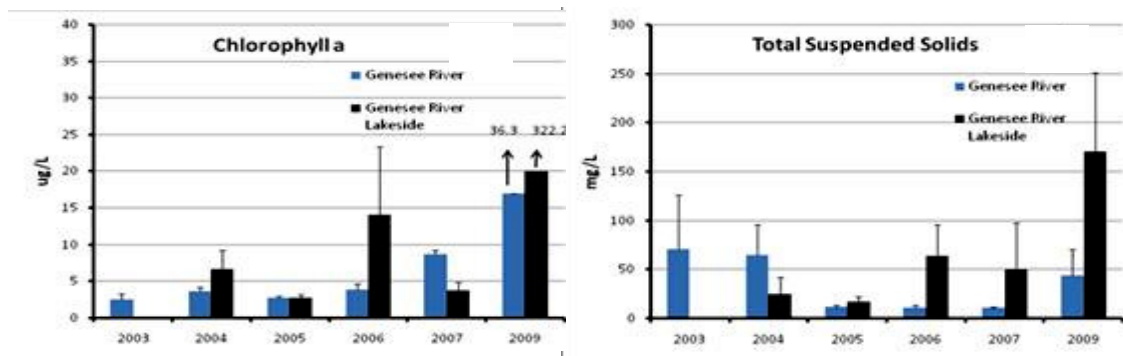


Figure 4.7. The average CHL/TSS concentrations collected during the past six years for the Genesee River site (black bars represent concentrations at the Lakeside) [Makarewicz, 2010].

Figure 4.7 shows the concentrations of suspended sediment and chlorophyll observed during spring/summer of 2006-2009. For monitoring, the sampling has been conducted on a monthly basis and was averaged to represent the concentration levels over a year. In addition, the sampling scheme has been based on a point-based procedure and the collected data does not represent a spatially averaged estimate.

4.3.1.2 Niagara River

The Niagara River, which originates from Lake Erie, is considered as the main source of incoming water to the Lake. The 58-km Niagara River which travels northward from Lake Erie is the major source of inflow into Lake Ontario. The river is the drainage outlet for the four upper Great Lakes having an aggregate basin area of $600,000 \text{ km}^2$. Due to the proximity to the residential areas, it is host to pollutants flowing into the Lake. Also, as water is carried away from Lake Erie, all of the pollution sources including nutrient loads and nuisance algae are transferred into Lake Ontario through the river. The massive volume of water and steep gradient of the river make it a suitable source of hydropower. The Niagara River discharge is estimated, on average, to exceed $5400 \text{ m}^3/\text{s}$, which forms over 80% of the total water flow into the Lake. It interrupts and mixes into the coastal boundary circulation, which under normal condition, makes the plume flow eastward. Although Lake Erie is considered as the steady source of particulates and contaminants to the river, the general atmosphere of neglect coupled with the increase in the intensity of human activities such as sewage outfalls from plants along the river significantly affects Lake Ontario's water quality [Hayashida *et. al.*, 1999]. Figure 4.8 shows nutrient loadings and concentrations of CHL and TSS in the river

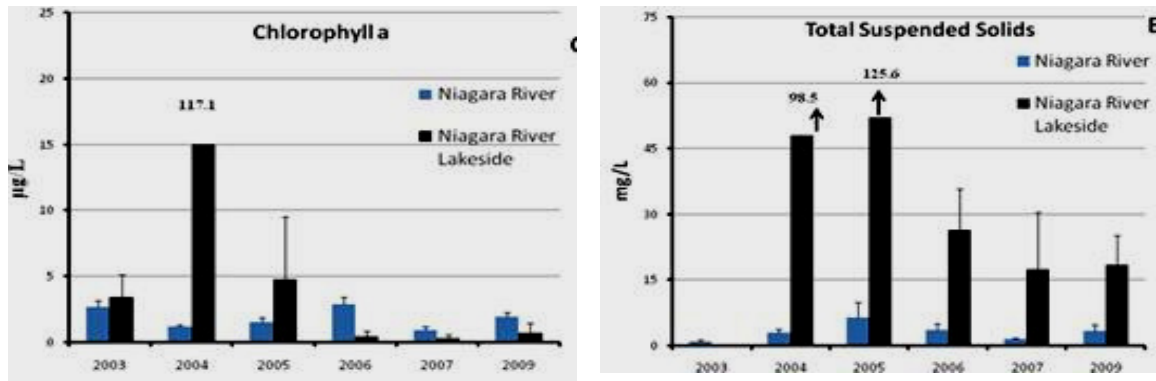


Figure 4.8. The Average CHL/TSS concentration collected during the past 6 years (dark bar represent concentrations at Lakeside) [Makarewicz, 2010].

during 2003-2009. In contrast to the Genesee River, it appears that the constituent concentrations in the Niagara River are at a reasonable range during this period indicating normal water quality conditions.

4.3.1.3 Onondaga Lake

Located in Onondaga County in NY State adjacent to the city of Syracuse, Onondaga Lake was considered as one of the most polluted lakes in the USA in the late 70s and early 80s. The lake was the topic of interest to local and federal agencies during that period. Concerns with its water quality prompted extensive research to monitor its environmental conditions and take appropriate actions to prevent further contaminations. This lake has been the recipient of a variety of nutrients, chemicals and thermal loads introduced from the surrounding industrial plants. All of the efforts paid off and today the environmental status of the lake is controlled and monitored on a weekly basis using deployed instruments. Currently, inflows from water treatment plants and fresh waters from small tributaries form the total volume of water entering the lake. Although its thermal stratification is primarily driven by the wind forcing and atmospheric heating and cooling, the residual waste loadings from the nearby abandoned waste bed continues to affect the density stratification [Effler, 1996; O'Donnell *et. al.*, 2010]. Figure 4.9, taken from [Ahsan and Blumberg, 1999], shows the lake's hydrological map with its major sources of inflows and the single outlet in the northern tip, which combines with the Seneca River. Onondaga lake, 7.6 km long and 2 km wide at its maximum width, is oriented northwest-southeast ward, i.e., nearly perpendicular

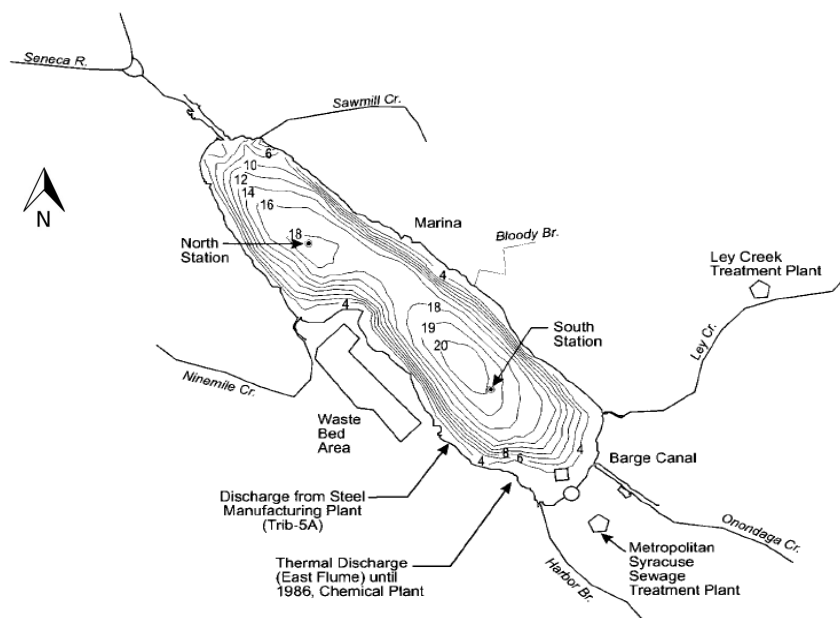


Figure 4.9. The hydrological and morphological structure of Onondaga Lake.

to the dominant winds. The lake receives surface runoffs from four major creeks including Ninemile Creek, Onondaga Creek, Ley Creek, and Harbor Brook (Figure 4.9). The other major sources of inflow come through the Metropolitan Syracuse Sewage Treatment Plant (METRO) facility and intermittent bidirectional flows from the Seneca River at the outlet of the lake [Effler, 1996]. The Upstate Freshwater Institute (UFI) and the Onondaga County Department of Health (DOH) monitor various biological, meteorological, and physical parameters via the observations made at the two deepest locations in the southern and northern basins.

4.3.2 Datasets

As stated, in this research, L7 data were used to calibrate the ALGE model which predicts the thermal structure and dissipation of material in water bodies. Table 4.2 contains the properties of L7 scenes that were used in this study. The data were made available through the USGS database. The cloud-free percentage and the availability of field measurements of any kind were the criteria used to choose the datasets. The datasets span a wide time range from May to October to help understand impacts of seasonal variations on the model performance. This leads to eight different sets of simulations for the sites.

4.3.2.1 Bathymetry Maps

The preliminary results showed that the aforementioned grid spacing are sufficiently small to capture the subtleties, i.e., small eddies, in the model domain. Moreover, the grid sizes for the Genesee and the Niagara sites were chosen to be $10 \times 10 \text{ km}^2$ and $18 \times 27 \text{ km}^2$, respectively. These dimensions were determined through several coarse simulations and appeared to create domains large enough to enable robust simulations. The meteorological data necessary to run the simulations were obtained from the National Data Buoy Center and the National Climatic Data Center. Although the wind data were generally taken from the nearest station to the study site, the other surface data, i.e., cloud heights, sky fraction, etc., were obtained from the local airports to represent the meteorological conditions. The modeled sounding data provided by the National Weather Service office at Buffalo were used to prescribe profiles of precipitable water and temperature to the code. The hourly inflow discharge and the river temperatures measured at the USGS stations were used to run the model for the Genesee and the Onondaga Lake sites. For the Niagara site, the data obtained from the US Army Corps of Engineers were utilized.

4.3.2.2 L7 Imagery

Since the objective of this research is to conduct a retrieval task of the physical properties of water, such as temperature and reflectance, the digital numbers have to be converted to meaningful physical quantities (TOA radiance). This is possible by applying the calibration coefficients obtainable from the metadata files. This is done for L7 to obtain the TOA

Table 4.2. The dataset applied in this study to calibrate the model

Scene	Row/Path	Date	Atmospheric condition	Registration
Genesee	30/16	7/14/2009	hazy	✓
	30/16	10/18/2009	clear	✓
Niagara	30/18	8/26/2008	clear	✓
	30/17	5/18/2009	clear	✓
	30/18	10/19/2010	clear	✘
	30/17	8/12/2011	clear	✓
Onondaga	30/16	5/30/2010	clear	✓
	30/15	6/26/2011	Cirrus clouds	✓

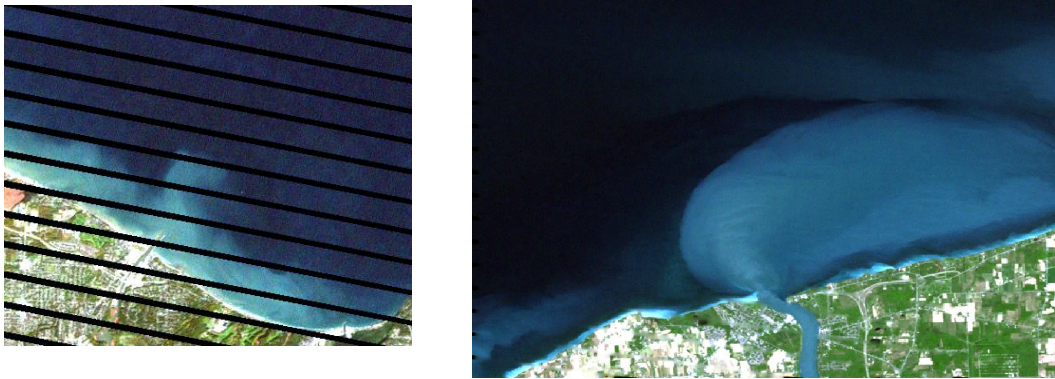


Figure 4.10. River plumes in the L7 imagery. The Genesee plume on Oct. 18th (left) versus the Niagara plume on May 18th (right)

radiance values [$W/m^2sr\ \mu m$] bearing the physical properties of water at the top of the atmosphere. L7 uses an oscillating mirror that sweeps across track in both directions. In order to compensate for this bow-tie pattern, two mirrors are placed in the optical chain of L7. These mirrors shift the image projected onto the detectors so that it is somewhat ahead of the across-track location at the start of the scan line and ends behind it [Schott, 2007]. After 2003, these SLC mirrors failed to function which caused gaps in the form of regular strips in ETM+ data (Figure 4.10). Using a Matlab built-in function, which fills in gaps utilizing pixel values on the edges, the missing data is estimated through interpolation. However, the interpolation does not achieve a perfect replacement for the missing data (particularly in the reflective domain) and care must be taken when calculating error values associated with retrieval process within gap areas.

(a) Identifying Sun Glint/ Atmospheric Effects Masking

As described in Section 3.5.3.5, the sun glint is a function of the sun-target-sensor geometry. The sun-glint effects become more significant at high solar elevation angles as well as under high wind conditions. The high winds generate capillary waves causing surface reflections towards the sensor's FOV at angles equal to the incident angles, i.e., Snell's Law. In this research, it is assumed that sun glint would not affect our methodology in the river plume simulations. In addition, Onondaga Lake under normal conditions does not contain glint-affected pixels. However, when attempting to retrieve constituents in the surroundings

of the river plumes in Lake Ontario, there are local areas contaminated with sun glint. In such cases, the contaminated pixels are identified and discarded in the constituent retrieval process. In doing so, the following procedure has been adopted to find the glint-affected areas. The method is a simple band ratio technique, which is also sensitive to atmospheric effects. When the atmospheric effects exhibit spatially heterogeneous patterns, in particular over inland waters, this technique performs well to discern locally affected areas. This method, in fact, helps avoid confusion when retrieving water constituents by identifying atmospherically affected areas.

The concept of this band-ratio method is that under glint-free condition the ratio of the TOA radiance of the SWIR bands should exhibit relatively high values with high local variations. The band ratio for a pixel in open waters where there is no atmospheric/sun glint effects is given as

$$\alpha = \frac{L_{SWIR\ 1}^{TOA}}{L_{SWIR\ 2}^{TOA}} \quad 4-4$$

where $L_{SWIR\ 1}^{TOA}$ and $L_{SWIR\ 2}^{TOA}$ indicate the image-derived TOA radiance and $\alpha > 1$ indicating higher levels of scattering in the atmosphere in the shorter wavelengths. When contaminated with the sun glint or atmospheric fronts, i.e., clouds, low fog, haze, etc., the ratio takes the following form

$$\alpha' = \frac{L_{SWIR\ 1}^{TOA} + \gamma_{SWIR\ 1}}{L_{SWIR\ 2}^{TOA} + \gamma_{SWIR\ 2}} \quad 4-5$$

where $\gamma_{SWIR\ 1}$ and $\gamma_{SWIR\ 2}$ are the additive components from the sun glint (solar spectrum) or atmospheric effects. Assuming that the two parameters are nearly equal, i.e., $\gamma_{SWIR\ 1} = \gamma_{SWIR\ 2}$, the following inequality is always true:

$$\alpha > \alpha'$$

Therefore, a pixel containing no information about the water constituents shows low values and must be removed or flagged for further atmospheric/sun glint removal process. In addition, since the two parameters, $\gamma_{SWIR\ 1}$ and $\gamma_{SWIR\ 2}$, dominate the very low water signals of the SWIR bands, the surface induced variability significantly decreases. In other words,

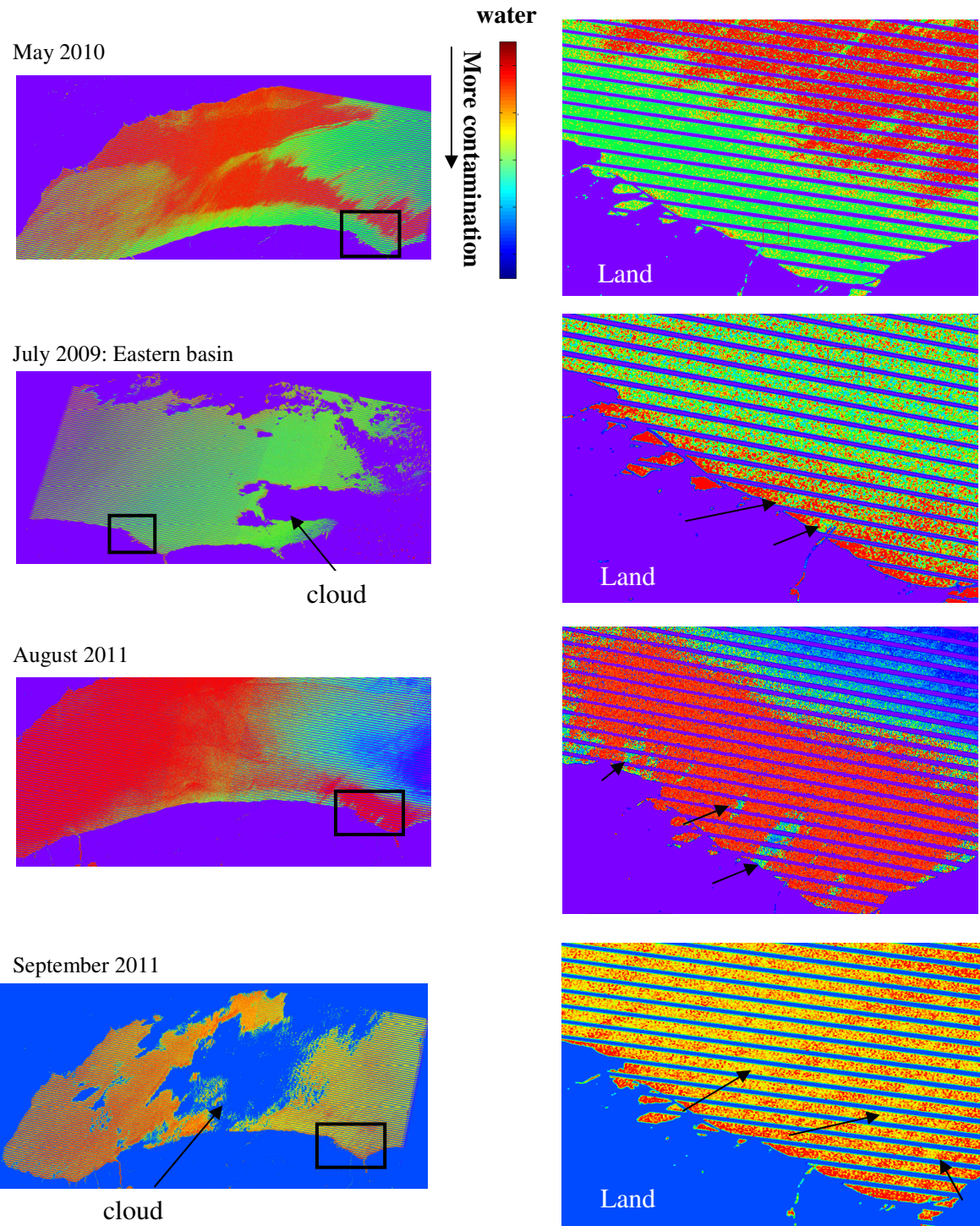


Figure 4.11. The SWIR band-ratio method for identifying glint or atmospherically contaminated areas. The lower values denote contaminated pixels. The images were locally averaged to obtain smoother transitions between different areas. The effected areas are specified with the arrows. The zoomed areas indicate the Rochester Embayment area where the Genesee River flows into the lake (black boxes).

when investigating the band-ratio products, the atmospherically contaminated pixels (e.g. a cloud deck) show smooth variability whereas over-water local variability, which primarily emanates from surface reflection, is more significant. Figure 4.11 shows a few examples of the normalized band-ratio images derived from the L7 imagery over Lake Ontario. The values closer to zero (blue color) denote the pixels affected by either sun glint or atmosphere as opposed to the red patterns indicating non-contaminated water bodies. The band-ratio products for May 2010 and August 2011 show interesting atmospheric patterns throughout the southern shores of the lake. This pattern is thought to be particles originating from the land areas, i.e., coastal aerosols in the lower atmospheric layers. It should be noted that even though the Genesee River carries high levels of inorganic particles into the lake, the band-ratio values over the plume appear insensitive to the concentration load and have values similar to the surrounding clearer waters. The extremely inhomogeneous atmospheric condition is notable in the Rochester Embayment for this day (July 2009). A similar pattern is observed for the Sep. 2011 data, when field work was conducted. While the sky seemed very clear, the very high winds resulting in wave actions generated a poor quality image due to sun glint. By choosing an appropriate threshold, one can either simply ignore the contaminated pixels or segment the scene and take a region-based approach to correct the glint or atmospherically affected patches independently.

This simple band-ratio may be even examined after the atmospheric removal to ensure uniform surface reflectance products with no atmospheric interference. One should note that since the NIR band is sensitive to high TSS concentrations, it is discarded for such a ratio technique. However, high concentrations of TSS might affect our estimation of contaminated pixels and care must be taken while examining this ratio. In addition to using the reflective bands, the thermal data could also provide hints on the atmospheric effects, in particular identifying the presence of cirrus clouds.

4.3.3 Field Observations

For the purpose of this research, six different field campaigns were attempted underneath L7 and EO-1. Although tasked prior to most of the campaigns, EO-1 only once happened to acquire imagery simultaneous with L7, i.e., 19th Oct 2010, over the Niagara site. The other tasks either failed to execute or acquired imagery under cloudy conditions. In addition to the successful collect in October 2010, three of the other campaigns underneath L7 were

Table 4.3. The field campaign attempts

	DOY	Site	Samples	Reflectance	Sky	Wind
5-5-2010	125	GN	11	✓	Aerosols	Relatively Calm
10-19-2010	283	NI	6	✓	Clear	Calm
6-26-2011	182	ON	14	✓	Cirrus Clouds	Calm
8-1-2011	220	GN	5	✓	Cloudy	Relatively windy
8-12-2011	228	GN	5	NA	Clear	Calm
9-13-2011	246	GN	8	✓	Clear	Windy

successfully conducted in cloud-free conditions. Table 4.3 contains different attempts for the field collects in the Rochester Embayment (GN), Niagara River mouth (NI), and Onondaga Lake (ON). The three successful campaigns, however, were collected when the Genesee River discharge represented low values, i.e., $< 20 m^3/s$. The very low discharge from the river makes the plume indistinguishable in L7 imagery where SLC-off gaps also exist. Moreover, the full potential of the L7-model integration may not be determined in such low inflow conditions. Therefore, the measurements taken at the Genesee River were used for the following purposes:

- Estimating the scattering prosperities of CHL and TSS
- qualitatively observe the seasonal variations of IOPs in the region
- Evaluate the calibration status of L7 for the specific dates

The only campaign conducted at Onondaga Lake (ON) was under Cirrus cloud contaminations creating a spatially non-uniform distribution over the lake. The description of the laboratory analysis along with the results is presented in the following sections.

4.3.3.1 Field/Laboratory Procedure

The measurements usually started an hour before L7 overpass and finished two hours after. Water samples were taken from various locations where the range of concentrations were believed to span a wide range. For each station, GPS position, time of the day, water condition and additional notes regarding the environmental conditions were recorded (eg. Figure 4.12). The samples were stored in 1-litre dark bottles and maintained cool until transferred to a refrigerator with standard temperature [Binding *et. al.*, 2008]. The number of samples varied from areas of high concentration with only one bottle to clear waters with 2-3

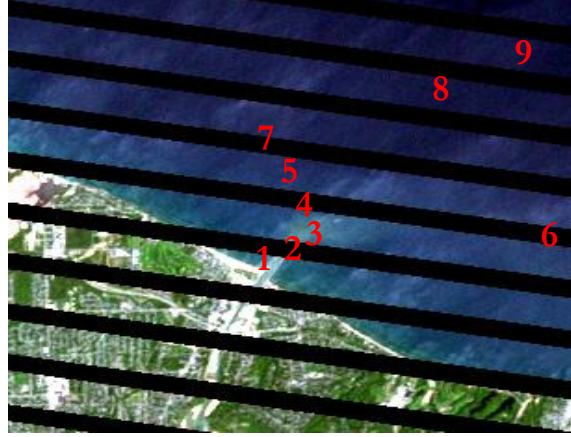


Figure 4.12. Field stations visited on May 2010

samples to ensure capturing sufficient amount of constituents on the filter for laboratory measurements. A quantitative filter technique (QFT), as described in [Binding *et. al.*, 2008], was applied to determine concentrations of constituents and their (IOPs).

(a) Concentration Measurements

Measuring the concentrations of CHL involved concentrating phytoplankton from the sample waters onto 25mm-wide Whatman filters. The volume of the samples depends on the first-order estimate of the CHL concentration. The low CHL concentrations require high filtered volumes while very low volumes of sample are needed at high CHL concentrations. The standard chlorophyll-a concentration measurement procedure, performed on two subsequent days, was followed in the laboratory measurements [Binding *et. al.*, 2008]. The measurements involve dissolving the samples in a glass tube filled with 3 *ml* of 90% acetone followed by rinsing with additional 1.5 *ml*, i.e., total extraction volume 4.5 *ml*. On the second day, after centrifuging the samples, the UV-2100 spectrometer was used to measure absorbance at 665*nm* and 750*nm* before and after acidification. The following expression was then applied to determine the chlorophyll-a concentration[Lorenzen, 1967]:

$$CHL = \frac{26.7[(A_{665}^o - A_{750}^o) - (A_{665}^a - A_{750}^a)]v}{V \times l} \quad 4-6$$

where A_{665}^o and A_{750}^o are the absorbance at 665 *nm* and 750 *nm* before acidification, A_{665}^a and A_{750}^a are the measurements after acidification, V [*l*] is the volume of water filtered, l [*m*]

represents the pathlength of the cuvette, v [ml] is the extraction volume, and 26.7 is the absorbance-absorption conversion factor. Moreover, CHL is assumed to have uniform vertical distribution within the water column. This assumption may introduce slight errors in the retrieval process which can be considered negligible in well-mixed water conditions occur in spring/fall [Stramska and Stramski, 2005] .

The total concentration of suspended solids was measured gravimetrically on pre-weighted Whatman filters after rinsing with distilled waters. The filters were dried in 75 °C oven followed by weighing. The TSS concentration was then calculated as the following:

$$TSS(g/m^3) = \frac{W_2 - W_1}{V_f} \quad 4-7$$

where W_2 and W_1 are weights of post- and pre-weighed filters and V_f stands for filtered volume.

Table 4.4. The concentrations of CHL and TSS together with CDOM absorption

Site	CHL (mg/m^3)	SSM (g/m^3)	CDOM (440nm) (m^{-1})
1	24	11.3	0.76
2	14	11.2	0.62
3	14.8	11	0.75
4	3.5	1.5	0.36
5	3	0.9	0.22
6	3	0.43	0.26
7	2.2	0.1	0.18
8	3.3	0.005	0.3
9	4	0.001	0.21

(b) Absorption Measurements

For the CDOM absorption measurements, a UV-2100 spectrophotometer was utilized. Following the filtration through 0.2 μm membrane filters into a 10-cm cuvette, the dual beam spectrophotometer, measures the absorptivity of the sample against blank (distilled water). The instrument slit width was increased to 5 nm to allow for more light going through the system and a higher SNR. Absorptivity (optical density, OD) was then converted to spectral absorption according to:

$$a_{CDOM}(\lambda) = \frac{2.303}{l} OD(\lambda) \quad 4-8$$

Where l is the cuvette length (10 cm) and OD is the wavelength dependent absorptivity [Binding *et. al.*, 2008]. Table 4.4 contains constituents' concentrations and CDOM absorption at 440nm for different stations observed on May 5th, 2010.

The total particle absorption was also quantified spectrophotometrically after concentrating water samples onto the 25mm-wide Whatman GF/F filters. The samples were refrigerated for less than 24 hours and then measured using the dual-beam spectrophotometer. In order to determine the CHL absorption spectra, chlorophyll pigments were extracted in methanol solvent for approximately 24 hours, depending on the CHL concentration. It is assumed that the remaining particles on the filters are non-algal components whose absorption spectra can be determined. The resulting spectra are subtracted from the total particle absorption to specify CHL absorption spectra [Kishino, 1985]. The sample absorbance was measured between 350 nm and 800 nm at 1 nm intervals against a blank filter saturated with distilled water as a reference. The spectral absorption of the total particulate matter, $a_p(\lambda)$, and non-algal particles, a_{NAP} , were then calculated from the total and the pigment-extracted samples, respectively. The geometric absorption pathlength of the material in suspension can be calculated as V_f/A_f where V_f is the sample volume and A_f is the effective area of the filter. It is assumed that the pathlength amplification factor (scattering loss factor) is constant over the spectrum ($\beta = 2$) [Cleveland, 1993].

$$a_p(\lambda) = \frac{2.303}{\beta(V_f/A_f)} OD(\lambda) \quad 4-9$$

In the above equation $\beta = 2$ is an approximation and there is a significant uncertainty regarding the assumption of constant β , particularly, in turbid waters over the plume. The measured spectra were subsequently normalized by the measured concentrations to achieve specific absorption coefficients in units of m^2/g for TSS and m^2/mg for CHL. The resulting spectra were further smoothed by an averaging filter to diminish noise effects. Figure 4.13 illustrates the corresponding measurements taken at the Genesee site in May 2010 and August 2011. The subplot (a) shows different reflectance spectra measured in May 2010. The dash-dotted blue curve shows the spectrum measured over the turbid waters. The high

peak at ~ 550 nm indicates high CHL concentration, i.e., $14 \text{ mg}/\text{m}^3$, while more than 2% reflectance at the high end of the VNIR region denotes high concentrations of TSS, i.e., $11.3 \text{ g}/\text{m}^3$. The other measurements taken at clearer waters were consistent with the concentrations. The most noticeable feature in the reflectance spectra is the Oxygen absorption feature at 760 nm , which suggests a large contribution from the skylight (downwelled radiance) and, as a result, significant sky glint. When imaging with hyperspectral sensors, this feature can be used to remove/reduce glint effects. The existence of the significant skylight, likely due to the coastal aerosol (Figure 4.11), was further confirmed through examining the L7-derived TOA radiance curve. The extraordinary high radiance values in the red and the NIR regions suggest considerable scattering in this region, which may be caused by the large particles in the lower atmosphere. Different MODTRAN built-in aerosol models with measured water vapor profiles were attempted to predict the type of aerosols. However, MODTRAN models failed to properly approximate the TOA radiance values in the red and NIR regions.

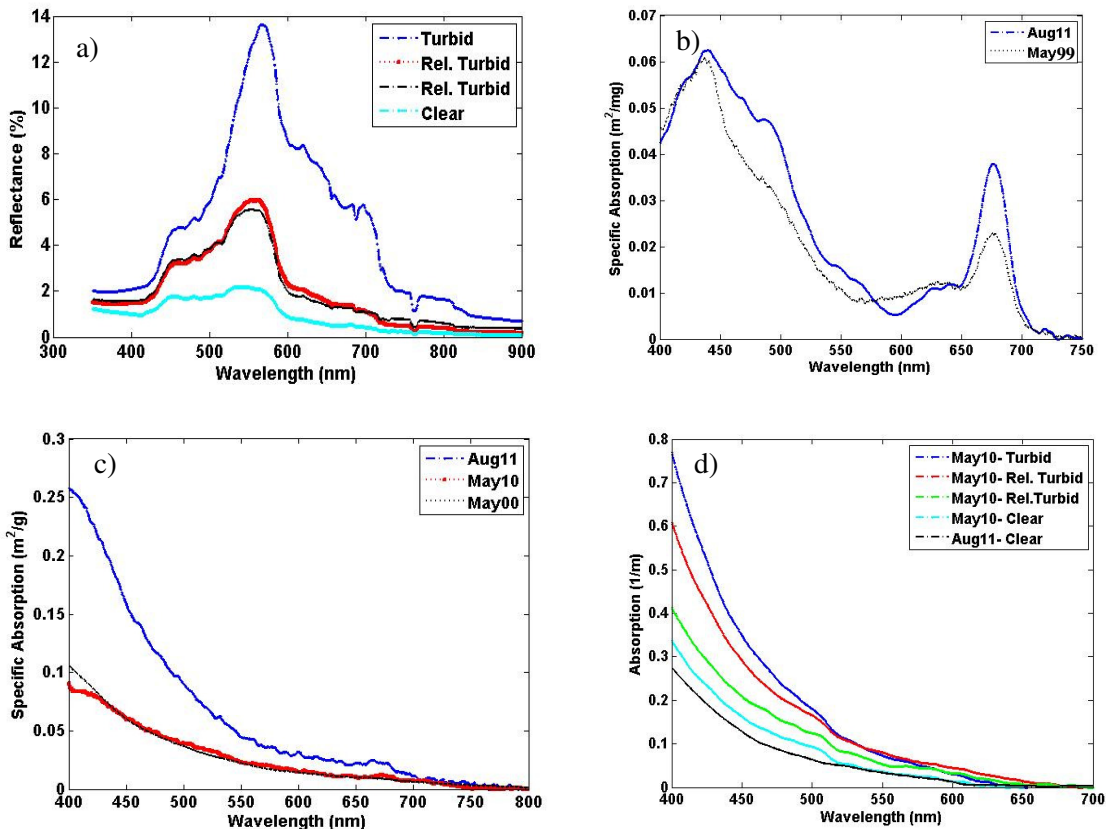


Figure 4.13. The reflectance spectra (a) together with the absorption measurements of CHL (b), TSS (c), and CDOM (d) associated with the field campaigns at the Genesee site

Since the river discharge exhibited very low values in this period, the measurements made in May 2010 were not used for validating the L7-model integration approach. In addition, since the downwelled skylight was not measured in this campaign no attempt was made to correct the reflectance spectra for the sky glint.

The CHL specific absorption spectrum measured in Aug. 2011 is over-plotted on the averaged CHL spectrum from [Raqueno, 2003] measured in May 1999 (Figure 4.13-b). Although the magnitudes of the spectra at 443 nm are the same, there are obvious discrepancies beyond this wavelength. Such differences in the shape of the spectrum, which predominantly influence the L7's blue and green band responses, could be attributed to seasonal variations in the phytoplankton community. Other CHL measurements, not shown because of high noise components, made in May 2010 are compatible with the measured ones in May 1999. A similar observation is evident in Figure 4.13-c where specific absorption of non-algal particles are shown. The TSS specific absorption observed in summer of 2011 appears more than twice as high as the ones measured in May 2010 and 2000. The slight peak at the ~ 677 nm indicates the imperfect extraction of the pigments in the extraction period, in part, due to the large CHL concentrations (Aug. 2011 at the Irondequoit Bay). The CDOM absorption spectra are also shown in Figure 4.13-d. The higher absorption values correspond to the higher concentrations of CHL, TSS, and nutrients near the river plume.

Figure 4.14-a shows the average CDOM absorption spectrum [1/m] and the specific absorption spectra of CHL [m^2/mg] and TSS [m^2/g]. The specific absorption spectra were obtained by normalizing the absorption spectra by the average concentrations, i.e., CHL ~ 3.8 ug/l and TSS ~ 1.8 g/m^3 , measured at the river mouth.

On the other hand, the surface-leaving reflectance measured just above water $r_d(\lambda,+0)$ had to be corrected for the diffuse skylight reflected off the water surface. In doing so, the Fresnel reflection coefficients (approximately 2.2% over the visible spectrum) estimated in the Hydrolight code was employed. The following correction was then applied to remove the surface-reflected impact:

$$R_c(\lambda,+0) = \frac{\pi[L_u(\lambda,+0) - |\rho_F(\lambda)L_{diff}(\lambda)|]}{E_d(\lambda)} \quad 4-10$$

where the $R_c(\lambda,+0)$ indicates the corrected unitless water-leaving reflectance just above the water, $L_u(\lambda,+0)$ denotes the surface-leaving radiance just above the water, $\rho_F(\lambda)$ is an approximation for the Fresnel reflection coefficient, $L_{diff}(\lambda)$ represents the diffuse sky radiance, which was measured in situ and validated with MODTRAN simulations, and $E_d(\lambda)$ is the total downwelled irradiance. The constant π has been incorporated to preserve the corrected reflectance unitless, i.e., comparable to the bidirectional reflectance factor (BRF) originally measured using the white reference panel. Although it varies with wavelength [Lee *et. al.*, 2010], $\rho_F(\lambda)$ was assumed spectrally independent, i.e., $\rho_F = 0.022$ [Doxaran *et. al.*, 2004].

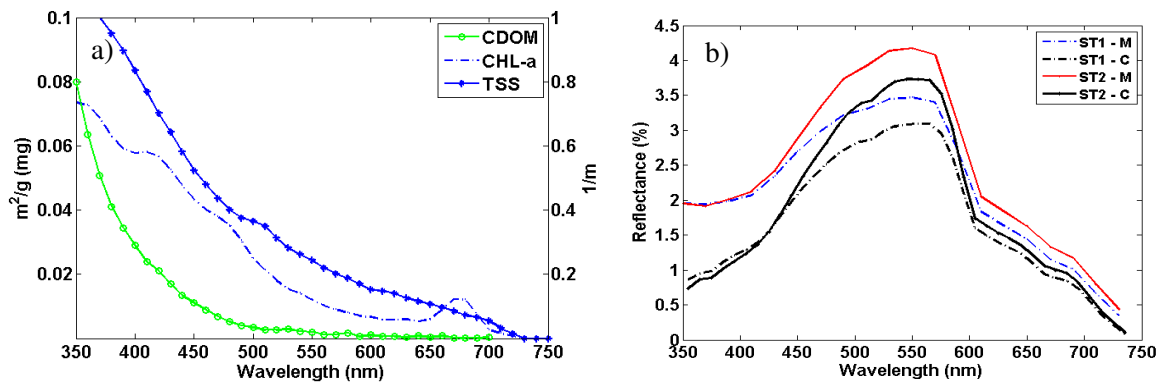


Figure 4.14. The spectral absorption measurements (a) as well as the radiometric measurements of the surface-leaving reflectance (b) made at the Niagara River mouth in Oct. 2010.

This approximation was obtained from the Hydrolight simulations for relatively calm waters, i.e., wind speed $< 2.4\text{ m/s}$, a clear sky, and viewing geometry adopted during the measurements. The measured reflectance spectra $r_d(\lambda,+0)$ [unitless] were then corrected using Eq. 4-10, (Figure 4.13-b). The reduction in the magnitude of the measured spectra (M) versus the corrected spectra (C) is most prominent in the very short bands, i.e., $\lambda < 400\text{ nm}$, where the diffuse skylight represents the largest effects. The correction appears to behave similarly at both stations (ST1 and ST2) even though the measurements were made 45 minutes apart. While the CHL concentrations at the two stations are nearly the same, the TSS concentration at ST2 was 0.40 g/m^3 higher than that for ST1. This slight difference in the TSS concentrations, which primarily manifest itself in the red and NIR region. In other

words, the reflectance spectrum in the red and NIR regions is largely driven by the backscattering ratio ($\tilde{b} = b_b/b$) of the suspended solids.

Figure 4.15 shows the surface CHL absorption spectra measured for seven different stations throughout Onondaga Lake in June 2011.

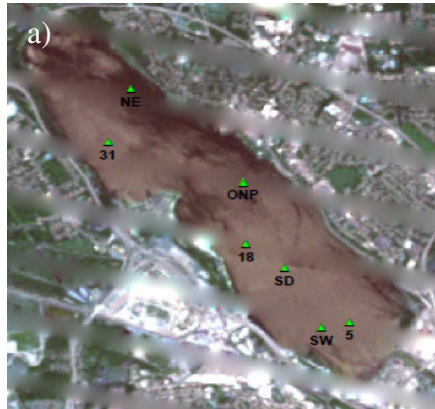


Table 4.5. Field stations for Onondaga Lake

Station	TSS	CHL	TEMP
SD	1.6	5.7	25.8
5	3	8.4	25.6
SW	5.2	12.2	25.8
18	2.7	5.6	26.5
ONP	4.6	14.6	26.2
31	1.8	8	26.5
NE	2.4	6.3	25.9

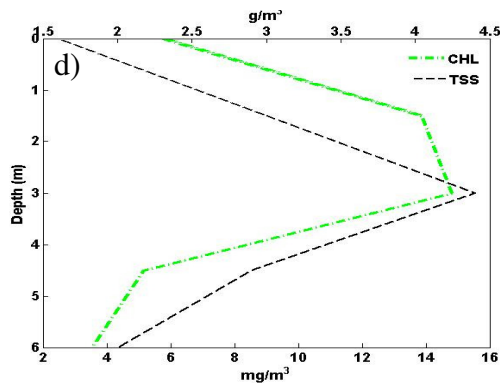
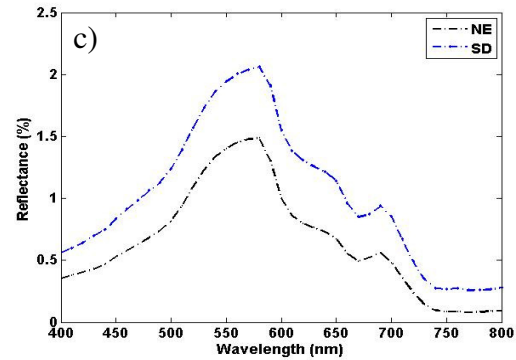
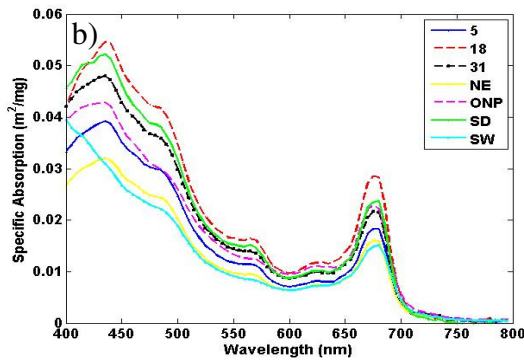


Figure 4.15. Field measurements conducted in June 2011 at the Onondaga Lake site. The CHL specific absorption spectra measured at the surface for seven different stations shown in (b). The surface reflectance (%) measured *in situ* for two station (SD and NE). The concentrations of profiles measured at SD are illustrated in (d).

The spectra were derived by subtracting an average non-algal particle (NAP) absorption spectrum, which was multiplied by the TSS concentration at each station, from the total particle absorption spectra measured in the laboratory. Due to the high levels of CHL concentrations, algal pigments were not properly removed during the extraction period and, as a result, the absorption peak at 677 nm was present in the measured NAP spectra. Thus, the measured NAP absorption spectra, which is not shown here, were discarded for deriving CHL absorption spectra. It is recognised that the total particle absorption beyond 670 nm is primarily determined by the CHL absorption. Therefore, one could examine the variability of the CHL absorption spectra by analyzing the magnitude of the peak at $\lambda = 677\text{ nm}$. The mean value of 0.021 with $\sigma = 0.0048$ shows more than 23% variability for $a_{ph}(677)$, which appears large for such a small lake. This observation adds to the complexity of most of the constituent retrieval techniques, which assume an average spectrum across the region of interest, and introduces errors when retrieving the concentrations over such spatially non-uniform areas. Figure 4.15-a illustrates the geographic locations of the stations. The most noticeable of the CHL spectra is the one measured at station SW where most of the discharge and nutrients from the METRO, Harbor Brook, and Onondaga Creek are concentrated. The accumulation of inflows is strengthened by the low wind forcing, thereby, leading to less vertical, horizontal mixing. Binding *et al.* (2006) state that the ascending trend observed in the CHL absorption below 440 nm is attributed to the excess of organic material. This trend is a unique feature found in the measurement taken at SW. This is consistent with high levels of TSS and CHL at the surface level for this station (Table 4.5). Figure 4.15-c shows the surface reflectance measurements made at SD and NE. Although the surface reflectance concentrations are nearly similar, the high levels of concentrations in the vertical direction, i.e., profiles, at SD (Figure 4.15-d) due to the stratification period can result in increased backscattering (surface reflectance). Note that the surface concentrations at NE are slightly higher than that of SD and the two measurements were not corrected for the temporally variable sky glint at the time of the measurements, when cumulus clouds were present. The latter further complicates the sky glint correction and, to some extent, can describe why the measurements at SD is higher than that at NE, i.e., larger diffuse light due to the existence of clouds when SD was visited. The surface distributions of the concentrations as well as surface temperatures (TEMP) [$^{\circ}\text{C}$] are given in Table 4.5. Moreover, the profiles of the

concentrations measured at the deepest location of the lake (station SD), are also shown in Figure 4.15-d. Given the top warm surface layer, $<3\text{ m}$, which has resulted from direct solar radiation coupled with low wind forcing, the profiles exhibit the typical Gaussian peak at the subsurface level.

(c) Estimating the Scattering Coefficients

Although the absorption coefficients of the constituents are specified through the lab measurements, there is still a need for estimating scattering coefficients. Ideally, these coefficients are determined with specific instruments (e.g. AC-S) deployed on site followed by post-processing. In the absence of such an instrument, the scattering coefficients can be obtained using analytical techniques. In this study, a curve fitting approach has been adopted to predict the scattering coefficients that best produce a water-leaving reflectance.

In this procedure, many Hydrolight simulations are performed by varying scattering coefficients while holding the absorption coefficients constant. The scattering coefficients are adjusted by applying scaling factors on a library of existing spectra.

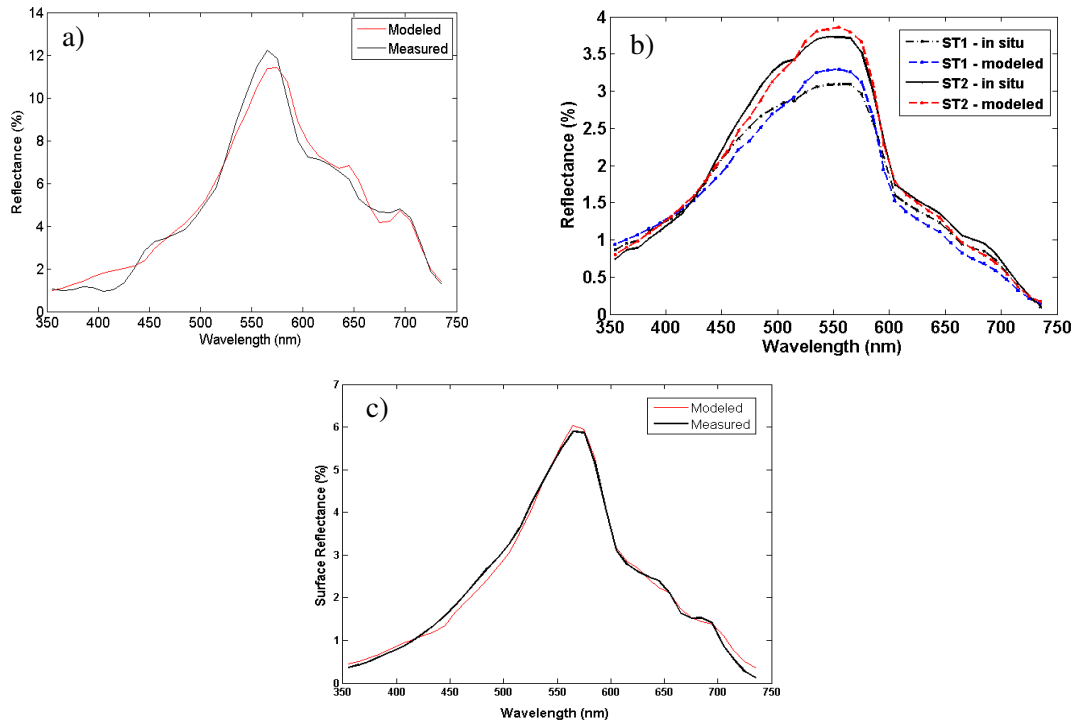


Figure 4.16. The best curves matching the measured spectra at the a) Genesee, b) Niagara, and c) Onondaga Lake sites.

In addition to varying the scattering coefficients of CHL and TSS, their concentrations are also adjusted over a small range to account for the uncertainties associated with the lab measurements. The simulated reflectance curves are then compared against the *in situ* measured reflectance. After spectrally resampling the measured spectra to the Hydrolight-derived curves, the RMSE is computed for each case scenario as a metric to measure their goodness of fit relative to the *in situ* measurements.

Figure 4.16 illustrates best curves estimated for the three sites. The average percentage errors over the range of 430-740 *nm* do not exceed 9.2%. The largest disparity was found for the Genesee site where the water was extremely turbid as depicted in the corresponding plot. It should be noted that the measured spectra for the Genesee and the Onondaga Lake sites were corrected for the sky glint, while the measured spectra shown for the Niagara sites were modified based on the description in the previous section.

Despite the successful identification of the scattering coefficients, varying the constituent concentrations, even over a small range, appeared to play the main role in controlling the magnitude of the spectrum. Therefore, when applying such methods, it is of importance to take samples of the water column profile to decrease the uncertainties related to the constituent concentrations.

It should be noted that the scattering phase functions used in this simulation to model the directional scattering due to chlorophyll and particles were the highly forward scattering Fournier- Forand (FF) model. This function is attractive due to its precision [Haltrin, 1998] and comes standard in the Hydrolight code. The user can choose from a library of Fournier-Forand models that are indexed based on their backscatter values (e.g. 1.4%). In the above simulations, equal backscattering ratios for CHL and TSS components were adopted at each site, i.e., 1.8% for the Niagara River, 2.5% for the Genesee River, and 2.2% for the Onondaga Lake was used. The FF-1.8% indicates that 1.8% of the incident energy is scattered backward into the illumination direction. It should be noted that several experiments were performed to examine the impacts of varying phase functions on the modeled reflectance spectra. The sensitivity analyses showed that varying phase functions only slightly alters the modeled spectra and, as noted, the concentrations and their associated absorption and scattering properties primarily control the shape and the magnitudes of the AOPs.

4.4. Retrieval of Surface Physical Properties from L7 Data

In order to be able to calibrate the ALGE model in the thermal domain and subsequently retrieve water constituents, the L7 imagery should undergo some processes in which the critical physical quantities are obtained. The physical parameters include “skin” temperature (T), hereafter temperature, and unitless surface reflectance (r_d). The temperature is derived from the L7 thermal imagery while reflective bands are utilized in the constituent retrieval. Both of the processes involve removing the atmospheric effects to achieve the surface properties of the water body. As described in Section 3.5.3, the atmospheric compensation can be conducted using either physics-based models or empirical methods. In the thermal domain, since the sensor reaching radiance is primarily influenced by the absorption bands and molecular/particle scattering is minimal, the unknown parameters specified in Eq. 3-25 can be readily obtained from a radiative transfer model, such as MODTRAN, given the water vapor content in the atmospheric profile is well known. The atmospheric removal in the reflective domain, however, may not be achieved unless the aerosols in the lower atmosphere are properly characterized. The following sections describe the procedure used in this study to retrieve the temperature and the surface reflectance from L7 imagery.

4.4.1 Temperature Retrieval

As stated, when imaging in the thermal infrared, the sensor measures the “skin” temperature. The Planck or blackbody equation is the expression that relates spectral exitance from a blackbody with its corresponding temperature and the wavelength at which we sense the blackbody. A blackbody is defined as an idealized surface that absorbs all of the incident electromagnetic flux. The Planck equation is expressed as

$$M_{\lambda} = 2\pi hc^2 \lambda^{-5} \left(e^{\frac{hc}{\lambda kT}} - 1 \right)^{-1} \quad [W/m^2 \mu m \text{ sr}] \quad 4-11$$

where h is Planck constant, $h = 6.632 \times 10^{-34} \text{ J.s}$, k represents the Boltzmann gas constant, $k = 1.38 \times 10^{-23} \text{ J/k}$, T is the temperature in K , c is the speed of light, $c = 3 \times 10^8 \text{ m/s}$. The spectral exitance of an object under study can be found by introducing the wavelength-dependent emissivity of that object. The emissivity (ϵ) is then defined as follow

$$\varepsilon(\lambda) = \frac{M_{\lambda}(T)}{M_{\lambda BB}(T)} \quad 4-12$$

where the numerator denotes the object's spectral exitance at temperature T and denominator represents spectral exitance due to the blackbody at the same temperature. Assuming we are referencing to a Lambertian radiator, spectral radiance can be related to the spectral exitance through "magic π " expression [Schott, 2007]:

$$L(\lambda) = \frac{M(\lambda)}{\pi} \quad 4-13$$

where $L(\lambda)$ is the spectral radiance. Therefore, we can now propagate radiance emitting from an object through the atmosphere to find the radiance reaching the sensor. By solving the governing equation, Eq. 3-30, in the thermal mode, one can obtain sensor-reaching radiance at the front of the sensor. The thermal components of governing equation can be re-written as

$$L(\lambda) = \varepsilon(\lambda)L_{T\lambda}\tau_2(\lambda) + E_{d\epsilon\lambda} \frac{1 - \varepsilon(\lambda)}{\pi} \tau_2(\lambda) + L_{u\epsilon\lambda} \quad 4-14$$

which is remotely observed ($L(\lambda)$). The problem becomes doing the inverse problem to derive the temperature buried in the spectral radiance from the blackbody, i.e., $L_{T\lambda}(\lambda)$. The upwelled, downwelled, and the atmospheric path transmission are obtained from the MODTRAN code simulated over the bandpass of the L7 thermal band, i.e., 10-13 μm , at 5nm spectral resolution. The MODTRAN-derived parameters resampled to L7's RSR functions (Eq. 3-30) together with the emissivity of water, i.e., $\varepsilon \cong 0.986$, which is nearly constant in the thermal domain, are employed to obtain a single value in the spectral radiance units. In order to find the correct temperature corresponding to the single value, a family of blackbody curves with various temperatures are generated. The area under the curve associated with each of these curves represents the total radiance emitted from the blackbodies of different temperatures out of which one would closely match the single value gained from solving Eq. 4.-14. In a similar fashion, the temperature corresponding to each pixel is retrieved. In this process, it is assumed that the atmosphere is spatially homogenous over the study areas; however, a qualitative analysis of the thermal channel helps to identify inconsistencies. Atmospheric transmission and upwelled radiance (self-emission) terms for the imagery over

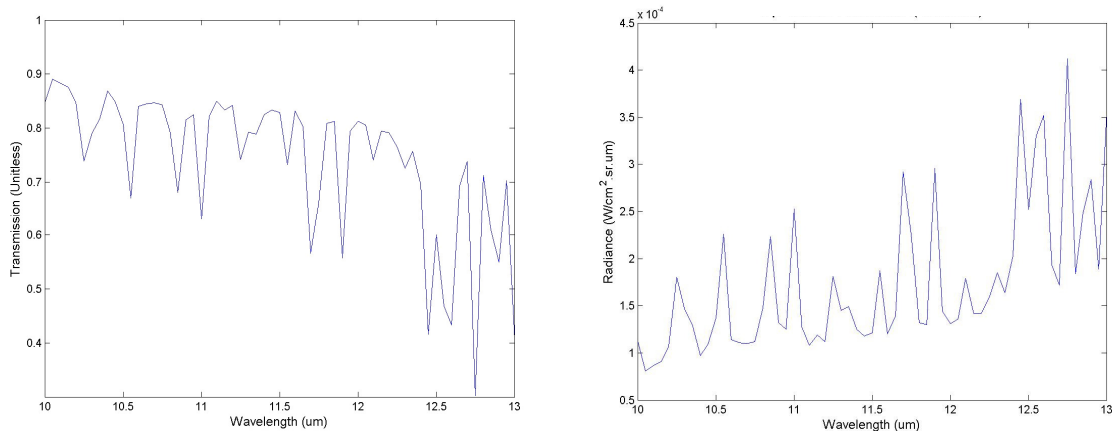


Figure 4.17. The spectral transmission and the up-welled radiance for a single MODTRAN run

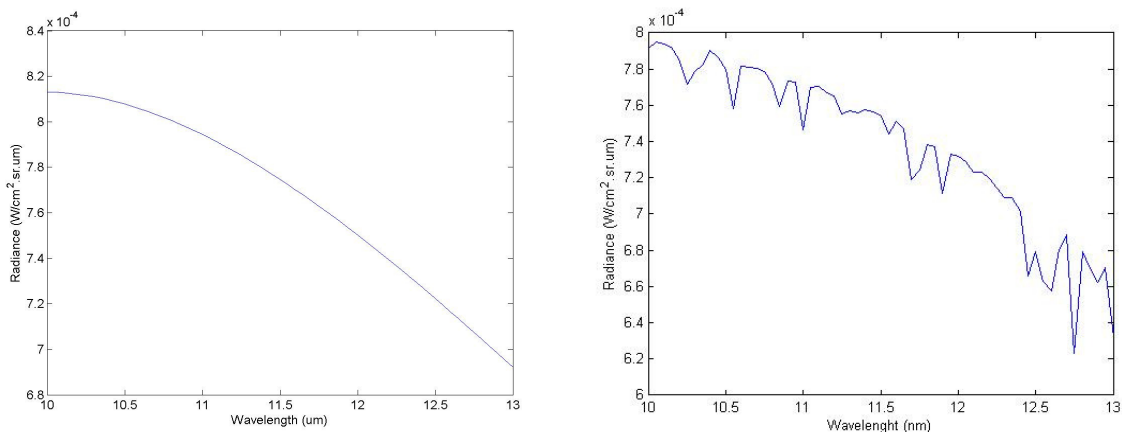


Figure 4.18. The Planck curve for a 15-degrees-Celsius pixel (a) propagated through the atmosphere (b).

the Genesee site in July 2009 are shown in Figure 4.17. A 60-layer set of radiosonde observations, which includes pressure, air-temperature and dew point temperature were used for this simulation. The narrow absorption lines in the transmission spectrum are primarily induced by water vapor [Schott, 2007]. Also, the spectral-dependence of the transmission and the self-emission spectra within the thermal region are well evident. Figure 4.18 illustrates the water-leaving radiance along with the associated at-sensor radiance for a 15 °C water pixel. As expected, at-sensor radiance closely follows the shape of the blackbody radiation with several absorption lines induced by the spectral transmission. The apparent (brightness) temperature for the above example turned out to be 13.3 °C, which is 1.7 °C cooler than the surface temperature.

4.4.2 Surface Reflectance Retrieval

In the atmospheric correction process, the goal is to derive the water-leaving reflectance using the TOA radiance values observed with the instrument. In order to compensate for the atmosphere in the reflective domain, the physics-based approach requires a suitable knowledge of the aerosols in the lower atmosphere. In the MODTRAN code, four different aerosol models, namely rural, maritime, urban, and troposphere, whose particle types, size-distribution, and as a result, their scattering phase functions are dissimilar. In addition to the aerosol models, the aerosol visibility parameter specifies the number density of the particles associated with each model [Schott, 2007]. Provided that the atmospheric water vapor profiles are available and the aerosol condition is well characterized with one of the four models, MODTRAN should perform reasonably well for an atmospheric removal task. It should be noted that any slight mis-calibration errors corresponding to the instrument give rise to erroneous surface reflectances. The physics-based models predict the atmospheric conditions based upon image statistics derived from dark waters. Due to the L7's slight mis-calibrations (see Section 5.1.1) together with the lack of knowledge on the atmospheric conditions for all of our datasets, it was decided to apply the ELM technique for all of the imagery to compensate for the atmosphere. The following sections explain the procedure for the two techniques.

4.4.2.1 Empirical Line Method (ELM)

The ELM technique is applied to convert at-sensor radiance to surface reflectance. In addition to its simple concept and implementation, the ELM technique is insensitive to first-order instrument errors. Therefore, any calibration errors associated with the imaging system are implicitly accounted for.

Here, only the procedure used for the Genesee site in July 2009 is described. A similar approach is applicable to the other study sites to conduct the atmospheric correction. As recommended in the standard ELM procedure [Karpouzli, 2003], the reflectance of at least two targets should be collected. In our case, deep water and beach sand reflectance are utilized as surface measurements. The beach sand reflectance measured *in situ* during the field campaigns represent the bright target reflectance. Figure 4.19 compares the very recent measurements with the retrospective measurements as well as the modeled deep-water

reflectance. The shape of the measured spectra is similar to the previous measurements while its magnitude shows slight differences, i.e. less than 2% on average. Since sand is considered as a radiometrically stable target (pseudo invariant) the measured reflectance is assumed valid for any other time of the year under a similar illumination condition. For the deep-water reflectance, the Hydrolight code is used. However, Hydrolight requires accurate knowledge of inputs including water constituents' concentration and the IOPs to be able to model the AOPs. Therefore, care must be taken when using simulations to estimate deep-water reflectance. The primary IOP component controlling the reflectance curve in the deep waters of Lake Ontario is the CHL scattering and absorption spectrum. To the first order estimate, the CHL specific absorption coefficients should not change and can be assumed constant. Seasonal effects may be the only factor causing changes in the shape of the spectrum. The CHL specific scattering coefficients can be assumed unchanged as well. Although the TSS concentration in the middle of the lake is negligible throughout the year, occasional high winds, upwelling/downwelling, and other physical processes may alter the particle loading, originating primarily from the Niagara River. Assuming very low particle load (< 0.05 units), the Hydrolight code can be provided with an average CHL specific absorption spectrum and the MODIS-derived CHL concentrations to simulate the reflectance associated with the deep waters. That being said, the CHL products of MODIS (Terra/Aqua) should be examined with other sources of data, i.e., MERIS, to ensure its validity. The invalid MODIS products come from failures in the proper characterization of the atmospheric effects.

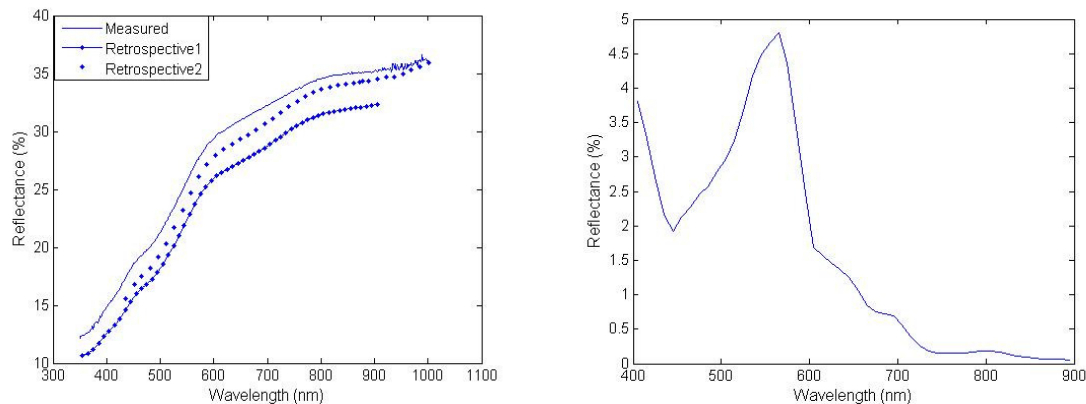


Figure 4.19. The measured sand reflectance spectra (solid line) compared with the retrospective measurements (dotted-line) along with the simulated deep water reflectance from Hydrolight

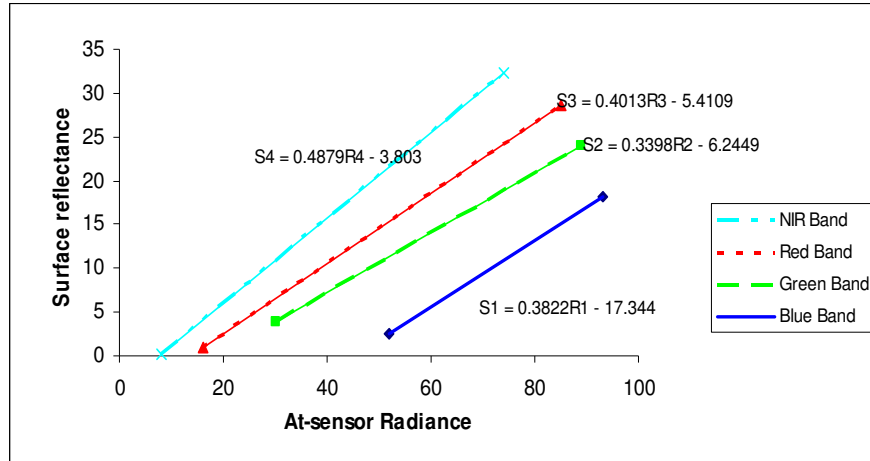


Figure 4.20. ELM equations of four different bands. S indicates reflectance values and R corresponds to at-sensor radiance.

The simulated reflectance spectrum for the deep lake waters is shown in Figure 4.19. The image-derived TOA radiance is obtained through ROIs drawn over the deep waters and beach sand adjacent to the study area. However, due to the existence of the missing data, finding pure beach sand pixels may not be an easy task.

Figure 4.20 illustrates the corresponding regression equations to be implemented on the image pixels as required by the ELM method. These equations transform image data point (radiance) to the surface reflectance domain. As stated in [Karpouzli, 2003], the slope of the lines is related to the atmospheric transmission whereas the intercepts are related to the path radiance effects.

4.5. ALGE Simulations

As stated in chapter 3, ALGE is a three-dimensional hydrodynamic model that is able to simulate the thermal structure and the movement and dissipation of material within bodies of water. The ALGE code models the dispersal of river/stream flows discharging into a larger body of water. In this study, ALGE is applied for simulating two river discharges entering Lake Ontario, i.e., the Genesee River and the Niagara River, as well as a small lake environment (Onondaga Lake) that receives waters from different tributaries and industrial discharges. We begin with describing the procedure pursued for the river plume simulations. The procedure is then extended for Onondaga Lake simulations.

4.5.1 River Plumes

In order to perform the river plume simulations, domains of definite sizes (Section 4.3.2.1) were defined to capture all of the variability induced by the local, meteorological variables. The domain must be sufficiently large to ensure that it allows for the extreme extents of the plumes during the simulation period. Not only do the locally derived environmental variables determine the orientation and the extent of the plumes, but also the lake circulation pattern influences their geometry and distribution. The lake circulation driven by the Coriolis effects along with the wind forcing are the primary factors influencing the orientation of the plume. Depending on the geometry of the shoreline, the impacts of the lake circulation can vary. In order to be able to properly model the river plumes, the lake circulation pattern is incorporated into the localized simulations. This is accomplished through applying the nudging technique, described in Section 3.4.7. In doing so, seasonal lake-wide simulations are conducted to obtain the temporal variability of the currents and thermal structure of the lake during the period during which the localized simulations are performed. The lake-derived time-series of the temperature/current velocities are then integrated to the localized simulations. The following section explains how the lake-wide simulations are carried out.

4.5.1.1 Lake-wide Simulations

The lake-wide simulations are performed based on a 73×188 Lake Ontario bathymetry map obtained from National Geophysical Database Center (NGDC). The horizontal grid size for this domain is 1.5 km and the vertical resolution was chosen to be 2 m throughout the lake. While the Niagara River discharge is considered as the mass source, the Saint Lawrence River is known as the sink source. The initial lake temperature, vertically and horizontally uniform, is specified for the code using the available MODIS products. For our purpose, the modeled radiosonde data derived from the National Weather Service office at Buffalo was found to well represent the amount of water vapor column throughout the lake. The model has been recently enabled to receive a time-varying 2D wind field across the lake over the simulation period. The wind data obtained from nine different stations (Figure 4.21) are spatially interpolated to generate a uniformly spaced 2D wind field. The wind data are observed at seven different stations surrounding the lake. In addition to the land-based

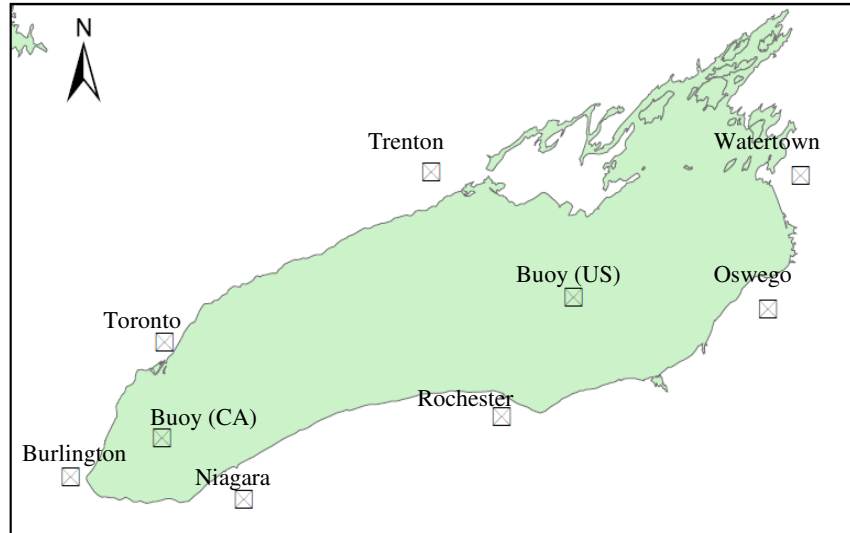


Figure 4.21. The locations of the stations where the wind data are used to produce the 2D wind field

stations, the wind data measured at two buoys in the lake were also used. The wind data were spatially interpolated using an inverse-distance weighting function to assign each node with a wind component in the x and y directions. The other meteorological parameters, including air temperature, dew point temperature, cloud height, etc., were derived from the Buffalo station and, to the first order, can be assumed spatially uniform throughout the lake. This assumption, however, may not be valid during all of the seasons and can introduce errors in the eastern basin of the lake. The cloud height and sky fraction are the parameters whose spatial distributions exhibit non-uniformities across the lake. The two parameters directly influence the available solar radiation and, consequently, the lake heat budget. The spatially non-uniform heat exchange from either the direct solar radiation or cloud radiations would lead to a poor performance of the model. On the other hand, the primary factor driving the thermal structure of the lake is the wind force obtained mainly from the land stations. The frictional forces, the pressure, and the relative humidity over the land do not necessarily represent the conditions over the lake. Any changes in such parameters tend to alter the wind forcing and, as a result, the long-term lake circulation pattern. Moreover, the high frequency wind gusts or calm periods occurring within the periods less than the hourly observations can result in trends not captured with ALGE. Therefore, it was decided to adjust wind data over a small range and observe the associated impacts on the lake-derived parameters in the areas of interest. The wind speed and wind direction were altered up to 20% of the originally

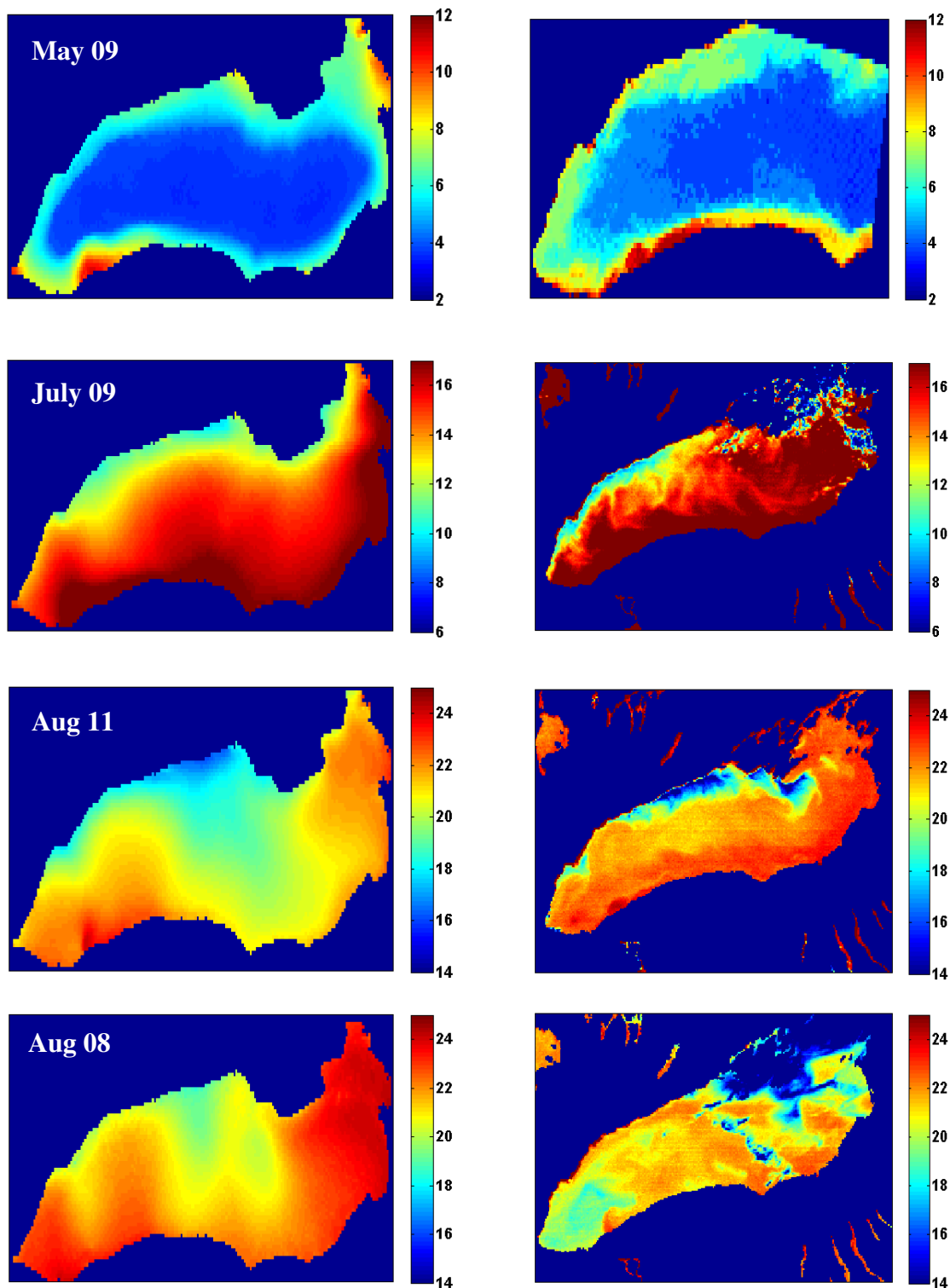


Figure 4.22. Model-derived, lake-wide simulation results (temperature) against the corresponding surface temperature obtained from the satellite observations. The model reasonably predicts the thermal structure of the lake. However, the model performance diminishes when the surface data are spatially heterogeneous. The units are in degrees-Celsius.

observed values. The best combination of wind speed and wind direction was determined by a comparison with the L7- or MODIS-derived surface temperature maps.

Five simulations were conducted to provide the corresponding localized simulations with the time-varying temperature/current velocities at their domain boundaries. The simulation periods were long enough to capture the seasonal variations, i.e., two months. Figure 4.22 illustrates the model-derived surface temperature maps along with the satellite-derived ones. The thermal bar has been nicely formed in the May 09 simulation. It is evident that in the early spring the lake is horizontally stratified while well mixed vertically throughout the lake. The lake's stability was experimentally examined by varying the wind patterns. These variations only slightly changed the thermal structure of the lake, likely due to the lake's large vertical and horizontal stability. Also, the modeled thermal bar appears slightly colder than that in the L7-derived map. This is related to the vertical resolution of the model, i.e., 2 *m*. The model predicts the average temperature of the top surface layer of the water column whereas the remotely sensed observed temperature corresponds to the top 1 *mm* of the surface layer ("skin" temperature). The July 09 data indicate a reasonable model performance when compared to the MODIS-derived surface temperature. However, local eddies and circulations are not captured with the model perhaps due to its coarse horizontal grid cells. The uniform thermal pattern of the lake during this period validates our assumption regarding the homogenous environmental conditions as well as solar radiation across the lake. A similar observation is notable in the results from the Aug. 11 simulation. It should be noted that both simulations were optimized by varying wind speed and wind direction to obtain the correct surface temperatures. As opposed to the above simulations, which properly approximated the lake-wide temperature distribution, the simulation result from Aug 08 was not as promising, even after adjusting the wind patterns. The spatially heterogeneous environmental condition is the main reason describing the poor results. In particular, the warm temperatures in the eastern basin have resulted from a combination of factors such as low wind speed and relatively high solar radiations. The wind energy in this region is mainly influenced by the local winds modeled through interpolation. However, visual inspection of cloud patterns in a few MODIS images over the period of simulation revealed non-uniformities across the lake with extensive periods of overcast in the eastern basin. This observation identifies that a 2D pattern of all of the environmental variables including air

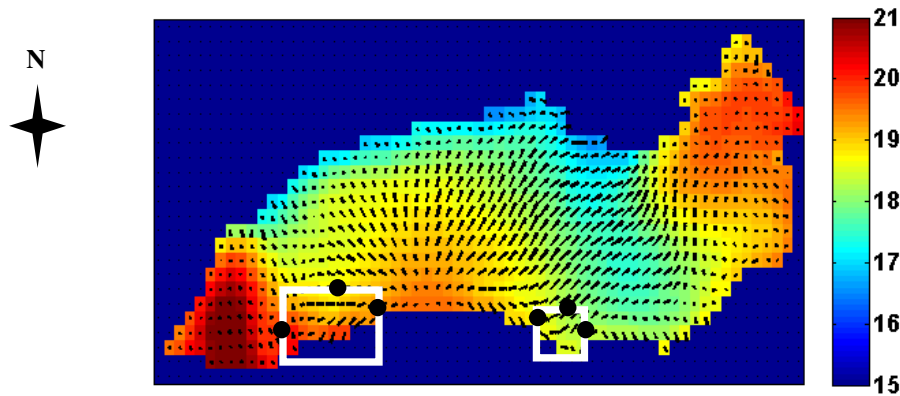


Figure 4.23. A temperature map [° C] derived from a lake-wide simulation overlaid with the surface current velocity vectors. The filled circles show the nodes from which the nudging vectors are extracted for each river plume simulation.

temperature, sky fraction, and cloud heights would enhance the model performance. In such stratified periods, any change in the temperature field would significantly affect the momentum and the current velocities in the domain. Thus, the derived temperatures and nudging vectors would fail to improve the localized simulations.

When the whole lake simulation is finished, the time varying temperature profiles of the localized-domain boundaries can be extracted. Accordingly, the surface velocities are obtained from three nodes located at three sides of the localized simulations. Figure 4.23 illustrates the domain boundaries for the Genesee and the Niagara sites overlaid onto a 2D model-derived surface temperature map and the current velocity vectors. The filled circles indicate the three nodes from which the hourly current velocity vectors are obtained. The three nodes are spatially distributed along the boundaries, i.e., west, north, and east sides, to properly capture the dynamics of the lake in the surroundings of the localized simulations. As described in Section 3.4.7, the nudging vectors derived for these three nodes are spatially weighted based on their distance from the shoreline to assign appropriate values to all the nodes along the boundaries. These surface velocity vectors are also vertically modeled using Eq. 3-22 and Eq. 3-23.

Figure 4.24 shows the magnitude and directions of the three nudging vectors extracted from three nodes in the west, north, and east sides of the localized Niagara simulation in Aug11. The nudging vectors are derived from the simulations run with the originally observed and the adjusted wind data. The wind data were adjusted by reducing its speed 20%

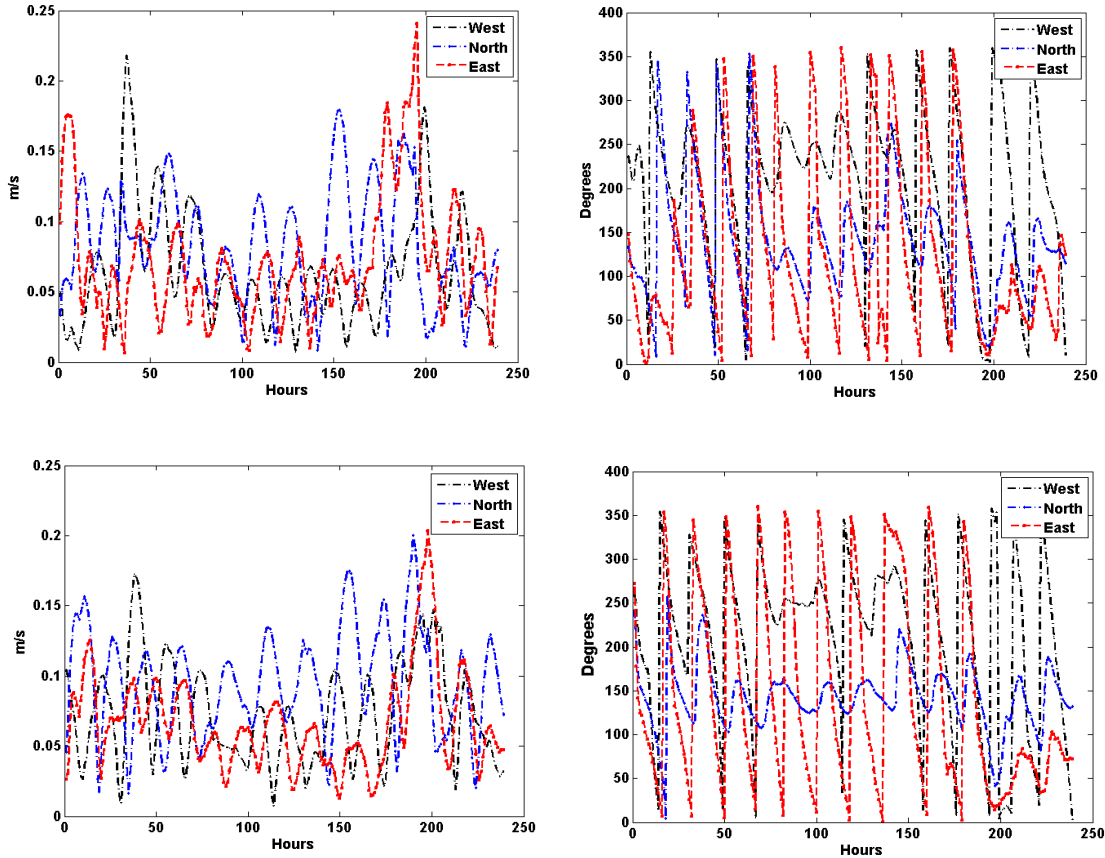


Figure 4.24. The surface current velocity magnitude and directions for the Aug 11 simulation. The upper frames correspond to the simulation with the originally observed wind data while the lower plots show the values resulting from the nudging oscillations in magnitude and direction after wind adjustments of the lake-wide simulation.

and rotating the wind axis -20° . The basic statistics show that the average current speed for the three nodes has slightly changed, i.e., $< 10\%$, whereas the average current direction remains nearly identical. It should be noted that the amount of change due to the wind adjustment depends on the wind magnitude and other environmental variables as well. In other words, varying the wind field may or may not significantly improve the current velocities, both in their magnitudes and directions. The vertical profiles of temperature were also extracted from the lake-wide simulations and were used to prescribe the thermal boundary advection during the localized simulation periods, i.e., 240 hours.

4.5.2 Model Stabilization (Long-term Simulations)

In order to calibrate the model using the L7's thermal imagery and eventually retrieve the water constituents, an LUT of various input parameters will be populated. The LUT is formed via many ALGE simulations, each of which can be very time-consuming. To reduce the computational burden, the code has been enabled to re-start for a shorter period of time during which the LUT is generated. In other words, the model is first allowed to stabilize for a sufficiently long period, e.g. 10 days, to predict the environmental conditions with the originally observed meteorological inputs. Then, it is re-started for a shorter period, i.e., 40 hours, to model various environmental conditions by refining input variables. It was believed that the 40-hour period was sufficiently long to capture a different environmental condition

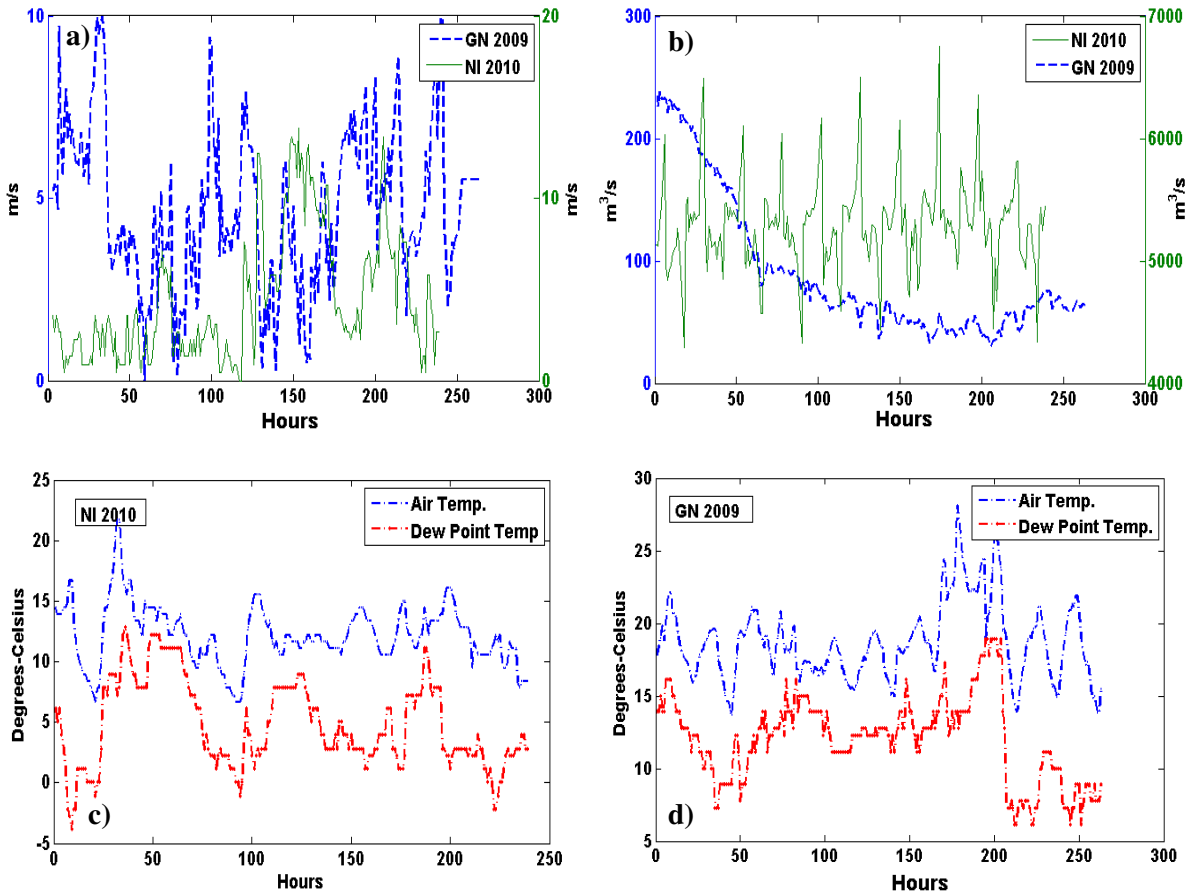


Figure 4.25. The wind data (a), the river discharge (b), and the air/dew point temperature (c and d) shown for July 2009 and Oct. 2010 simulations at the GN and NI sites. The GN simulation-time is 260 hours whereas that of NI is 240 hours.

induced by the adjustments in the input parameters. On the other hand, increasing this period could add to the computational expenses of the modeling effort. The L7's thermal data is used to calibrate the model while its reflective bands provide information to retrieve profiles of the water constituents. The long-term simulations are performed for all of the study sites, including Genesee (GN), Niagara (NI), and Onondaga Lake (ON). Figure 4.25 shows the wind data and the river discharge used for the July 2009 simulation at the GN site for 260 hours of simulation. The hourly river discharge for the GN simulation was obtained from the nearby USGS station, situated 5 km upstream, whereas the river temperature was taken from a nearby station in the region, i.e., Allen Creek. The wind data measured in the vicinity of the river mouth was obtained from the NBDC station while the other surface data were taken from the Rochester airport. For this simulation, the river temperature and the discharge measurements were on a daily basis; thus, the time series were up-sampled to maintain consistency with the model input formats. The failure in prescribing the model with hourly, time-varying temperatures diminishes its capability in predicting the dynamics of the temperature field when it discharges into the lake. The time-varying vertical profiles at the boundaries were obtained from the lake-wide simulations during the spring-summer of 2009. In a similar fashion, the current surface velocity vectors were derived from the whole lake simulation (Figure 4.23).

The Niagara simulations were performed by using the wind data observed at the Niagara Coast Guard. The other surface data are taken from the Buffalo airport. While the river temperature is derived from the NOAA's National Ocean Service (NOS) station located at the outlet of Lake Erie, the discharges are obtained from the US Army Corps of Eng. in Buffalo. Figure 4.25 illustrates the river discharge, the wind data, and the air/dewpoint temperature for the Oct. 2010 simulation at the NI site. It is evident that the Niagara River discharge is considerably greater than that of the Genesee River. The most notable observation is associated with the large variations of the Niagara River's discharge, i.e., $\sigma = 367 m^3/s$. Such significant high frequency variations may be related to uncertainties associated with the measurements. As opposed to the discharge at the NI, the discharge at the Genesee River exhibits smooth hourly variations with high values in the early hours decreasing exponentially following dry periods. Periods of wind gust and large variations are noticeable in the wind plot for both the NI and GN sites. The relatively dry air periods can be

inferred from the two plots showing the air/dew-point temperatures Figure 4.26 shows the discharge and the temperature of the Onondaga creek which is the major source of inflow into Onondaga Lake. The high discharge and low temperatures in the early spring, i.e., March, are noticeable. The average $12\text{ m}^3/\text{s}$ discharge in the early spring gradually decreases and reaches as low as $3\text{ m}^3/\text{s}$ in late May. It should be noted that the Onondaga Lake's simulation time was more than two months to allow enough time for the model stability. It is obvious that there are always errors associated with the environmental variables. These uncertainties may arise from either systematic errors corresponding to the observational instruments or the lack of temporal and spatial accuracy in the measurements, which may fail in properly representing the environmental conditions suitable for the model.

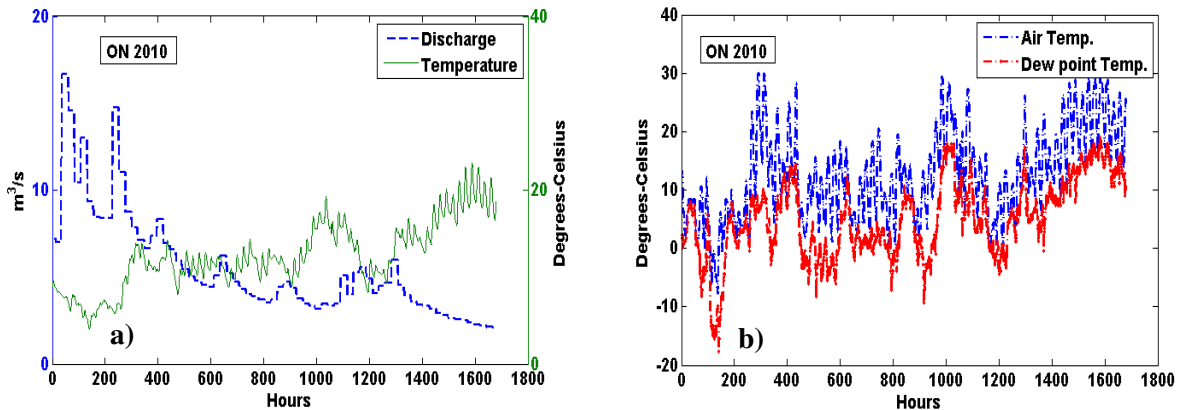


Figure 4.26. Onondaga creek's temperature and discharge (a) shown along with the air/dew point temperature (b) for the spring of 2010.

Both of these error sources can directly affect the simulations and result in erroneous outputs. In order to account for such errors the model is calibrated with the L7's thermal imagery. The following section describes the details on how the model is calibrated.

4.5.3 Model Calibration

The observation errors can be compensated with various techniques, including data assimilation, data feedback, etc. In this study, L7-derived temperature maps are treated as reference data to calibrate the thermally driven hydrodynamic model. This is accomplished through many simulations by adjusting environmental variables driving the thermal structure,

and material transport, within the water column. Through refining such variables, an LUT is populated which is then searched for the best agreement with the reference data.

There are a number of input variables controlling the fidelity of the model in predicting the state of the environment. While ALGE has to be provided with some constant variables, such as bottom drag coefficients and particle characteristics, the hourly measured variables are critical in the model performance. There are a number of hourly variables among which wind speed (WS), wind direction (WD), river discharge (RD), and river temperature (RT) are a set of parameters which significantly contribute to the fidelity of the model outputs when simulating a river plume or a lake circulation. Although other parameters, including air temperature, cloud height, precipitable water, etc. also influence the model performance, the earlier research efforts have proven that the former parameters are more crucial [Garrett, 1997; Garrett, 2002]. The latter variables may be more significant when the simulation of a different environment, such as Onondaga Lake, is desired. Ideally, it is of interest to refine all of the input variables. This, however, requires significant computational time.

Following the long-term simulations, ALGE is re-started for the last several hours by varying WS, WD, RD, and RT, which lead to many shorter simulations. Assuming a long-term simulation is 240 hours, the short-term simulations are initiated by extracting the 200th cube of the ALGE outputs, which has resulted from the model stabilization phase. For this study, the river plume simulations are re-started for 40 hours whereas the Onondaga Lake simulations are run for 96 hours.

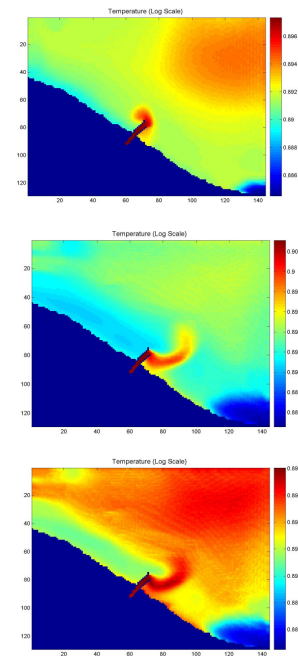
The strategy to vary input parameters was based on [Gerace, 2010]. Assuming that sources of instrumental errors are characterized with systematic trends, the observed quantities of the WS, RD, and RT can be modified by multiplying a percentage of the originally observed values. For instance, the range of coefficients is intended to span a reasonable range of variables in the LUT. The WD values, however, are manipulated in a different fashion. Additive/subtractive coefficients are applied to rotate the wind axis. Figure 4.27 shows three ALGE-derived surface temperature maps generated by applying the corresponding coefficients (Table 4.6) to the environmental variables for the Genesee plume simulations. Each combination of variables results in a different model output. The level of distinction between each combination depends upon the meteorological conditions and differs from one simulation to another one. The range of coefficients is determined through preliminary,

coarse-resolution simulations. The example increments shown in Table 4.6 are relatively coarse and correspond to the first iteration. By knowing which combination satisfies a minimum disparity with respect to the reference data, the second iteration is conducted with finer step sizes permitting a better model prediction of the flow. The cost function to choose the best agreement from the model outputs is described in the next section. From the model outputs shown in Figure 4.27, one could also infer that increasing the wind speed gives rise to more vertical mixing, which results in a cooler surface temperature. The change in the WD parameter primarily alters the orientation of the river flows while boosting the discharge makes the river plume larger and, as a result, larger mass of concentrations is transported into the lake. A similar procedure applies to the Onondaga Lake simulations where LUTs of many ALGE simulations are created.

Table 4.6. The coefficients used to re-start ALGE for the Genesee plume simulation

Range			
WS	WD	RD	RT
0.8- 1.2	(-10) -(+30)	1.0-1.3	0.9-1.1
Examples			
0.9	20	1.0	0.9
1.0	-10	1.1	0.95
0.8	-10	1.2	1.0

Figure 4.27. Three sample instances of ALGE-generated thermal plumes by varying input environmental variables. Variable ranges are arbitrary and for illustration purposes.



4.5.3.1 Cost Functions and Optimization

In order to measure the similarity between each model outcome and the L7-derived temperature maps, a metric needs to be defined. The metric should specify the level of agreement between the reference and the model-derived maps. In this study, two different metrics are defined. The first metric is the well-known RMSE and the second one is the spatial correlation (*SC*). The RMSE estimates the similarity between the 2D functions based

on a pixel-by-pixel basis whereas SC measures the structural similarities between two functions. The RMSE is expressed as follow:

$$RMSE = \sqrt{\frac{\sum_i (T_s^i - T_o^i)^2}{N}} \quad 4-15$$

Where T_s and T_o stand for the simulated and the observed surface temperatures, N represents the number of water pixels over which the metric is computed, and i is the pixel index. The minimum error is associated with the best model output, which resembles the reference data the most.

On the other hand, the SC is defined as

$$SC = \sum_i \sum_j m(i, j) \otimes r(i, j) \quad 4-16$$

Where SC is a value representing the degree of similarity, $m(i,j)$ is a model output, and $r(i,j)$ is the reference function, i.e., L7-derived temperature map. The operator \otimes indicates the 2D spatial correlation that implements “sliding” and summation over the indices of (i) and (j). The correlation operator is essentially very similar to the convolution operator and is identical to the convolution operator for symmetric functions. According to the linear systems and the Fourier-transform pairs, the above operation can be written in the form of the product of the Fourier transform of the two functions:

$$SC = \frac{M(i, j) R(i, j)}{\sum_{i,j} R(i, j)^2} \quad 4-17$$

Where $M(i,j)$ and $R(i,j)$ are the Fourier transform of the model output and the reference data, respectively. The term in the denominator is the normalization factor, which represents the total power spectrum of the reference data. The resultant of the above expression is a single number that corresponds to the similarity of a model output relative to the reference data. The greater the number, the more the model output is in agreement with the reference data. In other words, the SC metric has to be maximized to obtain the best match. However, the SC metric performs well when the river plume has a distinct, well-defined shape with respect to background lake waters. Therefore, this metric may not be suitable when examining the Onondaga Lake simulations. The two metrics defined in this section are

applied in the optimization process to select the closest match and, eventually, calibrate the model.

4.5.3.2 Sampling Scheme

In order to calculate the metrics that accurately identify the best model match with the reference data, a sampling scheme specific to the plume simulations was designed. In this scheme, an area over which the model performance is best corroborated is specified. The areas should be characterized with the highest sensitivity to the variations in the input parameters. Moreover, such a sampling scheme reduces the computational cost in the constituent retrieval process in which the Hydrolight simulations have to be carried out on a pixel-by-pixel basis (see Section 4.5.4.2). The sampling areas simply encompass the plume areas and their immediate waters to appropriately account for the model performance when simulating the river plumes (Figure 4.28). There was no sampling scheme designed for Onondaga Lake as its overall thermal pattern is evaluated.

4.5.3.3 Optimization

When different combinations of input parameters are employed to form the LUT, there is a similarity degree associated with each of the simulation results. The similarity degrees are calculated based upon either of the metrics introduced in the previous section. The procedure

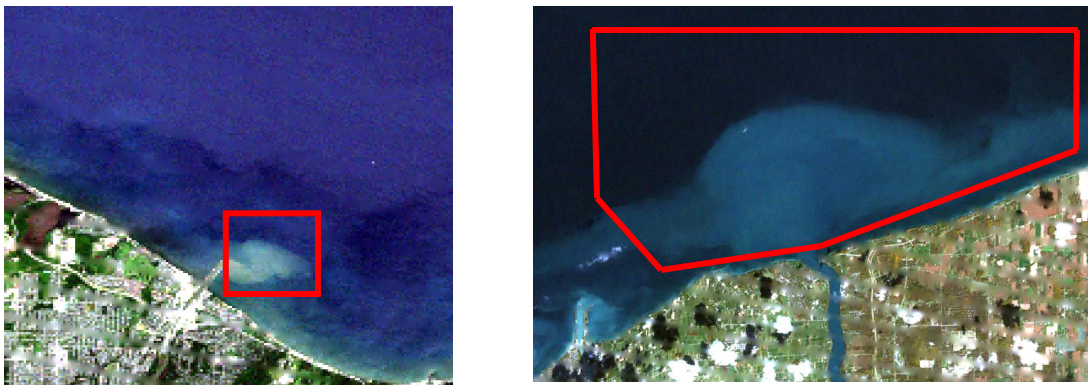


Figure 4.28. The sampling areas drawn for the case studies in July 2009 (Genesee) and Oct. 2010 (Niagara) to evaluate the model performance in the thermal domain. Depending on the shape of the plume the sampling area can differ.

explained for generating the LUT is an iterative process, which follows similar concepts as in the gradient descent approach. In the first round of iteration, the best solution (x_0) is found by searching the minimum/maximum error value associated with a vector of input parameters:

$$x_0 \rightarrow \begin{bmatrix} x^1 \\ x^2 \\ x^3 \\ x^4 \end{bmatrix} = \begin{bmatrix} WS_0 \\ WD_0 \\ RD_0 \\ RT_0 \end{bmatrix}$$

where the column vector indicates the coefficients that led to the best solution in the first iteration. When the most suitable combination of parameters is identified, the second iteration is carried out with a finer sampling of the input parameters, which makes the parameter space denser. However, re-iterating the process several times increases the computational burden. Therefore, an interpolation together with an optimization routine enables estimating the optimum solution among all of the model outputs. Figure 4.29 illustrates a schematic LUT with three dimensions. In reality, we have a 4D LUT, i.e., WS, WD, RD, and RT. Each node represents an error value computed from a metric for a single simulation with a definite set of environmental inputs. The optimization routine minimizes/maximizes a function fitted to the space nodes to predict the best solution.

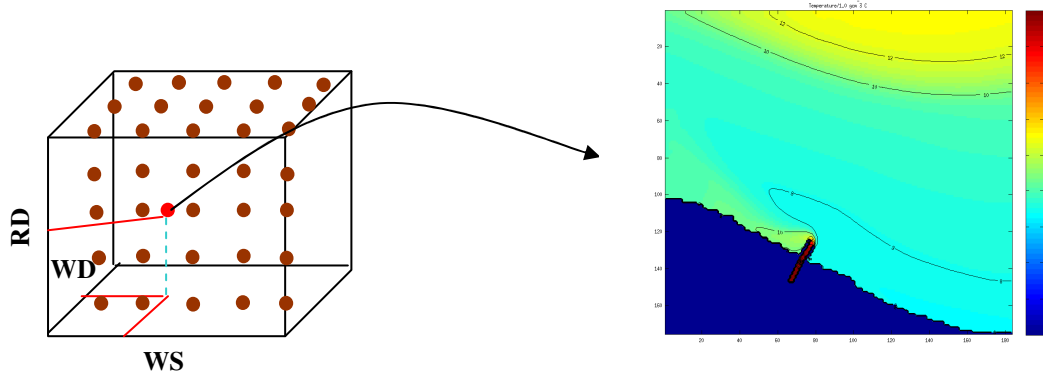


Figure 4.29. The schematic LUT formed of three dimensions. The sparse sampling of the three axes demands further optimization to search for the optimal solution. The best output is modeled by re-running the model using the inputs found in the optimization process

In order to ensure that the mathematically derived function properly represents the parameter space, the space sampling should be adequately dense. This is achieved by several model iterations to reasonably achieve a finely sampled space. In the model calibration process a 4D LUT (WS, WD, RD, RT) is generated in each iteration. Following a few iterations, when the variable increments are small enough, a 4D function is fitted to the space nodes representing error values associated with each run. Depending on the metric used to form the space, the function is minimized or maximized. The entire optimization process was conducted in Matlab. The Matlab's surface generator routine was extended to solve multi-dimensional problems, i.e., 4D in our case. The fitted function was then minimized/maximized using an unconstrained, non-linear optimization function called *Fminsearch*, which takes the initial search value and finds the optimum solution. *Fminsearch* uses the Nelder-Mead simplex algorithm as described in [Lagarias et. al., 1998]. This algorithm uses a simplex of $n + 1$ points for n -D vectors x . The algorithm first makes a simplex around the initial guess x_1 by adding 5% of each component $x_1(i)$ to x_1 , and using these n vectors as elements of the simplex in addition to x_1 . The minimization is performed by a set of iterative operations, including ordering, reflection, expansion, contraction, and shrinking. The function values at the vertices of the simplex are first ordered in the ascending format to find the best and the worst coordinates leading to the minimum and the maximum function values. Assuming we deal with a 2D problem we have three vertices, which represent a triangle, such that $x_1 < x_2 < x_3$ with x_1 and x_3 being the best and the worst points, respectively. The worst point is first reflected with respect to \bar{x} to produce a new point x_r (Figure 4.30-a). If the function value at x_r is smaller than the one at x_1 (a new minimum) then the triangle is expanded towards point x_e to improve the search direction (Figure 4.30-b). If the function value at x_r is greater than that at x_3 , then the triangle is contracted either outside (x_c) or inside (x_{cc}) of the original triangle. If the function values at these two coordinates are not smaller than the one at x_3 , then the triangle shrinks towards the best point (x_1) [Lagarias et. al., 1998]. In this iterative fashion, the best solution, which satisfies the best agreement with the reference data, is identified. The minimum/maximum value obtained with this procedure corresponds to a vector of input parameters (e.g. WS=1.053, WD=+2.4, RD=1.123, RT=1.012). This best combination of variables

(coefficients) is then applied to the environmental inputs to start the final simulation whose thermal output should most resemble the L7-derived temperature map. In this study, both metrics were attempted for the optimization. It should be noted that the inverse of the *SC* metric was employed for minimization.

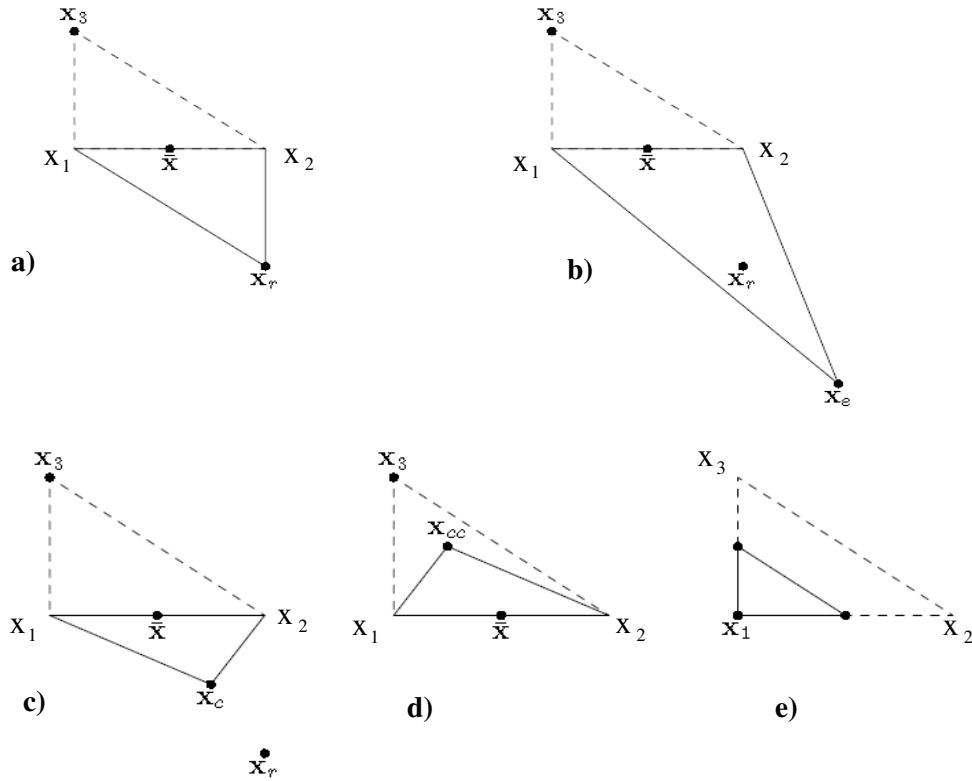


Figure 4.30. The Nelder-Mead simplex search method showing the reflection (a), the expansion (b), outside (c)/inside (d) contraction, and shrinking (e) [Lagarias *et. al.*, 1998].

4.5.4 Constituent Retrieval

After the model is calibrated for its input environmental variables as described above, the profiles of constituent concentrations, including TSS and dissolved matter, can be retrieved. The input parameters controlling the TSS (particles) profiles are their concentration, particle density (PD), and particle size (PS) while the profiles of dissolved matter are determined through only their concentration. Although the concentrations can be provided to the model as time-series, in this study, they are assumed constant over the period of simulations due to the absence of hourly observations. Similarly, the particle density and particle size parameters are assumed invariant and their initial estimates can be made based on previous

studies [Li, 2007]. By varying the three parameters associated with the TSS along with the concentration of dissolved matter, one is able to obtain various material loads that alter the optical regime within the water column. In other words, the short-term simulations are conducted by adjusting the above-noted parameters and fixing the environmental variables optimized in the calibration process. To simulate the water-leaving optical field associated with each ALGE simulation, the Hydrolight model is applied. Hydrolight simulates the remote sensing reflectance for each individual pixel. Assuming ALGE outputs 256 combinations of the input variables for an area covering 1000 pixels, the Hydrolight code needs to perform as many as 256000 simulations, which are computationally expensive. In order to avoid the computation burden, it was decided to conduct a sensitivity analysis to investigate the significance of particle density and particle size in this framework. If the two parameters do not make great contributions into the constituent retrieval process, then the number of variables are reduced to only the concentrations.

4.5.4.1 Sensitivity Analysis

In order to assess the effects of particle size (PS) and particle density (PD), multiple ALGE simulations were conducted for the Genesee site. Table 4.7 contains the range and combinations of the variables used in the experiment. Clearly, adjusting the two variables alters the settling velocity associated with the horizontal/vertical distribution of the particles (TSS) while the dissolved matter (CDOM) concentration remains unchanged. The ranges of the input parameters adopted for this study cover a feasible range appropriate for the Genesee site.

Table 4.7. The ranges of variables used in the sensitivity analysis

Particle density (gcm^{-3})	Particle size (um)			
		2	4	6
1.05	1.05/2	1.05/4	1.05/6	1.05/8
2.5	2.5/2	2.5/4	2.5/6	2.5/8

The combination of such parameters (Table 4.7) led to sixteen different ALGE long runs. This experiment was undertaken for the period of Oct. 2009 with a domain rotated 60° to enhance the stream flow into the lake, i.e., North direction to the right of the page. Figure 4.31 shows various sediment distributions corresponding to different particle sizes while

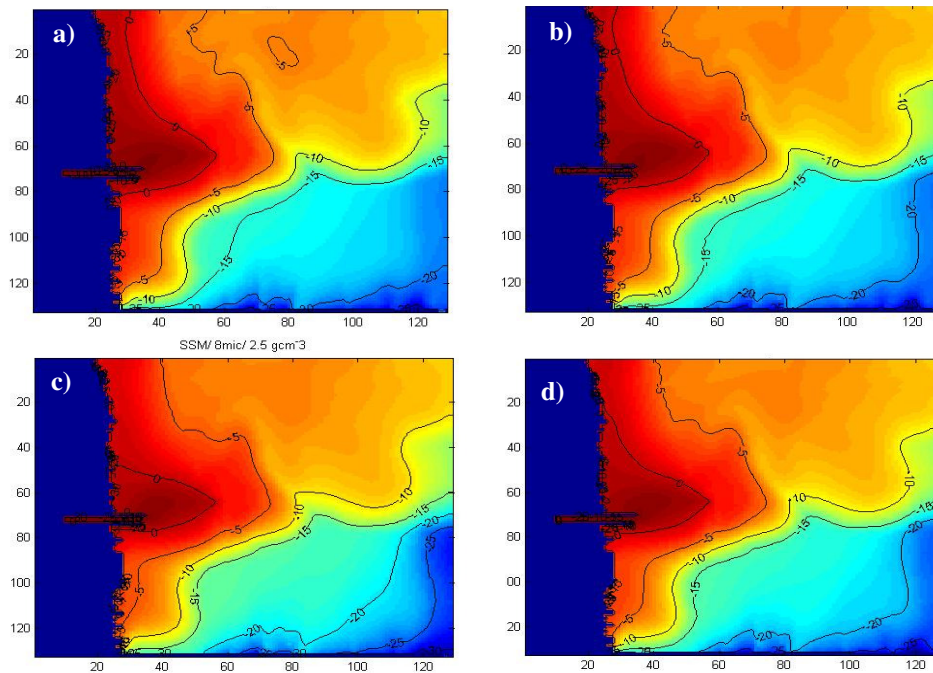


Figure 4.31. The variability of sediment concentration (log-transformed) with respect to particle size. Other inputs such as particle density ($PD= 2.5 \text{ gcm}^{-3}$) were constant. Particle sizes are (clockwise from upper left) 2, 4, 6 and 8 μm . The plots are log-transformed.

particle density remained constant. As seen, the extent of the plume is slightly different for the four experiments. The variations primarily occur on the lower right of the domain (deep waters) where concentrations are considerably low. It should be noted that the increment between sequential runs was chosen to be 2 μm . It appears that the 2- μm difference in the particle size does not significantly influence the sediment load. However, variations are more noticeable when results associated with 2 and 8 μm are compared, i.e., note the contours outlining the plume in Figure 4.31-a and -c. This confirms that 4-6micron increment in particle size would give rise to noticeable change, visually detectable in the sediment distribution map. That being said, this may not be true if other environmental conditions exist. As a result, such sensitivity analysis is case-specific and should be implemented independently prior to the experiment at hand for each timeframe. Figure 4.32 shows the sensitivity of ALGE relative to the changes in the particle density (PD) while particle size remained fixed. Although differences are clearly seen in offshore regions, the bulk of the plume has only slightly changed.

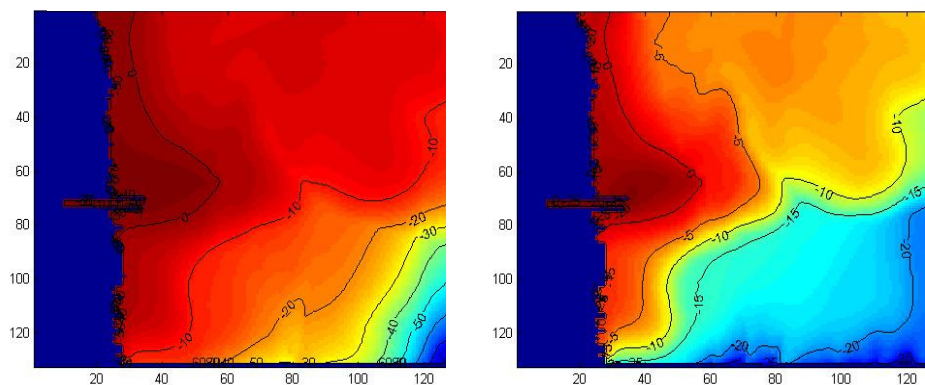


Figure 4.32. The sediment distribution maps (log-transform) with varying particle density. On the left, particle density is equal to 2.5 gcm^{-3} while it is 1.5 gcm^{-3} on the right map. Particle size in both cases was fixed to $4 \text{ }\mu\text{m}$.

It is also worthwhile mentioning that the level of sediment load throughout the offshore (non-plume) areas is on the order of 10^{-5} g/m^3 , which results in very subtle variations in the apparent optical properties of water. These variations can not be detectable through remote sensing systems, such as L7.

Overall, it is inferred that there exist some changes between the two plumes when their corresponding particle sizes are 4-6 units different. Also, there is slight variation in the sediment load in the plume areas due to 1 gcm^{-3} change in the particle density between the two different runs. This leads us to the conclusion that variations of PS and PD may alter the results to some extent when investigating the errors associated with the plume. It should be noted that the step sizes applied in this experiment may differ when other model parameters or environmental conditions apply. For instance, changing the domain size or discharge rate may alter the model sensitivity with respect to PS and PD. The experiments presented here were performed with very low discharge rates (Oct. 2009).

4.5.4.2 Procedure

By fixing the physical shape of the plume using the L7-derived temperature maps, we move forward to characterize the constituent loads using the reflective portion of the spectrum. In other words, we intend to relate the L7's visible bands to the water constituents. This is done through coupling ALGE with the Hydrolight simulations in which modeled

concentrations are plugged into Hydrolight to simulate the surface reflectance. The procedure is briefly described as the following bullet points:

- Background distribution
- Generate the LUT
- Extract constituents' profiles
- Simulate Surface Reflectance for a sub-sample of the area
- Error calculation and optimization

It is already recognised that the three optically active components of the water TSS, CDOM, and CHL are retrieved through our proposed integrated modeling system. Although ALGE handles the hydrodynamics of sediment transport and dissolved matter, it does not incorporate any biological factors enabling phytoplankton modeling. Therefore, we have to make some assumptions to simplify the problem at hand. The CHL concentration can be assumed to be highly correlated with the dissolved matter distribution. This is a valid assumption over a short period of time when the primary driving factor for the available nutrients is the relatively high discharge from the river flow. More precisely, CHL can be modeled as the dissolved tracer diluted into the lake waters by ignoring biological driving factors.

Moreover, when simulating moderate size plumes, such as the Genesee plume, ALGE predicts the sediment loads and the distribution of dissolved matter (CDOM) only within the mass of water entering large bodies of water. In other words, ALGE is unable to simulate the distribution of the above-noted constituents in the plume surroundings predominantly controlled by the lake circulations, and not by the local meteorological parameters. More specifically, over these regions, concentrations are often underestimated because of the limited interactions of the localized simulations with the dynamics of the lake, i.e. there is not much knowledge on material transport from lake circulations into the area of interest. Therefore, there is a need to estimate the background concentrations. The following sections

elaborate on the preceding issues followed by detailed discussions on how to generate a LUT for the purpose of constituent retrieval.

(a) Estimating Background Concentrations

To our knowledge, the most reasonable background concentrations can be achieved by using either the ancillary data or the L7 data itself. Due to the unavailability of the ancillary data, the L7 data enables us to retrieve the background concentrations in the vicinity of the river plumes. This can be accomplished through performing a constituent retrieval for a few pixels surrounding the plume representing the background concentrations. A full description of the constituent retrieval is given in Section 4.6.4. The averaged retrieved TSS, CDM, and CHL concentrations in the surroundings of the plume (Genesee plume only) are then applied as a constant background to be added to the model predicted concentrations. However, the background concentrations might spatially vary in the plume surroundings. In order to account for the variations, the constant values are considered as free parameters after the 2D LUT is generated using the ALGE simulations (see the following subsection). Adjusting the background concentrations is conducted in the constituent retrieval process in which multiple ALGE-derived concentrations are fed into the Hydrolight code. Note that adjusting the background concentrations were performed only for the Genesee plume simulations. For the Niagara plume simulations, since the plume relatively uniformly covers the entire domain, there was no need to add the background concentrations. Similarly, no background concentration was planned to add to the ALGE-derived concentrations when modeling Onondaga Lake particle distribution. More precisely, we assume that the model is able to predict particle distribution in such a small lake environment.

(b) ALGE-derived 2D LUTs

Following the determination of the four critical environmental variables, including the wind speed, the wind direction, the river discharge, and the river temperature, which helped fix the shape of the plume, the concentration of the particles and dissolved matter are varied to generate waters with various turbidity levels. The preliminary sensitivity studies showed that the other two variables, namely particle size and particle density, do not significantly contribute to change the optical regimes of the water bodies (Section 4.5.4.1). In other words, the change due to the changes in these parameters translates into very small changes in the

water-leaving optical fields around the edges of the plumes. That being said, an average estimation of such parameters had to be done prior to launching the simulations, particularly for the Onondaga Lake simulations. This is done via multiple coarse simulations by varying these parameters. In order to build up the 2D LUT, a similar procedure as in the thermal model calibration discussion, Section 4.5.3, was pursued. The concentration of particles (COP) and dissolved matter (COD) are the only parameters being adjusted in the multiple simulations. The variables are specified such that they span a reasonable range.

(c) Hydrolight Simulations

The concentration-to-reflectance conversion is performed using the Hydrolight code in which light-water interactions are modeled assuming the water column is formed of homogenous horizontal layers within a confined patch of water. The model generated concentration profiles are added to the vertically uniform background concentrations (the Genesee River plume only). As described in the previous sections, the background concentrations should be optimized simultaneously with the ALGE-derived profiles. In doing so, the background concentrations of TSS and CHL are varied by defining multiplicative coefficients, which systematically manipulate the concentration profiles. A combination of all of the four variables, i.e., COP, COD, background TSS, and background CHL, increase the number of Hydrolight simulations. For each ALGE-derived profile map, several combinations of vertically uniform backgrounds of TSS and CHL are added, which are subsequently provided to the Hydrolight code. In addition to the profiles of concentrations, IOPs including absorption and scattering coefficients as well as the phase functions are fed into the code. The Hydrolight parameters are tuned for the specific sites and dates/hours when the L7 image was acquired. The Hydrolight simulations, conducted with 10 nm spectral resolution ranging from 350-740 nm had to be resampled to the L7 response functions (Eq. 3-30). The individual values computed at the visible bands are then compared to the L7-derived surface reflectances on a pixel-by-pixel basis.

The Hydrolight simulations are performed in a similar fashion as in Raqueno (2003). In the light of this, different directories for different pixels are generated such that each directory contains the concentrations exclusive to that specific pixel. Other data files including the IOPs, the phase functions, and the wind files, which are common for all pixels, also reside in each directory. Submitted from each directory, Hydrolight simulations are run

independently through a Sun Grid Engine (SGE) cluster, i.e. open source batch-queuing system. This system enables simultaneous computations, up to 132 jobs in our case, and queuing of all submitted jobs. However, there needs to be a compromise between the computation time and total number of jobs. For instance, running Hydrolight for 36 different outputs of ALGE for 11000 pixels leads to 396000 jobs, which takes up to seven days to finish. It is, therefore, reasonable to reduce the number of simulations by restricting ourselves to a sub-sample of pixels throughout the study area. The problem arises as how to select for the sub-samples, which properly represent the entire domain.

It was found that the most efficient way to choose the sub-set of the area representing the model performance is to spatially restrict the evaluations over the plume areas. Therefore, ROIs over the plume areas for the Genesee and the Niagara Rivers were manually drawn to assess the ALGE outputs against the reference datasets. To further reduce the number of simulations in the constituent retrieval process, every 4th pixel within the sub-sampled areas were provided to the Hydrolight code. Preliminary experiments revealed that a quarter of the total number of pixels would be a reasonable representation of the entire area for evaluating the model performance. Furthermore, the missing data due to the L7 SLC-off were discarded.

(d) Error Calculation and Optimization

Analogous to the error calculation in the model calibration phase (Section 4.5.3.1), an error function was defined to evaluate each ALGE-generated output on a pixel-by-pixel basis. This gives an indication on how close each simulated reflectance map is to the L7-derived one. The cost function is expressed as below

$$J = \left[\frac{\sum_{\lambda} (R_m - R_o)^2}{3N} \right]^{\frac{1}{2}} \quad 4-18$$

Where R_m and R_o are the modeled and the observed surface reflectances, respectively. N represents the number of bands, i.e., the three visible bands, and λ stands for each band. It should be noted that the NIR band was avoided mainly to reduce the computational burden. However, it is believed that, incorporating the NIR band in such a physics-based constituent retrieval would not make a significant improvement within the plume areas and helps solely

to identify the edge of the plume. This is due to the low signal levels coupled with the poor radiometric fidelity of the L7 instrument.

Following a few short-term simulations, a similar optimization technique as in Section 4.5.3.3 was employed to minimize the cost function (Eq. 4-18) in the parameter space. When the best match is found, the ALGE code is re-run with the corresponding parameters to generate the final concentration products. The parameter space for the Genesee plume has four parameters, including the two initial concentrations (COP and COC), and the two background concentrations of TSS and CHL. Only the two concentrations, i.e., COP and COC, formed the parameter space for the Niagara River. As it will be described in Section 5.2.3.2, no attempt was done to retrieve the water constituents in Onondaga Lake due to the poor performance of the model in predicting the distributions of particles and dissolved matter. Note that the PS and the PD parameters had to be optimized in all cases, particularly in the Onondaga Lake simulations.

4.6. OLI's Potential for Coastal Water Studies

The new generation of Landsat will carry the Operational Land Imager (OLI), which has specifications that make it superior to the existing Landsat systems. The new features include the addition of a new coastal/aerosol band, i.e., $\lambda=443\text{ nm}$, an improved SNR, and enhanced radiometric resolution. Theoretically, these enhanced specifications should add to the capability of the Landsat systems for regular monitoring of water resources. In fact, when sensing water quality from space, the low signal level demands imaging systems with high SNR and radiometric fidelity [Gerace, 2010].

In this study, an EO-1 dataset, including Hyperion and ALI, acquired over the Niagara River plume is employed to evaluate the potential of the OLI sensor for coastal water studies. In order to investigate the contribution of OLI's new band in the constituent retrieval process, the Hyperion dataset is also spectrally resampled to the L7's response function (Eq. 3-30). In addition, the retrieved concentration maps are compared with those obtained from the nearly simultaneously acquired L7 data (Section 4.3.2.2). A cross-comparison between the simulated L7 and a simultaneously acquired L7 data provide insights on the effects of the quantization rate in the constituent retrieval task. On the other, comparing the retrieved concentrations from the simulated OLI and the simulated L7 would reveal the contribution of

the new spectral channel, i.e., 443 nm. The following sections elaborate on the procedures followed to achieve the aforementioned goals.

4.6.1 Datasets and Study Area

For this study, EO-1 datasets and a L7 images acquired nearly coincident are used. The L7 imagery, row/path 30/18, was captured on October 19th 2010 at 11:56AM EST. The L7's scanning mirror imaged the western basin of Lake Ontario while pointing slightly westward. Nearly simultaneously with the L7 overpass, EO1, tasked over the study area at (43.33° N , 79° W), collected a pair of images with its dual instruments, namely Hyperion and the ALI instruments. Hyperion is an imaging spectrometer operating since late 2000. Hyperion collects images through narrow spectral bands ($\cong 10nm$), ranging from 400 to 2500 nm at 30 m GSD. Hyperion delivers images with SNR ranging in 65-130 for relatively bright targets, i.e., 40%, which peaks within 550-700 nm region. However, images within short blue bands (396-430 nm) have a low SNR. Moreover, the spectral smile issue further affects the SNR and the sensor's fidelity particularly in the blue portion of the spectrum. The design specifications and the corresponding restrictions allow only for a relatively limited FOV resulting in strips of images stretched north-south ($7.5 \times 20 km^2$) [Folkman, 2001]. EO-1 was originally placed in an identical orbit as L7; however, over the past few years there have been some adjustments in its orbital configuration to maintain the mean equatorial crossing at

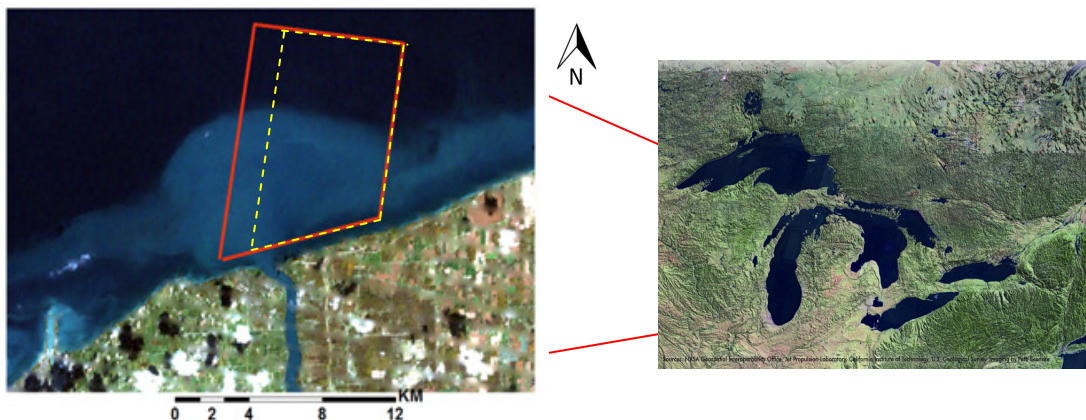


Figure 4.33. The study area covering the Niagara River plume (Section 4.3.1.2) discharging into the western basin of Lake Ontario. The red box ($\sim 100 km^2$) indicates the study area.

10AM local time. Therefore, EO-1's altitude is slightly lower than L7 listed in Table 4.8. The red box shown in Figure 4.33 indicates the overlap between the L7 and Hyperion data. Due to a slight difference in the ALI and Hyperion's line of sight, ALI does not exactly image the Hyperion swath. The common overlapping region of the two sensors is depicted in Figure 4.33 with the yellow box. As indicated in Table 4.8, while the solar positions are slightly different for the L7 and EO-1 acquisitions, there are obvious discrepancies in the viewing geometries. It is assumed that any effects caused by the differences in the viewing geometries and, as a result, the BRDF are minimal. In general, this is a valid assumption as uncertainties corresponding to the atmosphere and the IOP estimations dominate the error budget in the constituent retrieval errors [Gerace, 2010].

Table 4.8. The imaging geometry conditions

	L7	EO-1
Sun elevation ¹	34.5	32.9
Sun azimuth	160.4	153.9
Off-nadir	+6.5	-19.1
Sensor azimuth	278.2	98.2
Sensor altitude	705 km	695 km

Figure 4.34 illustrates the RSR profiles of L7, OLI and ALI [Barsi, 2011]. In general, the differences in the RSRs are most noticeable for the bands where the signal reaching the sensors is the highest. Hence, the disparity between the OLI and the ALI's RSR of the CA band can introduce some biases when comparing the OLI and ALI retrieved concentration maps. It should also be emphasized that L7 does not have the new CA band designed for OLI (Figure 4.34). The OLI is planned to acquire images in eight spectral channels within the VNIR-SWIR region. Table 4.9 summarizes OLI's band configurations. Using the band setting and the RSRs, the Hyperion data can be spectrally integrated over the OLI's response functions. Resampling Hyperion imagery to OLI spectral bands, it is important to make sure that Hyperion resembles the OLI data. In terms of the radiometric resolving power, Hyperion has a 12-bit digital quantizer which is identical to that of OLI. Also, OLI has been designed

¹ All of the units are in degrees.

to improve the average SNR up to four times L7 for the common target reflectances, i.e., 25% reflectors. This consideration is further discussed in the next section.

4.6.2 Data Preparation

The OLI data were simulated by spectrally resampling the Hyperion scene using Eq. 3-30. In order to provide insight on how the differences in the RSR functions would influence

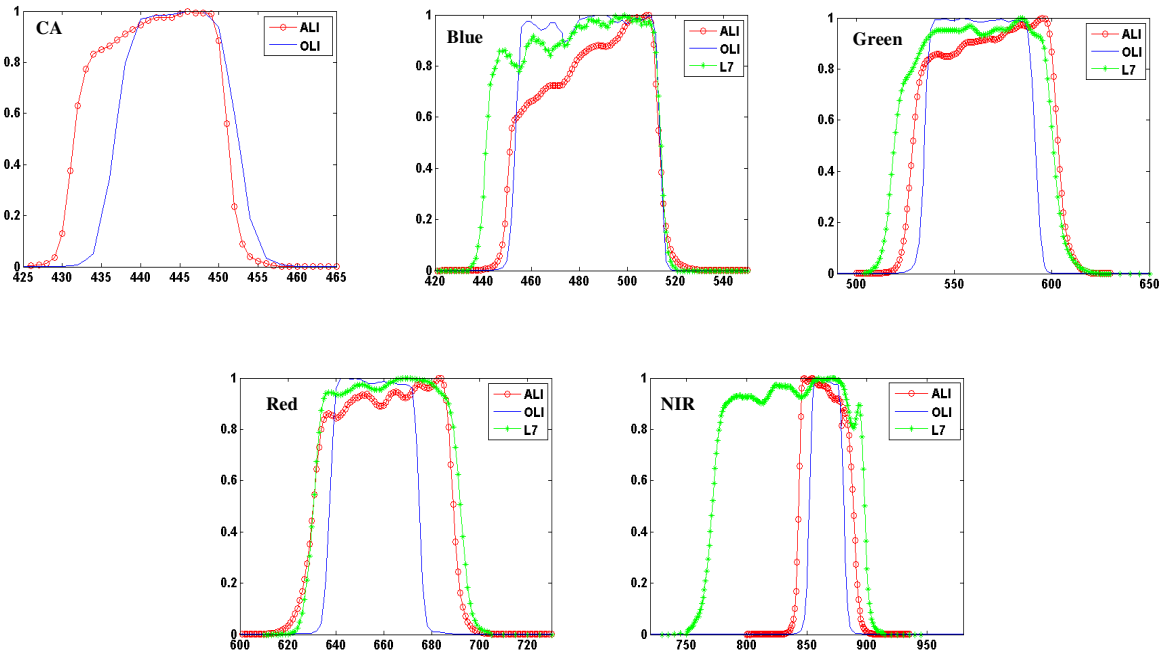


Figure 4.34. The band-specific, normalized RSRs of L7, OLI, and ALI shown for different portions of the spectrum [nm]. The differences are discernable in all of the bands, in particular in the NIR band.

Table 4.9. The band specifications of the OLI sensor

#	Band	Center Wavelength (nm)	Center Wavelength Tolerance (\pm nm)	Minimum Lower Band Edge (nm)	Maximum Upper Band Edge (nm)
1	Coastal Aerosol	443	2	433	453
2	Blue	482	5	450	515
3	Green	562	5	525	600
4	Red	655	5	630	680
5	NIR	865	5	845	885
6	SWIR 1	1610	10	1560	1660
7	SWIR 2*	2200	10	2100	2300
8	Panchromatic **	590	10	500	680
9	Cirrus	1375	5	1360	1390

the water constituent retrieval process, a simulated ALI (S-ALI) scene was also generated from the Hyperion data. An L7 scene was also simulated from the Hyperion dataset to compare the retrieved concentrations with the actually observed L7 data. As stated, this comparison enables testing the impact of the differences in the radiometric fidelity of the two systems, i.e., simulated L7 (S-L7) with 12-bit quantization versus 8-bit L7 imagery. On the other hand, performing a cross-comparison between the results from the simulated OLI (S-OLI) and simulated L7 (S-L7) allows us to examine the enhancement level due to the addition of the CA band.

When studying water using various flavors of remotely sensed imagery, it is important to obtain a measure to assess their suitability for a water constituent retrieval framework. Here, we define the scene-derived SNR to relatively quantify the applicability of each system in each spectral channel over bodies of water. The SNR, which is defined as the ratio of the mean and standard deviation, is calculated over the dark, uniform waters common in all the TOA radiance imagery. The scene-derived SNR implies the similar concept as environmental noise equivalent difference in radiance, i.e., $NE\Delta L$, specified in [Brando and Dekker, 2003].

Figure 4.35 shows the SNR derived for the Hyperion, L7, ALI, and the simulated data over dark waters of Lake Ontario. The center wavelengths (CW) for the multispectral systems indicate the shift in the spectral response. The generally low SNR in the short, blue bands ($\lambda < 450 \text{ nm}$) is primarily attributed to the sensor calibration issues.

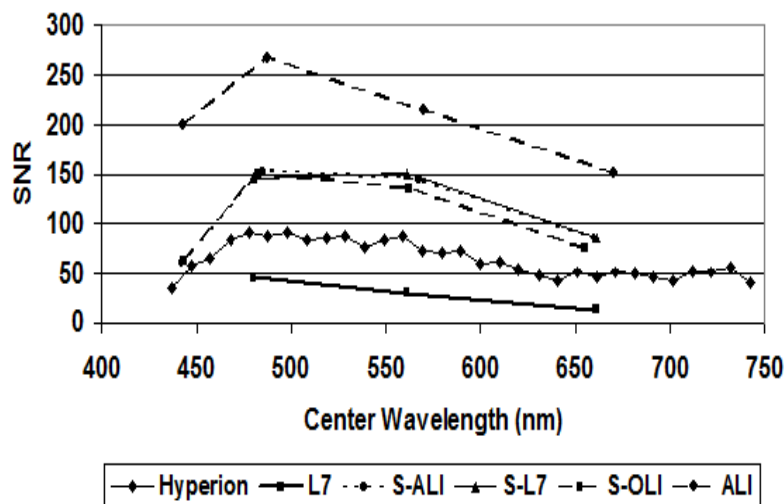


Figure 4.35. The spectral scene-derived SNR shown for different instruments

In addition to the atmospheric effects, the multispectral systems collect photons in relatively narrow spectral channels ($\Delta\lambda < 35 \text{ nm}$ in

Figure 4.34), which has resulted from the cumulative impacts of the systems' optical transmission and low detectors' quantum efficiency (QE) in this region. According to Figure 4.35, ALI outperforms the other datasets exhibiting 5 times better performance than L7. Hyperion, on the other hand, shows an average SNR of 66.6 in the visible range. The relatively low SNR of Hyperion data also reflects in the simulated multispectral datasets (S-OLI, S-ALI, and S-L7), which are the result of integrations across several bands. Due to the Hyperion's higher SNR and 12-bit radiometric resolution, the S-L7 shows higher SNR than the original L7 data. The 8-bit quantization level of L7 is unable to resolve subtle inter-pixel signal variations and introduces unrealistic, local variability. As expected, a cross-comparison between the S-OLI and S-ALI would aid in investigating the plausible disparities caused by the differences in the RSR functions when retrieving water constituents. In other words, a direct comparison between the S-OLI and ALI data potentially underestimates the performance of the future OLI onboard LDCM.

Prior to applying the atmospheric compensation, the EO-1 scenes undergo radiometric and geometric corrections. Because of the non-uniform detector-to-detector responses across track, both Hyperion and ALI suffer from considerable striping effects causing spatially unrealistic variations across the detector array. This artifact is, in particular, important when sensing uniform targets of low signal levels, i.e., water. A simple statistically driven technique was applied to take into account the striping effects [Schott, 2007]. To do so, each detector's response was adjusted via implementing a ratio factor obtained over a spatially uniform area in the original EO-1 scenes. The column statistics and the global statistic were used to build a ratio factor for each detector:

$$DN_{corrected(\lambda)} = DN_{\lambda} \left(\frac{Mean_{Global}}{Mean_{Detector}} \right) \quad 4-19$$

The above expression scales each pixel value by the ratio of the globally derived mean value and the detector's response. As a result of implementing the above equation, the variability in the detectors' response across track over the dark waters was 22% reduced.

The Hyperion and ALI images were geometrically slightly off relative to the L7 and the bathymetry chart obtained from the NOAA's geophysical database center. A second order polynomial function through selecting conjugate ground control points was implemented to correct the EO-1 scenes relative to the L7 imagery. The geometrically corrected L7 data was further assessed against the linear features, i.e., river mouth, shoreline, derived from the bathymetry map.

4.6.3 Atmospheric Compensation

After destripping the EO-1 imagery, the two images, in units of digital counts, were converted to the TOA radiance quantities by applying gain and offset coefficients. Although L7 calibration coefficients are well known for the scene, the Hyperion coefficients obtained from the metadata appeared to be outdated. A new set of coefficients [McCorkel, 2011] was applied to the Hyperion scene. The new, updated coefficients seem to improve the TOA radiance curve; however, the retrieved surface reflectances obtained via applying Eq. 3-25 along with the MODTRAN-derived atmosphere parameters, were not accurate when compared to the *in situ* measured spectra. More specifically, the derived surface reflectances were higher than the measured surface reflectances. Such preliminary results encouraged an ELM-based atmospheric approach in which the sensor's calibration issues are no longer an impediant factor (Section 4.4.2.1). Using the ELM technique for the Hyperion, ALI, and L7 imagery minimizes the inconsistencies due to the calibration issues and forces the relative retrieval errors to be associated solely with the sensors' capabilities.

The ELM technique was conducted based on the modeled and the *in situ* measured surface reflectance spectra in the deep and the shallow waters, respectively. The deep-water surface reflectance was modeled using the Hydrolight code provided with the MODIS-derived chlorophyll-a concentration (CHL $\sim 1 \mu\text{g}/\text{l}$), the average Lake's chlorophyll-a specific absorption, and the image acquisition geometries. The surface reflectance measured in the river mouth was also utilized as the bright target. The band-specific regression equations specified for a small range of radiance values should adequately compensate for the atmospheric effects in our study area (Section 4.4.2.1). The ELM technique was implemented for each dataset independently. The modeled and the *in situ* measured reflectances (Figure 4.14) were spectrally resampled to the response functions of each sensor

to represent the sensor-specific hyper/multi-spectral surface reflectance values (Eq. 3-30). Since the NIR channels of Hyperion over the study area were dominated by noise, it was decided to restrict our study to the visible bands. Therefore, 31 spectral bands covering 420-725 *nm* was employed for the constituent retrieval task. The Hyperion spectral bands were integrated over the OLI, ALI, and L7's RSRs to simulate their responses. Consequently, the five datasets, including the Hyperion, the S-OLI, the S-L7, the S-ALI, and the original L7, were made available to the retrieval algorithm.

4.6.4 Constituent Retrieval

In order to quantify water constituents on a pixel-by-pixel basis, the Hydrolight code is utilized. Hydrolight is a time-independent, plane-parallel radiative transfer model, which predicts the radiance distribution of the light field within and out of a water body [Mobley, 2008].

4.6.4.1 Hydrolight Initialization

The model is provided with the wavelength-dependent IOPs including scattering and absorption coefficients of CHL and TSS as well as the CDOM absorption. The measured absorption coefficients together with the estimated scattering coefficients (Section 4.3.3.1) were supplied to the code to populate the LUT. The standard Pop-Fry absorption and scattering coefficients of pure water are used for this study. Based on the earlier experimental attempts, the 1.8% Fournier-Forand backscattering phase functions for CHL and TSS were adopted for this study where moderately turbid waters were investigated. It is assumed that the measured/estimated IOPs represent the average spectra for the entire study area.

4.6.4.2 LUT Generation

The procedure followed here is based upon the principles described in [Raqueno, 2003] and shown in Figure 4.36. Raqueno, 2003, tested this approach on HSI imagery, i.e. the Airborne Visible/Infrared Imaging Spectrometer (AVIRIS) dataset, for the Rochester Embayment. By fixing the IOPs and the environmental conditions, an LUT of various combinations of water constituents was populated in a 3D parameter space by varying concentrations of CHL and TSS and a_{CDOM} at 440 *nm* to model wide spectrum of water

types. Associated with each triplet of the constituents, a modeled r_d (just above the water) is generated using a single forward simulation. Many simulations are needed to find the modeled spectra for all of the combinations of water constituents representing a broad range of water types. Here, a very finely sampled LUT is designed to minimize any possible errors due to optimization techniques to be applied subsequently. The increments for CHL and TSS concentrations were chosen to be $0.1 \text{ } \mu\text{g}/\text{l}$ and $0.05 \text{ g}/\text{m}^3$ whereas the CDOM absorption was scaled via applying multiplicative factors incremented by 0.2 [unitless]. The CDOM absorption at 440 nm , $a_{CDOM}(440) = 0.13 \text{ m}^{-1}$, measured in river waters, was treated as the basis and scaled within the range 0.1-1.0. In other words, by constraining $a_{CDOM}(440)$, it was assumed that the average *in situ* measured CDOM absorption spectrum in the river mouth (banks) exhibit the highest possible absorption due to the dissolved organic matter. This was done to avoid confusion in the simultaneous retrieval of concentration of CHL and CDOM absorption. The best combination of water constituents for an image pixel is the one that gives rise to a minimum disparity between the modeled r_d and the one derived for the associated image pixel after atmospheric correction (Section 4.6.3). In order to assess the best fit for each pixel, the cost function (J) defined as following has to be minimized:

$$J = \sum_{\lambda} w(\lambda) (r_d^m(\lambda, +0) - r_d^o(\lambda, +0))^2 \quad 4-20$$

With $r_d^m(\lambda, +0)$ being the modeled surface reflectance just above the water surface, $r_d^o(\lambda, +0)$ is the image-derived surface reflectance, $w(\lambda)$ is the weighting function, which stands for the band-specific SNR (Figure 4.35), and λ representing the number of wavelengths. The continuous modeled $r_d^m(\lambda, +0)$ with increments of 5 nm were spectrally integrated (Eq. 3-30) over the responses of the desired sensors, i.e., Hyperion, OLI, ALI, and L7. The relative spectral response of Hyperion was modeled as Gaussian functions each of which characterized with band-specific full-width-half-maximum (FWHM). By discarding the very short, blue bands of Hyperion, 31 spectral channels ($437 < \lambda < 732 \text{ nm}$) were available to measure the similarity of a simulation result to a pixel's spectra. The corresponding number of channels for the multispectral systems is four for OLI and ALI, and three for the L7.

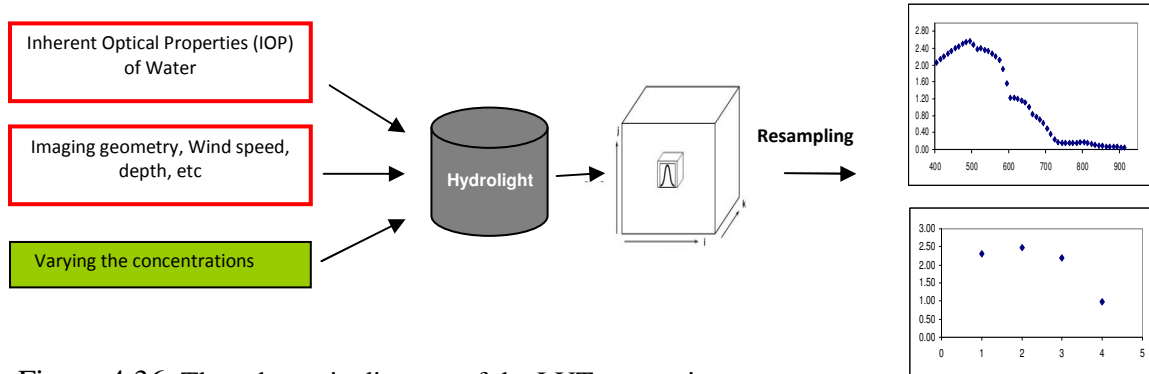


Figure 4.36. The schematic diagram of the LUT generation

The weighting function, i.e., $0 < w(\lambda) < 1$, is the spectral-dependent SNR values normalized to its maximum (eg. SNR @ $\lambda = 498 \text{ nm}$ for Hyperion). The weighting function assigns small weights to the spectral channels attributed with low SNR; thereby reducing their contribution in calculating the dissimilarity against the image-derived spectrum (Eq. 4.20). Although a band-specific, weighing function was applied when calculating the cost function (J) for the Hyperion data, an equally weighted function was adopted for the multispectral images.

Prior to implementing the LUT search, the spectral bands of the pixels with negative values, due to the low SNR and quantization rate, were set to zero allowing the pixels to participate in the retrieval process. Although a limited number of water samples were taken at the river mouth for validation purposes, the Hyperion-derived concentration maps are treated as truth permitting a robust accuracy assessment throughout the study area. In other words, the Hyperion-derived concentration maps are regarded as the best-case scenario achieved with a remote sensing system. For the further crosscheck of the CHL products, the Aqua (MODIS)-derived CHL maps were also used as a reference.

4.6.4.3 Optimization

A similar approach as in Section 4.5.3.3 was applied to search the LUT for the optimal solution. In order to find an optimal consistency between all of the Hydrolight-derived spectra $r_d^m(\lambda, +0)$ and that of an imaged pixel, Eq. 4-20 has to be minimized. With the LUT populated in the previous step, an optimization routine was developed in Matlab to search

and find the global minimum that best agrees with a pixel's spectra. For each image pixel, this routine first finds a subset of simulation results that satisfy a threshold and then uses a simplex search technique within this subset to allocate the most similar spectra (curve) to that pixel. Associated with the matched spectrum, there exist a triplet of water constituents, i.e., (CHL, TSS, a_{CDOM}), assigned to the pixel. It is recognized that the errors associated with the optimization technique due to the discretizations of the parameter space are minimal because of the small step sizes specified for the three components when forming the LUT.

4.7. Concluding Remarks

In this chapter, the methodology required to achieve the objectives defined in the Chapter 2 was described. First, we began by explaining the cross-calibration approach that was utilized to compare the calibration status of L7 with Terra-MODIS over deep, dark waters. It was stated that the most crucial step in performing the cross-calibration task over bodies of water is to properly account for the differences in the response functions of the two systems. In the second study, our proposed approach for integrating Landsat with the hydrodynamic model was elaborated. Prior to conducting the localized simulations, lake-wide simulations were launched to capture the circulation pattern in terms of its current velocities and thermal structure. After stabilizing the model, it is first calibrated in the thermal domain using the Landsat-derived surface temperature maps. The constituent retrieval is done by coupling the Hydrolight code with the ALGE model. In the third case study, a physics-based constituent retrieval approach was described to demonstrate the improvement levels of the OLI sensor over case II waters. The OLI data simulated from a Hyperion dataset will be compared with the existing Landsat, the ALI instrument, and Hyperion in this constituent retrieval task. This cross-comparison is made to thoroughly investigate how the OLI's enhance feature can aid in mapping water quality parameters in case II waters.

Chapter 5

5. Results

In this chapter, the results pertaining to the approach described in the previous chapter are presented. In order to be able to retrieve the water constituents over any type of water using remote sensing techniques, the desired imaging system has to be validated with regard to its calibration status. The analysis regarding the calibration status of the L7 instrument is given in Section 5.1. In this subsection, the historical calibration of L7 relative to that of Terra-MODIS over deep, dark waters is explained. The uncertainties associated with the calibration of L7 are assessed in the retrieval of surface reflectance and water constituents when physics-based models are utilized for atmospheric correction. The results of the L7-model integration are discussed in Section 5.2. Our proposed approach implemented for three different sites in various timeframes is evaluated and the sources of errors associated with the model are addressed. Finally, the results obtained to demonstrate the capabilities of the OLI sensor over the Niagara River plume draining into Lake Ontario are described in Section 5.3. The water constituent concentration maps drawn from the L7 instrument were compared with those gained from the Hyperion and the ALI instruments aboard EO-1. The analysis is comprised of evaluating the retrieval errors associated with the multispectral systems, including L7, simulated OLI, simulated ALI, simulated L7, and ALI relative to the Hyperion-derived concentration maps as references. The retrieval errors are also linked to the systems' characteristics, i.e., radiometric fidelity and band setting.

5.1. L7-MODIS Cross-calibration

The results of the cross-calibration of L7 and Terra-MODIS are presented in this section. While the cross-comparison over dark waters are given for the entire life time of the two missions, the L7-MODIS relative calibration over the RVPN site is also presented for only

the past few years, i.e., 2008-2011. The latter study aids in validating our findings over the dark waters in the above timeframe as compared to the recent findings

5.1.1 Over-water Cross-calibration

The historical trend study is obtained through calculating the percent differences between the mean values of the corresponding ROIs throughout 2000-2011. Figure 5.1 shows the long-term trends in the relative differences of L7 and Terra-MODIS obtained over the optically stable waters of Lake Tahoe (squares) and the Tr-Ar (triangles) sites. For completeness, the relative differences for the NIR band are also presented. The percent differences $\left(\left(\rho_{TOA}^{L7} - \rho_{TOA}^{MODIS}\right) / \rho_{TOA}^{MODIS}\right) \times 100$ are given in units of TOA reflectance (%), which translate into approximately similar percentage values in the TOA radiance domain.

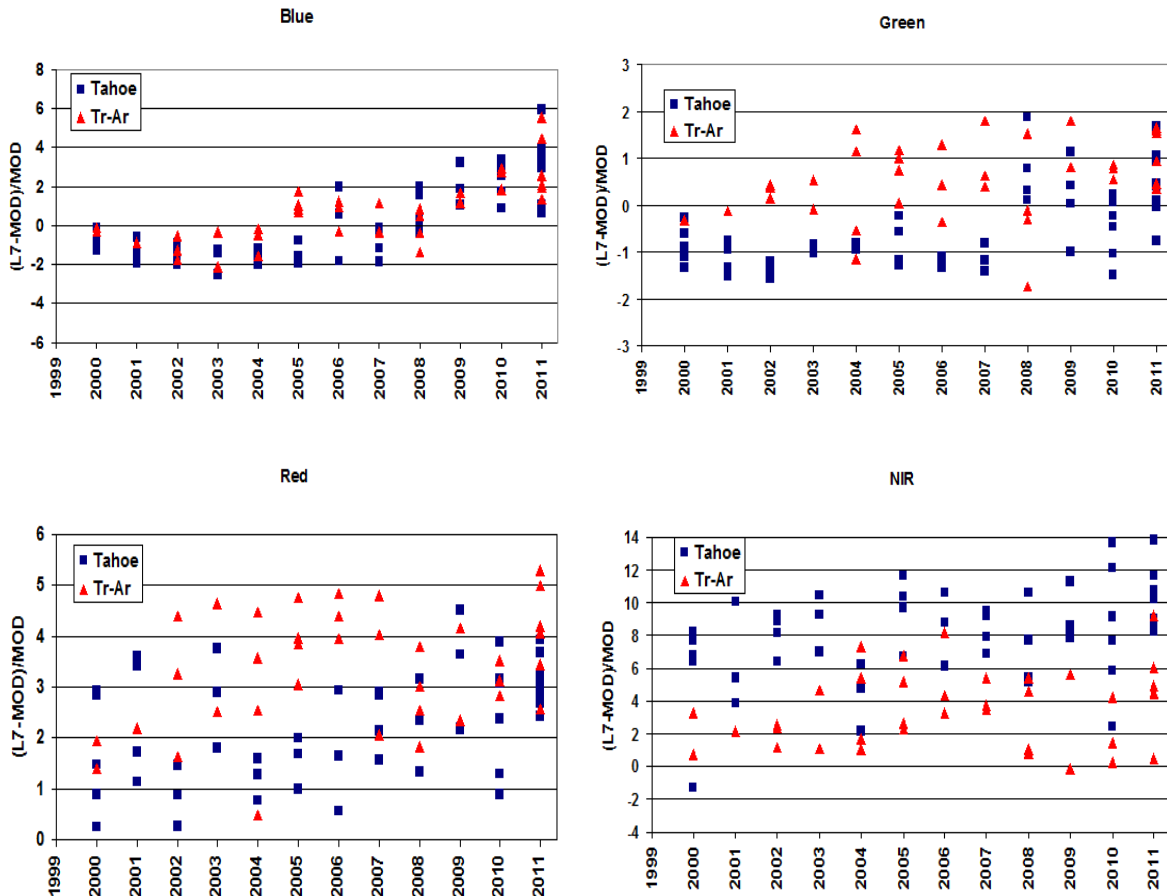


Figure 5.1. The historical cross-calibration trends of the relative differences between L7 and Terra-MODIS computed for Lake Tahoe and the tropical-arid (Tr-Ar) sites. The calibration differences in the blue and the green bands have increased in the recent years. The percent differences are expressed in units of TOA reflectance.

The average radiance values [$W/m^2 sr \mu m$] of the MODIS data for Lake Tahoe are 44.5, 19.8, 8.9, and 2.6 while the corresponding levels for the Tr-Ar sites are 54.2, 26.4, 13.6, and 4.5 for the VINR bands. It appears that L7 consistently exhibits higher responses in the red and the NIR bands in its entire lifetime whereas its response, on average, is smaller during 2000-2007 for the blue and the green bands. The L7's blue response has been slightly lower, i.e., -0.75%, on average, throughout most years, i.e., 2000-2007. However, the disparity between the sensors in this band increases, on average, up to +2.2% during the recent years, i.e., 2008-2011. This considerable change is related to the degradations in Terra's scanning mirror, which results in increased sensitivity to polarization, and in its onboard calibrators [Kwiatkowska *et. al.*, 2008; Xiong, 2011]. The significant Rayleigh scattering in the blue portion of the spectrum leads to highly polarized signals at the top of the atmosphere. Therefore, such errors are expected to be less important in the other visible bands [Kwiatkowska *et. al.*, 2008], although a discernable increase in the average difference in the green band is apparent as well. The L7's green band exhibits a rather stable trend with an average relative difference of -0.45% in 2000-2007. The overall trend in bias, however, shows a slight, gradual increase during the recent years. The relatively large coefficient of variation, i.e., $CV > 150\%$, associated with this band likely corresponds to the cumulative errors in estimating the surface reflectance (r_d) and atmospheric conditions, which lead to erroneous α_{λ_0} ratio (see Section 4.2.4). This is, in particular, the case for the Tr-Ar sites. It is important to note that there exist some signal-dependent differences in this band where the average disparity for the Tr-Ar sites is slightly higher than those measured for Lake Tahoe, i.e., +0.1% versus -1.12%. A fairly uniform bias was found in the L7's red band, on average, +2.27% from the post-lunch to the very recent years. This is the most stable trend among the visible bands as the CV remains below 40% in the entire mission. A +8.2% average bias was observed over Lake Tahoe for the L7's NIR response. Similar to the green band, there is a noticeable signal dependency in the trends with greater differences for lower signal levels corresponding to Lake Tahoe. The L7's low SNR over water bodies in the NIR band, i.e., ~ 6 derived from multiple scenes, diminish the ability to characterize the sensors' relative calibration stability. The noticeable scattered nature of the data points in this band ($CV > 210\%$) verifies the speculations regarding the differences introduced due to the slight

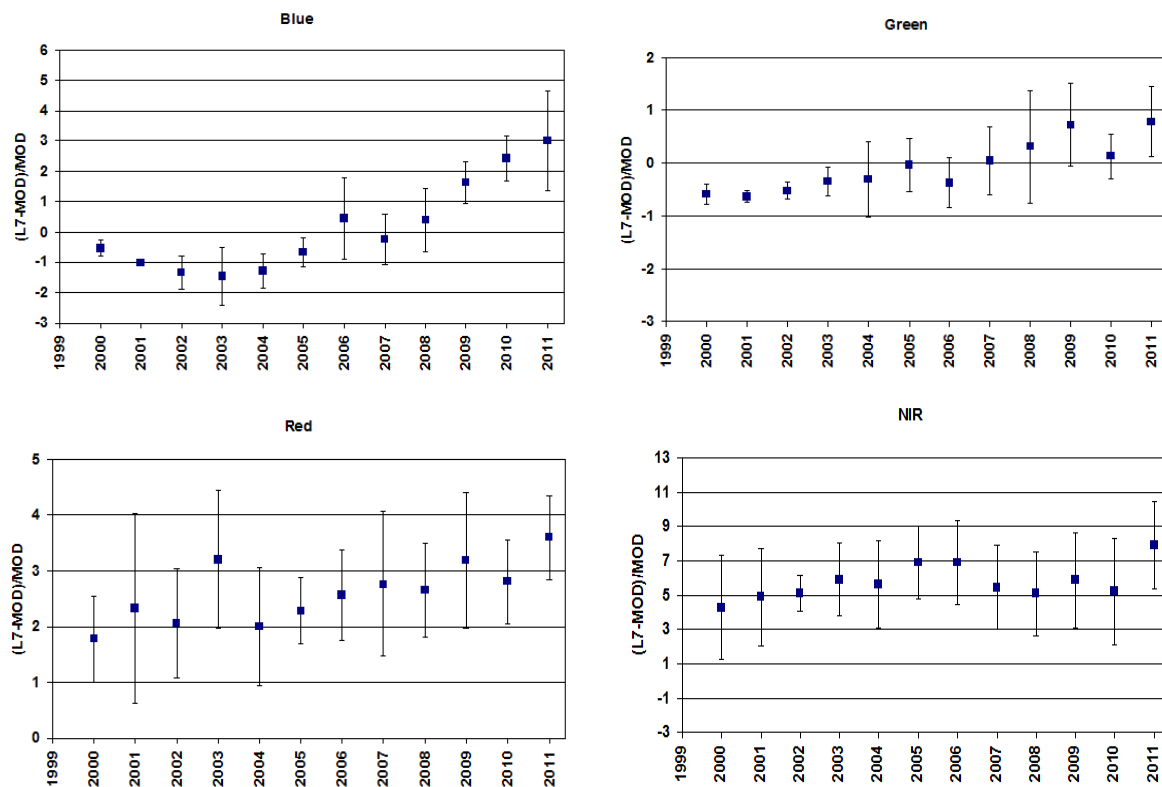


Figure 5.2. The site-independent annually averaged historical cross-calibration trends of the relative differences between L7 and Terra-MODIS. The data points from both sites were averaged for each year. The error bars indicate the standard deviation associated with each year.

variations in the atmospheric conditions between the two overpasses. The calibration issues in this band can yield incorrect retrieval of atmospheric parameters derived from the techniques that use the NIR band to estimate the atmospheric effects [Ruddick *et. al.*, 2000; Wang and Gordon, 2002]. More precisely, although the NIR band does not contribute to the retrieval of water constituents in most water types, the overestimation of the NIR response would directly influence the rigor of the above-noted atmospheric removal methods. In order to better visualize the relative differences over the years, the data points associated for both sites were averaged for each year. Figure 5.2 illustrates the historical trends corresponding to the averaged observations of both sites. The error bars denote the standard deviations associated with each year. The large standard deviations of the data points for the red and NIR bands indicate the inconsistencies in the atmospheric conditions. Based on the averaged observations, -1% and -0.5% differences for the blue and the green bands (2000-2007) and +2.6% and +5.6% disparities for the red and the NIR bands (2000-2011) can be inferred.

In order to obtain better insights in regard to the relative gain and bias between the sensors' responses in each spectral band, the scatterplots of the data points ($n=94$) corresponding to the averaged ROIs in units of TOA reflectance (%) are analyzed (Figure 5.3). As there is less certainty in the recent Terra's calibration status in the blue and the green bands, the data from 2008-2011 were excluded for these bands, i.e., $n=68$. The data points include the ROIs taken from both Lake Tahoe and the Tr-Ar sites. Linear regression models were fitted to the corresponding data points to measure the inconsistencies between the two sensors. The relatively high R^2 , i.e., > 0.99 , for all of the bands suggests a significant statistical robustness of the data points. The most consistent trend was found for the green band with 0.97 slope and +0.15 intercept. The greatest change in the relative gain was obtained for the red band, i.e., slope of 0.96.

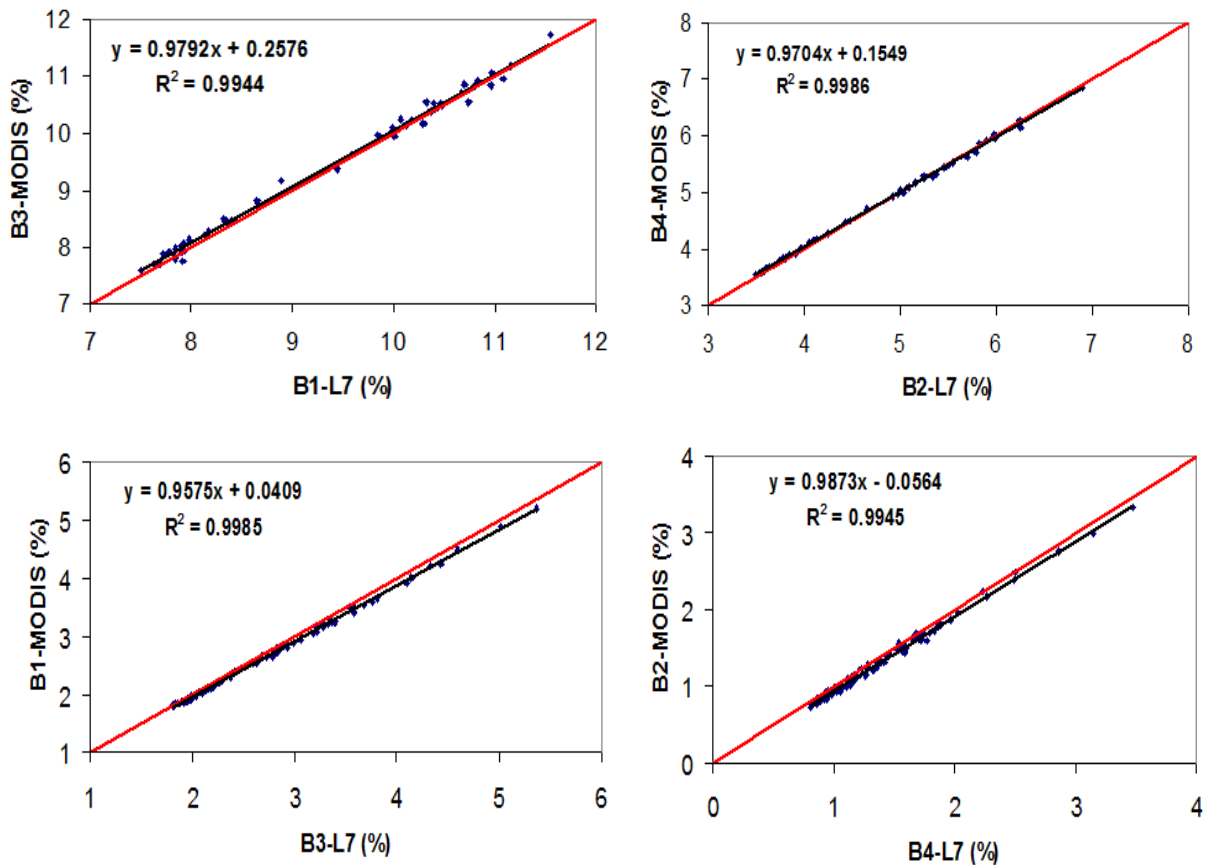


Figure 5.3. The band-specific scatterplots of the averaged ROIs derived from the corresponding L7-MODIS imagery in units of apparent reflectance (%). The 2000-2008 image-pairs only are incorporated. The red line represents the one-to-one slope.

As the signal-level rises in this band, the L7 output increases with a higher rate than that of MODIS. Using the linear regression coefficients of the red band, an average difference level for a 3% TOA reflector can be predicted as +3%, which is close to what obtained in the long-term study for the red band, i.e., 2.27%. As expected from the long-term study, the NIR band represents approximately a uniform difference over a reasonably large signal range, i.e., slope of ~ 0.99 . Based on the two forms of representing the relative L7-MODIS responses, it is inferred that the largest discrepancies in the blue band occur when imaging low signal levels while the red band shows the greatest relative differences in high signal levels. In general, L7 tends to slightly underestimate the blue signal, i.e., $<1\%$, and overestimates the red and the NIR responses up to 2.5% and 5.6%. The relative errors for the green band, although very small, are estimated to be less than 0.5%. In Section 5.1.3, the above-noted calibration uncertainties are treated as bias-only calibration errors in reference to Terra-MODIS as a well-characterized system for dark targets. The calibration errors are applied to several simulated TOA radiance curves to evaluate their effects in the retrieval of the diffuse surface reflectance (r_d) and the water constituents.

5.1.2 Over-land Cross-calibration

A similar procedure to that applied over the dark waters was also implemented over the RVPN site. This study aims at validating our methodology over the dark waters and

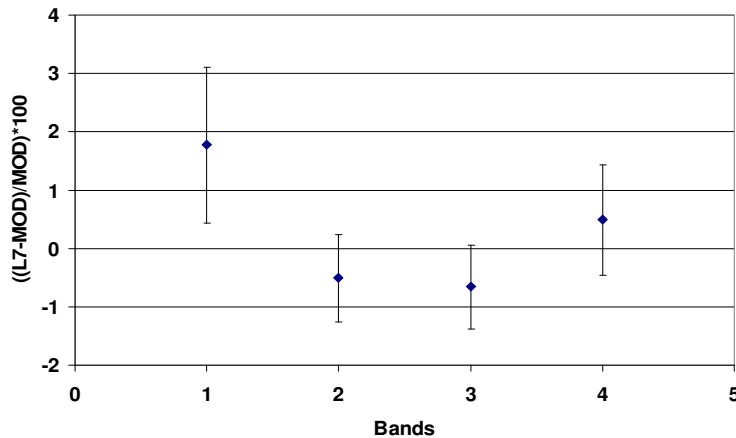


Figure 5.4. The percent differences for the L7-MODIS ROIs over the RVPN site. The error bars indicate the standard deviations associated with all of the ROIs.

demonstrating that the error levels lie within the L7's radiometric uncertainty, i.e., <5%, expressed in the TOA radiance domain. Figure 5.4 shows the average percent differences for a limited number of image pairs (11) acquired during 2008-2011. It is obvious that Terra's degradation in the blue band has significantly boosted the relative difference between the two sensors. The high error bar refers to the uncertainties in the atmospheric conditions. The relatively small positive biases in the green, red, and the NIR bands, i.e., -0.5%, -0.6%, +0.5%, respectively, are well in agreement with the L7's radiometric uncertainty requirements. The above-noted errors translate into -0.4%, -0.6%, and +0.5% difference in the TOA radiance domain whose average values for the RVPN site are 123.1, 133.2, 126.3, 93.7 [$W/m^2 sr um$] for the VNIR bands. The above-noted values were found to be consistent with the recent calibration efforts, which indicate L7's high calibration stability [Czapla-Myers, 2011]. Although due to the shape and magnitude of the RVPN site the differences in the RSRs are insignificant for this site [Teillet *et. al.*, 2007], the RSR adjustment factors were computed and applied for each image pair.

5.1.3 Impact of Calibration Errors on Surface Reflectance Retrieval

As described, in this section the relative calibration differences obtained for L7 are treated as calibration errors. In order to evaluate to what extent such small calibration errors would impact the retrieved r_d , which carries information about the in-water components, a series of sensitivity analyses using the MODTRAN code were conducted. This is a crucial part of this study as L7 is well calibrated for bright targets and the slight mis-calibrations found in this study lie within the L7's radiometric uncertainty.

Table 5.1. The variables applied for the MODTRAN simulation

	Visibility (km)	Type
Aerosol	5-80 (5)	Rural-Maritime-Urban
DOY	150-300 (30)	
	Water Types	
Lake Tahoe	(CHL=0.3, TSS=0)	
Lake Ontario	slightly turbid/mesotrophic	
	Moderately Turbid/eutrophic (CHL=4, TSS=4)	
	Turbid/eutrophic (CHL=10, TSS=10)	

Due to weak signals arising from a body of water together with the L7's low SNR, the calibration errors, even small, can contribute to erroneous retrieval of r_d . The calibration uncertainties introduce errors in the retrieved r_d only when physics-based models are used to remove atmospheric effects. Here, the band-specific bias-only errors, obtained for L7 in Section 5.1.1, are applied to approximate the errors when retrieving r_d .

In order to generalize our study, four different water types (Table 5.1), representing Lake Tahoe and Lake Ontario, USA, waters, were propagated through the average upper-air atmospheric columns of the two sites. The modeled reflectance spectra are illustrated in Figure 5.5. For each water type, various aerosol models and concentrations, specified by the visibility parameter, for different DOYs were included to capture a wide variety of signal levels and atmospheric conditions. Table 5.1 contains the range of the variables adjusted for the simulations. The MODTRAN-derived total sensor-reaching radiances, $L_t(\lambda)$, were then adjusted with the bias-only calibration errors as following:

$$L'_t(\lambda) = [1 + \beta(\lambda)]L_t(\lambda) \quad 5-1$$

where $\beta(\lambda)$ represents the band-specific biases, found in the previous section, and $L'_t(\lambda)$ is the un-calibrated TOA radiance. In other words, the simulated spectra, resampled to the L7's RSRs (Eq. 3-30), were adjusted -1%, -0.5%, +2.5%, and +5.6% in the blue, green, red, and the NIR bands, respectively. Then, the governing remote sensing equation (Eq. 3-25)

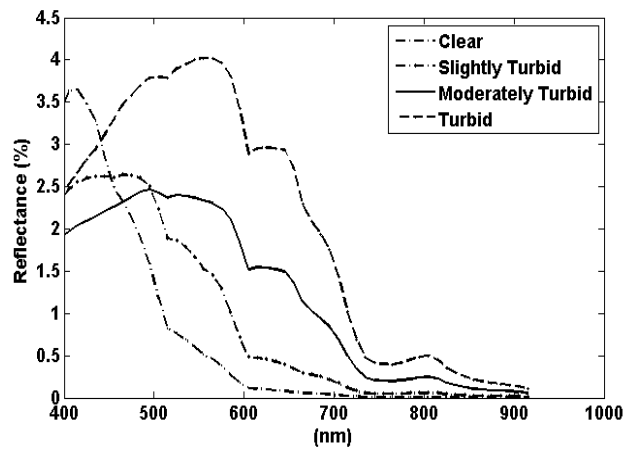


Figure 5.5. The modeled surface reflectance (R_d) for different water types.

was solved in the inverse mode (ignoring effects from sun glitter and whitecaps, which were also ignored in the forward mode) to retrieve the diffuse surface reflectance (r_d):

$$L'_t(\lambda) = [E_{s\lambda} \cos(\sigma_s) \tau_1(\lambda) r_d(\lambda) / \pi + L_{d\lambda} r_d(\lambda)] \tau_2(\lambda) + L_{u\lambda} + \rho_F \tau_2(\lambda) L_{d\lambda} \quad 5-2$$

Where $L'_t(\lambda)$ denotes the total, un-calibrated TOA radiance [$W / m^2 sr \mu m$] while other components are identical to Eq. 3-25. The last term is an additional component that takes into account the sky glint resulting from diffuse downwelled sky light reflected off the water surface. The Fresnel reflection coefficient is generally assumed constant for all of the spectral bands ($\rho_F \approx 0.02$). However, in this study, it is assumed that the modeled surface reflectance spectra, obtained from the Hydrolight code, are glint-free and we attempt to retrieve these spectra through solving Eq. 5-2 in the inverse mode. All of the components in Eq. 5-2 are obtainable via MODTRAN simulations except the $r_d(\lambda)$. After applying the bias-only errors (Eq. 5-1), Eq. 5-2 can be re-written to solve for the un-calibrated $r_d(\lambda)$, i.e., $r_d^U(\lambda)$, for each simulation. The retrieval errors are calculated using $\left| \frac{r_d^U - r_d}{r_d} \right| \times 100$. Figure 5.6 shows the retrieval errors, in units of percent reflectance, for different aerosol types and visibility (VIZ) when Lake Tahoe's reflectance was retrieved. For brevity, the results from simulations with urban aerosol are not presented. The errors are shown for each individual band for different aerosol visibility. The -1% error in the blue channel for a 2.5% water-leaving reflectance (Figure 5.5) translates to -6.2% error in the retrieved reflectance value at VIZ=25 km.

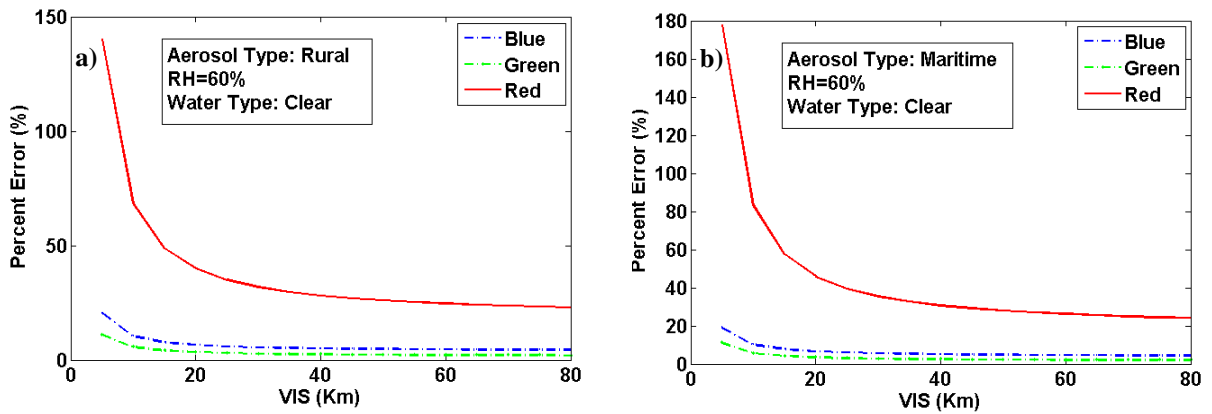


Figure 5.6. The band-specific retrieval errors derived for different aerosol types and visibility over Lake Tahoe waters.

According to the additive/subtractive nature of the calibration errors, L7 always tends to underestimate the retrieved r_i in the blue and the green bands (see Figure 5.7-b). As seen in Figure 5.6, a highly turbid atmosphere with significant aerosol content, resulting in large $L'_i(\lambda)$, induces larger retrieval errors. Moreover, due to the nature of maritime aerosol particles, i.e., strong scattering properties, the associated error levels are greater than that of rural aerosols. The retrieval errors were obtained by assuming a relatively dry upper-air atmosphere in the Lake Tahoe region. The NIR band was excluded in this analysis because it solely carries information about the water surface and is not commonly used for the water

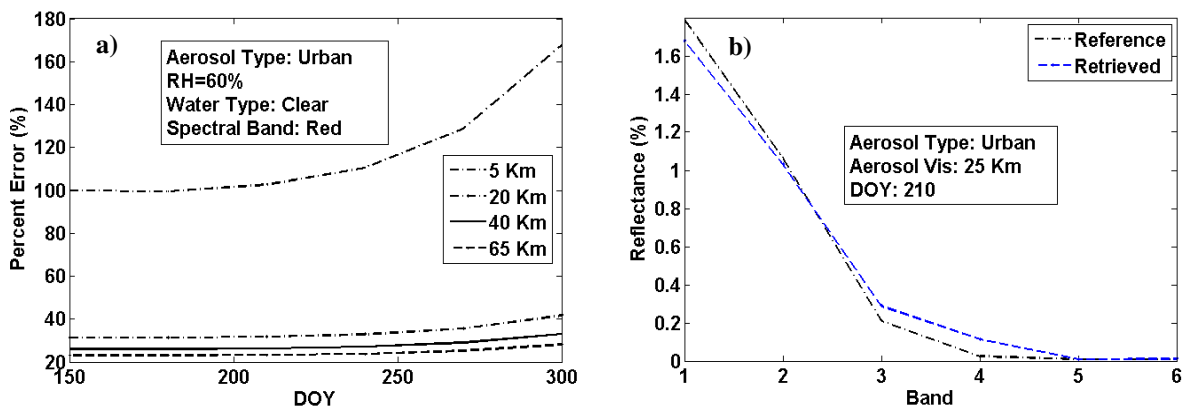


Figure 5.7. The simulation results for Lake Tahoe's clear waters. The percent errors shown for the red channel at different times of the year when various aerosol visibility are present (a). The right panel (b) illustrates the reference and retrieved reflectance curves for DOY=210 and a typical aerosol visibility (VIZ= 25 km).

constituent retrieval over clear waters. Figure 5.7-a illustrates the retrieval errors for different DOYs in the red band, which denote how the errors would change relative to the total, solar irradiance. As the solar radiation level decreases, which implies lower signal strengths from the water column, the retrieval errors increase. This indicates that the retrieval errors for the red channel at VIZ=25 km in mid fall is nearly 30% larger than those in mid spring/summer. The error levels are clearly much greater in turbid atmospheres. Figure 5.9-b shows a reference and a retrieved surface reflectance curve for a typical atmospheric condition in mid July, i.e., DOY=210. It is inferred that the slight calibration errors in the blue and the red bands, i.e., -1% and +2.5% respectively, results in errors on the order of -7% and -107% in

the corresponding bands when $r_d(\lambda)$ is retrieved over relatively clear waters. However, the -0.5% error in the green band introduces approximately -6% error in the retrieval process. The significant error level, not listed in Table 3, in the NIR band is attributed solely to the atmospheric composition, i.e., $L_u(835) \gg R_d(835)$. Figure 5.8 and 5.9 show the similar sensitivity analysis for the Lake Ontario's turbid waters (Table 5.1). In general, the percent errors are smaller than those obtained for Lake Tahoe. This is related to the greater number of photons emanating from turbid waters because of in-water scattering phenomena. In other words, significant aerosol content adversely affects the surface retrieval process.

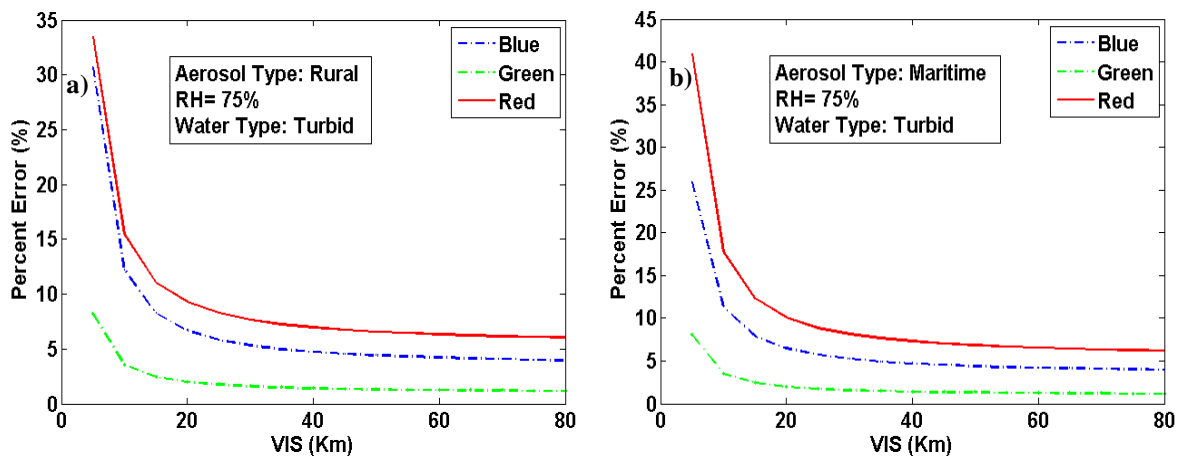


Figure 5.8. The band-specific retrieval errors derived for different aerosol types and visibility over Lake Ontario waters.

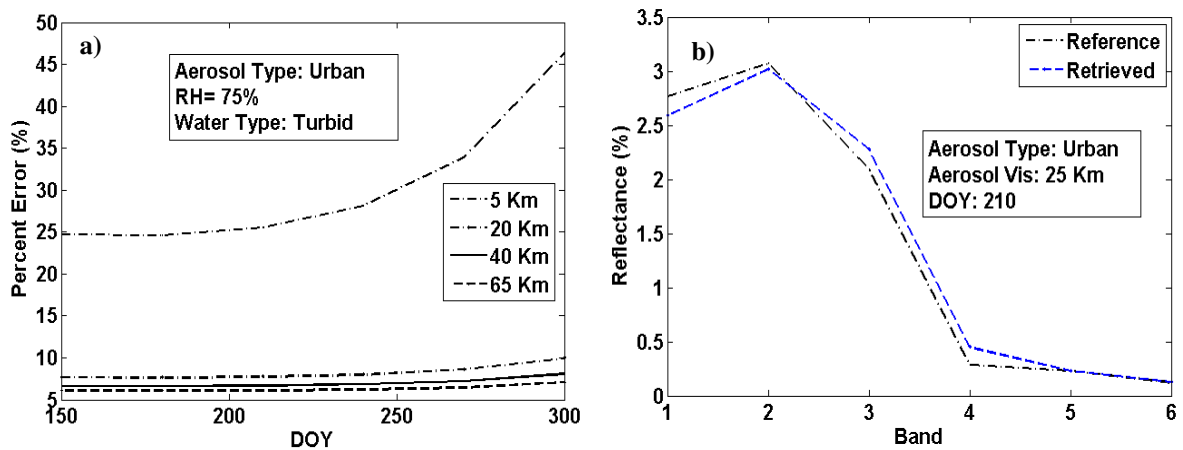


Figure 5.9. The simulation results for Lake Ontario's turbid waters. The percent errors shown for the red channel at different times of the year when various aerosol visibilities are present (left). The right panel illustrates the reference and the retrieved reflectance curves for DOY=210 and a typical aerosol visibility.

As expected, in both rural and maritime aerosol types the lowest retrieval errors are found in the green band due to its slight mis-calibration issues. The error trends in the red band closely resemble those in the other two bands due to higher signal levels in such waters. An average of 8% error was derived for typical aerosol conditions in mid spring/summer time for the red channel (Figure 5.9-a). The retrieval errors exponentially decrease relative to the increase in the aerosol visibility. This error level reaches 15% in mid fall when the sun zenith angle is high. Figure 5.9-b shows the input $r_d(\lambda)$ into the MODTRAN code versus the retrieved $r_d(\lambda)$ after incorporating the calibration errors. In such turbid waters (Table 5.1), the calibration errors cause an underestimation in the blue on the order of 0.18 units of reflectance, i.e., approximately 6% error (Figure 5.9-b). The highest percent errors, 57%, are predicted for the NIR band where only 0.28% water-leaving reflectance is modeled as input. Table 5.2 summarizes the percent errors associated with the reflectance retrieval tasks for different types of waters at DOY=210 with VIZ= 25km. The average errors of -7%, -3.5%, and +41% are derived in the blue, green, and the red bands, respectively, for all water types. The associated values for eutrophic, moderately turbid, waters (ignoring errors associated with Lake Tahoe in Table 5.2) are -7%, -2.5%, and +20% in the visible bands. Regardless of their direction, the small calibration errors, i.e., 1.3%, on average, for the visible bands obtained in Section 5.1.1, amount to noticeable inconsistencies when retrieving the surface physical properties. It should be noted that the Lake Tahoe's upper-air atmosphere is less humid than that in Lake Ontario. This implies that for identical water types higher retrieval errors are expected for Lake Ontario. The results obtained in this section are well in agreement with [Gordon, 1998] wherein the errors in the retrieved $r_d(\lambda)$ are quantified to be more than five times greater than those in the TOA reflectance/radiance.

Table 5.2. Band-specific percent errors (%) for different water types

		Blue	Green	Red	NIR
Lake Tahoe		-6.7	-6.1	+107.4	NA
Lake Ontario	Slightly turbid	-8.6	-3.8	+40.1	NA
	Moderately turbid	-6.8	-2.0	+14.1	NA
	Turbid	-6.1	-1.7	+8.5	+57.1

Although remarkable errors, in the relative sense, were found when retrieving $r_d(\lambda)$ in the NIR region, the errors are not applicable in the water constituent retrieval process in most water types unless turbid waters with in-water components of high scattering nature are studied. The noticeable calibration errors in the NIR band would significantly influence the atmospheric compensation methods that rely upon characterization of the atmosphere through this band.

5.1.4 Impact of Calibration Errors on Concentration Retrieval

A case study was conducted to quantify how the calibration errors ultimately influence the retrieval of the concentrations of water constituents. To do so, atmospherically corrected L7 imagery acquired over the Niagara River plume discharging into Lake Ontario was employed. The spectral reflectance, the ambient optical properties of the turbid waters, and the environmental conditions were measured concurrent with the satellite overpass, i.e., row/path 30/18, at 11:56 am EST on October 19th 2010 (Section 4.6.1). The ELM technique described in Section 4.4.2.1 was used to atmospherically correct the image. In order to test the impacts of the mis-calibrations, the L7-derived surface reflectance map was adjusted by applying Eq. 5-1 to generate the un-calibrated L7-derived surface reflectance, i.e., $r_d^U(\lambda)$. Considering the range of the concentrations in the study area, the average of the retrieval errors for the slightly turbid and moderately turbid waters listed in Table 5.1 (the second and the third rows), i.e., -7%, -2.5%, +26% for the visible bands, were considered. To retrieve the concentrations of CHL and TSS, an LUT-based technique followed by a spectral optimization was employed as described in 4.6.4. Due to the low sensitivity of L7 to the short, blue region of the spectrum, the third optically active component of the water (CDOM) was discarded in this case study. As a result of the model-matching technique, the concentration maps for the original L7, i.e., CHL (O) and TSS (O), and the un-calibrated L7 data (CHL (U) and TSS (U)) were produced (Figure 5.10). The concentration maps are slightly different from the results presented in Section 5.3.1. This is because, here, the CDOM absorption at 440 nm was held constant whereas all of the three in-water components were simultaneously retrieved in that section. In order to visually inspect the differences in the retrieved concentrations throughout the study area, error maps (*EMAPs*) [%] were produced using the following expression:

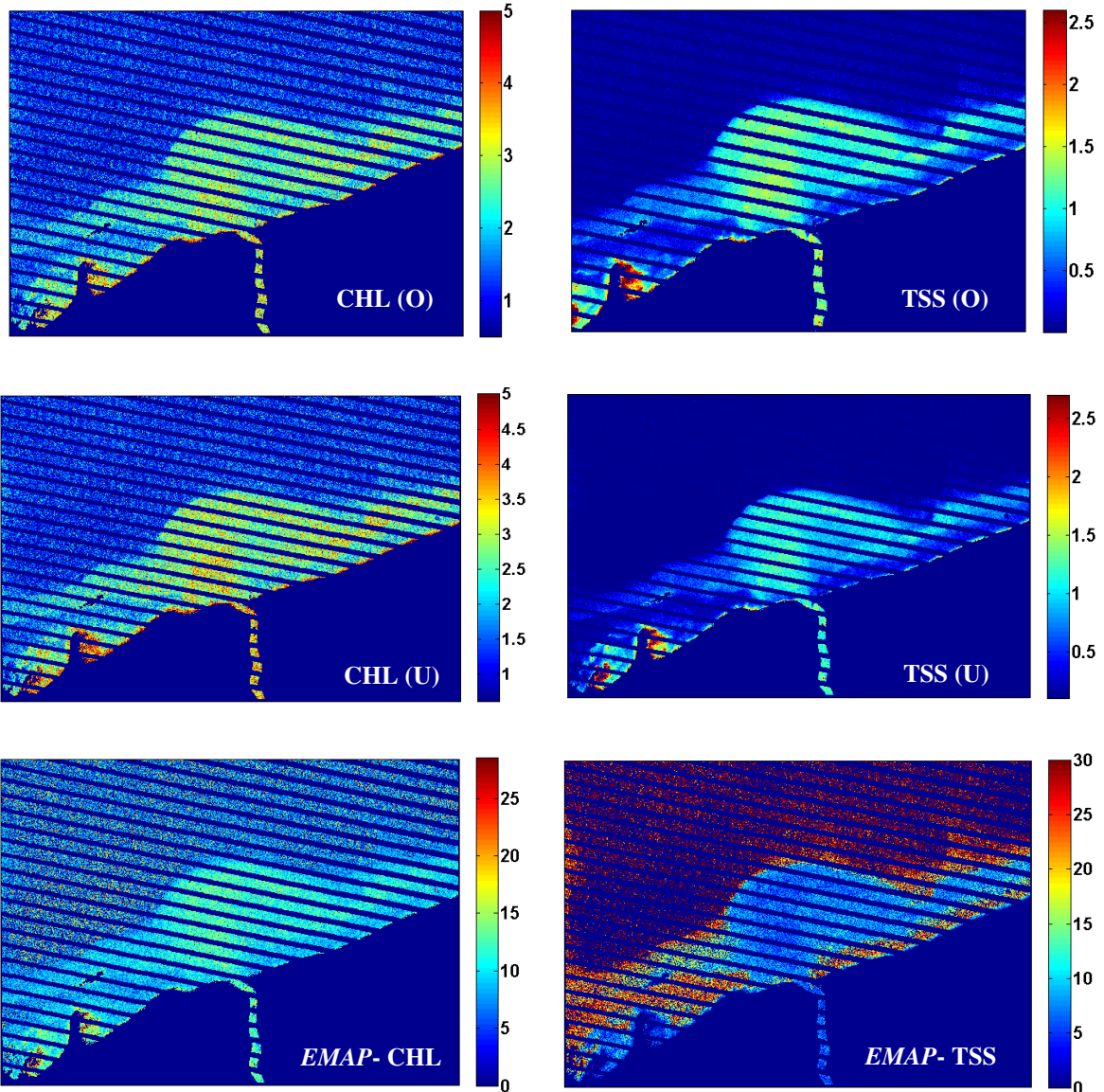


Figure 5.10. The CHL and TSS concentration maps derived from the originally observed L7 data (O) and the simulated un-calibrated imagery (U). The bottom frames show the *EMAPs* [%] calculated using Eq. 5-3. The calibration errors cause overestimation and underestimation of CHL and TSS concentrations, respectively.

$$EMAP_{i,j} = \left| \left(CHL_{i,j}^U - CHL_{i,j}^O \right) \left(CHL_{i,j}^O \right)^{-1} \right| \times 100 \quad 5-3$$

where i and j are the pixel indices and the superscripts O and U stand for original and un-calibrated CHL maps. A similar expression for analyzing the TSS map was also applied. The corresponding *EMAPs* are illustrated in Figure 5.10. The average CHL and TSS

concentrations derived from the original L7 data over the plume area are 3.5 ug/l and 1.5 g/m^3 , respectively. Overall, it was revealed that the current L7 data, if corrected for the atmospheric effects via physics-based models, results in, on average, 10% uncertainty in the concentration retrievals. L7 with such small bias-only calibration errors, i.e., -1%, -0.5%, 2.6% for the three visible bands, overestimates the CHL concentrations as high as 12% in the vicinity of the river mouth whereas it underestimates the TSS concentrations, i.e., on average, 6%, in the same area. In general, such a trend in the overestimation of CHL retrieval comes largely from the reduced surface reflectance in the blue and, to a lesser extent, in the green bands. In spite of the 26% increase in the red channel's reflectance due to mis-calibration, the TSS concentration is, in general, underestimated. This is because of the non-linear correlation of the TSS concentration with the L7's visible bands (primarily the green and the red bands). However, the error levels attributed to the TSS concentrations in the non-plume waters, where the signal level in the red band is approximately 50% of that in the plume area, reach as high as 30% (Figure 5.10), which can be attributed to the poor radiometric fidelity of L7 and its low SNR. However, the average errors associated with the CHL products over the plume and non-plume areas are nearly similar, i.e., 12% and 7% respectively (Figure 5.10). It should be noted that the magnitude and the direction of the errors in the retrieval of concentrations are site-specific. A high correlation coefficient, i.e., > 0.98 , calculated between the concentration maps derived from the original L7 and the un-calibrated dataset indicates that the spectral-dependent calibration uncertainties introduce only spatially uniform bias throughout the study area i.e., the relative spatial structure of the maps remain unchanged.

5.1.5 Summary

In this case study it was shown that L7 has slight mis-calibration errors relative to Terra-MODIS over the VNIR band. The small disparity between the two sensors was found to be 1%, 0.5%, 2.6%, and 5.6% for the blue, green, red, and the NIR bands. The differences were quantified during the period when Terra-MODIS exhibited reasonable performance, i.e., the 2008-2011 datasets were avoided for the cross-comparison of the blue and the green bands. The above-noted errors translated into 7%, 2.5%, and 26% errors (10%, on average, for the visible bands) in the retrieval of water-leaving reflectance when a physics-based model is

used for the atmospheric compensation. An average atmospheric condition, i.e., rural aerosol, VIZ=25 km, and 65% humidity, was considered for the simulations. By applying the retrieval errors associated to the surface reflectance, a 10% retrieval error, on average, was obtained for the retrieved concentrations of CHL and TSS. The 10% error in our study area is equivalent to 0.3 $\mu\text{g}/\text{l}$ and 0.15 g/m^3 . This error level corresponds to a 10% average error (for the visible bands) in the retrieval of surface reflectance. Assuming that the errors at the sensor level and the surface level are linearly correlated, we can anticipate the acceptable calibration errors when retrieving water constituents. In general, if we assume that a 20% error in the retrieval of concentrations is acceptable for our application, an equivalent 20% error is expected for the surface reflectance retrieval. As shown in this study, since a 1.3% calibration errors resulted in a 10% average error in the retrieved surface reflectance, a 20% error in the reflectance corresponds to approximately 2.5% sensor calibration error (TOA reflectance), averaged over the visible bands. However, this estimate is based upon a typical atmospheric condition. In a turbid atmosphere, the surface reflectance retrieval is subject to higher errors demanding a sensor characterized with smaller calibration uncertainties. In addition, this case study examined the retrieval errors for moderately turbid waters. Provided clear water bodies, such as Lake Tahoe, or oceanic waters, are studied, the calibration errors more significantly affect the retrieval errors. Although spectrally independent average calibration errors were summarized here, it is anticipated that significant calibration errors in the green and the red bands have the largest contribution to the retrieval of TSS when using Landsat 7. For the OLI sensor, the CA band is also very critical in the retrieval of CHL (see Section 5.3).

The impacts of the calibration errors in other water types characterized with different optical properties can dramatically alter the results presented here as the case study. The noisy nature of the concentration maps, particularly in the clear waters, is due to the poor radiometric fidelity of L7 and its low SNR. As the signal level rises, the unrealistic, spatial variations decrease. With the advent of the new generation Landsat (LDCM), it should be possible to achieve more accurate concentration maps with fewer artifacts in both clear and turbid waters. Furthermore, using experimental techniques, such as ELM, for the atmospheric correction, the impacts of sensor calibration errors are minimal.

5.2. L7-Model Integration

In this section the results pertaining to the coupling of the ALGE model, the Hydrolight simulations, and the Landsat imagery are presented. In reference to the methodology, described in the Section 0, a long-term ALGE simulation for each timeframe is carried out to stabilize the model. Following the model stabilization, the ALGE model is first calibrated in the thermal domain and then the calibrated model is coupled with the Hydrolight model to estimate the water-leaving optical field for multiple ALGE simulations conducted for different concentration of sediment and dissolved matter. The results, thus, are described by explaining the model outputs in the following order:

- The long-term simulations for all the periods at each site (Table 4.1)
- The model calibration
- The constituent retrieval in the reflective domain

The model calibration phase and the further procedures were conducted solely for the timeframes when the ALGE model predicted the thermal structure of the water body reasonably well in the model stabilization stage.

5.2.1 Long-term Simulations (Model Stabilization)

In this study, the ALGE model was first allowed to stabilize for an adequate amount of time, i.e., 10 days for the river plumes and approximately two months for the Onondaga Lake simulations. Such long-term simulations are presented for different sites beginning with the Genesee River plume followed by the Niagara River plume and Onondaga Lake simulations.

5.2.1.1 Genesee River Plume

The Genesee plume simulations were carried out for two periods, i.e., July 2009 and October 2009. The number of experiments at this site was limited by the extent of the plume governed by the precipitation levels and the discharge. Besides the inability to fully evaluate the model performance when the river flow represents small discharges ($< 30 m^3/s$), L7 can not resolve the spatial structure of the plume at such fine scales. In order to demonstrate such a limitation, the simulation in October 2009 when the discharge exhibits small values ($< 20 m^3/s$) is presented. Figure 5.11 provides a qualitative way of evaluating the ALGE

performance in such a dry season. The ALGE-derived surface parameters (surface temperature and the particle distribution) are compared to the L7-derived surface temperature map and the reflective radiance field (RGB) obtained from the L7 imagery. Although ALGE predicts a plume stretching westward, no particular thermal pattern is seen in the L7 thermal field (Figure 5.11-c). Instead, a relatively uniform pattern is observed in the L7 data, which has not been modeled through the model. This is due to the relatively low vertical resolution (3 m) of the model for this particular simulation. However, the warmer pattern in the north-northeast part of the domain has been properly predicted through the simulation. By further inspecting the L7 RGB imagery, it is inferred that the bright inshore waters, shown in Figure 5.11-d, are the result of re-suspension due to the breaking waves and the river plume has less contribution to the inshore-offshore color contrast. Furthermore, one should note that

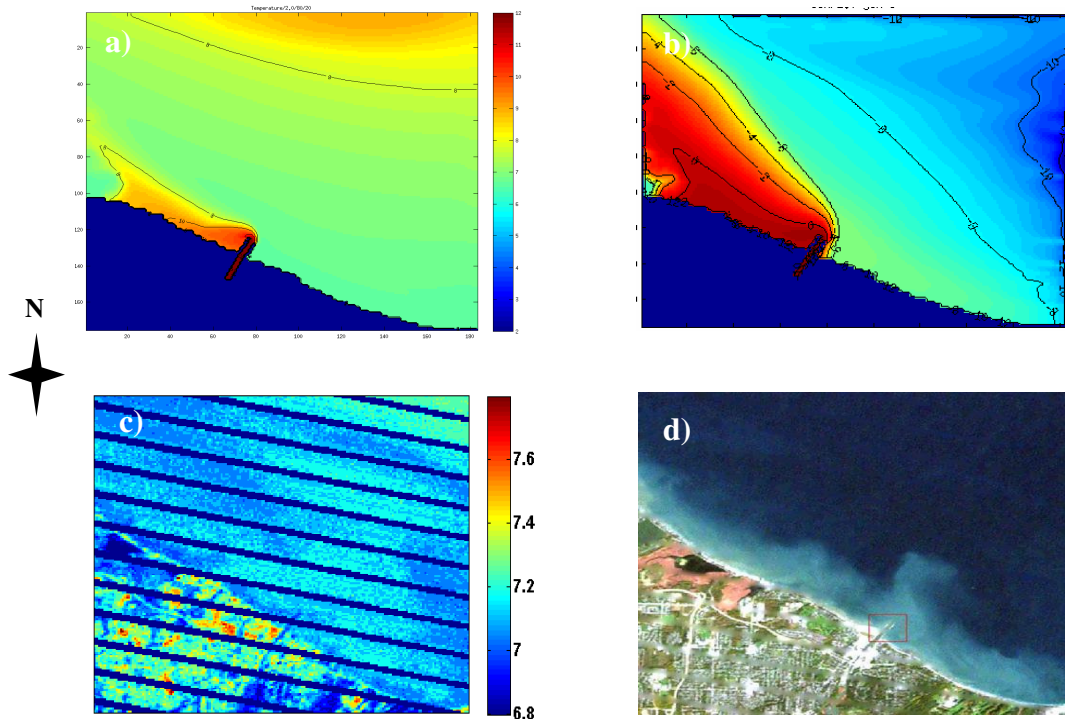


Figure 5.11. The Genesee River plume simulation results for Oct. 2009 along with the L7-derived surface temperature map and the corresponding RGB image

the Landsat image has been radiometrically enhanced to enable distinguishing inshore turbid waters from clear deep waters. Since ALGE, as currently configured, is unable to simulate re-suspension phenomena, the model-generated particle distribution map (Figure 5.11-b)

does not resemble the reference data (Figure 5.11-d). Due to such uncertainties, the model calibration and the constituent retrieval were not carried out for this timeframe.

Figure 5.12 shows snapshots (zoomed areas) of the long-term simulations in the thermal domain for the Genesee River plume in July 2009. In each case the plume along with corresponding wind speed [m/s], wind direction [degrees] and river discharge [m^3/s] are shown. From the plume shapes at different hours, it is understood that a combination of these parameters control the shape of the plume. At the 45th hour, for example, the plume exhibits the largest extent due to the large discharge rate and moderate wind speed. At the hour of 245, although the river discharge (RD) is relatively large, the high wind forcing supersedes the other variables and pushes the plume towards the east without expansion in the lake waters. It should be noted that the wind direction is the direction from which the wind blows. Figure 5.13 illustrates the sediment distribution at the corresponding hours of the simulations as in Figure 5.12 when the particle size and particle density were held constant to

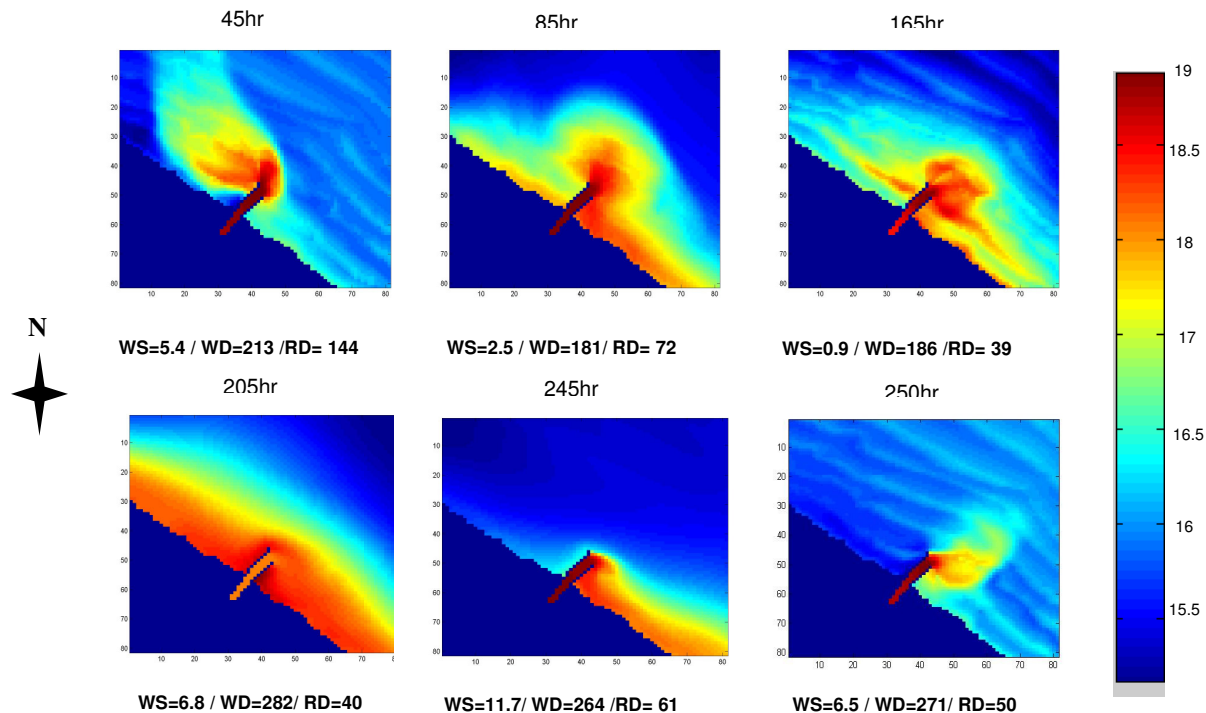


Figure 5.12. The snapshots of the ALGE thermal simulations with various input parameters. Temperature values are in Celsius and WS, WD and RD denote wind speed, wind direction and river discharge, respectively.

4 μm and 2.5 g/cm^3 , respectively. As expected, the particle distribution closely correlates with the thermal plume; however, the sediment load expands further offshore representing low concentrations. In addition, it is evident that the initial sediment concentration within the lake waters is assumed zero and all sediment originates from the river. This causes the non-plume areas to contain low concentrations, on the order of $10^{-7} \approx 0 \text{ gm}^{-3}$, at some particular hours when the discharge rate is low (eg. 250th hour), which may not be true especially in shallow areas (due to breaking wave effects or/and overall sediment concentration in lake water). This confirms the fact that we need to add some background concentration (sediment and dissolved matter) to the ALGE outputs when modeling moderate sized river plumes. The dissolved matter distribution maps (not shown here) closely resemble sediment distributions as one expects. The range of concentrations of CDOM and particles, of course, highly rests

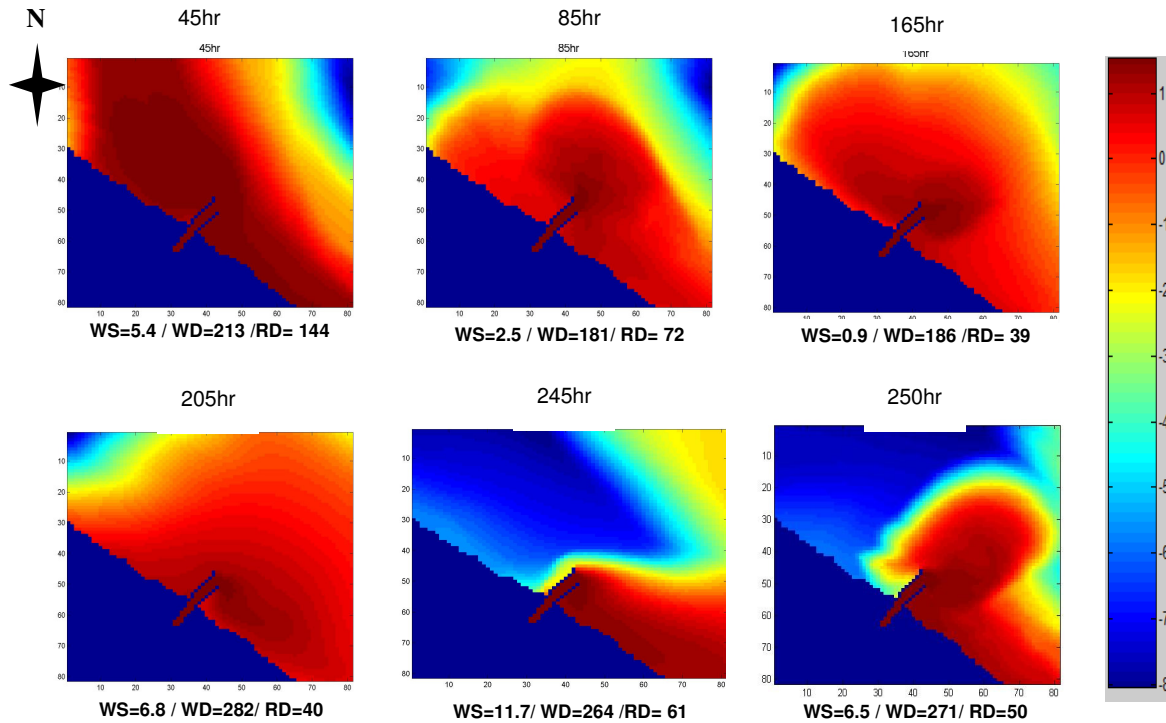


Figure 5.13. The snapshots of ALGE particle simulations with various input parameters. The concentrations are log-transformed in units of g/m^3 . The WS, WD and RD denote wind speed, wind direction and river discharge respectively.

rests upon the initial concentrations, which were chosen to be equal in this case. If we adjust the particle size and particle density to small values then the particle distribution maps tend to duplicate the distribution maps for the dissolved matter. In other words, low settling

velocities drive the particles further offshore in the same manner as the dissolved tracer modeling. It is worthwhile pointing out that although only wind speed, wind direction and discharge rate are described here as main contributors in the modeling process, a combination of all different input parameters such as surface data, radiosonde data and discharge rate as well as the grid size influence the plume simulation.

Figure 5.14 shows the last hour of the long-term ALGE simulation along side the L7-derived temperature map (Figure 5.14-b). Following the long-term simulation, it appears that the ALGE model tends to slightly overestimate the extent of the plume while correctly predicting its orientation towards northeast as derived from the L7 data. Quantitatively, the average RMSE calculated over the plume area was found to be 0.34°C , which resulted from providing the code with the originally observed meteorological inputs.

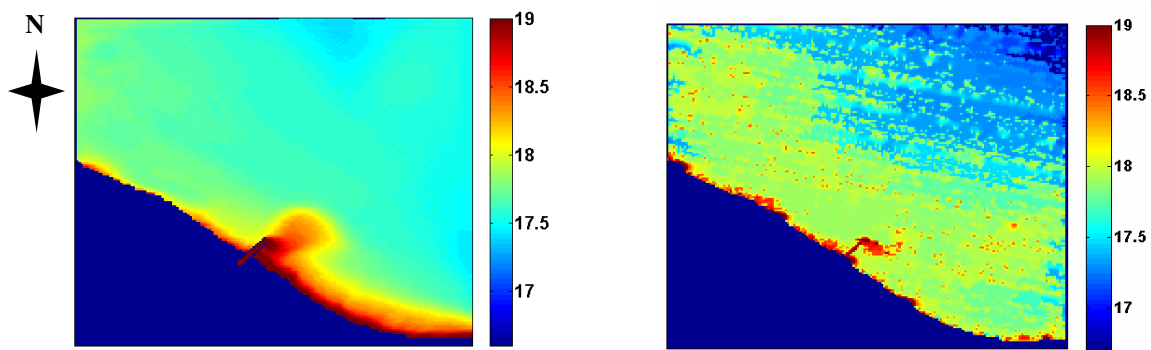


Figure 5.14. The Genesee plume simulation in July 2009 after the long-term simulation (263 hours)

While the shape of the plume has been reasonably modeled, the overall domain temperature in the offshore areas has been predicted slightly colder than the observed surface temperature, i.e., 17.78°C versus 18.17°C , on average. This small disparity is in part due to the inherent differences in the skin and the bulk temperature predicted through the model. Moreover, a small increase in the WS yields cooler temperature across the domain, which has not been accounted for in the stabilization phase. The cold front measured through remote sensing in the northeast corner of the domain is also missing in the model domain. This is related to the failure in properly simulating the boundary temperature obtained from the lake-wide simulation (Section 4.5.1.1).

5.2.1.2 Niagara River Plume

The ALGE simulation was carried out for the Niagara simulation at four different timeframes out of which only one simulation exhibited a good agreement with the L7-derived maps. The long-term simulation results of the surface temperatures are presented in the chronological order Table 4.1.

Figure 5.15 compares the results from the model stabilization in Aug. 2008. The L7-derived temperature map ($^{\circ}\text{C}$) shows the relatively large extent of the plume. The large spread of the plume in the lake waters is likely induced by the combination of different factors, including high horizontal mixing, below-average discharge ($< 5350 \text{ m}^3/\text{s}$) rate, and prevalent south-easterly winds ($\sim 157^{\circ}$) during the course of the simulation. A combination of these metrological parameters driving the plume to the west complicates the modeling efforts as the lake circulation pattern is generally towards east. Therefore, despite supplying

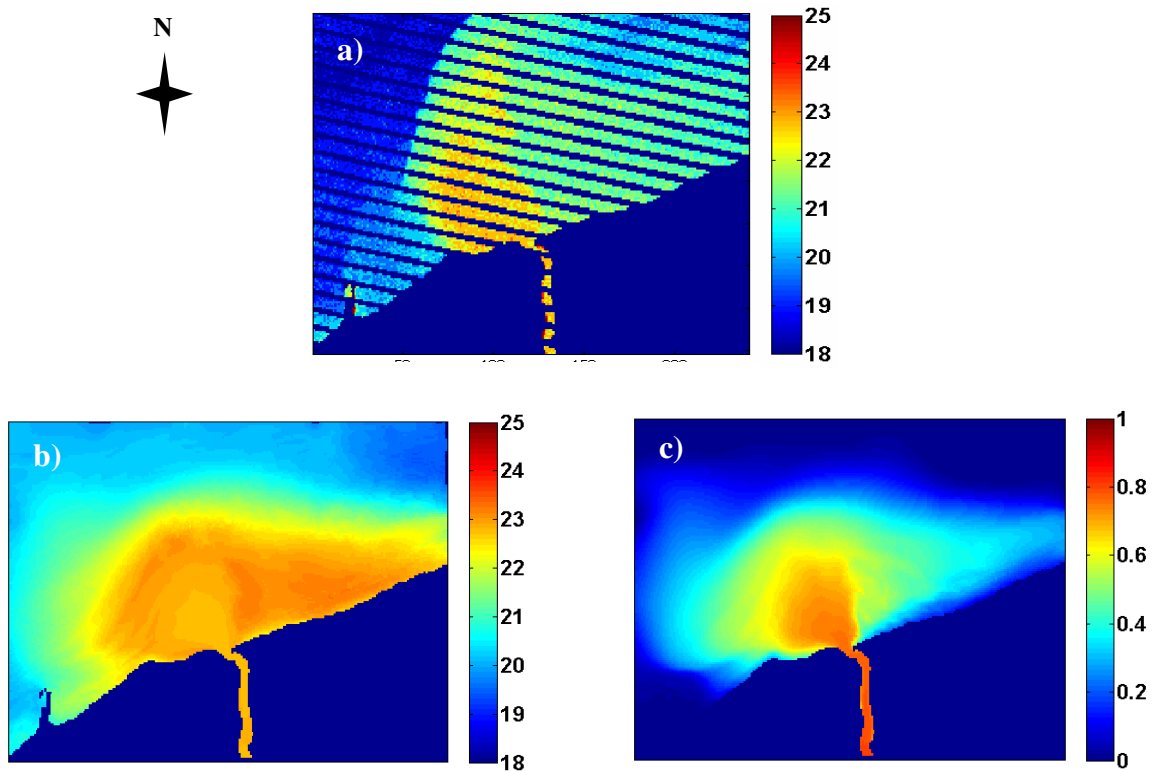


Figure 5.15. The Niagara simulation results for the Aug. 2008. Frame (a) represents the image-derived "skin" temperature [$^{\circ}\text{C}$]. Plots (b) and (c) illustrates modeled surface temperature and normalized particle distribution maps, respectively.

all of the locally observed meteorological data, if the current velocities obtained from the lake-wide simulations are incorrect, the model is unable to perform well as seen in Figure 5.15-b. The temperature profiles obtained from the lake-wide simulation do not seem to properly represent the boundary condition, as the thermal plume does not show a large gradient on its west side as seen in Figure 5.15-a. The other plausible reason contributing to the mis-prediction of the plume is the limited extent of the domain relative to that of the plume in this timeframe. In order to assess as to whether the extension of the domain size improves the modeling effort, the domain size was extended twice, i.e., $27 \times 35 \text{ km}^2$, the regular size adopted for this study. To reduce the computational expenses of such an extensive area, the spatial resolution was set to 240 m while the vertical resolution was remained 1 m . The extension of the domain, however, did not improve the modeling effort

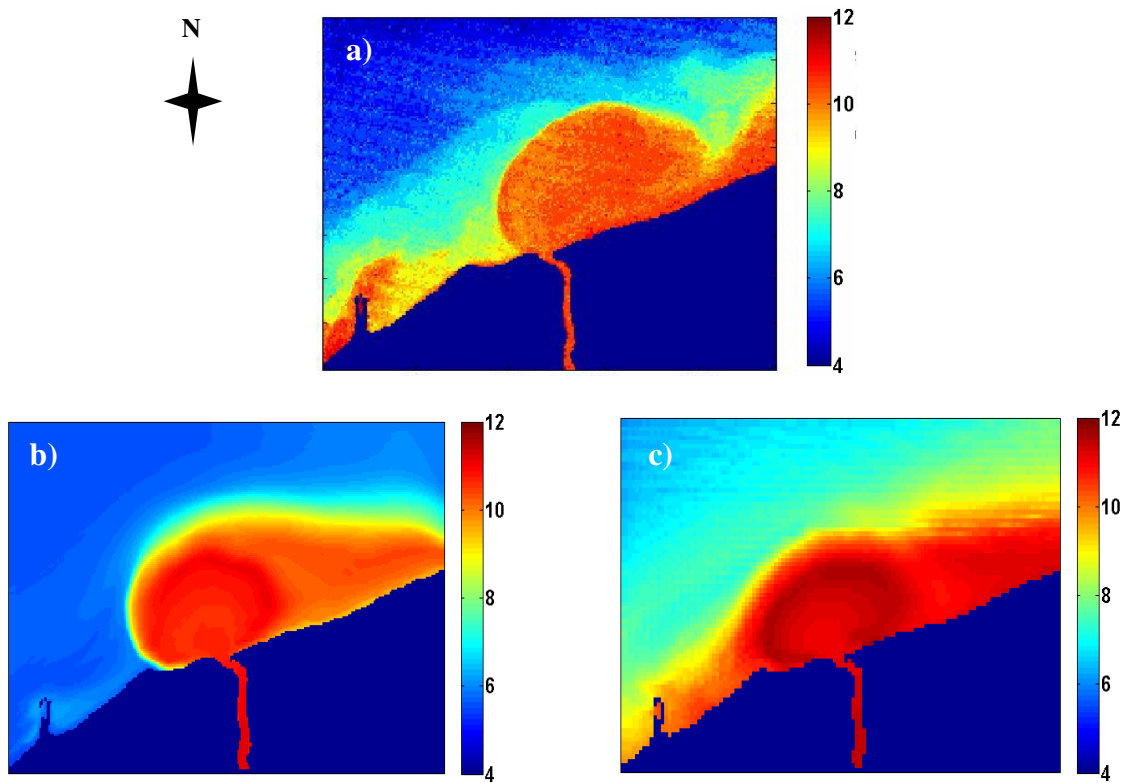


Figure 5.16. The Niagara simulation results for May 2009. Frame (a) represents the image-derived "skin" temperature [$^{\circ}\text{C}$]. The lower plots illustrate modeled surface temperature maps without (b) and with (c) applying the nudging vectors.

strengthening the speculations about the inaccurate lake-derived variables (current velocities and profiles of temperature) prescribed at the boundaries. Figure 5.15-c shows the normalized particle distribution for the same simulation, which indicates high correlation with the temperature distribution and underestimation of the plume in size.

Figure 5.16 illustrates the modeled surface temperature versus the L7-derived "skin" temperature (Figure 5.16-c) for the Niagara River in May 2009. Figure 5.16-b is the simulated surface temperature without applying the nudging vectors and boundary temperatures whereas Figure 5.16-c indicates the results when the noted lake-wide variables are incorporated. Neither of the simulations appears to accurately predict the extent of the plume. The distribution map shown in Figure 5.16-c has resulted from multiple modifications of the current velocities via either scaling the nudging vectors or optimizing the lake-wide simulations by adjusting the 2D wind pattern. More precisely, the presented outcome comes from a simulation integrated with the boundary variables taken from a lake-wide simulation with 132% increase in the 2D WS and rotating the wind axis 35°. The warm region in the southwest corner of the L7 observation is due to the relatively small discharge entering from the Port Weller harbour (Canada), which has not been incorporated in any of the Niagara simulations. In addition to attempting to find a correct shape of the plume in the stabilization phase, changes made in the locally observed environmental variables, i.e., WS, WD, RD, and RT, did not enhance the model outputs. Similar to the results in Aug. 2008, we believe that these inconsistencies are primarily associated with the characterization of the lake circulation pattern, which, over this timeframe, has significantly driven the plume towards the east (note the west edge of the plume in Figure 5.16-a). The visual comparison between the model results with and without applying lake-derived quantities supports this speculation.

Figure 5.17 presents the simulation outcomes carried out for October 2010 timeframe. As seen, the shape of the plume has been reasonably well captured by the model, which was supplied with the temporally variable lake-derived boundary conditions. Although the extent of the plume towards the east and the west has been well simulated, some temperature differences throughout the non-plume areas are evident where the ALGE model has predicted higher temperatures than observed with the L7 instrument.

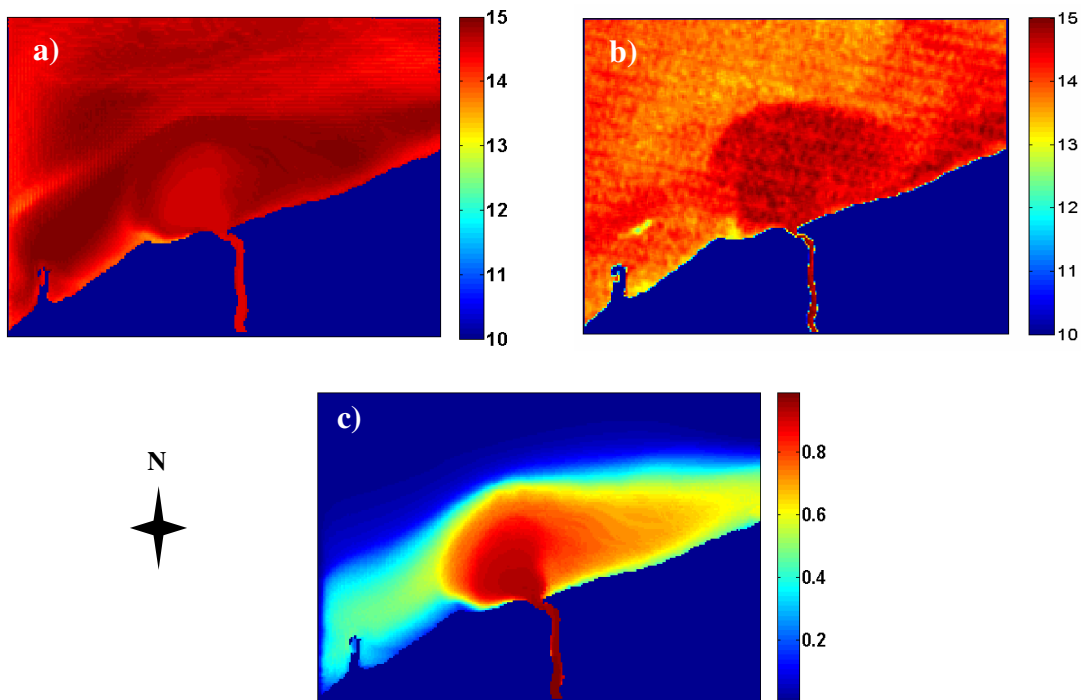


Figure 5.17. The Niagara simulation results for the Oct. 2010 period. The top frames show the modeled surface temperature (a) and L7-derived skin temperature (b). The lower plot (c) illustrates the normalized particle distribution map.

This discrepancy can be possibly related to the inaccurate thermal advection at the boundaries, where the colder bodies of water derived from the lake simulation have surrounded warmer waters in the non-plume areas influenced primarily by the solar heat exchange during the localized simulation, i.e., 10 days. Note that the lake-wide simulation was optimized against the MODIS-derived SST map. Nevertheless, slight uncertainties caused by the coarse-resolution lake simulation can further complicate the heat exchange at the boundaries. The spatial pattern indicating warmer waters on the east-northeast of the domain have come from a large eddy in the lake, which was not captured with the lake-wide simulation, and, consequently, was not incorporated in the time series of temperature profiles. L7 has been unable to distinguish the temperature differences in the core of the plume (Figure 5.17-a) when the river temperature slightly dropped ($\Delta T < 0.24^\circ C$) in the last 10 hours of the simulations. This is evident from Figure 5.17-b and the time series of the river temperature not presented here. The flow of relatively colder waters created a relatively cold inner side and a warm ring on the edge of the plume (Figure 5.17-a). It should be noted

that the noise equivalent difference in temperature ($NE\Delta T$) for L7 is about $0.28^\circ K @ 280^\circ K$ for the high gain setting used in this study. This insufficient radiometric resolution will be improved in the new Landsat whose radiometric capability has been dramatically enhanced. The normalized particle distribution is also shown in Figure 5.17-c. It should also be noted that the stretched, cool region in the west side of the plume (nearby the pier) corresponds to a ship and its wake. The results presented for Oct. 2010 will be further discussed in Section 5.2.2.1 where the model is calibrated and the water constituents are retrieved.

Figure 5.18 illustrates the results obtained from the last attempt for modeling the Niagara River plume in Aug. 2011.

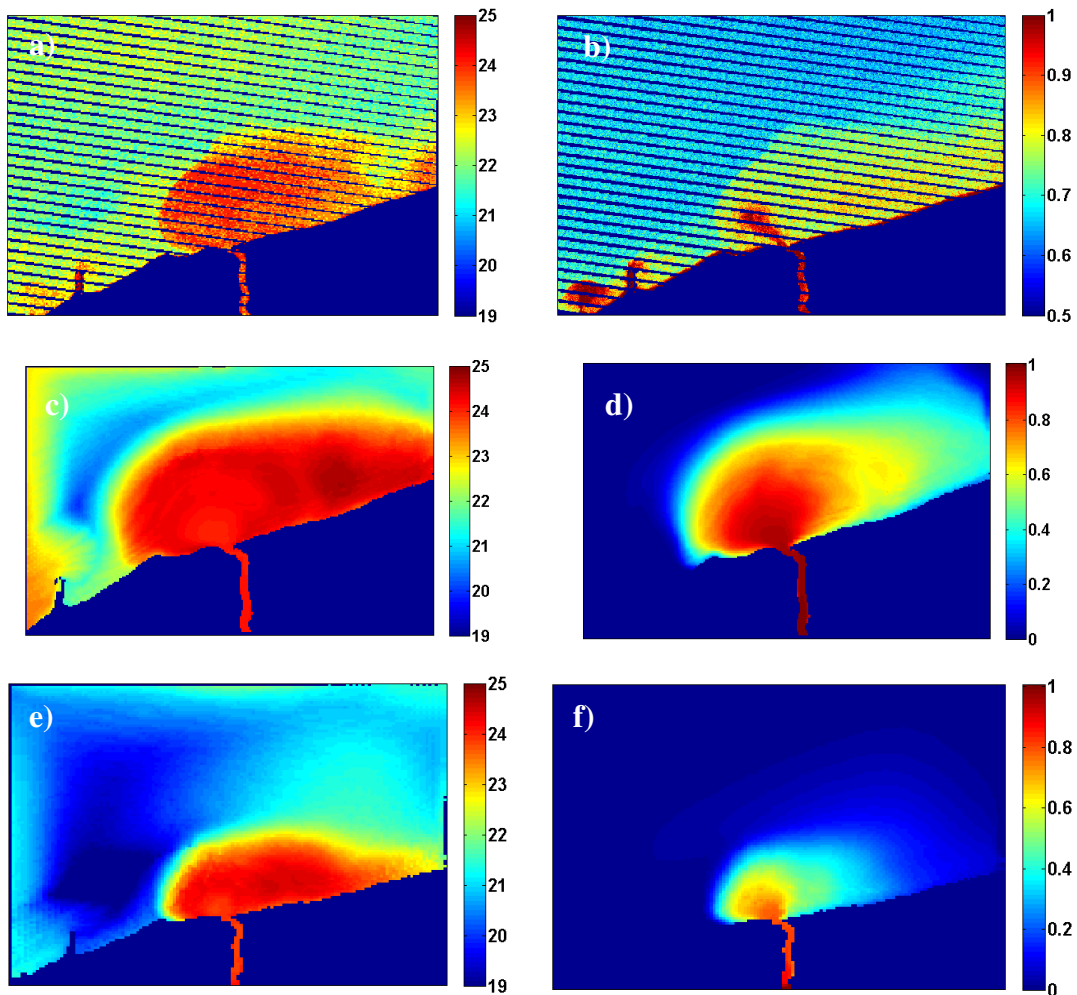


Figure 5.18. The Niagara simulation results for Aug. 2011 timeframe. The simulations were performed for two different sizes, i.e., the adopted size (b) and (c), and a larger domain (d) and (e).

The plots show the thermal and particle distribution of the plume from simulations resulting from two domain sizes, i.e., $18 \times 27 \text{ km}^2$ vs. $27 \times 35 \text{ km}^2$. Figure 5.18-a and -b illustrate the L7-derived temperature map as well as the normalized radiance field associated with the red channel for the larger domain size. Clearly, the discontinuity between the non-plume area and the boundaries in the temperature domain can be seen (Figure 5.18-c). As described in the previous modeling effort in Oct. 2010, although the surface boundary temperature was optimized with that obtained from L7, the ALGE code fails to vertically and horizontally mix with the boundary and produces a noticeable gradient around the boundaries. It was believed that such uncertainties might have been induced by the limited extent of the domain inhibiting the plume to realistically expand. The simulation result with the larger domain size and reduced horizontal cell (240 m) is shown in Figure 5.18-e and -f). The plume has expanded towards the northeast, which to some extent resembles the L7-derived map (note that Figure 5.18-a and -e are of the same domain size). Even after extending the domain size, the inconsistency between the lake-wide simulation and the localized one still exists. In addition to the large gradients throughout the boundaries, the size of the plume has been underestimated. This can be associated with the relatively low spatial resolution of the model domain (240 m). The underestimation of the plume is also evident from Figure 5.18-f, in which the particle distribution is plotted. Figure 5.18-d also shows the particle distribution in the regular domain (smaller). In both cases, the model has failed to accurately model the particle distribution at the core of the plume, i.e., the sediment load has evenly dispersed around the stream centerline as opposed to what the imagery shows. This discrepancy corresponds to a failure in the ALGE code to appropriately model the material dispersion in such a large plume. It should be noted that sensitivity analysis (Section 4.5.4.1) showed that alterations in the characteristics of the particles, such as particle density and particle size, do not significantly improve its distribution.

5.2.1.3 Onondaga Lake

The performance of the ALGE code in a small lake environment was evaluated for two timeframes, namely May 2010 and June 2011. As in the river plume simulations, the objective is to calibrate the hydrodynamic model followed by the retrieval of the water

constituents. The calibrated ALGE model is then expected to predict the status of the lake at any point in time when no suitable imagery is available.

The model stabilization phase for the Onondaga Lake simulations was chosen to be considerably longer than those of the river simulations because a) it enables capturing a wide spectrum of the physical processes and b) the computational time was no longer a restriction because of the spatial scale of the lake (Figure 4.15). Therefore, the model was stabilized by running over two months for each period. The horizontal grid spacing was set to 60 *m* and the vertical resolution was 1 *m*.

Figure 5.19 illustrates the results of the long-term simulations for May 2010. By visual inspection of the L7-derived surface temperature map (Figure 5.19-a) and that obtained from the model (Figure 5.19-b), one can infer that ALGE when supplied with the originally observed meteorological data, reasonably models the surface, thermal structure of the lake, i.e., on average RMSE < 0.38 °C .

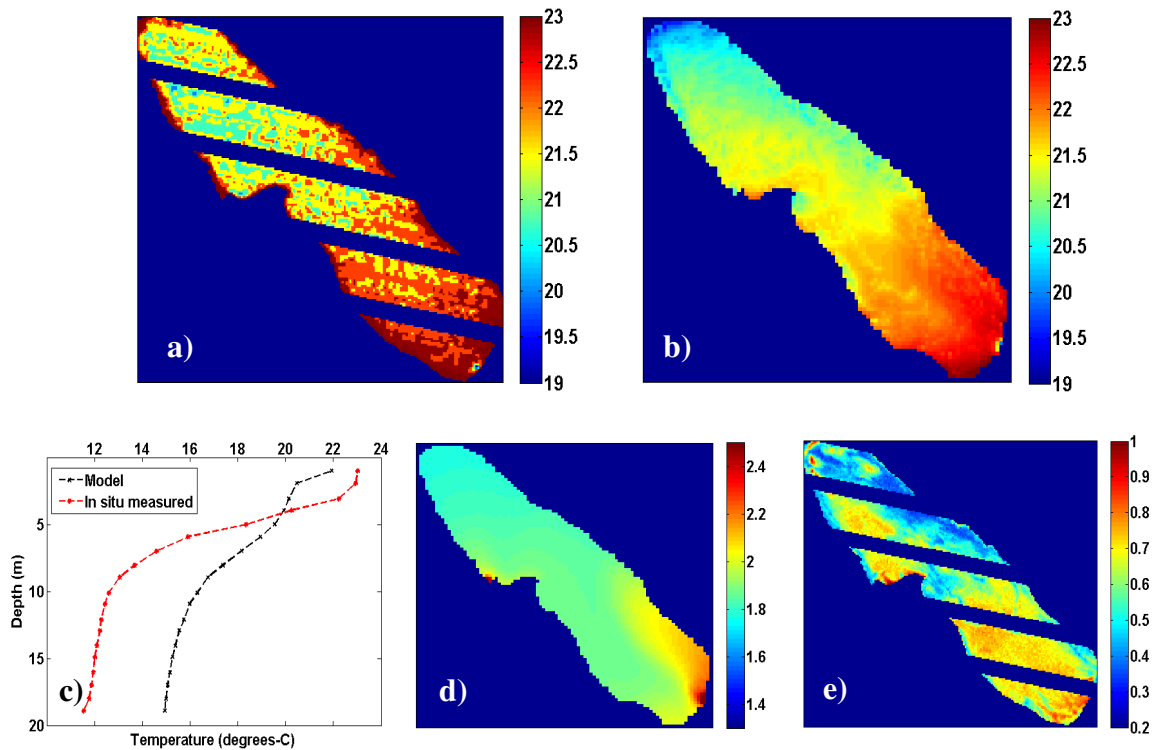


Figure 5.19. The simulation results at Onondaga Lake along with the vertical profile shown for the south deep station (c). Frames (a) and (b) show the L7- (a) and model-derived (b) surface temperature maps, respectively. The plots (d) and (e) correspond to the modeled particle distribution map and the L7-derived normalized radiance field for the red channel, respectively.

That being said, the in situ measured profiles of the temperature and that derived from the model at the south station shows disparities in the vertical structure of the lake. While the in situ measurements indicate a relatively well-mixed top layer, the model predicts a slowly varying temperature in this region. The mixing at the top few meters of such a lake in this season is primarily governed by the wind stress. This will be demonstrated in Section 5.2.2.2 when the model is particularly calibrated for the wind speed. The warm areas stretched along the shoreline are due to the adjacency effects, which can not be avoided at this scale.

Figure 5.19-d and -e compare the modeled particle distribution [g/m^3] and the normalized radiance field imaged by the L7 instrument, which is the representative of the turbidity level. As seen, there is not much correlation between the two plots, particularly, in the vicinity of the discharge from the Ninemile Creek (Figure 4.9), even though the model was prescribed with the inflow from this creek as the second mass source. For this simulation, small particle density ($1.1 g/cm^3$) was adopted after several experimental coarse resolution runs. The large settling velocities yielded non-uniform particle distributions with high concentrations near the discharges. Nevertheless, there exists some spatial patchiness especially in the north end of the lake, which the model was not able to capture. These inhomogeneous patches can be attributed to re-suspension phenomena or occasional return flow from the lake's outlet, i.e., Seneca River, [Ahsan and Blumberg, 1999]. Furthermore, as described in Section 4.3.1.3, besides Onondaga and Ninemile Creeks there are other discharges adding to the complexity of this modeling effort. In the model calibration phase (see Section 5.2.2.2), we incorporate another source flow to the model and investigate the improvements. Also, it is worthwhile noting that in contrast to the river simulations, insignificant correlation between the thermal and the reflective domain is notable when modeling the dynamic of such a small lake. This fact contradicts our assumption of the proposed approach, i.e., the thermal and reflective domains should exhibit significant correlation. Another important issue associated with the Onondaga Lake simulation is the importance of the environmental variables controlling the heat budget reaching the lake surface, i.e., sky fraction and cloud height. In the above experiment, it was found that the two parameters taken from the Syracuse Airport underestimates the heat budget driving the lake cooler than its real temperature ($RMSE > 5^\circ C$), which were obtained from the in situ and remotely sensed measurements. After providing the code with more realistic cloud heights

and sky fractions over the course of the two-month period, the results shown in Figure 5.19-b was obtained. In other words, in contrast to the short-term (10-day) river plume simulations (where the ambient lake temperature is driven predominantly by the boundary temperatures and the initial lake temperature), the modeled lake temperature at Onondaga Lake is dominated by the available solar short wave radiation and long-wave radiation from the clouds. In addition to these two variables, wind patterns (speed/direction) also alter the lake's thermal structure whereas the effects due to the inflow temperatures/discharges are rather minimal. It should also be noted the average lake temperature on March 21st (2010) obtained from UFI [Perkins, 2011] was used to initiate the simulation.

Another attempt was made to perform a long-term simulation at Onondaga Lake in June 2011 (Figure 5.20) when field measurements were carried out to support the validation of the model and our proposed approach. However, the image quality turns out to be poor due to the cloud conditions and, particularly, cirrus cloud contaminations over the lake. Nevertheless, surface temperature measurements and water sample profiles taken underneath Landsat (Figure 4.15) made it possible to assess the model performance while not being able to follow our routine procedure.

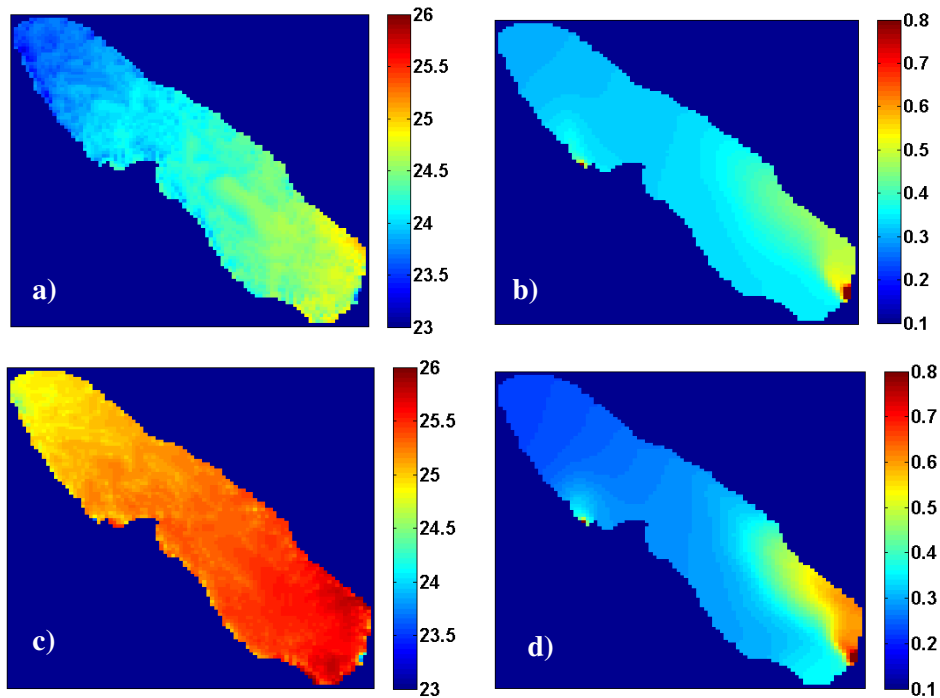


Figure 5.20. The simulation results obtained from the originally observed wind data (a) and (b), and the smoothed wind data (c) and (d).

For this simulation, as suggested by [Ahsan and Blumberg, 1999] the time series of wind speed was smoothed by applying a 5-hour window to mitigate the high frequency gusts and to take into account the canopy effects. Ahsan and Blumberg (2000) stated that the surrounding canopy and the urban structure influence the wind patterns reducing the wind stress and, as a result, mixing especially along the lake's shoreline. The simulation results with the originally observed surface data are shown in Figure 5.20-a and -b where the surface temperature and the surface distribution of the particles are plotted. By comparing the model-derived surface temperature map (Figure 5.20-a) with the *in situ* surface temperature measurements for the six field stations (Table 4.5), an RMSE $<1.45^{\circ}\text{C}$ was found. The large difference can be largely related to the shielding effects from the canopy structures that alter the wind pattern surrounding the lake. Figure 5.20-c illustrates the modeled surface temperatures when the smoothed wind data were supplied to the model. The change in the wind pattern significantly reduced the disparity to, on average, less than 0.45° , with the largest difference (RMSE $\sim 1.2^{\circ}\text{C}$) found in the northern side of the lake, where Ninemile Creek enters the lake. The large difference in the surface temperature distribution in this part of the lake may have come from the failure in providing the model with accurate river temperatures for the Ninemile Creek. In other words, we assumed that the time-series of river temperatures are identical for both discharges, i.e., Onondaga Creek and Ninemile Creek (Figure 4.9). Although varying the wind pattern reasonably improved the temperature field, the particle distributions (Figure 5.20-b and -d) remained relatively unchanged. For both simulations, ALGE was prescribed with an initial concentration of $3.5\text{ g}/\text{m}^3$, which remains constant during the course of the simulations (two months). While ALGE is capable of obtaining time-varying concentrations, there are no such regular measurements made in the tributaries discharging into the lake. It is believed that due to the very low discharges ($< 3\text{ m}^3/\text{s}$) recorded for the two inflows, ALGE has been unable to properly model the material dispersion in the lake even though a small particle density was adopted ($1.1\text{ g}/\text{cm}^3$). This is also evident from the distribution of the dissolved matter (not shown here) obtained from the model and compared with the field measurements (Table 4.5). However, incorporating multiple mass sources in the modelling effort can enhance the overall particle/temperature distribution in the lake (see Section 5.2.3.2).

5.2.2 Model Calibration

The calibration process aims at finding the realistic thermal structure of the water bodies. In this research, when simulating river plumes, the calibration implies finding the correct extent of the river plumes; however, the accurate, overall temperature distribution of the lake is sought when modeling Onondaga Lake. In both cases, the calibration was carried out via optimizing the modeled surface temperature outputs against those obtained from the remotely sensed data (Section 4.4.1).

5.2.2.1 River Plumes

Figure 5.21-a and -b show the model outputs associated with the model stabilization (long-term simulation) and the optimization for the Genesee River plume, respectively. Figure 5.21-c, on the other hand, illustrates the spatially smoothed (3×3 window) surface temperature obtained from the L7 data.

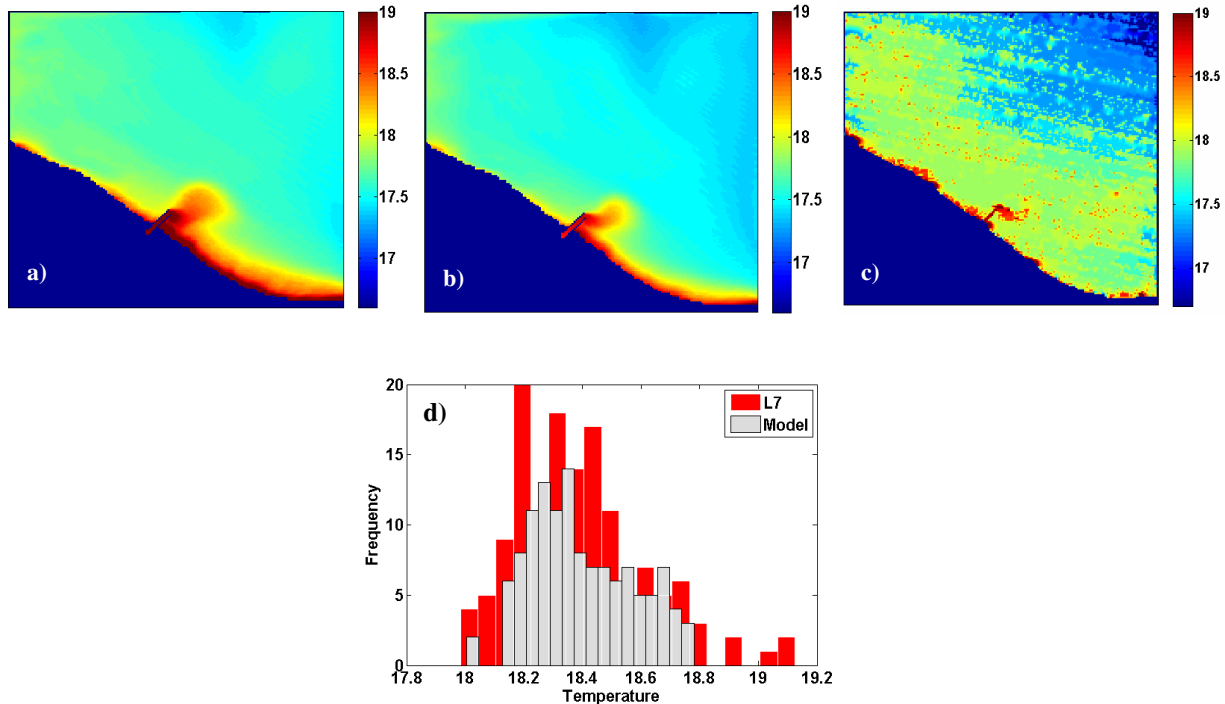


Figure 5.21. Model calibration results at the Genesee River site (a, b) shown with the L7-derived surface temperature map (c). The long-term simulation result (a) has improved after iterations and optimization (b). The histogram of the surface temperatures extracted over the plume area for the model output and the L7-derived map is shown in (d).

Following the long-term simulation (identical to the results presented in Section 5.2.1.1), it appears that the ALGE model tends to slightly overestimate the extent of the plume while correctly predicting its orientation towards northeast as observed in the L7 data (Figure 5.21-c). The physical shape of the plume is clearly improved (Figure 5.21-b) by refining the input variables after three series of iterations followed by the optimization. Quantitatively, the average RMSE calculated over the plume area was found to be 0.34°C by providing the code with the originally observed meteorological inputs (Figure 5.21-a). Following the optimization, the RMSE was reduced to 0.27°C demonstrating enhanced model predictions (Figure 5.21-b). This model prediction has resulted from a combination of 4.9% increase in the WS, rotating the wind axis $+9.2^{\circ}$, 10% increase of the RD, and 5.4% increase in the RT. The largest degree of adjustment was made for the river discharge, which is measured ~ 5 km upstream (Section 4.3.1.1). As noted earlier, the 5.4% boost in the river temperature was applied to the daily averaged measurements obtained from the nearest creek in the region. The availability of the hourly RT observations in the stream would improve the model performance and mitigate uncertainties related to the other variables. In other words, the input variables are non-linearly correlated and large errors associated with one variable have to be compensated with the others. By more closely comparing Figure 5.21-b and -c, it was found that the overall temperature throughout the domain, which is driven primarily by the wind stress, appears to be cooler than that of L7. This is due to the 4.9% increase in the wind speed, which intensifies the vertical mixing and cooling of the surface waters. It should be emphasized that the best model output was determined by taking a subset over the plume and the spatial patterns in the non-plume areas were avoided (Section 4.5.3.2). The statically derived plot (Figure 5.21-d) gives a more quantitative way of comparing the model output and the L7-derived surface temperature map over the plume area totaling 124 pixels. The tail in the higher end of the L7-derived histogram can be attributed to the adjacency effects near the pier causing an overestimation of the temperature. The 8-bit quantization of the L7 has led to a less uniform histogram when compared to that of the model. The errors due to the quantization artifacts, especially at the peak of the plume, are noticeable. Figure 5.22 illustrates the results for the Niagara River in a similar fashion as for the Genesee River. The iterations followed by the optimization improved the discrepancies between the model output and the reference data, i.e., the average RMSE calculated throughout the domain was reduced

from 0.54°C to 0.46°C . The major difference is most notable at the boundaries where time varying temperature profiles were being prescribed during the simulation. The warm pattern on the northeast side of the domain is the extension of a large eddy in the middle of the lake, which has not been captured in the localized simulation at the Niagara River. Figure 5.22-b exhibiting the highest consistency with the L7-derived thermal map, i.e., 0.46°C , was obtained by multiplying the WS with 1.192, i.e., 19.2% increase, rotating the wind axis $+8.8^{\circ}$, boosting the RD and RT 4.2% and 3.1%, respectively. Although spatially resampled, the L7-derived temperature map still contains relatively significant spatial variability as shown in 5.22-c and -d (evident from the spikes present in the histogram). Figure 5.22-d illustrate the histogram derived from a subset of pixels ($n=943$), which shows insignificant correlation between the model output and the reference image. The poor radiometric fidelity of L7 is more noticeable in the Niagara River than in the Genesee River due to the large extent of the plume. It is also interesting to notice the dynamic range

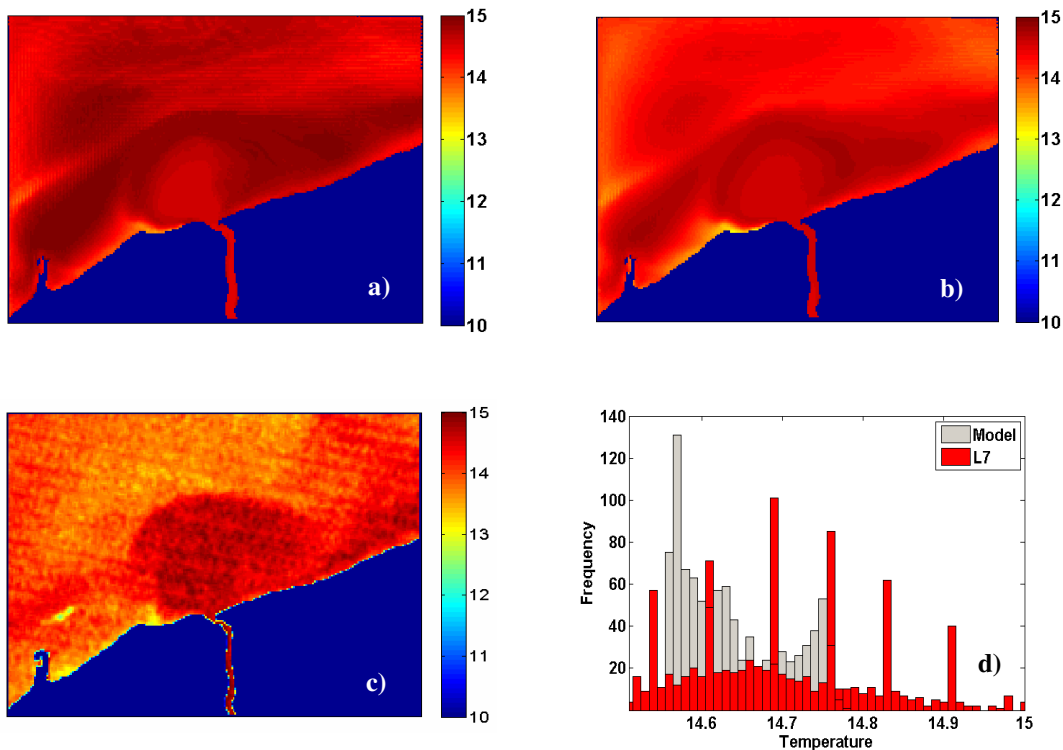


Figure 5.22. Model calibration results at the Niagara River site shown with the L7-derived surface temperature map. The long-term simulation result (a) has improved after iterations and optimization (b).

associated with the model output and the reference data. As described in Section 5.2.1.2, L7 has been unable to distinguish the temperature difference in the core of the plume (Figure 5.22-b) when the river temperature has slightly dropped ($\Delta T < 0.24^\circ C$) in the last 10 hours of the simulations. In addition to the L7's radiometric considerations, the ALGE model has not been able to accurately simulate the current velocities/temperature variations at the boundaries. These boundary conditions were extracted from a lake-wide simulation driven by identical river flow inputs and meteorological data, but with 2D wind fields computed from the adjacent weather stations and lake weather buoys (Figure 4.21). Moreover, due to the computational limitations, the lake-wide simulation was conducted at a relatively coarse resolution of 1.5 km horizontal and 2 m vertical, that may have not been adequate to capture the subtle circulations/structures required for the plume simulations. Also, note that the individual turbulent eddies apparent in the MODIS image in Figure 4.22 are much larger than the limited computational domains used for the river plume simulations. It would have been necessary to simulate these eddies accurately in time and location to generate correct boundary conditions for the limited area river plume simulations.

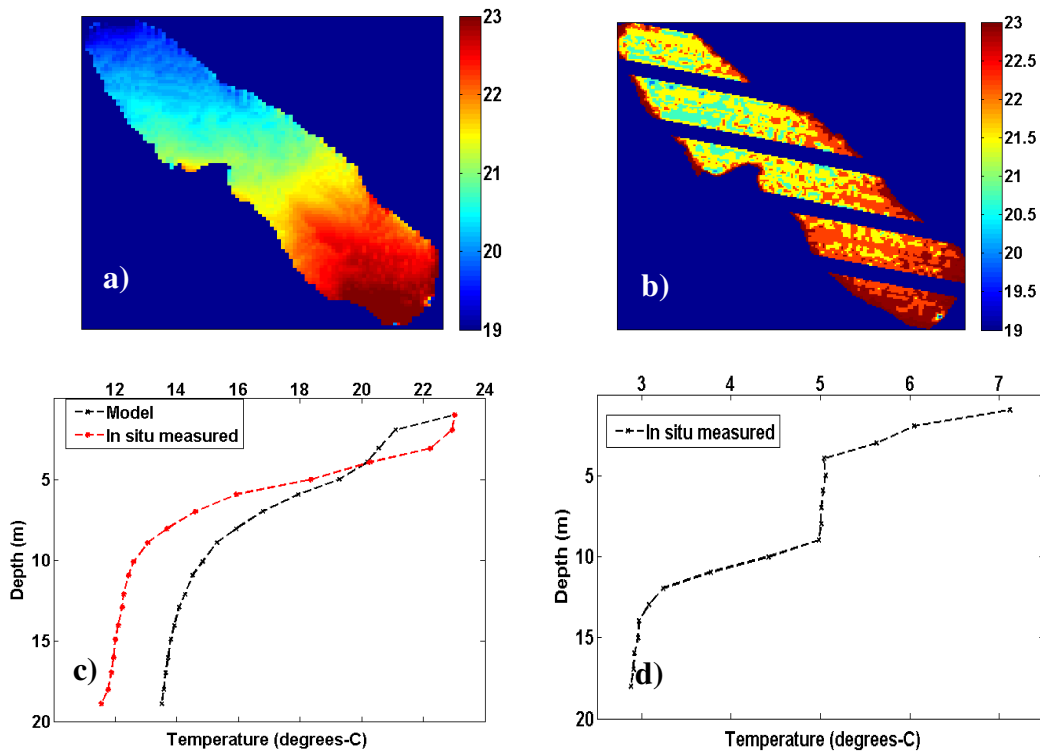


Figure 5.23. The calibrated model output (a) shown for Onondaga Lake along with the L7-derived surface temperature map. The temperature profiles measured/modeled at the south deep station

5.2.2.2 Onondaga Lake

The model calibration at Onondaga Lake was carried out for May 2010, as a good quality image was available. In addition to the two main flow sources provided to the model, a third inflow representing the Harbor Brooks discharge at the southwest corner (Figure 4.9) of the lake was also incorporated to enhance predicting the thermal structure and the material transport in the southern portion of the lake. Figure 5.22 shows the matched model output against the L7-derived surface temperature. The best model output (RMSE < 0.56 °C) resulted from 22% reduction in the originally observed WS and rotating the wind axis (WD) -28°. As explained, the observed wind pattern in the wide, open areas of the lake can be largely different from that along the lake's shoreline introducing uncertainties in the modeling process. This issue has been compensated via the above-mentioned adjustments. However, the variations in either the flow temperatures or the discharges appeared to be trivial when adjusting during the calibration. However, it will be demonstrated in Section 5.2.3.2 that the discharges have to be considerably boosted to produce particle distributions close to the L7-derived. Briefly, this large adjustment is due to the absence of inputs from Metro and the Ley Creek on the south east corner of the lake (Figure 4.9). Figure 5.23-c shows the *in situ* measured temperature profile versus that obtained from the model at the south deep station. As shown in Figure 5.23-c, although the surface temperature is in agreement with that observed, there is a relatively significant difference (RMSE > 1.86 °C, on average, through the water column) in the vertical distribution of the temperature in the deeper waters (> 8 m). This inconsistency can be attributed to the inaccurate initialization of the model where a vertically uniform lake temperature was assumed. More precisely, the measured temperature profile (Figure 5.23-d) observed on the starting day of the simulation (March 21st 2010) could have made a great impact in the model performance. Note that an average 6 °C (vertically uniform) was used as the initial lake temperature for this experiment.

5.2.3 Constituent Retrieval

5.2.3.1 River plumes

After fixing the shape of the plume in the calibration phase, the sediment load (COP) [g/m^3] and the volume of the dissolved matter (COD) [ug/l] were adjusted by optimizing

the modeled water-leaving reflectance (r_d) against the L7-derived surface reflectance products (r_d) across the visible bands. As noted, in this study, it is assumed that the CHL distribution is modeled as a dissolved component similar to COD. Figure 5.24-a and -d illustrate the image- and model-derived TSS and CHL surface distribution maps in the proximity of the plume area ($1 \times 1 \text{ km}^2$). The model outputs shown in Figure 5.24-c and -d have provided the best agreement with the L7 imagery in the surface reflectance domain (r_d), i.e., on average, RMSE < 0.0055 [unitless] calculated over the plume.

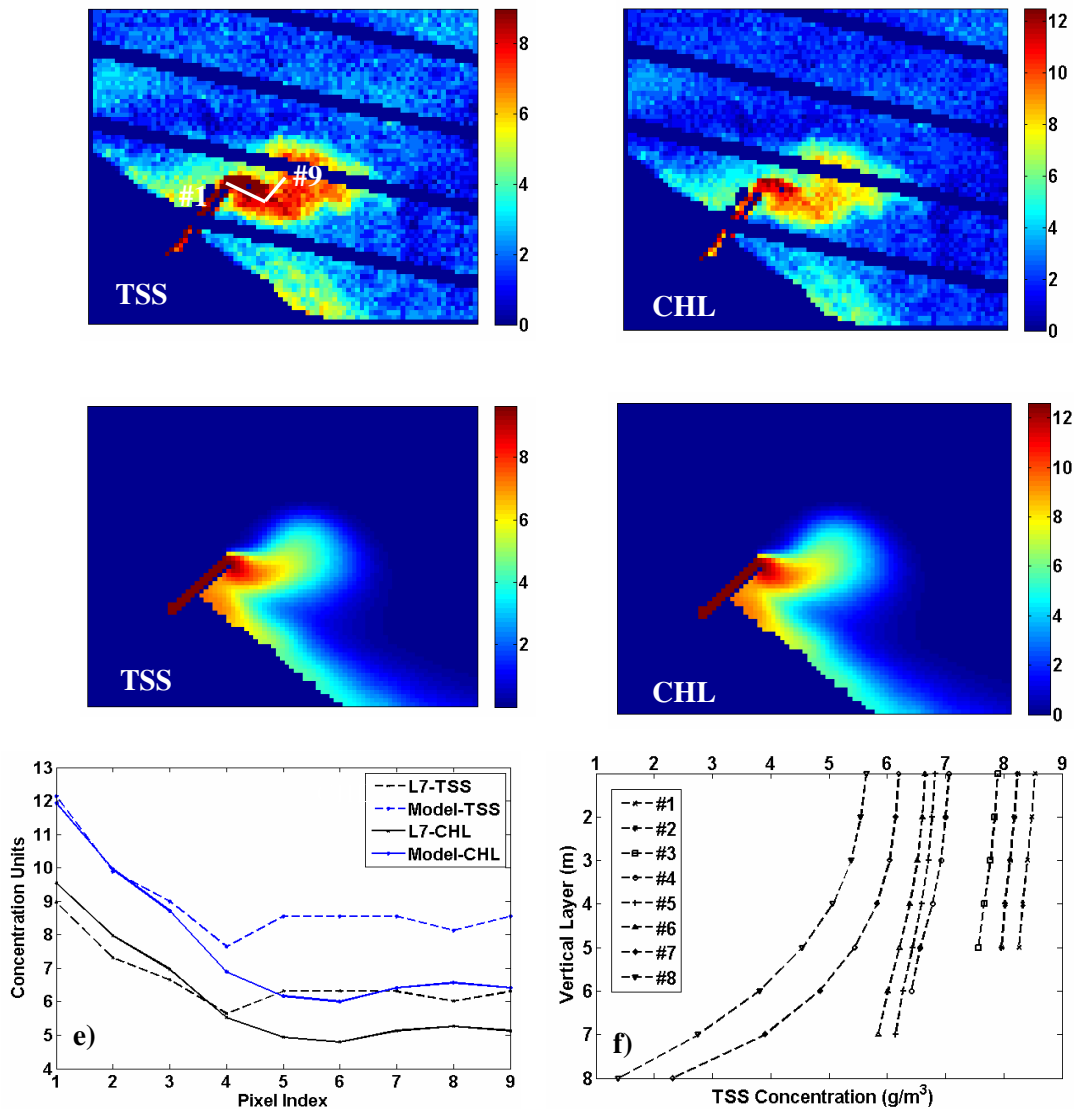


Figure 5.24. The TSS and CHL derived from the L7 data (top row) and the best model output (second row) for the Genesee plume. The surface distribution obtained along the model and L7 products are shown in (e). The vertical profiles derived along the same transect are also plotted in (f).

The distribution maps produced from the L7 imagery were based upon an independent, LUT-based approach where various water types are simulated with the Hydrolight code (Section 4.6.4). It should be noted that the L7-driven concentrations contain artifacts, such as adjacency effects and atmospheric haze, which were identified through inspecting the Short-Wave-InfraRed (SWIR) bands (Section 0). The west side of the pier, for instance, is clearly affected by the haze and the reflection off the pier resulting in seemingly higher concentrations of water constituents. However, the re-suspension phenomenon could also strengthen the in-water scattering, and as a result, greater water-leaving signal in the near-shore area. As expected, the distribution of particles and the dissolved matter has nearly identical shape owing to the relatively low settling velocity of the particles allowing for a realistic prediction of the particle distribution. Figure 5.24-e shows the surface distribution of the TSS and CHL along the plume centerline, i.e., the white polyline in L7-derived TSS map (Figure 5.24) compared for the model and the smoothed L7 imagery. The concentrations are very consistent close to the pier while the disparities increase up to 25% towards the end of the transect. The discrepancy is, in part, due to the spatially inhomogeneous atmosphere, as inferred from the analysis of the SWIR bands (Section 0), and the underestimation of the constituents by the ALGE model as the plume expands northward. In addition, the lack of the accurate knowledge of the particle size and density, river discharge, river temperature, hourly COP and COD, and perhaps current velocities at the boundaries introduce uncertainties in the model performance. The vertical profiles of the particles associated with the pixels along the transect are shown in Figure 5.24-f. These profiles cannot obviously be quantified through remotely sensed measurements due to the limited penetration depth of the light field through the water column. A relatively uniform vertical distribution in such turbid waters resulting from large turbulence and vertical mixing near the pier is noticeable. The uniformity tends to decrease towards the tip of the plume. As expected, the presence of the thermocline, which was observed with the similar trend in the model's thermal output profiles, has affected the vertical distribution of the TSS in the deeper zone where the concentrations are lower at the bottom ($<3 \text{ g/m}^3$).

Figure 5.25 shows similar plots to that of the Genesee River for the Niagara River plume ($19 \times 28 \text{ km}^2$). The matched model outputs correspond to the surface reflectance map that most resembles that obtained from the L7 reflective imagery. The disparity between the

model output and the image products was found to be less than 0.009 units of reflectance, on average, over the plume area. Although the optimal concentration maps exhibit, on average, the minimal disparity against the L7-derived concentrations, the maximum concentrations (e.g. $\sim 1.6 \text{ g/m}^3$) shown on the image-derived products have not been achieved with the model due to inconsistencies in the spatial distribution of the constituents. The differences in the spatial distributions can be identified in Figure 5.25-e where the surface distributions along the transect (shown as the pink polyline drawn on the L7-derived TSS map) across the plume is plotted.

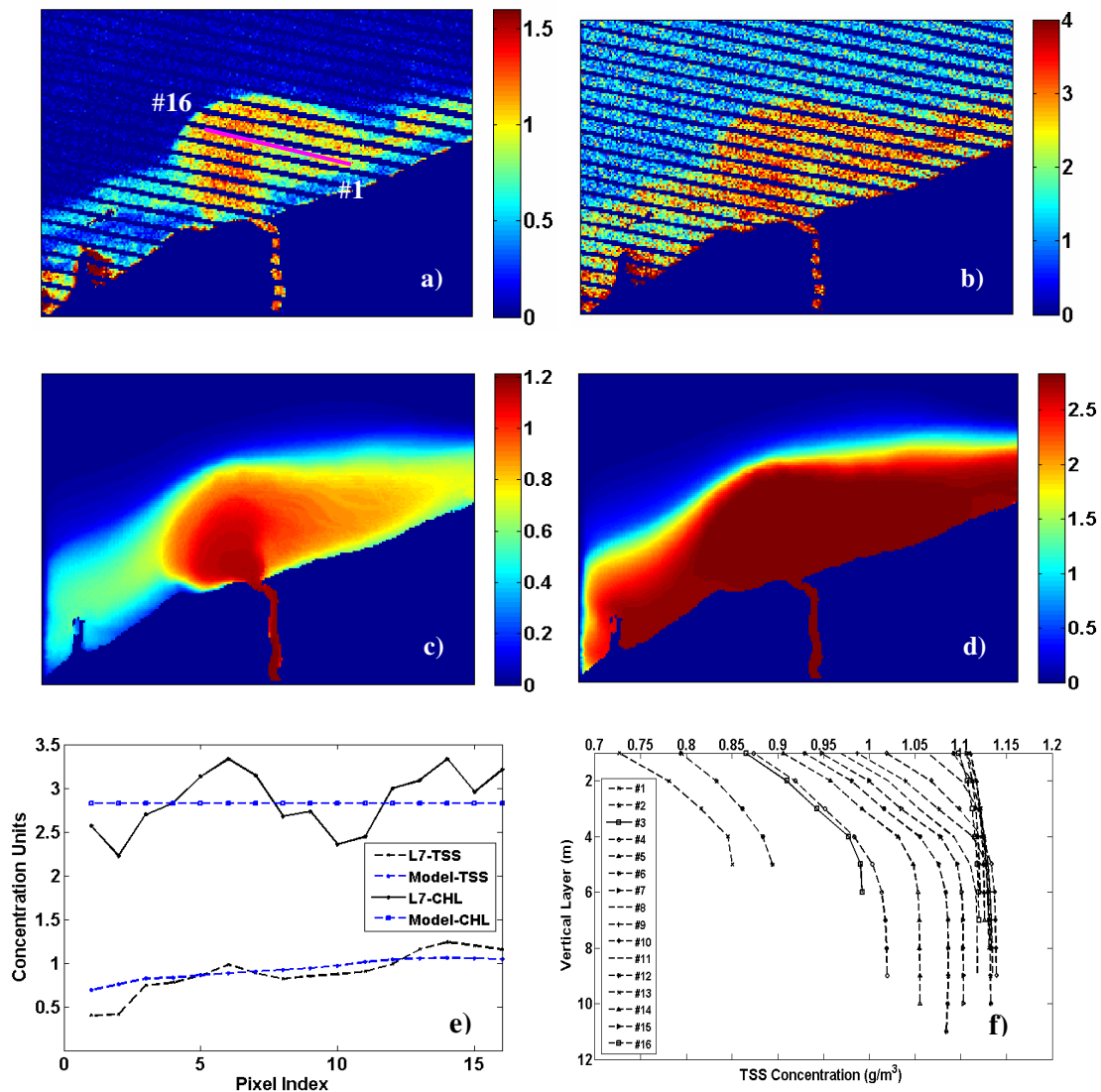


Figure 5.25. The TSS and CHL derived from the L7 (a-b) data and the best model output (c-d) for the Niagara plume. The surface distribution obtained along the model and L7 products are shown in (e). The vertical profiles derived along the same transect are also plotted in (f).

Due to the natural co-existence of the phytoplankton with the suspended particles in the plume waters, there is a relatively high correlation ($\rho_\alpha > 0.62$) between the CHL and the TSS concentration maps as shown in the L7-derived products. The ALGE model, however, is unable to take into account biological factors that influence the distribution of the chlorophyll-a in such a large scale. This is evident from surface distribution of CHL across the plume representing constant quantities (Figure 5.25-e). On the other hand, the TSS distribution has been rather well simulated through the model even though incorporating the hourly measured concentrations can significantly enhance the model predictions. The vertical profiles of the TSS concentration along the transect (#1 to #16) is also shown in Figure 5.25-f. At a depth of ~ 5.5 m, the thermocline causes a relatively large gradient in the concentrations, which can be clearly identified in most of the extracted profiles. Nonetheless, more uniform distributions across the highly concentrated, well-mixed areas (core of the plume with 1.1 g/m^3) were found. With the calibrated model in the thermal and reflective domains, one can re-start the model over a specific timeframe (e.g. ± 50 hours) around the hour at which the model was calibrated to either pre-cast or fore-cast the spatial and vertical distributions of the water constituents providing the meteorological/environmental variables are made available through *in situ* measurements. It should be emphasized that the ALGE model is currently capable of incorporating tidal oscillations and could be used in areas with tide effects. The simulation capabilities of ALGE can also be developed to incorporate biological components affecting phytoplankton communities if needed.

5.2.3.2 Onondaga Lake

Figure 5.26 shows the best particle and CHL map derived from the model as compared to the normalized radiance field (red channel) image representing the turbidity (Figure 5.26-c). The surface reflectance generated from the model outputs showed a relative consistency with that of the L7 data, i.e., on average RMSE ~ 0.0112 (1.12%) reflectance units. The level of agreement is lower than those obtained for the Genesee and the Niagara River plume simulations. In contrast to the river plume simulations where the RD was held fixed in the constituent retrieval process, here, we adjusted the discharges to achieve consistent particle/CHL distributions relative to the L7 imagery. As described in Section 5.2.2.2, this is due to the fact that no correlation was found between the modeled surface temperature and

the particle distribution and change in flow is trivial when calibrating the model in the thermal domain. Although incorporating three inflows, i.e., Onondaga Creek, Ninemile Creek, and Harbor Brooks, dramatically improved the particle/CHL distribution compared to the simulation with only two sources, there are some differences between the observations and the model outputs in the proximity of the Ninemile Creek discharge.

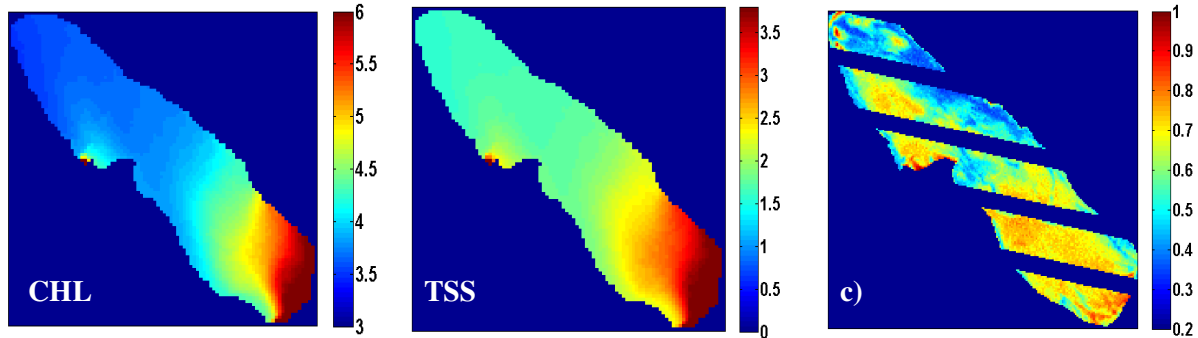


Figure 5.26. The CHL and TSS maps derived from the ALGE model for Onondaga Lake. Frame (c) indicates the normalized radiance field associated with the red channel of L7.

As in most of the experiments, ALGE has underestimated the material distribution even after making the discharges nearly twice larger than the *in situ* measurements. In other words, the Onondaga Creek and the other two creeks' discharges were boosted 85% and 94%, respectively, to achieve the "best" output. Following such adjustments, the average inflow during the last 90 hours of the simulations became $3.1 \text{ m}^3/\text{s}$. Furthermore, the relatively clearer waters along the east shoreline (Figure 5.26-c) were not captured with the model. This is due to the fact that Onondaga Lake receives numerous nutrients and chemicals from the tributaries and the METRO (Figure 4.9), which complicate the simulations of the suspended solids and their distributions. This complication has not been modeled in the ALGE code but it can be developed via the knowledge of the nutrients, their concentrations, and their physical properties. It should be emphasized that for the Onondaga Lake simulations, the model configuration was slightly varied to examine whether there is an improvement in the outputs. These alterations include modeling the salty water, changing the absorbance rate (*distk* parameter in the *param.dat*), and changing the turbulence modeling. Although slight changes were observed, such modifications did not considerably enhance the model

performance. The profiles of the particle and dissolved matter are not shown as the in situ measurements for this date was unavailable.

5.2.4 Summary

In this section, the L7 data were integrated with the ALGE model to calibrate the model and eventually retrieve the water constituents via coupling the model outputs with the Hydrolight. Our proposed approach was examined for eight different periods at three different sites. It was inferred that following the model stabilization phase, the model has to achieve reasonable outputs resembling the reference data, i.e., 10%-20% errors. If a close agreement with the reference data is achieved then adjustments of the environmental variables followed by the retrieval of the water constituents can be conducted. In other words, large differences in the results from the model stabilization and the reference maps must be investigated prior to the calibration stage.

It was shown that, when the discharge is above its annual average value, the ALGE model is able to reasonably model the Genesee River plume providing that hourly environmental variables, including the river temperature, are available. The particle/dissolved matter distribution can be improved by incorporating hourly variable concentrations, which are not currently available for the site.

It was also found that the model performance when modeling the Niagara River plume is restricted by the ability to accurately model the lake circulation pattern in terms of its temperature and current velocity. The lake circulation patterns are obtained through conducting nearly seasonal lake-wide simulations. The possible steps towards improving the whole lake simulations are a) incorporating 2D cloud height and sky fraction data b) initializing the code with a profile of an averaged lake temperature. It was also realized that an accurate modeling of the thermal structure of the lake does not necessarily yield reasonable nudging vectors. This was the case when modeling the Niagara plume in May 2009 (Figure 4.22 and Figure 5.16). This is perhaps related to the non-ideal environmental conditions, such as frequent wind gusts, not captured by the hourly measurements of the wind, driving small eddies in the springtime. Moreover, the lake-wide simulations were conducted at 1.5 *km* horizontal spacing, which may not be adequate to model such small-scale processes.

The Onondaga Lake simulations conducted for two timeframes appeared to be promising in the thermal domain when appropriate adjustments of the wind patterns are made. It was also found that all the input discharges into the lake should be incorporated in the simulations to allow for realistic particle/dissolved matter distributions. Furthermore, the discharges have to be increased nearly twice to produce surface concentrations similar to those observed *in situ*. More importantly, obtaining inputs from various sources complicates the simulations and necessitates modeling of other components of the water body, including nutrients and different types of particles.

5.3. OLI's Potential for the Retrieval of Water Constituents

As described throughout this research, the OLI sensor aboard LDCM is expected to improve our ability to retrieve water constituents in case II waters. The OLI's enhanced features relative to the L7 technology include the addition of the new short, blue band at 443 *nm*, its improved SNR due to primarily its pushbroom design, and its superior radiometric fidelity, i.e., 12-bit. In general, the improved SNR and its radiometric capability provide a great improvement when sensing targets of low signal levels, i.e., water. The addition of the new band centered at the chlorophyll-a absorption peak makes this instrument comparable to the ocean color satellites, such as MODIS and SeaWiFS, designed specifically for global monitoring of the primary production. However, similar to Landsat-5 and Landsat-7, LDCM resolves a greater spatial detail suitable for monitoring coastal/inland waters, which may not be achieved with the ocean color satellites. In addition, coastal waters are optically complex waters where the ocean color algorithms valid for ocean waters may fail in the retrieval of water constituents. In this section, the retrieved concentrations from the Hyperion, the simulated OLI (S-OLI), the simulated ALI (S-ALI), ALI, the simulated L7 (S-L7), and L7 are qualitatively and quantitatively compared. This comprehensive cross-comparison provides the opportunity to evaluate the concentration maps based on the systems' characteristics, including the number of spectral channels, radiometric resolution, and the differences in the RSRs (Figure 4.34).

According to the description of the approach in Section 4.6, the physics-based model (Hydrolight) was used to generate a 3D LUT spanning plausible ranges of concentrations measured *in situ* nearly coincident with the satellite overpasses. The ranges of constituents

are $0.5 < \text{CHL} < 6.0$ [$\mu\text{g}/\text{l}$], $0.01 < \text{TSS} < 2.7$ [g/m^3], and $0.1 < a_{\text{CDOM}} < 1.0$ ($0.013 < a_{\text{CDOM}}(440) < 0.13$ [m^{-1}]). It is believed that, under normal environmental conditions, the *in situ* measured water constituents (Section 4.3.3) in the river mouth approximately represent the constituents' upper bound in the entire study area. In other words, there is no need to expand the ranges beyond the above-noted realistic values, which can help avoid confusions when simultaneously retrieving three parameters. The prior knowledge of the constituents allowed us to generate a finely sampled LUT while reducing the computational time. Although a field campaign was performed in the vicinity of the river discharge, we used the Hyperion-derived concentration maps as a validation source since extensive "truth" was unavailable as in most similar studies.

5.3.1 Qualitative Comparison

Figure 5.27. provides a qualitative way of comparing the retrieved concentration maps of CHL [$\mu\text{g}/\text{l}$] and TSS [g/m^3] as well as the CDOM absorption index maps which indicate $a_{\text{CDOM}} @ 440\text{nm}$ [m^{-1}]. By visually inspecting the CHL maps (first column) and using the Hyperion-derived concentration (top row) as the validation source, one can infer that S-OLI, S-ALI, and ALI have been able to reasonably map the CHL concentration. Although there are some discrepancies in the average concentrations over the plume area (see Table 5.3), the (simulated) multispectral systems leveraging four spectral bands produced CHL maps similar to that generated from the Hyperion instrument. The S-L7 and the L7 datasets, however, failed to correctly retrieve the CHL concentrations over the plume area where the TSS concentration is, on average, $1.0 \text{ g}/\text{m}^3$ and $a_{\text{CDOM}}(440) = 0.1 \text{ m}^{-1}$ (equivalent to CDOM index=0.8), which were derived from Hyperion. In other words, regardless of the differences in the radiometric resolution of the two images (S-L7 and L7), the absence of the short blue band at 443 nm has resulted in a significant overestimation of the CHL in the plume area. Nevertheless, in the areas of low concentrations of TSS and dissolved organic matter (offshore region), the CHL concentrations retrieved from the two images (Figure 5.27) are consistent with those obtained from Hyperion, ALI, and S-OLI. In this area, the S-L7, particularly, produced a smooth CHL field whereas the L7-derived map shows

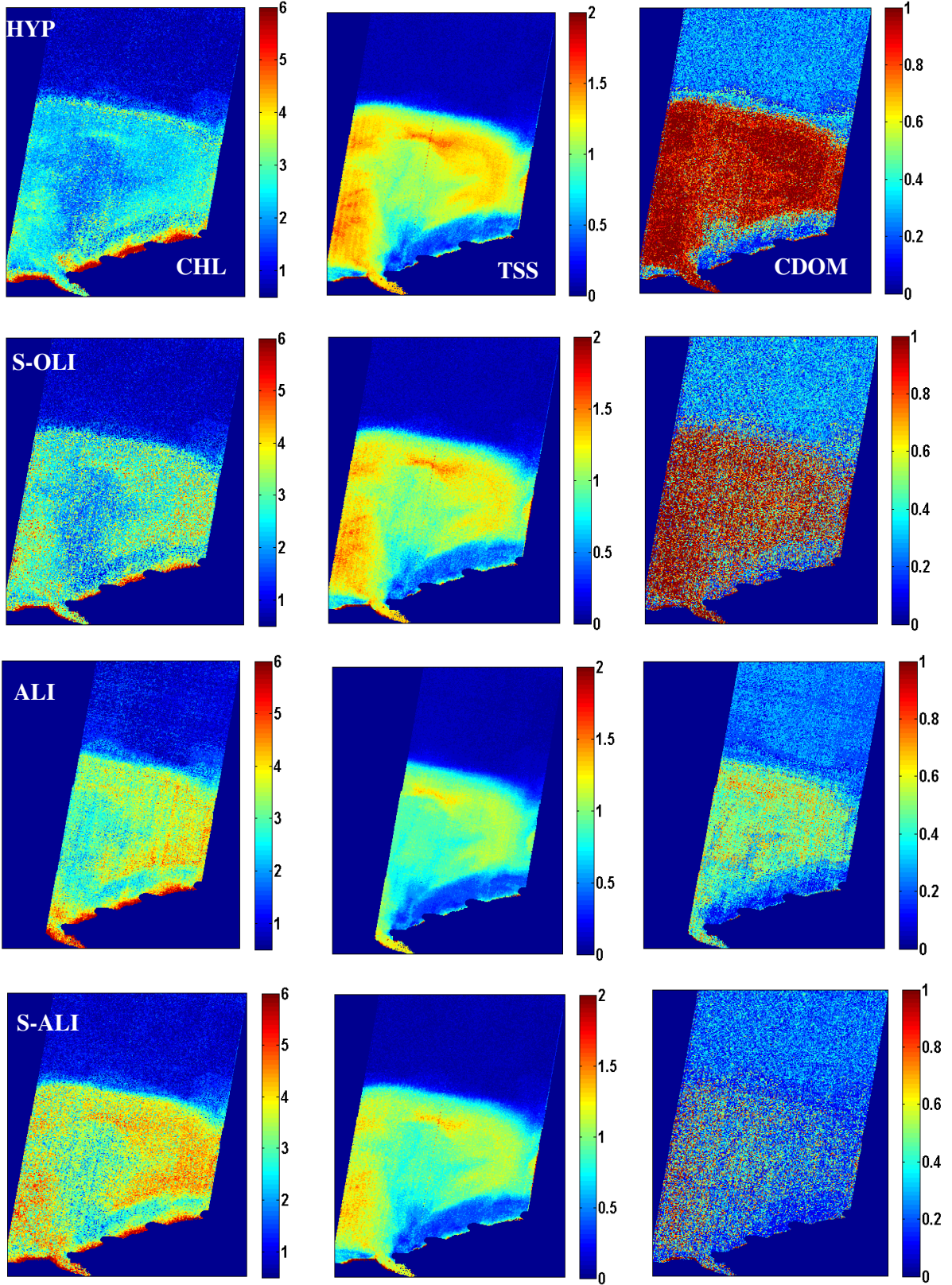


Figure 5.27. The concentration maps derived from Hyperion, S-OLI, ALI, and S-ALI.

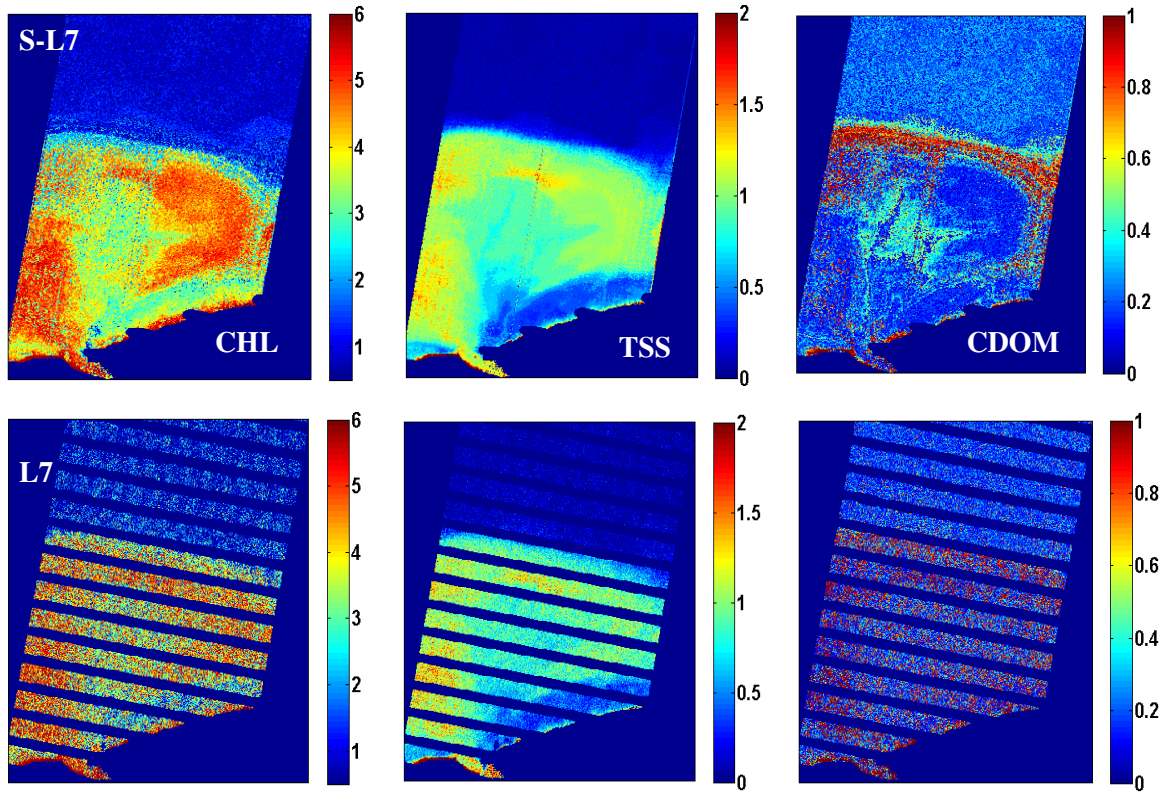


Figure 5.27. (continued) The concentration maps derived from S-L7 and L7.

significant local variability due to its poor radiometric fidelity. The derived TSS maps are also shown in Figure 5.27 (second column). A general overview of the concentration maps indicates that all of the systems including S-L7 and L7 were able to reconstruct the circulation pattern associated with the Niagara River plume. For the multispectral systems, this is primarily due to the high correlation between the combination of green ($\lambda \approx 562 \text{ nm}$) and the red bands ($\lambda \approx 655 \text{ nm}$) with the turbidity level, i.e., the short blue band $\lambda \approx 443$ and the blue band $\lambda \approx 482$ do not largely contribute in the TSS retrieval. That being said, there are discrepancies in the average TSS concentrations over the plume area (see Table 5.3), with ALI, S-L7, and L7 slightly underestimate the concentration. The concentrations in the offshore areas ($< 0.1 \text{ g/m}^3$) have been well retrieved using all the instruments although the L7-derived map exhibits significant spatial variability due to its 8-bit quantization rate. The effects of the poor radiometric resolution of L7 can be also seen over the plume area.

The CDOM index maps indicative $a_{CDOM}(440)$ are shown in the third column of Figure 5.27. The CDOM maps represent the multiplicative factors used to scale up/down the *in situ* measured spectra (Figure 4.14). To obtain the actual absorption level at 440 nm, one has to multiply the assigned values (Figure 5.27) with the *in situ* measured $a_{CDOM}(440) = 0.13 [m^{-1}]$. By a visual inspection, it is inferred that the map produced from the S-OLI closely resembles that obtained from the Hyperion dataset. However, ALI, which, on average, under-predicted the CDOM absorption over the plume, has also produced a realistic spatial distribution. The fact that the two multispectral systems were able to retrieve the distribution of the CDOM absorption considerably confirms the applicability of such instruments as a reasonable replacement for a hyperspectral system, such as Hyperion. This is primarily related to the placement of the spectral channel at 443 nm, which, among the other bands, is the most sensitive channel to the CDOM absorption. On the other hand, the CDOM map generated from the S-ALI shows a significant underestimation relative to the S-OLI- and Hyperion-derived maps. This disparity is largely due to the improvements in the responses of the CA and, in part, the blue bands of the OLI sensor with respect to that of ALI (Figure 4.34). The failure in the retrieval of CDOM absorption using S-L7 and L7 supports the considerable enhancement in the performance level of OLI/ALI due to the addition of the CA band centered at 443 nm. In the plume area, the retrieval algorithm allocated either 0.1 or 1.0 to the L7 pixel values; while S-L7 significantly underestimated the CDOM absorption. That being said, S-L7 produced realistic values on the edge of the plume and nearby the shoreline where the TSS concentration is less than $0.5 g/m^3$. The average absorption values obtained from all of the multispectral datasets except L7 in the offshore areas are in close agreement with that of Hyperion. Similar to the CHL and TSS concentration maps derived from L7, the L7-derived CDOM map also shows significant variability in the offshore areas.

In order to provide another way to visually investigate the differences between the water constituent maps in the plume area, the histograms of the difference maps using the Hyperion-derived maps as references are plotted. The difference maps were produced by subtracting the Hyperion maps from those obtained from the multispectral datasets. In other words, the positive values indicate overestimation of a dataset relative to that of Hyperion. The total numbers of data points in the plume area common in all datasets amount to

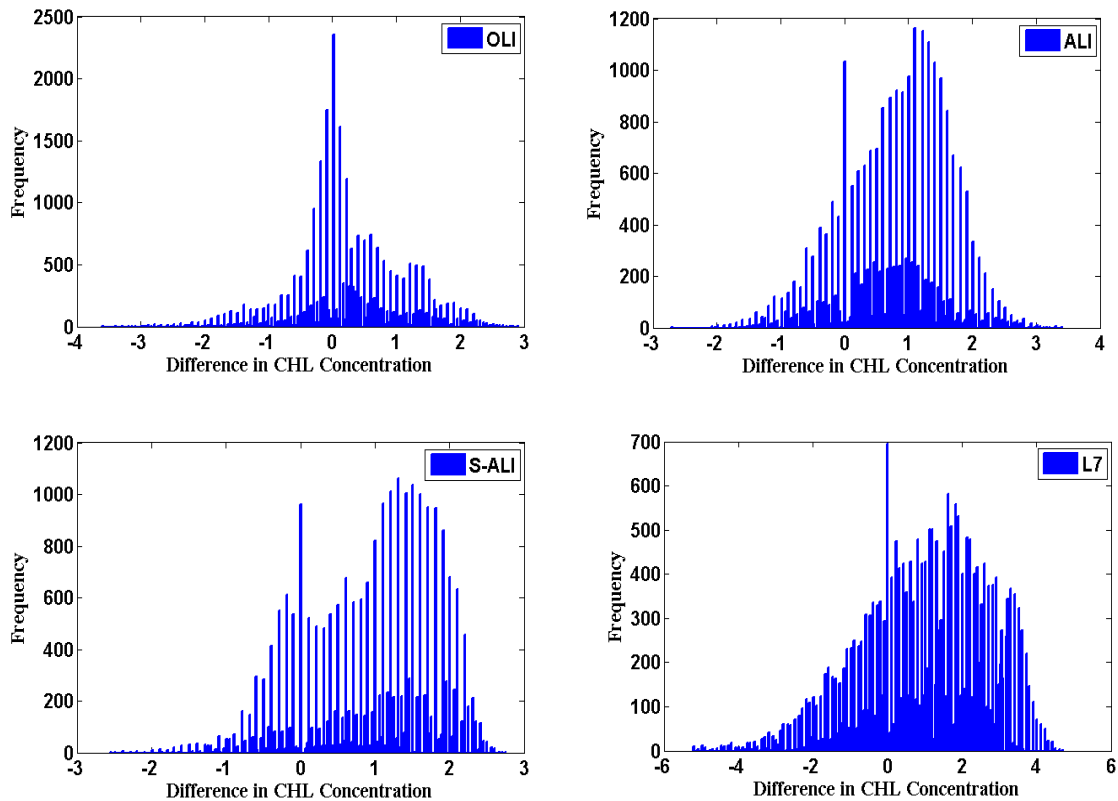


Figure 5.28. The histograms associated with the difference maps of CHL concentrations over the plume using the Hyperion-derived map as a reference.

approximately 27000 pixels. Figure 5.28 shows the histograms associated with the CHL difference maps in units of $[ug/l]$. Ideally, it is desired that all the data be situated at zero.

The plot corresponding to the S-OLI difference map shows a nearly Gaussian distribution with a relatively high peak at zero and a small dispersion from the center. The other histograms demonstrate that the other datasets, including ALI, S-ALI, and L7 tend to overestimate the CHL concentration when compared to the Hyperion-derived map in turbid waters. In addition, the large dispersion of the histogram associated with the L7 data ranging from -6.0 to 6.0 ug/l confirms the high variability of the L7-derived map and the poor radiometric fidelity of this instrument. It is also important to note that the histograms corresponding to S-ALI and ALI represent similar features, S-ALI shows larger dispersion as the dataset was drawn from the noisy Hyperion dataset. For brevity, the plot from S-L7 is not shown. The results were similar to that of L7 but with less dispersion.

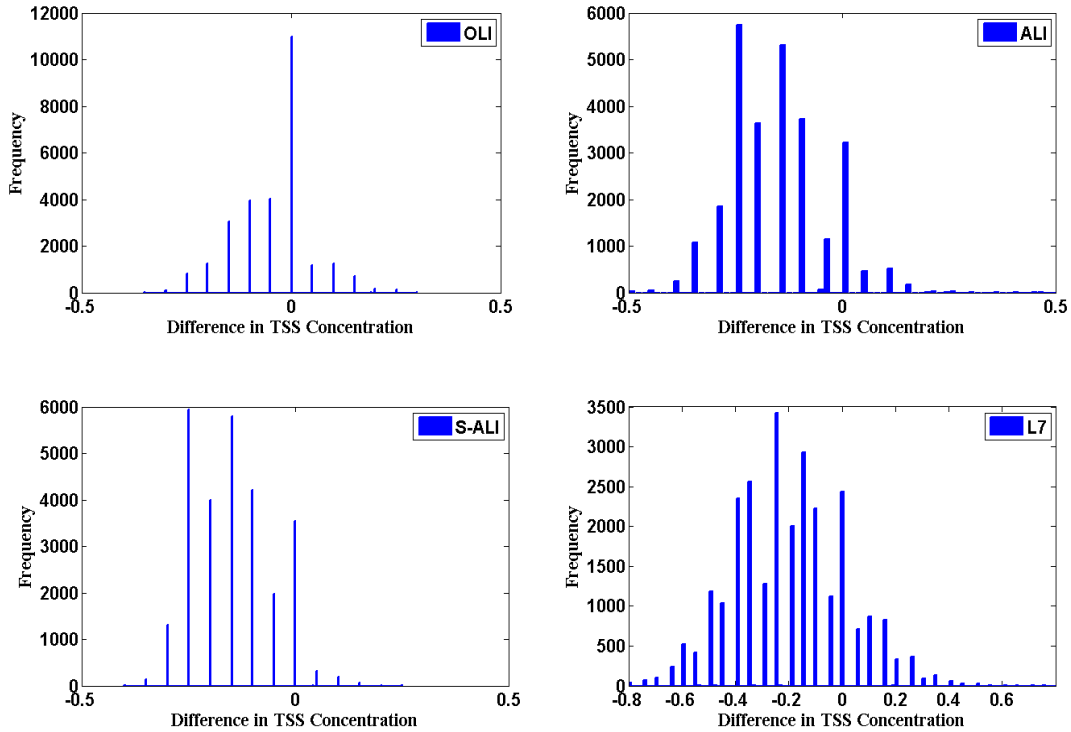


Figure 5.29. The histograms associated with the difference maps of TSS concentrations over the plume using the Hyperion-derived map as a reference.

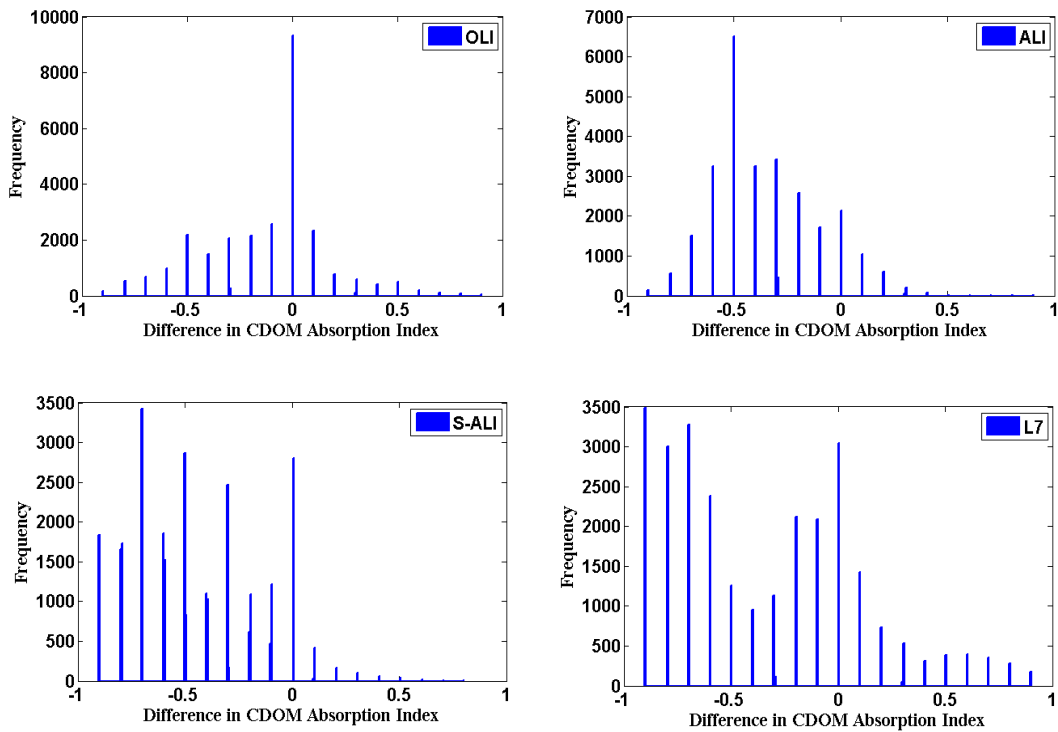


Figure 5.30. The histograms associated with the difference maps of CDOM index maps over the plume using the Hyperion-derived map as a reference.

Figure 5.29 illustrates the histograms associated with the difference maps of TSS concentrations. A general overview of the plots denotes that the multispectral systems tend to underestimate the TSS concentrations relative to Hyperion. Among the histograms, the one obtained from S-OLI shows the largest similarities with the Hyperion-derived map. As in Figure 5.28, similar features are found in the histograms of S-ALI and ALI for the difference maps of TSS concentrations. Similar to Figure 5.28, the histogram associated with L7 exhibits a large dispersion due to the L7's poor radiometric resolution and its low SNR over bodies of water.

The histograms obtained from the difference maps of CDOM indices are shown in Figure 5.30. As in the results from the difference maps of CHL and TSS concentrations, the CDOM map derived from S-OLI resembles that of Hyperion the most. While the histogram associated with ALI shows the underestimation of CDOM indices, the S-ALI-derived plot indicates a large dispersion as well as an underestimation of the indices over the plume. The largest dispersion either positive or negative is found in the L7-derived plot, which highlights the inability of the L7 instrument to retrieve CDOM absorption.

5.3.2 Quantitative Comparison

Table 5.3 provides a quantitative comparison between the concentration maps obtained via the different datasets over the turbid (plume) waters ($TSS > 0.5 \text{ g/m}^3$) and the offshore areas. This table includes the basic statistics, including the mean and the CV (the standard deviation over the mean) expressed in [%]. The CV gives an indication of the spatial variability, which is mainly affected by a dataset's SNR and radiometric resolution. Note that the statistics were derived from ~27000 pixels over the plume and ~20000 pixels in the offshore areas covered by all of the datasets. Based on these first-order statistics, it is inferred that the multispectral datasets always overestimate the CHL concentration relative to the Hyperion dataset over the plume area. However, over the non-plume areas, the CHL concentrations are well predicted by the multispectral systems, i.e., +0.10, on average, (except L7) for an average 0.81 ug/l . A similar observation was found in the non-plume areas for the TSS concentration. Although the TSS map derived from the L7 data appears to be its most accurate products, its poor radiometric fidelity yields high spatial variability, i.e., CV=30%, over the plume area. This is 7%, on average, larger than those from the other data.

Table 5.3. The area-specific basic statistics for the concentration maps

Instrument	Constituent	Plume		Offshore	
		Mean	CV	Mean	CV
Hyperion	CHL	2.49	24%	0.81	34%
	TSS	1.06	24%	0.08	31%
	CDOM	0.83	28%	0.26	33%
S-OLI	CHL	2.8	30%	0.82	32%
	TSS	1.01	24%	0.08	36%
	CDOM	0.67	45%	0.28	39%
ALI	CHL	3.3	20%	1.00	35%
	TSS	0.90	23%	0.07	36%
	CDOM	0.45	35%	0.23	29%
S-ALI	CHL	3.5	21%	0.93	32%
	TSS	0.90	24%	0.07	40%
	CDOM	0.32	73%	0.22	44%
S-L7	CHL	3.9	22%	0.91	29%
	TSS	0.90	23%	0.07	38%
	CDOM	0.29	80%	0.22	38%
L7	CHL	3.6	37%	1.17	71%
	TSS	0.8	30%	0.07	91%
	CDOM	0.41	80%	0.21	80%

The same trend, but much more significant, is found for the non-plume areas (CV=91%).

When retrieving the CDOM absorption, the lowest spatial variability comes from the ALI-derived map. This corresponds to the ALI's high SNR, i.e., 200 versus, on average, 50 for the other scenes (Figure 4.35). On the other hand, the relatively low SNR associated with the Hyperion's blue bands ($\lambda < 450 \text{ nm}$) lead to unrealistic variability in the CDOM maps obtained from Hyperion, S-OLI, and S-ALI. The average CDOM absorption for all the datasets in the plume area indicates the CDOM index of ~ 0.8 [unitless] ($a_{CDOM}(440) \approx 0.1 \text{ m}^{-1}$), which is $\sim 20\%$ lower than what was measured *in situ* at the river mouth (Figure 4.14).

Figure 5.31 illustrates the overall RMSE calculated over the plume area by using the Hyperion-derived concentrations as references:

$$RMSE_C = \left(\sum_{i,j} (C_{i,j} - R_{i,j})^2 / N \right)^{1/2} \quad 5-4$$

Where C is the concentration map, R is the reference map obtained from Hyperion, N stands for the number of pixels, and i and j are the pixel indices.

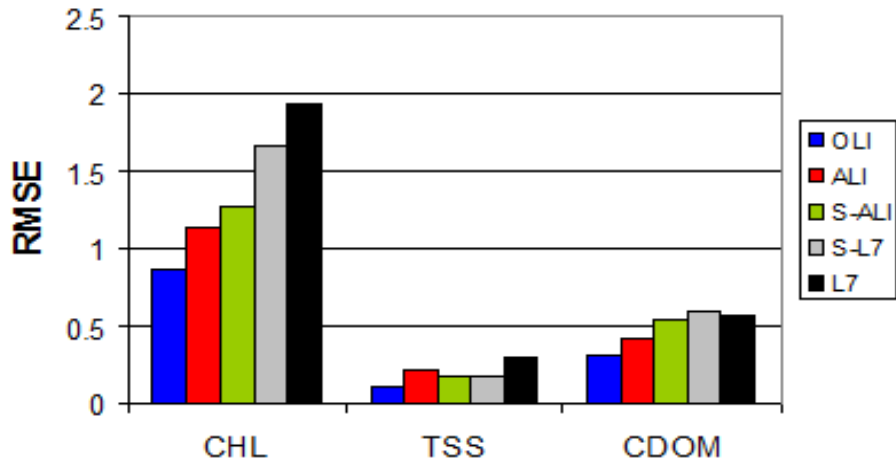


Figure 5.31. The RMSE values obtained for each concentration map for different datasets over the plume area.

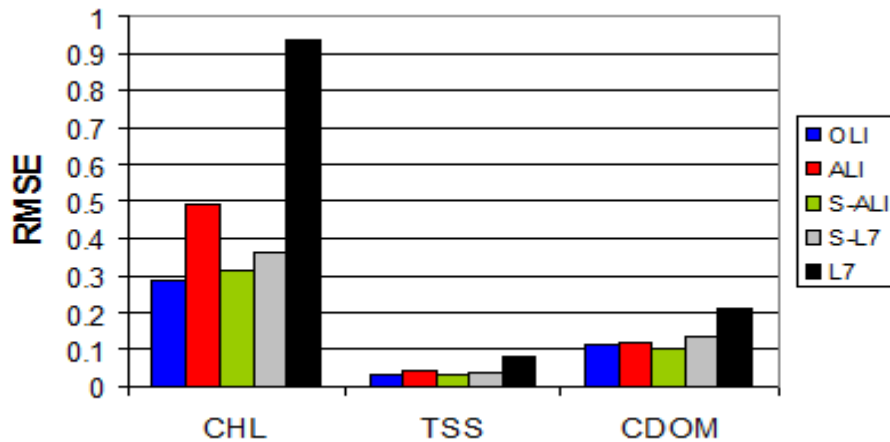


Figure 5.32. The RMSE values obtained for each concentration map for different datasets over the non-plume area.

As expected from the qualitative analysis and the average concentration values listed in Table 5.3 for the plume area, the lowest overall RMSE value comes from the S-OLI dataset. While the RMSE for the CHL map, which is derived from S-OLI, remains below $< 0.8 \text{ ug/l}$ (25% error in average sense), the derived RMSE for the TSS map was found to be $< 0.1 \text{ g/m}^3$ (8% error, on average). The RMSE associated with the CDOM map also represented < 0.32 [unitless] disparity, which is equivalent to 40% average error. Note that these error levels consist of the errors due to inconsistencies in the IOP estimation as well.

The relatively large difference in the CHL derived for the S-OLI and S-ALI are directly related to the differences in the RSRs, which implies improvements in the response of the OLI sensor. The enhanced RSRs of the OLI's spectral channels can be also inferred from the errors obtained for the CDOM maps. The largest errors from the S-L7 and L7 (> 60%, on average) confirm the inability of the conventional Landsat system in the retrieval of the chlorophyll-a concentration when compared to the enhanced systems with an additional band and better radiometric fidelity. However, the existing Landsat system (L7) is sufficiently reliable for TSS retrieval in turbid waters as shown in Figure 5.31. The disparity between S-L7 and L7 in the TSS retrieval suggests the improvement level (15% versus 25%) solely due to the enhanced quantization of the S-L7. When investigating the RMSE associated with the ALI-derived maps, it can be concluded that the ALI instrument designed as a testbed for the OLI sensor demonstrates nearly similar errors to those of S-OLI. However, a comparison between the CV values for ALI and S-OLI (Table 5.3) demonstrates how smooth the ALI-derived concentrations are relative to those of S-OLI (simulated from Hyperion). The CVs obtained for ALI exhibit the expected variability in the future OLI sensor.

Figure 5.32 illustrates the overall error values calculated throughout the non-plume areas (~ 20000 pixels) using Eq. 5-4. As in the plume area, the errors associated with the S-OLI show the closest agreement with the Hyperion-derived concentrations of CHL and TSS. However, S-ALI exhibits a slightly better performance than S-OLI when retrieving CDOM indices, i.e., 24% versus 31% average error. That being said, higher spatial variability was found for the S-ALI than that in S-OLI (Table 5.3). Based on these observations, it is concluded that the disparity between the response functions of OLI and ALI is most noticeable in turbid waters than in slightly turbid waters. Therefore, similar performance for the two instruments is expected in relatively clear waters with ALI exhibiting more spatial variability in such areas. Nonetheless, the ALI-derived CHL concentration map shows larger errors than the other concentrations derived from S-OLI, S-L7, and S-ALI (shown also in Table 5.3 where the average ALI-derived concentration is $1 \mu\text{g}/\text{l}$ versus $0.82 \mu\text{g}/\text{l}$ from Hyperion). This can be related to the slight inconsistencies in the atmospheric correction process when determining the average scene-derived radiance values. The L7-derived errors, however, are much greater than those of other datasets, particular, when CHL and CDOM absorption maps are desired.

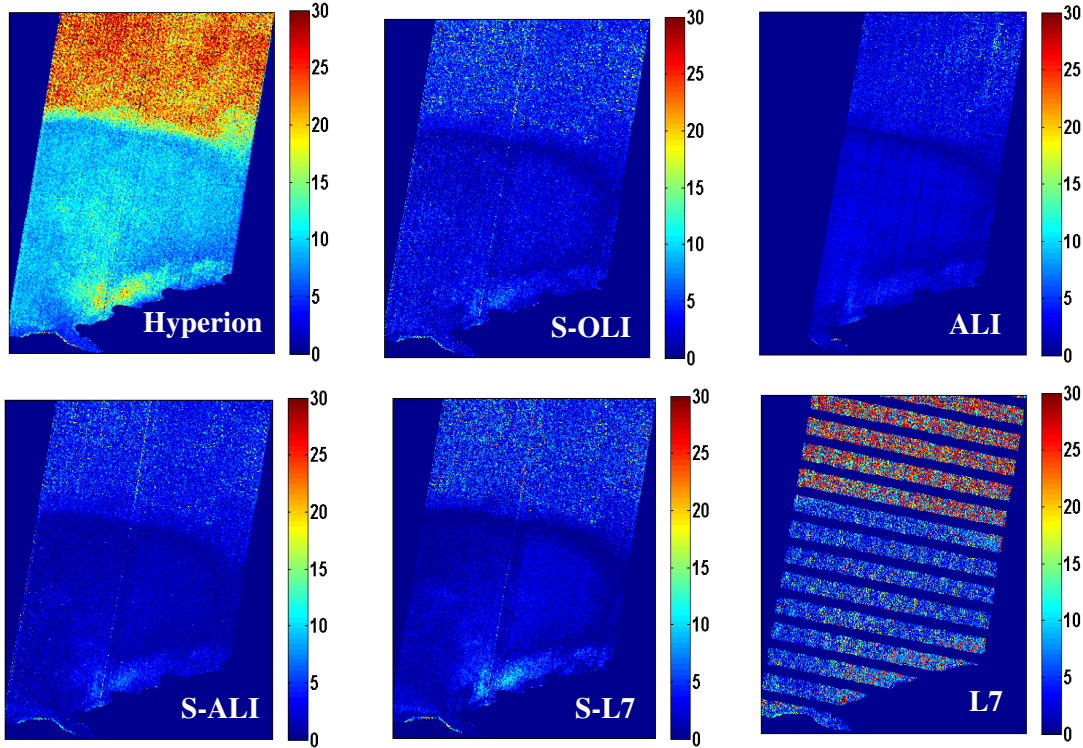


Figure 5.33. The error maps [%] derived for each dataset

Figure 5.33 illustrates the error maps ($EMAP$) [%] for the concentration maps derived from all of the original datasets. These maps measure the goodness of fit between a pixel's curve and the corresponding matched curve via computing the percent difference error averaged over the number of bands:

$$EMAP_{i,j} = \sum_{\lambda} \left| \frac{(Obs_{i,j}^{\lambda} - Mod_{i,j}^{\lambda})(Obs_{i,j}^{\lambda} + Mod_{i,j}^{\lambda})^{-1}}{N} \right| \quad 5-5$$

Where i and j are pixel indices, Obs and Mod denote the image- and the model-derived values, and N is the number of bands over which the dissimilarity is computed. The percent errors specify the uncertainties associated with the spectral optimization technique applied in this study.

As described in Section 4.6, $N=31$ for Hyperion, $N=4$ for S-OLI, ALI, and S-ALI, and $N=3$ for S-L7 and L7. In addition to evaluating the level of disparity between the matched curve and that of the image pixel, the $EMAP$ provides a synoptic overview on whether the averaged IOPs used in the study area properly represent ubiquitous optical properties in the entire domain. Besides, it gives an indication of noise level in different parts of the image. In other words, a high percent error associated with a pixel suggests an ill-shaped image-derived

curve. As seen in Figure 5.33, the *EMAP* associated with Hyperion exhibits the highest inconsistencies relative to the modeled spectra. Based on the ranges of errors corresponding to this map, three zones can be defined, namely the offshore zone ($20 < EMAP < 30$), the plume surroundings ($13 < EMAP < 22$), and the plume area ($EMAP < 12$). The large discrepancies in the offshore zone imply the noisy nature of the Hyperion-derived spectrum for each individual pixel as compared to smoothed modeled curves. This is confirmed with an average 28% error where the Hyperion's scene-derived SNR is 66.6 on average (4.6.2). The plume surroundings exhibit relatively moderate error levels, which can be related, in part, to low signal levels. However, the average IOPs measured in the river mouth where $TSS > 1.3 \text{ g/m}^3$, $CHL > 2.7 \text{ ug/l}$, and $a_{CDOM}(440) \approx 0.13$ do not well represent the IOPs in such a zone where low TSS concentrations ($TSS < 0.4 \text{ g/m}^3$) are present [Binding *et. al.*, 2008]. Therefore, care must be taken when interpreting the predicted concentrations in such areas (Figure 5.27) where high concentrations of CHL and relatively low concentration of TSS and dissolved matter have been determined. By analogy, similar segments as in the Hyperion-derived *EMAP* can be identified for the multispectral datasets; however, the percent errors are significantly smaller than those derived from Hyperion. Among the multispectral *EMAP*s, ALI shows, on average, the lowest error values throughout the area (due to its relatively high SNR) whereas the *EMAP* corresponding to the L7 dataset represents the highest error levels, particularly, in the offshore zone. In addition, the *EMAP* associated with the S-L7 shows relatively large spatial variations, which are slightly higher than those of S-ALI and S-OLI, in the offshore zone. It appears that the addition of the short blue band contributed in reducing the disparity between the modeled spectra and the image-derived curves.

Overall, the low signal levels and the spatial non-uniformities of the IOPs contribute to the mis-match in the spectral optimization process. It is expected that the OLI sensor will deliver high SNR imagery comparable to that of ALI. Although not severe in this study, the spatial heterogeneity of the IOPs is considered as the primary impeding factors. One possible solution when retrieving constituent over extensive areas is to relax the IOPs over a plausible range and perform constrained optimization in the retrieval process.

5.3.3 Summary

In this case study a Hyperion dataset was utilized to demonstrate the capability of the OLI sensor for coastal/inland water studies. A physics-based, LUT approach followed by an optimization was carried out to retrieve concentrations of water constituents on a pixel-by-pixel basis. The OLI-derived concentrations were analyzed against those obtained from Hyperion, ALI, simulated ALI, simulated L7, and L7. In general, using the Hyperion-derived concentrations as the validation source, it was found that OLI outperforms the existing multispectral systems both in terms of its radiometric fidelity and its spectral band configuration. Comparisons made with the existing Landsat showed that not only does the OLI sensor provide more realistic TSS maps than those of L7, i.e., 20% better, on average, throughout the study area, but also it enables a relatively robust retrieval of the surface distribution of CHL and CDOM absorption. It was shown that OLI achieves 25%, 12%, and 35% errors in the retrieval of CHL, TSS, and CDOM relative to the Hyperion-derived maps over the entire area. Moreover, the OLI system with its enhanced capabilities was found to exceed the ALI sensor in performance. This was demonstrated by comparing the results from the simulated OLI and simulated ALI datasets where the differences in the retrieval process were solely associated with the systems' response functions. Over the plume area, the simulated OLI imagery outperformed the ALI dataset in the retrieval of CHL, TSS, and CDOM on the order of 20%, 7%, and 19%, respectively. The differences between the two systems were not noticeable in the clearer waters; nonetheless, the simulated OLI produced smoother maps than the simulated ALI. Also, the simulated OLI sensor was found to perform better than the existing ALI dataset, although the ALI generated maps with small spatial variability, which is expected for the actual OLI sensor. With the OLI sensor in operation from 2013, time-series of regional, high-fidelity water quality maps, which have never been achievable, can be made available for studying coastal/inland waters.

Chapter 6

6. Conclusions and Recommendations

This research effort addressed the potential of the Landsat Data Continuity Mission (LDCM) in a water-study framework. The availability of Landsat imagery over the past four decades have made significant impacts in the way human-being monitors and studies the environmental trends at regional/global scales. Among the wide variety of its application areas, such as forestry, agriculture, and crop assessments, L7 also plays a crucial role in water resource monitoring. However, its design specifications, i.e., 8-bit quantization and three visible spectral channels, aiming at investigating land targets, have limited its applicability. In this study, we used L7 imagery as a surrogate for the LDCM to examine a novel approach for monitoring the dynamics of coastal/inland waters. The procedure introduced here is applicable to the next generation Landsat (LDCM) whose specifications have been dramatically enhanced relative to those common to the typical Landsat satellites. LDCM carries the OLI and TIRS instruments to image the globe in both the reflective and thermal spectral channels. While the two instruments have enhanced radiometric fidelity (12-bit), the OLI sensor is also equipped with an additional band centered at 443 *nm*, which was added specifically for water studies as well as for aiding the removal of the atmospheric effects.

In order to apply our proposed approach to L7 data for monitoring the dynamics of coastal/inland waters, one has to ensure that it meets the uncertainty requirements defined for the mission, i.e. 5% units of TOA radiance. Although L7's calibration status has been regularly monitored over medium- to high-reflective targets since its launched, no rigorous study has been conducted to examine its status over dark targets (water). Therefore, prior to implementing our procedure, the calibration status of L7 was evaluated using a cross-

calibration technique over several calibration sites whose optical properties are relatively stable.

6.1. Cross-calibration

The primary impeding factor in performing such an on-orbit cross-comparison is the lack of knowledge on the effects of the differences in the sensors' relative spectral response functions. This is further complicated when sensing signals primarily contaminated by the atmospheric effects. A model-based technique was proposed to account for such differences. In this method, several atmospheric conditions as well as multiple water types were incorporated to estimate the closest TOA radiance observed by the MODIS sensor at each calibration site. The historical trend studies verified Terra's significant degradation over the past three years, i.e., 2008-2011. It was found that, during 2000-2007, L7 has registered slightly lower signal levels in the blue and the green bands than MODIS. On the other hand, L7 tends to overestimate signals in the red and the NIR bands. The disparities, on average, were quantified as -1%, -0.5%, +2.5%, and +5.6% in units of TOA reflectance [%] in the blue, green, red, and the NIR bands. The corresponding differences over the RVPN site were found to be consistent with the recent studies with the exception in the blue band where the Terra instrument exhibits significant degradations. The small over-water calibration differences, negligible when imaging most land targets, were further analyzed via propagating them to the surface reflectance domain followed by the retrieval of water constituents. This was accomplished by treating the calibration differences as bias-only errors and considering Terra-MODIS as the reference system. The model-based simulations under typical atmospheric conditions showed that the calibration errors, on average, lead to -7%, -3%, and +26% errors in the blue, green, and red bands when retrieving r_d for eutrophic/moderately turbid waters. A case study conducted in a site with comparable nutrient/turbidity levels demonstrated that such errors introduce 10% uncertainty when retrieving the concentrations of water constituents. Such bias-only errors cause overestimations in the predicted CHL concentration and underestimate the TSS concentration. This error level, however, is a large fraction of the 25-30% error typically considered acceptable for characterization of water. The calibration errors in the NIR band, although not significant when retrieving water constituents over most waters, can cause considerable errors in

estimating the atmospheric conditions if physics-based models are utilized. The new generation of Landsat (LDCM) with its advanced technology is expected to outperform L7 when studying water resources. This new capability will require rigorous, over-water characterizations of its calibration stability to facilitate the use of physics-based techniques for atmospheric corrections and, consequently, reliable retrieval of bio-physical parameters. Also, it should be noted the sensor calibration issues can be mitigated through in-scene methods, such as ELM.

6.2. L7-Model Integration

In the second task, the ALGE model was used in conjunction with the L7 imagery to improve our ability in predicting the dynamics of the coastal/inland waters. In this process, both the thermal and the reflective bands of the L7 data were applied in the water constituent retrieval task. While the thermally driven ALGE model is calibrated through L7 thermal imagery, the reflective imagery are used to optimize the input concentrations of water constituents provided to the model. In the thermal domain, the L7-derived surface temperature maps are considered as the truth with which the best modeled surface temperature is found. This is done through modeling various environmental conditions by varying input parameters, such as wind speed, wind direction, river discharge and river temperature. The optimal input concentrations are obtained via comparing a subset of the modeled surface reflectance with that produced from L7. The Hydrolight code was used to simulate the water-leaving reflectance for various concentration maps modeled through ALGE.

The above approach was examined for two different river plumes of different sizes in six various timeframes. This approach was also applied in a small lake environment to fully investigate the model performance. From the model calibrations in the Genesee River plume, it was found that the ALGE model is capable of reasonably modeling the shape of the plume when the river discharge is sufficiently large. Although the average adjustments of the environmental variables were less than 6%, the model performance can be still improved by supplying the hourly measured river temperatures and concentrations. Accurate current velocity and the hourly temperature profiles at the boundaries derived from the whole lake simulation also can largely contribute to the success of the model. However, due to the

geometry of the Rochester Embayment area, the Genesee plume is less affected by the lake circulation pattern when compared to the Niagara River plume. If there is good knowledge of the IOPs, the profiles of water constituents can be estimated through coupling of ALGE and Hydrolight. The estimated discrepancy over the plume area in the constituent retrieval process was found to be less than 0.68% in units of surface reflectance, i.e., $RMSE < 0.0068$. It was also found that ALGE underestimates the extent of the plume when modeling the dissipation of particle and dissolved matter. Although the Genesee plume was modeled in another period (Oct. 2009) when the discharge was below annual average, further simulations of the Genesee plume needs to be carried out to ensure its functionality in various environmental conditions.

The Niagara River plume simulation was attempted for four timeframes out of which only one (Oct. 2010) provided a realistic shape of the plume ($RMSE < 0.34^\circ C$). The distributions of the particle and dissolved matter, however, were not in full agreement with the remotely sensed observations resulting in, on average, 0.009 units of reflectance. The mis-prediction of the material distribution was also observed in the Niagara plume modeling. In the other case studies of the Niagara River plume, the primary reason causing the model to fail is the failure in the lake-wide simulation from which the hourly current velocities and the temperature profiles are derived. The massive Niagara plume draining into the western basin of Lake Ontario is significantly influenced by the eddies and circulations in this region from west to east, which is primarily driven by the Coriolis force and dominant westerly winds. The complex eddies in the coastal regions are formed as a result of a combination of several physical processes, including the input flux from the river, upwelling/downwelling processes due to occasional/persistent wind forcing, and buoyancy forces. Such small-scale circulations interacting with the river plume may not be captured with a discrete model domain in space and time. It is believed that when accurate current velocities and temperature profiles are available, the model performance should dramatically improve when modeling the Niagara River plume in most occasions. In addition, initiating the model with an average lake-wide temperature profile could improve the modeling effort. Currently, the ALGE model is only capable of accepting a vertically uniform initial temperature estimated from the MODIS data.

Two other simulations were also done for Onondaga Lake. The main variables contributing to the thermal structure of the lake are the wind pattern and the parameters

controlling the available heat budget, i.e., the sky fraction and the cloud height. The impeding factor adversely affecting the Onondaga Lake simulation is the alterations in the wind pattern due to natural and man-made obscuration surrounding the lake. To account for such environmental impacts, the wind speed was reduced 28% and the wind axis was rotated 22° for May 2010 period. It was found that smoothing the wind pattern could enhance the model performance. The variations in the river discharge and river temperatures made no significant impact in predicting the overall thermal structure of the lake. Following calibrating the model in the thermal domain, it was revealed that there is not significant correlation between the surface temperature and the material distribution in the lake, which invalidates our primary assumption. The relatively large nutrient loads from the tributaries and sewage discharges further complicate this inconsistency. Incorporating more *in situ* measurements and more lucid knowledge of the nutrients and their physical properties could enhance the model performance in such an environment. Also, it was shown that adding all the mass sources could improve the material transport/distribution.

Overall, the proposed approach works well for monitoring river plumes and inland waters if the noted improvements, including better lake-wide simulations in space and time, flexible simulations of material transport via enabling the code to receive more information regarding the particle size and particle density, and the ability to add several input fluxes with variable time-series of temperature and discharge. Owing to the LDCM's enhanced characteristics, it is possible to more accurately calibrate the model in both thermal and reflective domains, especially, when modeling small-scale water features, such as the Genesee River plume and complexities in Onondaga Lake.

6.3. OLI's potential for Water Studies

A comprehensive cross-comparison between the water constituent concentrations derived from Hyperion, ALI, L7, simulated OLI, simulated L7, and simulated ALI was performed to fully investigate the improvement levels in the OLI sensor when studying case II waters. In this analysis the Hyperion-derived concentration were considered as the validation source. The analysis showed a dramatic improvement in the retrieval of CHL and $a_{CDOM}(440)$ using the S-OLI data relative to the L7 data. The failure in the retrieval of CHL and

a_{CDOM} (440) through S-L7 further emphasized the large contribution of the new spectral band at 443 nm when retrieving the two components. The relatively low spatial variability in the retrieved concentrations from S-OLI indicates significant improvements with respect to L7 due to the enhanced radiometric fidelity. Although L7 failed to accurately map these two components, its derived TSS map appeared to be comparable to those of the other datasets. However, its poor radiometric fidelity causes unrealistic spatial variability. The smoothest concentration maps were obtained from the ALI dataset whose SNR was found to be the greatest the water bodies. However, when comparing the concentrations derived from the S-OLI and the S-ALI datasets, it was inferred that the differences in the RSRs of the systems clearly influence the retrieval process. The enhanced responses of the OLI sensor improved the averaged concentration levels throughout the area, especially, in the turbid waters. The averaged concentrations, in particular, CHL and a_{CDOM} (440) derived from the S-OLI dataset showed significant improvements when compared to those obtained from S-ALI. Note that the Hyperion-derived maps were treated as the truth map. According to the outcome of this cross-comparison, it was revealed that the OLI sensor is expected to significantly outperform the existing L7 data when sensing case II waters. Nevertheless, the TSS concentration maps of L7 over turbid waters should be well comparable to those of OLI, which facilitate long-term monitoring of turbidity level over coastal and inland waters. Moreover, the new technology and better sensor characterizations of the OLI sensor allow for more accurate retrievals of concentrations when compared to the ALI sensor. It should be also emphasized that the spectral optimization technique, which is typically used in conjunction with the hyperspectral datasets, proved to perform well when retrieving constituent concentrations from the multispectral systems. This can be inferred when comparing the concentration levels derived from the S-OLI and the Hyperion imagery.

6.4. Recommendations

This effort used L7 imagery as surrogate to demonstrate an integrated approach allowing for monitoring of coastal waters at spatial scales that may not be feasible through coarse-resolution space-borne systems. A cross-calibration technique was also introduced to evaluate the calibration status of L7 over deep, dark waters. This cost-effective method can

be extended to monitor the calibration stability of LDCM whose enhanced capabilities enable the use of physics-based techniques for the retrieval of surface properties and in-water optical properties. The improved performance of the OLI sensor for water studies was analyzed against other flavors of datasets, including Hyperion, ALI, and L7, throughout relatively turbid waters. The following task-specific suggestions are made to aid in developing similar studies

In order to be able to estimate a missing component of the IOPs, such as the scattering coefficients, the curve fitting technique described in Section 4.3.3.1 can be utilized providing that the *in situ* water-leaving reflectance has been already corrected for the sky glint effects. The skylight reflecting off the water surface, depending on the total signal level, can introduce wavelength-dependent errors to the measured spectrum. To avoid the post-processing of the measurements just above the water surface, one can follow the practical instructions found in [Lee *et. al.*, 2010]. For the curve-fitting technique to represent the physical reality of the IOPs and the concentrations, the knowledge of concentrations and absorption coefficients are required.

The ALGE computation expenses can be well diminished through optimizing several coarse-resolution simulations in any environment. Such simulations provide intuitive understanding of the dominant variables controlling the modeling efforts; thereby performing an efficient calibration of the model in the thermal domain. To further enhance the model performance, the code should be modified such that it would be capable of obtaining a temperature profile of the lake as initial lake temperature particularly during the stratification periods. Furthermore, the material transport should be improved to allow for a better representation of the sediment load in river plume modeling.

The ELM atmospheric correction has to be performed using pure pixels for the reference targets. In the absence of pure beach-sand pixels, one may use turbid waters as the bright target to enable the atmospheric removal over water bodies. Care must be taken when studying an extensive area where atmospheric pattern may be spatially non-uniform. The SWIR bands can be utilized to enable identifying atmospherically non-uniform areas.

In a water constituent retrieval task, multiple measurements of IOPs over the different water types are needed to ensure that an average would work. If the IOPs are measured in only one water type, the IOPs need to be slightly varied to produce realistic concentration maps for various water types present in the study area.

In order to accomplish an accurate, over-water cross-calibration the atmospheric condition needs to be estimated through either a spectral optimization technique or the band-ratio method suggested by [Ruddick *et. al.*, 2000]. A broader spectrum of aerosol models is suggested to be used in this process to gain a better estimation of the atmospheric condition. To check for consistencies in the atmospheric conditions between the satellite overpasses, the expected differences in the SWIR responses (due to differences in RSRs) are compared with the image-derived differences.

To ensure that the cross-calibration results are valid, the reference sensor has to record valid responses, i.e., no negative values. The Terra-MODIS instrument, however, has recently been registering "negative" radiance values over Lake Tahoe area due to significant degradations in the system. Therefore, applying a well-calibrated system as a reference is necessary. The availability of the recently launched Visible/Infrared Imager/Radiometer Suite (VIIRS) aboard NPOESS Preparatory Project (NPP) mission allows for cross-comparisons with the existing L7 or the next generation Landsat.

Although Lake Tahoe as well as a few other sites, such as Lake Malawi and Red Sea, were introduced as potential sites for an over-water cross-calibration, more research is needed to identify other suitable sites, including lake and open waters, to facilitate an even more robust cross-comparison.

7. Bibliography

- Ahsan, A. K. M. Q. and Blumberg, A. F. (1999). Three-Dimensional Hydrothermal Model of Onondaga Lake, New York. *Journal of Hydraulic Engineering* 125(9): 912-923.
- Barsi, J. A. (2011). Personal communications. Greenbelt, MD, USA.
- Berk, A., Bernstein, L. and Robertson, D. C. (1989). MODTRAN: a moderate resolution model for LOWTRAN 7, Spectral Sciences.
- Binding, C. E., Bowers, D. G. and Mitchelson-Jacob, E. G. (2005). Estimating suspended sediment concentrations from ocean colour measurements in moderately turbid waters; the impact of variable particle scattering properties. *Remote Sensing of Environment* 94(3): 373-383.
- Binding, C. E., Jerome, J. H., Bukata, R. P. and Booty, W. G. (2008). Spectral absorption properties of dissolved and particulate matter in Lake Erie. *Remote Sensing of Environment* 112(4): 1702-1711.
- Bowers, D. G., Binding, C. E. and Ellis, K. M. (2007). Satellite remote sensing of the geographical distribution of suspended particle size in an energetic shelf sea. *Estuarine, Coastal and Shelf Science* 73(3-4): 457-466.
- Bowers, D. G., Braithwaite, K. M., Nimmo-Smith, W. A. M. and Graham, G. W. (2009). Light scattering by particles suspended in the sea: The role of particle size and density. *Continental Shelf Research* 29(14): 1748-1755.
- Boyce, F. M. (1974). Some aspects of Great Lakes physics of importance to biological and chemical process. *Journal of Fisheries Research board of Canada* 31: 41.
- Brando, V. E. and Dekker, A. G. (2003). Satellite hyperspectral remote sensing for estimating estuarine and coastal water quality. *Geoscience and Remote Sensing, IEEE Transactions on* 41(6): 1378-1387.
- Bryant, R., Moran, M. S., McElroy, S. A., Holifield, C., Thome, K. J., Miura, T. and Biggar, S. F. (2003). Data continuity of Earth Observing 1 (EO-1) Advanced Land Imager (ALI) and Landsat TM and ETM. *IEEE Transactions on Geoscience and Remote Sensing* 41(6): 1204-1214.
- Chander, G., Meyer, D. J. and Helder, D. L. (2004). Cross calibration of the Landsat-7 ETM+ and EO-1 ALI sensor. *IEEE Transactions on Geoscience and Remote Sensing* 42(12): 2821-2831.

- Chander, G., Mishra, N., Helder, D. L., Aaron, D., Choi, T., Angal, A. and Xiong, X. (2010(b)). Use of EO-1 Hyperion Data to Calculate Spectral Band Adjustment Factors (SBAF) between The L7 ETM+ and TERRA MODIS Sensors. *2010 IEEE International Geoscience and Remote Sensing Symposium, Honolulu, HI, USA, IEEE*.
- Chen, X., Lu, J., Cui, T., Jiang, W., Tian, L., Chen, L. and Zhao, W. (2010). Coupling remote sensing retrieval with numerical simulation for SPM study--Taking Bohai Sea in China as a case. *International Journal of Applied Earth Observation and Geoinformation* 12(Supplement 2): S203-S211.
- Cleveland, J. S., Weidmann, A.D. (1993). Quantifying absorption by aquatic particles: A multiple scattering correction for glass-fiber filters. *Limnology and Oceanography* 38(6): 6.
- Czapla-Myers, J. (2011). Personal Communications
- Del Castillo, C. E. and Miller, R. L. (2008). On the use of ocean color remote sensing to measure the transport of dissolved organic carbon by the Mississippi River Plume. *Remote Sensing of Environment* 112(3): 836-844.
- Doxaran, D., Cherukuru, R. C. N. and Lavender, S. J. (2004). Estimation of surface reflection effects on upwelling radiance field measurements in turbid waters. *Journal of Optics A: Pure and Applied Optics* 6(7): 690.
- Dudgale, S. (2007). An evaluation of imagery from an unmanned aerial vehicle (UAV) for the mapping of intertidal macroalgae on Seal Sands, Tees Estuary, UK. *Geography Department M.Sc. by Research*, 132.
- Effler, S. W. (1996). *Limnological and Engineering Analysis of a Polluted Urban Lake: Prelude to Environmental Management of Onondaga Lake, New York* New York, Springer-Verlag
- Folkman, M. A., Pearlman, J., Liao, L.B., Jareck, P.J. (2001). EO-1/Hyperion hyperspectral imager design, development, characterization, and calibration. *Hyperspectral Remote Sensing of the Land and Atmosphere Sendai, Japan, SPIE*.
- Franz, B. A., Kwiatkowska, E. J., Meister, G. and McClain, C. R. (2007). *Utility of MODIS-Terra for ocean color applications - art. no. 66770Q. Earth Observing Systems Xii*. J. J. Butler and J. Xiong. 6677: Q6770-Q6770.
- Garrett, A. J. (1995). ALGE: A 3-D thermal plume prediction code for lakes, rivers and estuaries. Aiken, South Carolina., Savannah River Technology Center: 76.
- Garrett, A. J. (2002). Analyses of MTI imagery of power plant thermal discharge *Proceedings of SPIE*, Proceedings of SPIE.

- Garrett, A. J., Hayes, D. (1997). Cooling lake simulations compared to thermal imagery and dye tracers. *Journal of Hydraulic Engineering* 123: 14.
- Garrett, A. J., Irvine, J. M., King, A. D., Evers, T. K., Levine, D. A., Ford, C. and Smyre, J. L. (2000). Application of multispectral imagery to assessment of a hydrodynamic simulation of an effluent stream entering the Clinch River. *Photogrammetric Engineering and Remote Sensing* 66(3): 329-335.
- Gerace, A. D. (2010). Demonstrating Landsat's New Potential to Monitor Coastal and Inland Waters. *Imaging Science* Ph.D. Thesis, 172.
- Gitelson, A. A., Schalles, J. F. and Hladik, C. M. (2007). Remote chlorophyll-a retrieval in turbid, productive estuaries: Chesapeake Bay case study. *Remote Sensing of Environment* 109(4): 464-472.
- Gordon, H. R. (1998). In-orbit calibration strategy for ocean color sensors. *Remote Sensing of Environment* 63(3): 265-278.
- Gordon, H. R. and Wang, M. (1994). Retrieval of water-leaving radiance and aerosol optical thickness over the oceans with SeaWiFS: a preliminary algorithm. *Appl. Opt.* 33(3): 443-452.
- Green, R. O., Pavri, B. E. and Chrien, T. G. (2003). On-orbit radiometric and spectral calibration characteristics of EO-1 Hyperion derived with an underflight of AVIRIS and in situ measurements at Salar de Arizaro, Argentina. *IEEE Transactions on Geoscience and Remote Sensing* 41(6): 1194-1203.
- Hakvoort, H., de Haan, J., Jordans, R., Vos, R., Peters, S. and Rijkeboer, M. (2002). Towards airborne remote sensing of water quality in The Netherlands--validation and error analysis. *ISPRS Journal of Photogrammetry and Remote Sensing* 57(3): 171-183.
- Haltrin, V. I. (1998). An analytic Fournier-Forand scattering phase function as an alternative to the Henyey-Greenstein phase function in hydrologic optics. *IGARSS '98. 1998 IEEE International Seattle, WA, USA.*
- Hayashida, T., Atkinson, J. F., DePinto, J. V. and Rumer, R. R. (1999). A Numerical Study of the Niagara River Discharge Near-Shore Flow Field in Lake Ontario. *Journal of Great Lakes Research* 25(4): 897-909.
- Holst, G. C. (2008). *Electro-optical Imaging System Performance*. Bellingham JCD Buliding and SPIE.
- Hook, S. J., Clodius, W. B., Balick, L., Alley, R. E., Abtahi, A., Richards, R. C. and Schladow, S. G. (2005). In-flight validation of mid- and thermal infrared data from the Multispectral Thermal Imager (MTI) using an automated high-altitude validation site at Lake Tahoe CA/NV, USA. *IEEE Transactions on Geoscience and Remote Sensing* 43(9): 1991-1999.

- Jensen, J. R. (2006). *Remote Sensing Of The Environment: An Earth Resource Perspective*. Upper Saddle River, Prentice Hall.
- Jensen, J. R., Kjerfve, B., Ramsey Iii, E. W., Magill, K. E., Medeiros, C. and Sneed, J. E. (1989). Remote sensing and numerical modeling of suspended sediment in Laguna de Terminos, Campeche, Mexico. *Remote Sensing of Environment* 28: 33-44.
- Karpouzli, E., Malthus, T. (2003). The empirical line method for the atmospheric correction of IKONOS imagery. *International Journal of Remote Sensing* 24(5): 7.
- Kishino, M., Takashi, M., Okami, N., Ichimura, S. (1985). Estimation of The Spectral Absorption Coefficients of Phytoplankton in The Sea. *Bulletin of Marine Science* 37(2): 8.
- Kleespies, T. J. and McMillin, L. M. (1990). Retrieval of Precipitable Water from Observations in the Split Window over Varying Surface Temperatures. *Journal of Applied Meteorology* 29(9): 851-862.
- Kunte, P. D., Zhao, C., Osawa, T. and Sugimori, Y. (2005). Sediment distribution study in the Gulf of Kachchh, India, from 3D hydrodynamic model simulation and satellite data. *Journal of Marine Systems* 55(3-4): 139-153.
- Kutser, T., Pierson, D. C., Kallio, K. Y., Reinart, A. and Sobek, S. (2005). Mapping lake CDOM by satellite remote sensing. *Remote Sensing of Environment* 94(4): 535-540.
- Kutser, T., Vahtmäe, E. and Praks, J. (2009). A sun glint correction method for hyperspectral imagery containing areas with non-negligible water leaving NIR signal. *Remote Sensing of Environment* 113(10): 2267-2274.
- Kwiatkowska, E. J., Franz, B. A., Meister, G., McClain, C. R. and Xiong, X. X. (2008). Cross calibration of ocean-color bands from Moderate Resolution Imaging Spectroradiometer on Terra platform. *Applied Optics* 47(36): 6796-6810.
- Lagarias, J. C., Reeds, J. A., Wright, M. H. and Wright, P. E. (1998). Convergence Properties of the Nelder--Mead Simplex Method in Low Dimensions. *SIAM Journal on Optimization* 9(1): 112-147.
- Lee, Z., Ahn, Y.-H., Mobley, C. and Arnone, R. (2010). Removal of surface-reflected light for the measurement of remote-sensing reflectance from an above-surface platform. *Opt. Express* 18(25): 26313-26324.
- Lee, Z., Carder, K. L., Hawes, S. K., Steward, R. G., Peacock, T. G. and Davis, C. O. (1994). Model for the interpretation of hyperspectral remote-sensing reflectance. *Appl. Opt.* 33(24): 5721-5732.

- Li, N., Mao, Z, Zhang,Q,Wang, D, Bai, Y,Pan,D (2008).The numerical simulation and remote sensing of the thermal discharge from the Qinshan Nuclear Power Station. *Remote Sensing of Inland, Coastal, and Oceanic Waters Noumea, New Caledonia SPIE*.
- Li, Y. (2007). An Integrated Water Quality Modeling System with Dynamic Remote Sensing Feedback. *Imaging Science Ph.D.*, 172.
- Li, Y., Vodacek, A., Raqueño, N., Kremens, R., Garrett, A., Bosch, I., Makarewicz, J. and Lewis, T. (2008). Circulation and Stream Plume Modeling in Conesus Lake. *Environmental Modeling and Assessment* 13(2): 275-289.
- Lorenzen, C. J. (1967). Vertical Distribution of Chlorophyll and Pheo-pigments - Baja California *Deep-Sea Research* 14(6): 735-&.
- Makarewicz, J. C., Nowak, M.J. (2010). Genesee River Environmental Health Report. Rochester, The College at Brockport, State University of New York: 5.
- Maritorena, S., Siegel, D. A. and Peterson, A. R. (2002). Optimization of a semianalytical ocean color model for global-scale applications. *Appl. Opt.* 41(15): 2705-2714.
- McCorkel, J. (2011). Updated Hyperion Calibration Coefficients. Boulder (CO).
- Mobley, C. D. (1994). *Light and Water: Radiative transfer in natural waters*, Academic Press, Inc.
- Mobley, C. D., Sundman, L.K. (2008). Hydrolight 5, Ecolight5 User Guide. Bellevue, Sequoia Scientific, Inc.: 97.
- Murtugudde, R. G., Signorini, S. R., Christian, J. R., Busalacchi, A. J., McClain, C. R. and Picaut, J. (1999). Ocean color variability of the tropical Indo-Pacific basin observed by SeaWiFS during 1997-1998. *Journal of Geophysical Research-Oceans* 104(C8): 18351-18366.
- O'Donnell, S. M., O'Donnell, D. M., Owens, E. M., Effler, S. W., Prestigiacomo, A. and Baker, D. M. (2010). Variations in the Stratification Regime of Onondaga Lake: Patterns, Modeling, and Implications. *Fundamental and Applied Limnology* 176(1): 11-27.
- Perkins, M. (2011). Upstate Freshwater Institute. Syracuse
- Rao, Y. R. and Schwab, D. J. (2007). Transport and Mixing Between the Coastal and Offshore Waters in the Great Lakes: a Review. *Journal of Great Lakes Research* 33(1): 202-218.
- Raqueño, R. V. (2003). Hyperspectral Analysis Tools for Multiparameter Inversion of Water Quality Factors in the Lake Ontario Rochester Embayment. *Environmental and Resource Engineering Ph.D. Thesis*, 165.

- Ruddick, K. G., Ovidio, F. and Rijkeboer, M. (2000). Atmospheric correction of SeaWiFS imagery for turbid coastal and inland waters. *Applied Optics* 39(6): 897-912.
- Schladow, G. (2011). Tahoe: State of the Lake Report Incline Village, UC Davis, Tahoe Environmental Research Center 79.
- Schott, J. R. (2007). *Remote Sensing The Image Chain Approach*. New York, Oxford University Press.
- Schwab, D. J., Meadows, G.A., Bennet, J.R., Schultz, H., Liu, P.C., Campbell, J.E., and Dannelongue, H.H. (1984b). The response of the coastal boundary layer to wind and waves: analysis of an experiment in Lake Erie. *Journal of Geophysical Research* 89: 10.
- Scott, D., Schwab, D.J., Zuzek, P, and Padala, C. (2004). Hindcasting wave conditions on the north American Great Lakes. *8th International workshop on wave hindcasting and forecasting, Hawaii, USA*.
- Sheng, J. and Rao, Y. R. (2006). Circulation and thermal structure in Lake Huron and Georgian Bay: Application of a nested-grid hydrodynamic model. *Continental Shelf Research* 26(12-13): 1496-1518.
- Steissberg, T., Schladow, G. and Hook, S. (2010). Monitoring Past, Present, and Future Water Quality Using Remote Sensing, Tahoe Environmental Research Center and Jet Propulsion Laboratory (NASA): 108.
- Stramska, M. and Stramski, D. (2005). Effects of a nonuniform vertical profile of chlorophyll concentration on remote-sensing reflectance of the ocean. *Appl. Opt.* 44(9): 1735-1747.
- Teillet, P. M., Barker, J. L., Markham, B. L., Irish, R. R., Fedosejevs, G. and Storey, J. C. (2001). Radiometric cross-calibration of the Landsat-7 ETM+ and Landsat-5 TM sensors based on tandem data sets. *Remote Sensing of Environment* 78(1-2): 39-54.
- Teillet, P. M., Fedosejevs, G., Thome, K. J. and Barker, J. L. (2007). Impacts of spectral band difference effects on radiometric cross-calibration between satellite sensors in the solar-reflective spectral domain. *Remote Sensing of Environment* 110(3): 393-409.
- Thomas, A., Byrne, D. and Weatherbee, R. (2002). Coastal sea surface temperature variability from Landsat infrared data. *Remote Sensing of Environment* 81(2-3): 262-272.
- Thome, K. J., Biggar, S. F. and Wisniewski, W. (2003). Cross comparison of EO-1 sensors and other Earth resources sensors to Landsat-7 ETM+ using Railroad

- Valley Playa. *IEEE Transactions on Geoscience and Remote Sensing* 41(6): 1180-1188.
- Tzortziou, M., Subramaniam, A., Herman, J. R., Gallegos, C. L., Neale, P. J. and Harding, J. L. W. (2007). Remote sensing reflectance and inherent optical properties in the mid Chesapeake Bay. *Estuarine, Coastal and Shelf Science* 72(1-2): 16-32.
- Wang, M. H. and Gordon, H. R. (2002). Calibration of ocean color scanners: how much error is acceptable in the near infrared? *Remote Sensing of Environment* 82(2-3): 497-504.
- Wang, P., Boss, E. S. and Roesler, C. (2005). Uncertainties of inherent optical properties obtained from semianalytical inversions of ocean color. *Appl. Opt.* 44(19): 4074-4085.
- Wright, H. (1997). Qualitative and Quantitative Analysis of the Changes in Vegetation, Sediment and water on Seal Sands in the Tees Estuary between 1992 and 1994. *Geography* M.Sc. by Research, 89.
- Xiong, X. (2011). NASA Goddard Space Flight Center. Personal Communications.
- Yang, H. and Gordon, H. R. (1997). Remote sensing of ocean color: assessment of water-leaving radiance bidirectional effects on atmospheric diffuse transmittance. *Appl. Opt.* 36(30): 7887-7897.